Development and Characterisation of Noncovalently Functionalised Graphene Field-Effect Transistors and Their Application as Specific Biosensors

Laura von Lüders, M. Sc.

Vollständiger Abdruck der von der Fakultät für Elektrotechnik und Informationstechnik der Universität der Bundeswehr München zur Erlangung des akademischen Grades eines

Doktors der Naturwissenschaften (Dr. rer. nat.)

genehmigten Dissertation.

Gutachter/Gutachterin:

1. Prof. Dr. Georg S. Duesberg

2. Prof. Dr. Martin Hegner

Die Dissertation wurde am 06.06.2023 bei der Universität der Bundeswehr München eingereicht und durch die Fakultät für Elektrotechnik und Informationstechnik am 28.11.2023 angenommen. Die mündliche Prüfung fand am 06.12.2023 statt.

der Bundeswehr
Universität München

Development and Characterisation of Noncovalently Functionalised Graphene Field-Effect Transistors and Their Application as Specific Biosensors

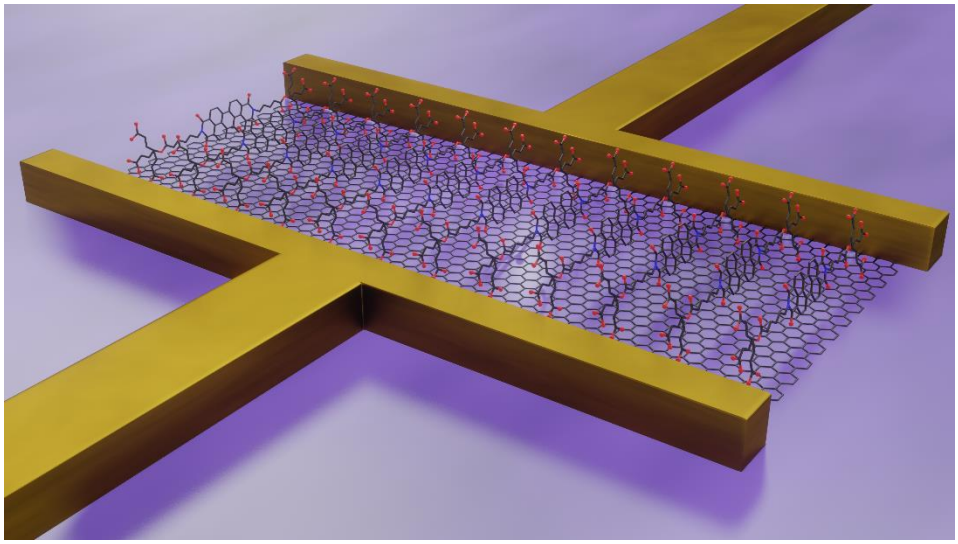

by

Laura von Lüders, M. Sc.

under the supervision of Prof. Georg S. Duesberg

This thesis is submitted to the University of the Bundeswehr Munich, Institute of Physics, EIT 2, Faculty for Electrical Engineering and Information Technology, for the degree of Doctor rerum naturalium (Dr. rer. nat.)

May 2023

Declaration

I hereby declare that the presented thesis is my own work and every content was acquired, analysed and written by myself if not stated otherwise. This thesis is submitted to the Institute of Physics, EIT 2, Faculty of Electrical Engineering and Information Technology at the University of the Bundeswehr Munich and is not under consideration at any other German or foreign university.

_____

Laura von Lüders

Abstract

This thesis presents a detailed investigation of the development and characterisation of a reliable and specific biosensor based on graphene. The entire procedure involves multiple processing steps, each of which is characterised using various techniques including Raman spectroscopy, scanning electron microscopy (SEM), atomic force microscopy (AFM), and electrical measurements. High-quality monolayer graphene is grown *via* chemical vapour deposition (CVD) and subsequently noncovalently functionalised with one out of two perylene derivatives. Both are found to self-assemble homogeneously on the graphene surface, with layer heights of 1.1 nm to 1.5 nm derived by AFM. The following wet-chemical transfer onto a SiO_2/Si substrate finalises the so-called Functional Layer Transfer (FLaT) of graphene. The resulting sample is structured into a graphene field-effect transistor (GFET) array consisting of eleven devices on one chip. Onto the carboxylic groups of the perylene molecules, anti-methamphetamine antibodies (methamphetamine-ABs) are coupled specifically. Indirect measurements using a second antibody conjugated with gold nanoparticles are used to develop and optimise a reliable treatment protocol for the specific functionalisation. The study reveals the stable and homogeneous perylene FLaT graphene surface, with a reliably functionalised methamphetamine-AB monolayer of approximately 5.1 nm. Subsequently, a variety of electrical measurements is conducted and the specificity of the biosensor towards methamphetamine validated. A strong signal dependency with the methamphetamine concentration is found, where the limit of detection is not observed at the lowest concentration of 300 ng/ml. No cross-reactivity towards a placebo molecule of similar size is observed. To investigate the versatility of the protocol, fragment antigen-binding regions (Fab) of the anti-cortisol antibody are immobilised on the perylene functionalised graphene. The homogeneity and coverage of the anti-cortisol Fab fragments can be improved; however, the biosensors do detect cortisol at a concentration of 10 µg/ml. Furthermore, the study examines the stability and lifetime of the methamphetamine-ABs immobilised on the GFETs and reveals that the antibodies remain functional for at least 17 hours in ambient conditions. A comprehensive comparison of the two perylene molecules used indicates a slightly more homogeneous self-assembly of the typically used molecule, but a possibly improved sensing behaviour when using the newly synthesised perylene molecules.

Zusammenfassung

Diese Arbeit präsentiert eine detaillierte Untersuchung der Entwicklung und Charakterisierung eines zuverlässigen und spezifischen Biosensors. Der gesamte Prozess umfasst mehrere Schritte, von denen jeder mit diversen spektroskopischen und (elektronen-)mikroskopischen Techniken und elektrischen Messungen charakterisiert wird. Hochwertiges monolagiges Graphen wird mittels chemischer Gasphasenabscheidung (CVD) hergestellt und anschließend nicht-kovalent mit einem von zwei Perylen-Derivaten funktionalisiert. Beide zeigen eine homogene Selbstorganisation auf der Graphenoberfläche, wobei Profilhöhen von 1,1 nm und 1,5 nm abgeleitet werden. Die anschließende nasschemische Übertragung auf ein SiO_2/Si-Substrat finalisiert den sogenannten Functional Layer Transfer (FLaT) von Graphen. Die resultierende Probe wird zu einem Graphen-Feldeffekttransistor (GFET)-Array mit elf GFETs strukturiert. Auf die Carboxygruppen der Perylenmoleküle werden spezifisch Anti-Methamphetamin-Antikörper (methamphetamin-ABs) gekoppelt. Indirekte Messungen unter Verwendung eines mit Goldnanopartikeln konjugierten zweiten Antikörpers werden verwendet, um ein zuverlässiges Protokoll für die spezifische Funktionalisierung zu entwickeln und zu optimieren. Die Studie zeigt eine stabile und zuverlässig funktionalisierte methamphetamin-AB-Monolage von etwa 5,1 nm. Anschließend werden verschiedene elektrische Messungen durchgeführt und die Spezifität des Biosensors gegenüber Methamphetamin validiert. Es wird eine starke Signalabhängigkeit von der Analytkonzentration festgestellt, wobei die Nachweisgrenze noch nicht erreicht wird. Es wird keine Kreuzreaktivität gegenüber einem Placebo-Molekül ähnlicher Größe beobachtet. Um die Vielseitigkeit des Protokolls zu untersuchen, werden Fragment-Antigen-Binding-Regionen (Fab) des Anti-Cortisol-Antikörpers auf dem FLaT funktionalisierten Graphen immobilisiert. Die Homogenität und Abdeckung der Anti-Cortisol-Fab-Fragmente können verbessert werden; trotzdem werden 10 µg/ml Cortisol erkannt. Ein umfassender Vergleich der beiden verwendeten Perylenmoleküle deutet auf eine leicht homogenere Selbstorganisation des üblicherweise verwendeten Moleküls hin, aber möglicherweise auf ein verbessertes Sensorenverhalten bei Verwendung der neu synthetisierten Perylenmoleküle.

Acknowledgements

Firstly, I would like to thank Prof. Georg S. Duesberg for taking me on as a master's student, despite my limited knowledge of 2D materials at that time, and I am especially grateful that he subsequently accepted me into his group as a PhD student. Right before I started my PhD, he said: “It’s going to be some of the most stressful and frustrating years, but also some of the best years of your life.” And, what can I say, he was absolutely right. I would very much like to thank Georg Duesberg for believing in my ability to dive into the new topic, and especially educate myself in the field of biosensing, which developed to be my new passion. I am additionally grateful for the possibility to attend conferences and meet new people.

Furthermore, I would very much like to thank Dr. Kangho Lee for his constant support and guidance throughout the past years. Especially for introducing me to several laboratory techniques but also for his very patient nature when answering my questions or proofreading my work, as well as for the interesting and fruitful discussions.

I would like to thank Dr. Tanja Stimpel-Lindner for her support with whichever problem occurred concerning tools or administrative matters, and Dr. Torsten Sulima, who supported me with his detailed knowledge of IT and paper work. I would also like to thank Dr. Josef Biba for his helpful insight in the tools and lab work, as well for his constructive support in general matters. Special thanks go to Peter Frank, Daniel Tonigold and the past members of the technical workshop for their support, with whom I always had a fun time together.

I am grateful for the support of Dr. Cian Bartlam, who provided me with his deep insight into chemistry and AFM-related topics. Special thanks go to Dr. Cormac Ó Coileáin, who was always available for discussions and editing.

I would like to thank Dr. Rita Tilmann for her easy-going and positive nature, which brought so much joy to the office and the labs, for her emotional support and finally, for her friendship. I am extremely happy to have shared an office with her, Oliver Hartwig and Max Prechtl for so many years, and I am grateful for all the relaxing nerve gun fights between interesting scientific and non-scientific discussions.

I would like to thank Mark Viebrock and Sebastian Klenk for their aid in chemistry-related discussions. Many thanks also go to Nikolas Dominik, Natalie Galfe, Stefan Heiserer, Simon Schlosser, Andreas Schels, Florian Herdl and Jonathan Preitnacher who I had the pleasure of spending so much time with.

I would like to thank everyone in the institute for making my time as enjoyable as it had been, for the numerous interesting and challenging times but also for the fun, happy and delightful moments. I will keep these years in honourable memory.

I would like to thank my friends for their emotional support and for keeping me busy in the life outside university. Finally, I would like to thank my parents Nina and Peter for making everything possible in my life that was in their power, for allowing me to make my own mistakes while always knowing that they had my back, for supporting me in every decision and always encouraging me to keep going and stay curious. I am so very grateful for my brothers Benedikt and Phillip who inspire me and show me all the possibilities that are waiting out there. Last but not least, I sincerely thank my husband Christian for his constant emotional support, for being my best friend and for being my tower of strength.

Table of Contents

Abbreviations

AFM ..... Atomic force microscopy
APS ..... Ammonium persulfate
AuNP..... Gold nanoparticle
BSE..... Backscattered electrons
CDR..... Complementary determining regions
CM..... Chemical mechanism
CNP ..... Charge neutrality point
CVD..... Chemical vapour deposition
DI water..... Deionised water
DMSO..... Dimethyl sulfoxide
EDC..... N-(3-dimethylaminopropyl)-N′-ethylcarbodiimide hydrochloride
EM..... Electromagnetic mechanism
FLaT..... Functional layer transfer
FTIR..... Fourier-transform infrared spectroscopy
FWHM..... Full width at half maximum
GERS..... Graphene-enhanced Raman spectroscopy
GFET ..... Graphene field-effect transistor
GO ..... Graphene oxide
HOMO ..... Highest occupied molecular orbitals
HOPG..... Highly oriented pyrolytic graphite
IPA ..... Isopropanol
IR..... Infrared
LOD..... Limit of detection
LPE ..... Liquid-phase exfoliation
LUMO..... Lowest unoccupied molecular orbitals
MFC ..... Mass flow controller
MOSFET ..... Metal oxide semiconductor field effect transistor
NHS ..... N-hydroxysuccinimide
PBASE..... 1-pyrenebutanoic acid succinimidyl ester

PBI ..... Perylene bisimide
PMMA ..... Poly(methyl metacrylate)
PSPD ..... Position-sensitive photodiode
PTA Perylene-3,4,9,10-tetracarboxylate
PTCDA 3,4,9,10-perylenetetracarboxylic 3,4:9,10-dianhydride
rGO ..... Reduced graphene oxide
rpm ..... Rounds per minute
SAM ..... Self-assembled monolayer
sccm ..... Standard cubic centimetres per minute
SE ..... Secondary electrons
SEM ..... Scanning electron microscopy
SERS ..... Surface-enhanced Raman scattering
SiC ..... Silicon carbide
STM ..... Scanning tunnelling microscopy, Scanning tunnelling microscopy
vdW ..... Van der Waals

1 Introduction

1.1 Two-Dimensional Materials

Beginning with the successful isolation of a freestanding graphene in 2004 *via* micromechanical exfoliation from graphite, the research community has shown intensive interest in two-dimensional (2D) materials.[1] These materials consist of single sheets of a layered 3D crystal that can be separated from the bulk material due to the weak van der Waals forces between the individual layers. The isolated crystalline 2D sheets typically derive mechanical stability from their strong covalent in-plane bonds and are often stable in ambient conditions. This anisotropy is also reflected in their properties, with characteristics that often differ between in-plane and out-of-plane behaviour. The unique physical and chemical properties of 2D materials arise from their ultra-thin nature, are highly dependent on their structure and often differ significantly from their bulk counterparts. For instance, graphene demonstrates excellent high charge carrier mobilities along the plane of the 2D sheet, which are the result of quasiparticles so-called massless Dirac fermions.[2] Since the ideal graphene is sp^2 hybridised, one of the four valence electrons per carbon atom interconnect and form weak π-bonds with neighbouring electrons, creating a charge carrier gas that allows electrons or holes to escape from the confinement present in the 3D graphite.[1,3] Upon other exciting characteristics due to the 2D confinement, this discovery led to an increasing interest in isolating monolayers of other layered 2D materials.[4] Since then a number of different materials have been discovered, which have a broad range of properties, including interesting electrical, optical, chemical and physical properties.[5–8]

Graphene is a single layer of carbon atoms arranged in a hexagonal lattice structure, which is stable in ambient conditions although 2D crystals were supposed to be thermodynamically unstable, even could not exist in the past.[9,10] It is known for its exceptional mechanical, thermal, and electrical properties that are beneficial for numerous applications including composites,[11–13] membranes,[14] energy storage,[15,16] solar cells[11,17] and in a variety of electronic devices.[14,18–20] Despite the excellent charge carrier mobilities of graphene, the application of the 2D material in some electrical devices is limited due to the lack of a band gap. As a consequence, it is not possible to “turn-off” graphene devices in general, which are therefore

always conductive.[21] This is disadvantageous for the use of graphene as a transistor channel in digital logic devices, where a bandgap for device modulation is required. To open a bandgap in graphene, the introduction of uniaxial strain,[22] formation of nanoribbons[23] or doping[24] can be used, which, however, simultaneously degrade graphene's inherent electronic properties. Nonetheless, the "zero-bandgap" nature of graphene is still highly beneficial in other applications that do not require "turn-off" of devices, e.g. analogue devices.

One of the most exciting applications of graphene with extensive interest in improvement is its use in biosensors, which are devices that can detect biological molecules with high sensitivity and specificity. Biosensors have numerous applications in medical diagnosis and monitoring,[25–29] drug delivery,[30,31] or tissue engineering,[32] among others. In the literature, various types of biosensors can be found, ranging from the classic enzyme-linked immunosorbent assay (ELISA),[33,34] over surface plasmon resonance (SPR),[35] fluorescence resonance energy transfer (FRET),[36] to graphene field-effect transistors (GFETs)[29,37,38] and many more. They are used in numerous fields including disease marker recognition, health monitoring[38–41] or for the detection of drug abuse.[42–45] Various approaches have been carried out to receive best possible sensitivity, specificity and reproducibility. With the advancing nanomaterials, a new field of innovative functional materials was discovered. Especially for graphene, the high surface area and extraordinary electrical conductivity and mobility improve the sensitivity of biosensors.[46] However, developing specific biosensors for the detection of a particular biological molecule remains a significant challenge. In order to achieve this goal and to fully realise the potential of graphene, it is necessary to modify its surface chemistry and to obtain specific functional groups that can selectively bind to the target molecule.[47] In recent years, different routes to modify the surface chemistry have been investigated, which can be separated into covalent and noncovalent functionalisation.[27,48,49] Noncovalent functionalisation is a widely adopted approach for exploiting the properties of graphene while keeping its inherent properties. This technique involves the self-assembly of organic molecules on the surface of graphene without causing defects or disturbing the lattice structure of graphene, thereby preserving its electrical properties.[50,51] Up to now, significant progress has been made in the development of non-covalently functionalised graphene biosensors for the detection of a wide range of biological molecules, including proteins,[52] DNA,[53,54] and pathogens.[27,50,55–57] However, it is challenging to meet all requirements in one biosensor, namely to target specific molecules and achieve low cross-reactivity, to use it in a versatile way and adapt it to different target molecules, and to achieve a concentration-dependent signal, which is necessary for several applications.

Overall, the study of 2D materials and their functionalisation is an exciting and rapidly evolving field, with the potential to revolutionise various areas of science and technology. The aim of this dissertation thesis is to investigate the use of noncovalently functionalised graphene for the realisation of specific biosensors for the detection of a particular biological molecule. The thesis will focus on the design and synthesis of specific functional groups for the selective binding of biomolecules to the graphene surface, as well as the development of a sensitive and reliable biosensor platform for the detection of the target molecule.

1.2 Outline

This dissertation thesis covers the complete spectrum from the synthesis of graphene to its noncovalent functionalisation, the fabrication of graphene field-effect transistors and the final characterisation of the specific and reliable biosensors.

In chapter 2, a general introduction to graphene's crystallographic structure and resulting exceptional properties is given, and interesting applications are identified. Several synthesis methods to adjust to the requirements of different applications are stated and compared. In this thesis, only graphene synthesised from chemical vapour deposition (CVD) is used, which has been found to be most suitable for the aim of this work. Furthermore, different approaches for surface modification are given, out of which noncovalent functionalisation is chosen for this work. The theory of the specific coupling processes relied upon in this thesis is addressed. Several characterisation techniques are used throughout the thesis, of which the working principles are explained.

Chapter 3 focusses on the methods required to obtain specific GFET biosensors. Two graphene transfer processes are presented and the steps to structure the transferred graphene towards a GFET are described. Additionally, the necessary functionalisations steps to obtain a specific biosensor are introduced.

In chapter 4, a full characterisation of the CVD grown monolayer graphene is presented using scanning electron microscopy (SEM), atomic force microscopy (AFM) and Raman spectroscopy. The same characterisations are performed on functionalised graphene, where especially the two transfer processes are compared. Raman spectroscopy of the perylene bisimide (PBI) molecule, which is mostly used throughout the thesis, is comprehensively investigated.

In chapter 5, the specific coupling of antibodies to the perylene molecule on graphene is investigated and the working principle is proven. Several tests using a marker visible in SEM

are conducted to investigate the necessity of the linker molecule, the coupling procedure and the optimal parameters to obtain the highest receptor density. Several aspects including the antibody concentration and the protocols to remove unwanted molecules are examined in greater detail. The development of a homogeneous biosensor platform using the visualisation of receptor sites by gold nanoparticles are demonstrated.

The subsequent chapter 6 focusses entirely on the characterisation of GFET biosensors due to functionalisation with antibodies and the subsequently applied analyte. A renewed optimisation of anti-methamphetamine antibody concentration is conducted and subsequently methamphetamine antigen successfully detected. The specificity of the coupling procedure as well as its concentration-dependency is verified. For consistency, the two initial transfer processes are compared using electrical characterisation. A time-dependency on the binding of methamphetamine to the methamphetamine biosensor platform is investigated. Additionally, the stability of the methamphetamine biosensor platform is tested and the lifetime of methamphetamine biosensors examined.

A second perylene molecule is introduced starting from its synthesis to the final GFET biosensor in chapter 7. The molecule as a powder and as self-assembled monolayer on graphene is characterised using SEM, AFM, Fourier-transform infrared spectroscopy (FTIR), Raman spectroscopy as well as electrical measurements. The two perylene molecules are compared in terms of their efficiency and antibody coupling characteristics. Finally, their quality as a methamphetamine biosensor is compared. As an outlook, the detection principle is applied to the cortisol antibody system in first attempts.

In the end, the conclusion is drawn in chapter 8 and an outlook for possible interesting future work is presented.

2 Background

In this chapter, the fundamentals for the development of a reliable and specific graphene biosensor are presented. This includes the structure, synthesis and characterisation of graphene with its specific functionalisation to realise reproducible graphene biosensors. This is followed by the theoretical background of the characterisation methods used throughout the thesis.

2.1 Graphene

Graphene is the 2D allotrope of carbon, consisting of a single sheet of hexagonally arranged carbon atoms. As one of the best known and most understood 2D materials, graphene is still in the centre of attention in many research fields.[12,58–61] It is becoming of increased interest for industrial applications, such as for solar cells,[61] touch screens,[62] or anti-corrosion coating[63] as well as in the sensor field as wearable and pressure sensors[12,64] or biological and chemical sensors.[65–67] With its unique (opto)electronical,[60–62,68,69] mechanical[63,64,70] and chemical properties,[40,58,71,72] it offers a variety of research fields from synthesis to the final product suitable for everyday use.

2.1.1 Structure

Graphene is a single layer of sp^2-hybridised carbon atoms, which form a hexagonal crystal lattice (see Figure 1).[69] The unit cell of the honeycomb structure is set up by two triangular sublattices, each characterised by the lattice vectors a_1 and a_2. Their respective starting atoms A and B (red and green, respectively) are separated by the carbon-carbon distance (c) of 1.42 Å.[70,73] The first Brillouin zone (blue) is magnified in Figure 1b), with its six high symmetry points at the corners. Due to symmetry, these points are labelled K and K′. The reciprocal lattice vectors b_1 and b_2 originate from the Brillouin centre (Γ).

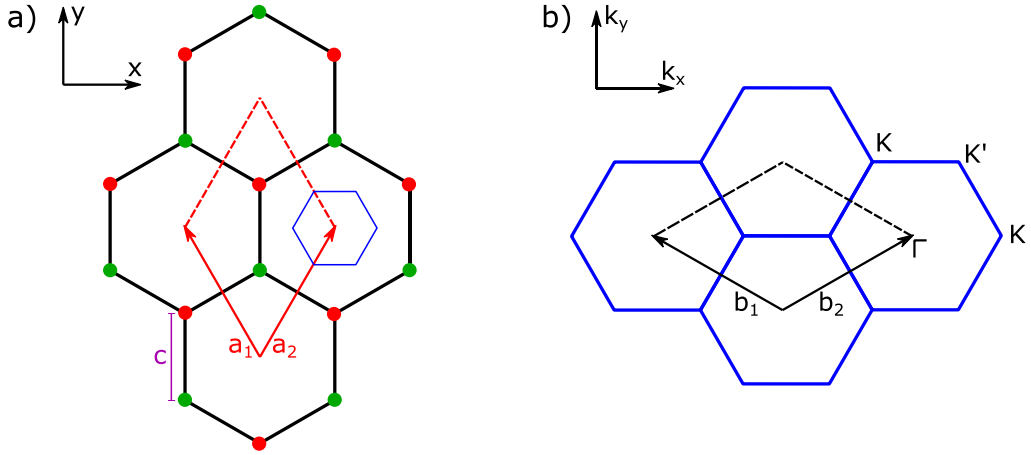

Figure 1. a) Hexagonal graphene lattice with the two sublattices indicated by red and green atoms. The unit cell is spanned-up by the lattice vectors a_1 and a_2. The parameter c displays the inter carbon-carbon distance of 1.42 Å. The first Brillouin zone (blue) is magnified in b) with its reciprocal lattice vectors b_1 and b_2 originating in the Γ-point. The high symmetry points K and K′ are displayed at the edges. Image modified after Jorio *et al.*[74]

The graphene honeycomb structure results from the hybridisation of two 2p orbitals and one 2s orbital per carbon atom.[70] This generates the three in-plane sp^2 orbitals with angles of 120° to each other. Thus, σ bonds between the covalently bound neighbouring carbon atoms are formed. Perpendicular to these three σ bonds, one "free" p orbital exists, which interacts with the "free" p orbitals from neighbouring atoms forming π-bonds.[75] This results in delocalised electrons over the 2D crystal lattice and are the essence of graphene's extraordinary electrical properties.[58] The resulting electronic band structure can be described as a cone, where conduction and valence band are separated but touch at the K- (or Dirac) points. Thus, graphene is considered a semi-metal or a "zero-bandgap" semiconductor. The dispersion relation is linear near the Dirac-points, given the equation:

$$E = \nu_F h\kappa \quad [69] \tag{1}$$

with the energy E, the Fermi velocity ν_F ~10^6 ms^{-1}, the Planck's constant h and the wave number κ.[18] This mimics the mathematical description of massless Dirac fermions resulting in the electrons having zero effective carrier mass at the Dirac points.[2,69,76] In graphene, the electron transport mechanism relies on electron-electron interaction rather than electron-lattice interaction.[69] The Dirac point is also known as the charge neutrality point (CNP), because the majority charge carriers change from electrons to holes (or vice versa) at these locations, granting the ambipolarity of graphene. This can be seen in Figure 2a-c), where n-type doping, no doping and p-type doping are depicted, respectively.

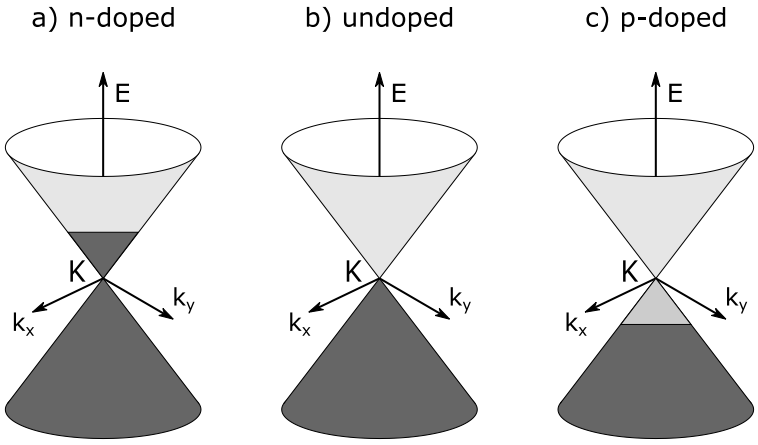

Figure 2. Dirac cones in three doping constellations: a-c) n-doped, undoped and p-doped, respectively. The colouring reveals electrons and holes as majority charge carriers for a) and c), respectively. The linear dispersion through the K- or Dirac point in the centre is displayed. Image modified after Jorio *et al.*[74]

2.1.2 Properties and Applications

Graphene has a variety of exceptional properties that cannot be found in this combination in any other material. Those properties are highly investigated and can be useful for a number of applications. The electrical properties, which are probably the best known and most widely used ones, are a result of graphene's interesting band structure, as described in the previous chapter. The extremely high charge carrier mobilities of up to 200,000 $cm^2V^{-1}s^{-1}$ [77,78] and electrical conductivities in the order of 10^6 $S\,m^{-1}$ [64] at room temperature expose graphene to be an excellent material for various electrical applications including graphene field-effect transistors (GFETs), sensors and optoelectronic modulators.[60,69,79] GFETs have a high transconductance compared to other transistors, which is a measure of the ability of a transistor to amplify a signal expressed in Siemens (S). As a result, graphene based transistors can be used in higher frequency operation than conventional silicon based transistors.[63] Adding to this, the high spin-carrier lifetime make graphene useful for spintronics and terahertz research.[59,60] The major limiting factor of the electron transport mechanism are scattering processes, which occur due to a defective lattice, charge impurities, grain boundaries as well as cracks or wrinkles in the graphene.[80]

A second interesting electrical property lies in the ambipolarity of graphene. By tuning the Fermi energy of graphene *via* the change of the electrostatic field, the conduction regime can continuously be changed between electron and holes as charge carriers.[69,77] This enables graphene to be used in a field-effect transistor (FET) configuration, but GFETs inherently

do not compete with conventional semiconductors, e.g. Si[58], due to the limited on/off current ratio.

As a consequence of the "zero-bandgap" nature of graphene, it can absorb a broad spectrum of light from ultraviolet to infrared (IR) and terahertz. In the visible spectrum, graphene absorbs 2.3 % of the incident light.[69,81] The absorption can be controlled by electrostatic gating or doping, which tunes the Fermi energy of graphene. As a result, the mid-IR regime can become more transparent, which can be exploited in dynamic optical device applications.[14,60,63] The optical properties combined with the electrical ones make graphene extremely interesting as e.g. organic light emitting diodes which are used in touch screens or applications such as solar cells or transparent electrodes.[61,62,68]

As a result of the three covalent σ bonds per carbon atom, graphene has exceptional mechanical properties with a Youngs modulus of 1 TPa[69,70] and a tensile strength of 130 GPa,[69,82] granting the material a high mechanical strength and structural robustness.[63,64] Furthermore, graphene exhibits a high thermal conductivity of approximately 5,000 $W\ m^{-1}K^{-1}$,[64,69,70] allowing for quick heat dissipation in electronic devices. Due to graphene's chemical inertness, it is highly desired for applications as gas barrier,[83] water purification,[63] water quality sensors[80] or anti-corrosion coating.[63] It has been found that the introduction of strain into graphene's lattice due to e.g. bending of the material results in a measurable signal, making graphene an interesting choice for both wearable and pressure sensors.[12,64]

The two-dimensional nature of graphene grants not only a very light-weight material with 0.77 $mg\ m^{-2}$,[63,71] but also a high surface-to-volume ratio, making it highly sensitive to its environment. It is especially sensitive to electrochemical changes in its vicinity,[58] which finds applications as a transducer for biological or chemical sensors.[65–67] A wide range of sensors has been developed so far, modifying either the structure of graphene itself or its surface to the specific application, including the introduction of defective sites or the functionalisation of the surface with molecules. Numerous contributions with novel applications and reviews about the improvement of graphene-based sensors have been published in the past years.[40,58,71,72] An interesting class of sensors are GFETs, combining the excellent electrical properties with the "all-surface" nature of graphene. In this case, graphene acts as the transducer material, granting high sensitivity and fast response times.[58] Graphene is also highly sensitive to even small amounts of contamination, which has severe effects on the conductivity and doping of the graphene-based device.[84] Numerous researchers have attempted to reduce these contaminations ranging from simple procedures such as annealing,

encapsulation or plasma etching, to highly elaborate methods using atomic force microscopy for surface cleaning or complicated transfer procedures.[85–88]

2.1.3 Production of Graphene

The various production techniques to obtain graphene can be divided into two groups, which are characterised by their different approaches: top-down and bottom-up.[89] As each method has its own advantages and disadvantages in terms of the quality and performance of graphene, careful consideration must be given to selecting the most suitable one for each specific application.[47,90]

In the most common top-down approaches, individual graphene layers are separated from bulk graphite.[47,91] This is possible due to van der Waals (vdW) forces holding the individual graphene layers together to build the three-dimensional structure. These vdW forces are weak in comparison to the covalent bonds within the graphene 2D plane, making it possible to cleave the layers without disrupting the single graphene sheet itself.[91]

Most of the applications mentioned in the section 2.1.2 Properties and Applications require scalable graphene with reliably high quality to ensure reproducible device performance. This is best conducted using bottom-up approaches which are based on the assembly of carbon atoms to form the graphene layer.[91,92]

In the following, the main representatives of each approach will be discussed.

2.1.3.1 Mechanical Exfoliation

The first time a single sheet of graphene was obtained, Geim *et al.*[1] exploited the weak vdW forces between graphene layers using mechanical exfoliation. In the original method, when adhesive tape was placed onto a highly oriented pyrolytic graphite and subsequently peeled off, multi-layered graphene flakes were stuck to the tape. After repeatedly pressing a fresh tape to the graphene multilayer flakes on the first tape, the flakes were gradually thinning and eventually a single layer of graphene remained on the tape. This was then pressed to the desired substrate and the tape carefully removed, leaving high-quality monolayer graphene behind.[69] Since then, the technique has evolved and a number of graphene sheets have been fabricated. Their analyses have provided the research community with valuable information about optical, electrical and mechanical properties of the non-defective, pristine 2D material.[93] The highest electron mobilities were measured on mechanically exfoliated graphene and the superior mechanical properties of graphene can be best observed here. Major drawbacks are the low throughput and lack of scalability, with only a few tens of

micrometres in lateral size per graphene flake.[93] Thus, this approach is highly impractical for industrial implementation and mainly used for fundamental research and proof-of-concept applications.[90]

2.1.3.2 Liquid Phase Exfoliation

A second highly investigated top-down approach is liquid phase exfoliation (LPE).[90] Graphite powder is first dispersed in a solvent and shear forces, e.g. ultrasonication, are introduced to separate into individual layers.[94] The first obtained dispersion contains a broad distribution of flake sizes and thicknesses. Through several steps of centrifugation, this distribution can be narrowed down to receive relatively homogeneous dispersions. Scalability has proven to be a delicate issue since the lateral size decreases with the layer thickness. The dispersions can be drop-casted, sprayed or transferred using Langmuir-Blodgett method onto a desired substrate and a film structured by graphene flakes is obtained. LPE has been highly investigated in the past years due to the relatively low levels of defects, while having low production temperature, time and cost. The optimisation of this production technique in terms of yield, stability and size-thickness distribution has its focus on the variation of solvents, force modulation as well as centrifugation.[90,95] The addition of surfactants may be beneficial as it enhances the dispersion stability, but requires a stronger washing procedure to obtain clean and high quality dispersions. The control of quality, flake size and layer number within formed graphene films still remains challenging and it results in restricted application feasibilities.[95] Further exfoliation techniques such as electrolytic exfoliation or chemical exfoliation have been proposed, but all have in common, that the graphene flake size is extremely limited.[96] While LPE might not be the best production method toward high performance electronics, applications in composite materials for granting additional mechanical strength, catalysis or in energy storage is suitable and have been intensively studied.[12]

2.1.3.3 Reduced Graphene Oxide

To obtain graphene oxide (GO), graphene is intentionally exposed to strong acids, resulting in the creation of oxygen moieties in the graphene lattice. The resulting defects can then be used to covalently bond molecules to the GO. After a subsequent reduction through chemical and thermal treatments, reduced graphene oxide (rGO) is obtained. However, some oxidised defects remain on the graphene basal plane, which are open for further covalent functionalisation as well.[47,97] While this material is inexpensive and easy to process, a large

amount of defects in the material remains and results in low mobilities in comparison to other types of graphene.[58]

2.1.3.4 Chemical Vapour Deposition

In chemical vapour deposition (CVD), gaseous precursors in a carrier gas flow are directed over a heated substrate in a growth chamber.[93] Typically, two types of systems are differentiated, hot-walled and cold-walled CVD systems. The former involves heating both the walls of the reactor and the growth substrate, commonly using a quartz tube surrounded by a heating element (see Figure 3). Although this method provides uniform substrate heating and easy construction, there is a risk of contamination from heated side walls and uncontrolled chemical reactions due to overheating. On the other hand, cold-walled reactors have a heating mechanism inside the chamber, which is insulated from the outer walls. This reduces the likelihood of uncontrolled effects, even if the walls are contaminated, and facilitates consistent results. However, there may be uneven growth rates due to an inevitable temperature profile over the catalyst unless appropriately accounted for.

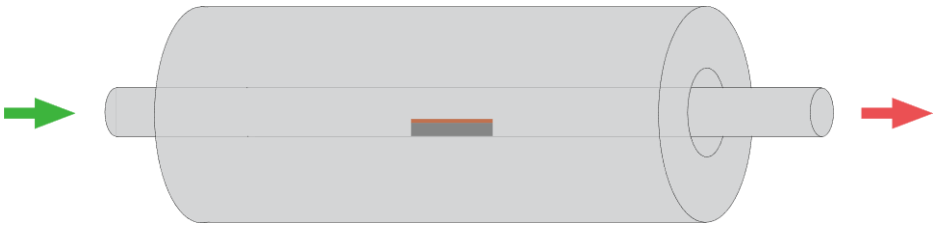

Figure 3. Illustration of a CVD growth quartz tube furnace with the inlet for gases on the left (green) and direction of exhaust to the right (red). In the centre of the furnace is a quartz boat (dark grey) with Cu foil (dark orange) on top as catalyst for graphene growth.

A wide range of growth substrates can be chosen, out of which some are more preferable due to a more desirable morphology, specific surface area and quality of the synthesised graphene.[47] To quicken the growth process and decrease the temperature needed for the growth process to occur, a catalytic substrate can be chosen, which was found to simultaneously increase the graphene quality.[98] Copper (Cu) and nickel (Ni) as transition metals are the most widely used catalytic substrates for graphene growth. The solubility of carbon in Cu is comparably low at the growth temperature (0.005 carbon wt%) and upon cooling, the solubility decreases further.[60,99] In contrast to this, the solubility of carbon in Ni is much higher and multilayers are formed.[99]

For graphene growth, hydrocarbons such as methane (CH_4) are used as precursors. At elevated temperatures, these precursors thermally decompose and leave atomic carbon to

interact with the chosen substrate. Typically, polycrystalline Cu foil is used, on which the carbon species migrate until they start a nucleus or join existing nuclei. The nucleation is generally initiated at locations with lowest activation energy. A nucleus starts either through the statistical nucleation process, when supersaturation[100] is reached or at defective sites of the substrate, where the activation energy is less. Thus, the graphene starts to grow on different nucleation sites and in random orientations on the typically used polycrystalline Cu foil. More carbon adatoms join at the edges and eventually merge the domains into a continuous, large-scale polycrystalline film.[87,101] For Cu, the growth process is self-limiting, resulting in a monolayer of graphene.[102–104] The lattice mismatch of graphene on Cu is small, resulting in a high quality film due to less strain within the material.[105] This, however, is damped by the mismatch of the thermal expansion coefficients between graphene and Cu, resulting in compressive strain after growth.[106] As a consequence, thermal expansion folds might arise in the graphene layer.[87]

The concentration of precursors, temperature, and pressure can regulate the density of nucleation on the Cu foil and the number of layers of the synthesised graphene.[47,60,93] In the case of too high temperatures, the diffusion of adatoms on the surface might become too quick, resulting in possible 3D structures rather than a 2D monolayer. In contrast, a temperature too low doesn't provide enough energy for the desired arrangement of adatoms, which might result in a highly polycrystalline or amorphous film. The benefit of graphene growth on Cu lies in the wide range of possible parameters to obtain monolayer graphene.

The inherent carbon concentration in the Cu foil was found to result in high graphene flake nucleation during CVD growth.[107,108] Thus, a pre-treatment of the Cu foil with a diluted oxygen flow was found to remove the carbon from the foil and, thus, decrease the graphene nucleation greatly.[109] The resulting enrichment of oxygen in the Cu foil can successfully be reduced by a subsequent hydrogen treatment.[108] Kraus *et al.*[109] observed a strong reduction of defects in the graphene layer as well as the growth of large monolayer flakes by oxygen pre-treatment and the targeted use of hydrogen in their sophisticated research of CVD growth kinetics. Additionally, hydrogen plays an important role in the catalysis of hydrocarbon decomposition, controlling the graphene growth rate and carbon surface concentration. The decomposition reaction contains several steps, which can be found in literature.[99,110] The basic decarbonisation reaction is the following:

$$CH_4 \rightarrow C_{gr} + 2H_2$$ [109] (2)

The introduction of H_2 into the growth process of graphene leads to a reduction in the growth rate, thereby enabling greater control over the process.[111]

CVD grown graphene is scalable and in theory unlimitedly large films can be grown.[104] Most often, graphene is grown on a metallic substrate, which is unsuitable for most applications. Thus, it has to be transferred onto an insulating substrate for following processes, which often involves the use of polymers. However, polymeric residues are challenging to remove completely and likely deteriorate the electronic system of graphene by forming unwanted charge trap points onto the surface resulting in doping effect.[98,112] Despite this obvious obstacle, the charge charrier mobilities were found to compete with mechanically exfoliated graphene, showing the high potentials of CVD grown graphene.[60,68,113] Even though relatively high growth temperature and inherent layer transfer remain an issue, the benefits of CVD growth prevail. These include the scalability and controllability of the process, resulting in highly crystalline monolayer graphene with strong homogeneity throughout the layer.[3] These criteria are highly sought in the commercial and industrial applications, therefore CVD growth may be the most promising synthesis approach.[70]

2.1.3.5 Epitaxial Growth

A second large-scale graphene production is epitaxial growth *via* thermal decomposition on a substrate.[47,114] Silicon carbide (SiC) has most commonly been used as substrate due to its semi-conductor nature and the possibility of direct integration after graphene growth.[115] At elevated temperatures around 1000 °C, the Si atoms sublime, leaving the carbon atoms to rearrange and form a graphene film.[47,98] This results in a lattice mismatch and strain especially in the lower levels of the SiC, while the top graphene layer is usually not as much affected.[116,117]

The main advantage of epitaxial growth is the direct integration of graphene as electrical devices on the semi-conductor substrate without having to transfer the graphene first.[47,116] During growth, an intermediate buffer layer develops, which degrades the electrical properties of the produced graphene. Several attempts to overcome this issue have been moderately successful, with the inclusion of intercalating dopants being one example.[115] Further drawback of this method are the high temperatures required during growth as well as high cost of the SiC.[47,98,115]

2.2 Graphene Surface Modification

Pristine graphene is characterised by a conjugated π-electron system and fully saturated 2D surface, which is chemically inert due to the lack of dangling bonds. Even though the chemical inertness is highly desired in some applications, it is a huge disadvantage in others, such as for (bio)sensors.[67] In that case, the specificity towards a specific molecule is required which is not given by pristine graphene itself.[97,115] Here, the all-surface nature of graphene is beneficial, making the material extremely sensitive to the surrounding environment. As a result, functionalisation of graphene has proven to be very effective.

The term functionalisation contains all approaches to manipulate and control the properties of a material. In the case of graphene, that mainly includes modifications to the electronic and chemical properties to enhance the performance in device applications.[115] Various functionalisation methods exist, which are characterised by different approaches. The careful evaluation of which method to use is the key for a successful application. The main methods can be classified into noncovalent functionalisation and covalent functionalisation, which will be discussed in the following sections.[48]

2.2.1 Noncovalent functionalisation

This type of graphene functionalisation is characterised by the adsorption of molecules on the 2D surface without the formation of actual chemical bonds. Instead, functionalities are introduced *via* physical matters such as π-interaction, electrostatic, hydrogen bonding, coordination bonding or vdW forces, giving it the name physisorption or physical adsorption.[47,118] This has the advantage that graphene's conjugated π-system remains intact, keeping its intrinsic properties untouched.[95,97] Noncovalent functionalisation is non-destructive to the graphene layer and, in principle, reversible.

π-interactions exist for large conjugated molecular systems that come in the vicinity of graphene, interacting with its π-system.[48] Especially for the self-assembly of conjugated systems, π-interaction is important.[119] Perylene molecules are a great example for noncovalent functionalisation of graphene, since they have a conjugated core and individual functionalities can be introduced easily. The basic perylene (Figure 4) consists of five benzene rings with all carbon atoms being sp^2-hybridised.

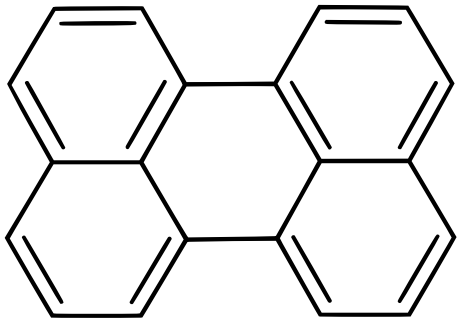

Figure 4. Basic perylene molecule with five benzene rings and sp^2-hybridised carbon atoms.

Graphene is negatively charged in nature and can interact with positively charged molecules *via* electrostatic interaction.[47] Additionally, the introduction of molecules onto the graphene results in charge transfer between them. If the molecular redox-potential of the molecule lies below the Fermi level of graphene, electrons move from graphene to the molecule and a p-type doping effect on the graphene can be observed. This occurs vice versa for n-type doping. Molecules with a strong permanent dipolar momentum induce an electric field, resulting in charge carrier doping on the graphene.

2.2.2 Covalent Functionalisation

In contrast to noncovalent functionalisation, covalent functionalisation relies on chemical bonds between the graphene and the functionalising structure (chemisorption). By breaking bonds in the conjugated π-system of graphene, new bonds open onto which molecules can be bound covalently. This structurally changes the hybridization from sp^2 to sp^3, altering the structural, chemical, optical and electrical properties of graphene.[47] For electrical applications, the resulting introduction of scattering sites and, thus, degradation of electrical properties is unwanted.[48]

One approach is the introduction of point defects such as vacancies or incorporating specific atoms in the graphene lattice, referred to as substitutional doping. This destroys graphene's structure as well but has effects on some electric properties especially for opening the bandgap, producing n- or p-type semiconductors out of graphene. The most widely used doping atoms in the lattice are boron or nitrogen due to their similar size to carbon.[115]

For biosensing applications, the excellent electrical properties of graphene are required and, therefore, noncovalent functionalisation is chosen for this work.

2.2.3 Immunochemistry

Immunology is the scientific study of the immune system, which involves the production of antibodies to recognise and neutralise foreign substances such as invading microorganisms and toxins. An immunoassay is a laboratory test that uses the principles of immunology to detect the presence or concentration of a specific substance in a sample. It involves the use of antibodies, which are proteins produced by the immune system to recognise and bind to specific molecules called antigens.[120]

The assay performed in this work is a homogeneous non-competitive immunoassay. In a homogeneous immunoassay, neither the antibody nor the substance of interest is labelled. Instead, the binding of the antigen to the unlabelled antibody is detected and measured using a variety of techniques, such as changes in mass, electrical conductivity, or fluorescence. In a non-competitive immunoassay, the antigen is measured directly, without the use of a labelled competitor molecule. Homogeneous non-competitive immunoassays are simple and easy to perform, needing no labelling or further molecules than the antibody and its antigen.

2.2.3.1 Antibody Structure

Antibodies are proteins, which consist of polypeptides and are produced by the immune system to identify and bind harmful substances such as bacteria or viruses. The antibody structure is generally Y-shaped and divided into two identical light (L) and a heavy (H) chains (see Figure 5a). Each of those chains consists of one variable (V) subunit at the end of each antibody arm. The remaining units are constant (C). Each antibody arm is referred to as Fab fragment (Figure 5b), being comprised of the variable region and the following constant subunit. Thus, each antibody can, in principle, bind to two antigens, one on each Fab.[121]

Each variable unit contains three complementary determining regions (CDR), which interact to recognise antigens. They are situated in the outermost part of the variable unit, called paratope, which is in direct contact to the antigens. The individual characteristics of the CDR determine the binding and type of antigens. For the binding of large proteins, the paratope is usually relatively flat, while small molecules tend to bind into cavity-like structures.[122,123]

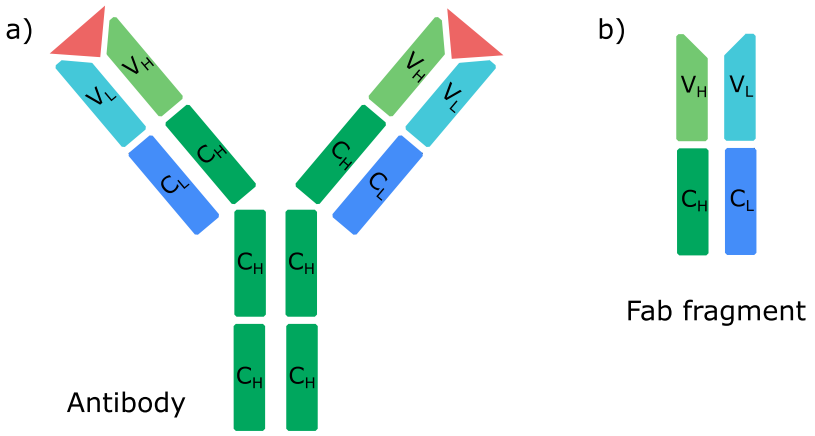

Figure 5. Schematic image of a) a monoclonal antibody with respective antigen (red) and b) the Fab-fragment.

For application, polyclonal or monoclonal antibodies can be used. To obtain polyclonal antibodies, an animal host is immunised against the desired target and the produced antibodies separated from their serum. Each antibody has generated individual CDRs against different antigen determinants, which are called epitopes. Thus, the specificity and affinity of each antibody is slightly different, resulting in disadvantages such as cross-reactivity.[124]

In contrast, monoclonal antibodies are cloned from a single antibody separated after its generation in the animal host. This ensures high specificity as well as high affinity against their antigen. In principle, an endless supply of the very same antibody can be produced.

2.2.3.2 Crosslinking Chemistry

Antibodies consist of a variety of functional groups, out of which amine groups are the most important ones in this work. They can be found over the whole antibody structure and usually point outward due to their polar nature. This makes them easily accessible for crosslinking chemistry, linking the antibody to the carboxylic group of a second molecule. This covalent bond is highly specific and robust, making it a key factor in the success of biosensing. One disadvantage is the loss of orientation control during immobilisation, because amine groups prevail over the whole antibody area.[125] In the following, the procedure of the crosslinking chemistry will be explained.

When the carboxylic acid groups of the molecule encounter the N-(3-dimethylaminopropyl)-N′-ethylcarbodiimide hydrochloride (EDC), an active intermediate is formed (see Figure 6). Due to its instability in aqueous solutions, N-hydroxysuccinimide (NHS) is introduced. This creates an NHS ester, which is amine-reactive and more stable than the previously formed intermediate. Upon the introduction of antibodies, the NHS ester is replaced and the amine

groups of the antibodies can be efficiently conjugated to the carboxyls, forming stable and robust amide bonds.[121,126]

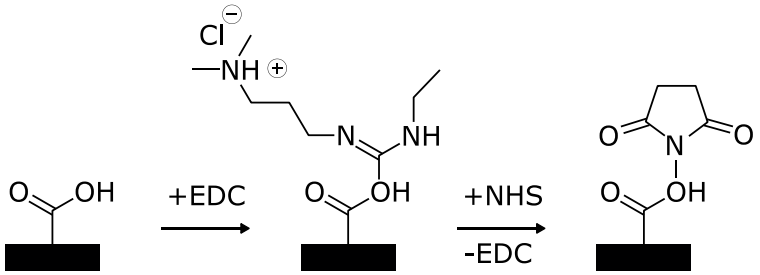

Figure 6. Reaction protocol for the binding of amines onto carboxylic acid groups using EDC/NHS chemistry.

2.3 Theory of Characterisation Methods

2.3.1 Raman Spectroscopy

Raman spectroscopy is a highly effective method to identify and characterise materials in a quick and, in principle, non-destructive way. It can provide structural and compositional information, with which material damage, strain and additional chemical components can be identified with high resolution and precision.[127,128]

This spectroscopic technique was invented by C. V. Raman in 1928,[129] who detected the process of inelastic scattering. It relies on the scattering interaction of incident monochromatic visible or IR light with the material to be analysed. An incoming photon excites the energetic state of an atom by the amount of energy the photon has. The system eventually falls back to a rotational or vibrational state and emits a photon with the same energy corresponding to the difference between the states. In most cases, the incoming and outgoing photons are of the same energy E. This process is called Rayleigh or elastic scattering (see Figure 7). Inelastic scattering involves a phonon n, on the other hand, and occurs with a much lower probability. Following the law of energy conversion, the emitted photon t has a different energy than the incoming one i.

$$E_i = E_n \pm E_t \tag{3}$$

The measured energy difference between the incident and returning photons is said to be the Raman shift. Stokes-Raman scattering and anti-Stokes-Raman scattering refer to the processes in which the emitted photon has less or more energy, respectively, than the

incoming photon (see Figure 7).[127] Molecular systems at room temperature usually appear in their ground state, gaining energy from the incident photon and transferring some of the energy into a molecular vibration, which results in Stokes-Raman scattering. Vice versa, anti-Stokes Raman scattering occurs when energy from a vibration is emitted with a photon. These molecular vibrations are unique for each material and the molecular structures can be identified.[130] The resonant Raman effect describes the increased scattering intensity when the energy of the incoming photon matches or is close to an electronic state of the molecule. Due to the "zero-bandgap" nature of graphene, every energy addition of an incoming photon results in a stationary state. This leads to greater perturbation efficiency and, thus, larger Raman signal intensities.[127]

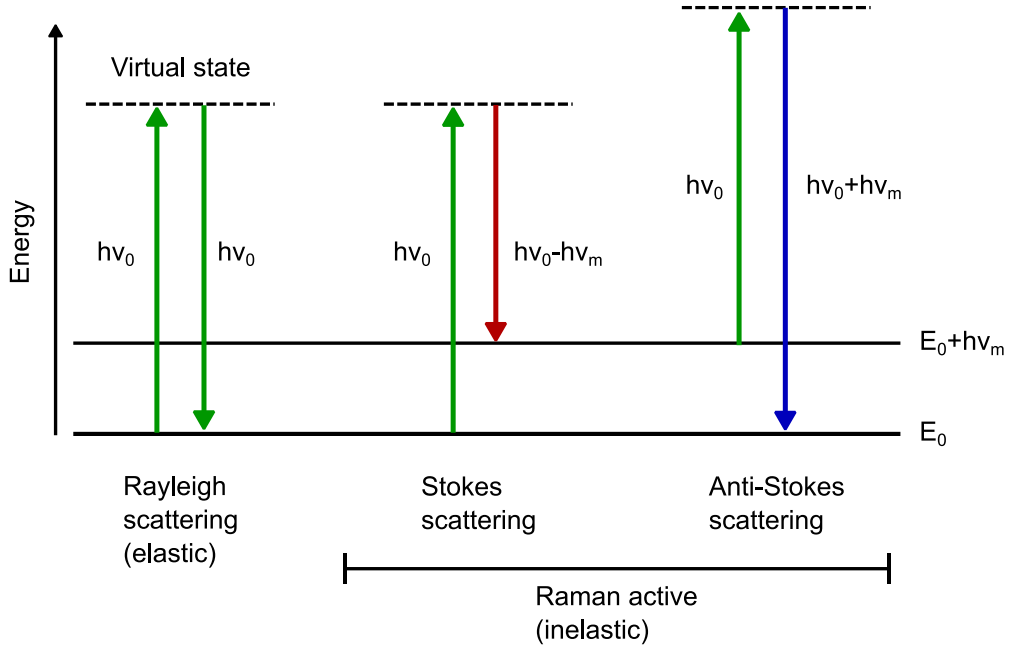

Figure 7. Customised Jablonski diagram, showing three of the typical scattering processes from left to right: Rayleigh, resonant Stokes and resonant anti-Stokes transitions.

2.3.1.1 Graphene-Enhanced Raman Spectroscopy

Surface-enhanced Raman Scattering (SERS) is a widely exploited effect to enhance the Raman signal of molecules to aid their analysis. Their Raman peak intensity is increased due to two underlying mechanisms: electromagnetic mechanisms (EM) and chemical mechanisms (CM). In the former, an enhancement of the electromagnetic field originates from plasmonic interactions of incident light with the substrate, which is typically a rough noble metal. In CM, the coupling of the substrate to the molecule induces charge transfer and the interlacing of electronic states and molecule orbitals, which lead to an enhancement.[131,132] While EM

typically is the stronger SERS effect, CM is dominant in graphene-based analysis, leading to the graphene-enhanced Raman spectroscopy effect (GERS).[132]

It has been found that several aspects affect the enhancement in GERS, ranging from material-related to system-related factors. For molecules that exhibit a structure and symmetry similar to graphene's, the coupling mechanism is stronger and the GERS effect increased.[132,133] Additionally, the relative molecular orientation and the distance to graphene are of interest.[131] The highest occupied molecular orbitals (HOMO) and lowest unoccupied molecular orbitals (LUMO) of molecules can be regarded as similar to valence and conduction bands, respectively, in semiconductors. The energy difference of the Fermi level of graphene to the HOMO/LUMO gap of the molecule is significant, as it contributes to the charge transfer and the efficiency of the laser excitation.[134] The enhancement is stronger when the excitation energy matches the gap between the graphene Fermi level and the molecules HOMO/LUMO gap.[131,132] Generally, the GERS effect decreases when the distance between the molecules to the graphene is larger.[135]

2.3.1.2 Raman Spectrum of Graphene

A typical monolayer graphene Raman spectrum is displayed in Figure 8. The scattered photon energy is presented on the x-axis as the wavenumber, in the units of cm^{-1}, indicating the spatial frequency of the scattered light relative to the incident one. In the positive direction of the x-axis, the Raman scattering of molecular vibrations due to Stokes-Raman scattering are presented.

Graphene has six normal modes which are divided into optical and acoustic phonons that are made up by two transversal and one longitudinal branch. The shapes of the phonon branches define the shapes of the graphene Raman peaks. More details on the origin of graphene Raman peaks can be found in literature.[127,128,136]

The most relevant Raman peaks for the quality control, number of layers, as well as strain and doping level detection in graphene are situated in the range of 1100-4500 cm^{-1}.[74] All Raman related details here are given for a laser wavelength of 532 nm, which is the main laser excitation source used in this work. The so-called G peak can be found ~1580 cm^{-1}, results from the only first-order scattering process at the Γ-point, the centre of the Brillouin zone.[128,137,138] This peak corresponds to the in-plane vibrations of the C-C bonds, is independent of incident photon energy and is typical for sp^2-hybridised carbon.[139] The G peak position and full width at half maximum (FWHM) is very sensitive to strain and doping.[140,141]

The remaining two peaks originate from resonant scattering processes, making them dependent on incident photon energy. The peak originating from the breathing mode of the hexagonal carbon rings can be found at 1350 cm^{-1} in the Raman spectrum and is known as the D peak.[137] It is only observable when the graphene lattice exhibits defects, because additional momentum is required to activate it.[142] Thus, the peak intensity I_D increases with the amount of defective sites in the lattice.[74,128,143] These are considered to be edges of and especially within a graphene film, such as grain boundaries. As a result, the D peak is usually taken into account for the quality control of graphene.[144]

The 2D peak is located at approximately 2700 cm^{-1},[74,127,145,146] which is the overtone of the D peak, does not require any defects in the graphene lattice to occur due to momentum conservation using a two-phonon scattering process and is, therefore, always present.[138,143] With increasing graphene layer number, the peak position shifts to higher wavenumbers. Monolayer graphene can be fitted as a sharp Lorentzian peak with a FWHM(2D) of $< 35\ cm^{-1}$.[127] The peak broadens with additional graphene layers due to the splitting of the electronic band structure.[130,142,147] The intensity ratio of the 2D to G peak I_{2D}/I_G above roughly 1.5 suggests monolayer graphene, which needs to be taken with care, because strain and doping might play a role as well.[147] Especially the position of the 2D peak varies a lot with strain and doping.[130] It has been found, that tensile strain results in a red-shift of both G and 2D peaks, and compressive strain in a blue-shift.[148,149] For a complete discussion on the intensities and shifts due to strain and doping, please refer to literature.[87,141,149–153]

Additional lower intensity peaks can be found in graphene Raman spectrum, out of which some will be described in the following. A defect peak is located at ~1620 cm^{-1}, which is called D' and is only found in defective graphene.[137,153] It's second order peak, called the 2D' peak, is found at ~3240 cm^{-1} and is always present.[146,154] The D+D'' peak at ~2450 cm^{-1} originates from a double-resonant scattering process and is also always visible in the spectrum.[138,146]

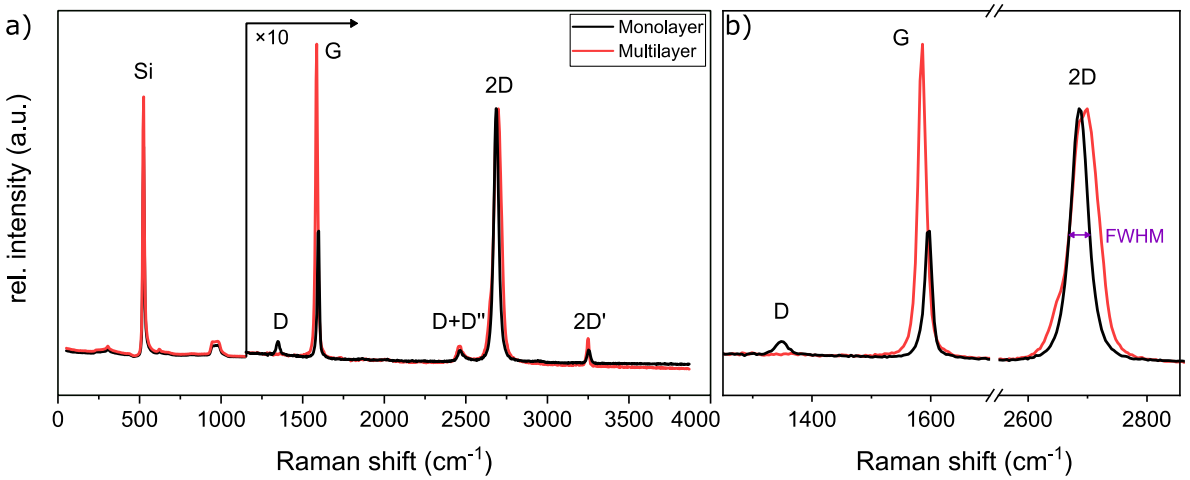

Figure 8. Typical Raman spectra of mono- and multilayer graphene in black and red, respectively. a) entire wavenumber region, with Si, D+D'' and 2D' indicated. From 1150 cm^{-1} onwards, the spectra were enlarged for better visualisation. b) magnified wavenumber region with the most relevant Raman peaks D, G and 2D at approximately 1350 cm^{-1}, 1580 cm^{-1} and 2700 cm^{-1}, respectively, and the FWHM displayed.

2.3.1.3 Raman Spectrum of a Perylene Bisimide Derivative

The 3,4,9,10-perylenetetracarboxylic 3,4:9,10-dianhydride (PTCDA) was first investigated using Raman spectroscopy in 1987 by Akers *et al.*[155] In their study, the prominent Raman peaks are listed to be at 1304 cm^{-1}, 1381 cm^{-1}, 1572 cm^{-1} and 1591 cm^{-1}, which will be referred to as P1, P2, P3 and P4, respectively, hereafter. In the publication by Scholz *et al.* in 2000,[156] the Raman spectrum of PTCDA on passivated Si(111) was studied at the excitation wavelength of 530.8 nm (2.34 eV). Several Raman modes dominate the spectrum (measured from 1200-1700 cm^{-1}), which can be found at 1305 cm^{-1}, 1381 cm^{-1}, 1572 cm^{-1} and 1590 cm^{-1}.[156] The mode positions found by the two publications are in good agreement with each other. A more recent study measured PTCDA on WSe_2 and found the peaks P1-P3 to be at 1307 cm^{-1}, 1389 cm^{-1} and 1582 cm^{-1}, respectively, which are slightly shifted to higher frequencies.[134] The peaks P1 and P2 result from C-H in-plane bending while C-C stretching is dominant for peaks P3 and P4.[156]. In a different study,[157] only P1 is the result of C-H bending activity and the remaining peaks are due to C-C stretching. The peaks at higher frequencies are the consequence of overtones or peak combinations, such as the peak at 2676 cm^{-1} resulting from the combination of peaks P1 and P2.[157]

As discussed in the section 2.3.1.1 Graphene-Enhanced Raman Spectroscopy, a molecule with similar structure to graphene is likely to exhibit a GERS effect. This is true for perylene derivatives, which have a conjugated core (see Figure 4). When the Fermi-level of graphene

is in the HOMO/LUMO gap of the molecule, energy transfer from the molecule to graphene occurs. This results in a quenching of the fluorescent signal and a clean Raman signal.[135]

In the study of Berner *et al.*,[51] the packing density of perylene bisimide (PBI) molecules on graphene was investigated. The Raman signal is strongest for highest packing density due to the formation of a controlled and homogeneous self-assembled monolayer (SAM) on graphene. High packing density is indicated by peaks P1 and P2 having higher intensity than the G peak. A contaminated graphene sample after conventional transfer (see section 3.1.2.1 Conventional Graphene Transfer and Functionalisation) was exposed to PBI, resulting in low packing density (Figure 9, bottom). In contrast to this, another sample was annealed after transfer and before PBI application, due to which the graphene surface was cleaner and the PBI adsorbed with a higher packing density (Figure 9, top). The Raman P1 and P2 peak positions in Figure 9 at 1303 cm^{-1} and 1383 cm^{-1},[51] respectively, are in good agreement with the ones stated by Akers *et al.*[155] and Scholz *et al.*[156]

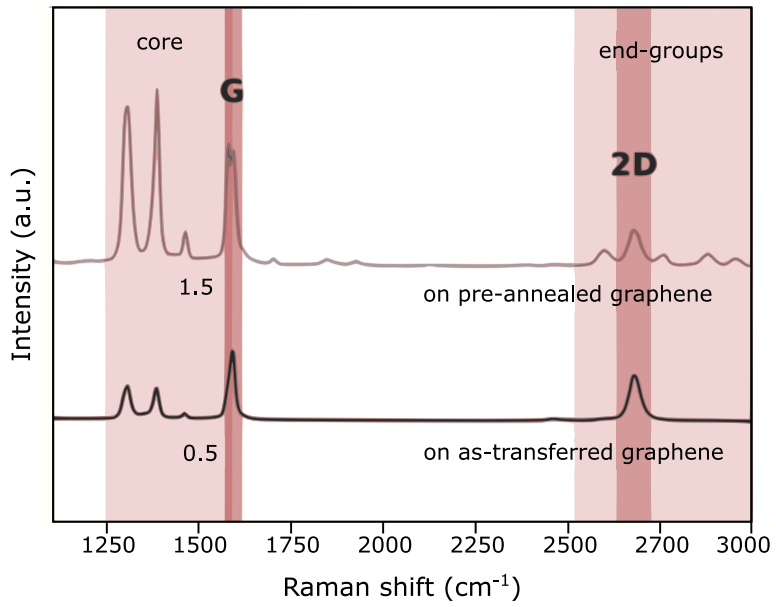

Figure 9. Raman spectra of PBI on pre-annealed graphene (top) and on as-transferred graphene (bottom). The intense P1 and P2 peaks in the pre-annealed graphene indicate high packing density. Modified after Berner *et al.*[51], copyright granted by The Royal Society of Chemistry.

2.3.2 Atomic Force Microscopy

In 1986, Binning *et al.* developed atomic force microscopy (AFM) from scanning tunnelling microscopy (STM) and set the base to one of the most widely used tools to image topographies with sub-nanometre resolution.[158,159] The standard system consists of a sharp tip at the end of a cantilever that scans across a surface. An incoming laser beam is reflected

off the back of the cantilever onto a position-sensitive photodiode (PSPD) detector consisting of four quadrants to trace the cantilever position.[160] The technique relies on near-field forces between the tip and the sample.

The AFM is primarily operated in contact or in tapping mode. In the former, the tip is constantly located in a controlled height with respect to the surface of the sample. Using a feedback loop, the force between tip and sample is kept constant, resulting in elastic bending of the cantilever when the topography changes.[159] This cantilever displacement deflects the laser beam, resulting in a position change on the PSPD. The resulting signal can be transformed into topography or height information.

In tapping mode, the cantilever oscillates at a frequency typically slightly below its resonant frequency. The tip is only in contact with the sample surface in the trough of each oscillation cycle. This is advantageous for the analysis of organic molecules as there is typically reduced force between the surface and the tip compared to contact mode, which results in less damage to the sensitive films and less dragging motion. A feedback loop keeps either the amplitude or the frequency constant, which is then used to generate the z-height and map the topography of the sample.[161]

2.3.3 Scanning Electron Microscopy

The main principle of scanning electron microscopy (SEM) consists of generating an electron beam by a field emission gun or by thermionic emission. It is conventionally accelerated to a high energy in the range 0.1-30 kV and focussed on a sample. The electron beam scans across a sample in a x-y pattern to acquire high-resolution images in the micro- and nanoscale.[162] The incident electrons interact with the sample in various ways (displayed in Figure 10) and electrons with different characteristics are ejected from the interaction volume within a sample. The most widely exploited electrons are backscattered electrons (BSE) and secondary electrons (SE).

BSE result from an elastic scattering process of incident electrons on atoms of the sample. They emerge from 50-300 nm within the sample and are deflected from the surface at large angles. Typically, they have high remaining energies compared to e.g. SE. For 2D materials, the usage of lower acceleration voltages is beneficial since the electron penetration depth is dependent on the incident electron energy. The electrons interact differently with elements of different atomic numbers and BSE can, therefore, give information about the chemical composition of the sample.

SE are generated by the inelastic scattering of incoming electrons with the valence electrons in the sample. In contrast to BSE, the resulting electrons are emitted closer to the surface (5-50 nm) at small angles, which is due to their lower energy. Thus, SE are more surface sensitive and are interesting to gain topographical information. For imaging graphene, SE is especially useful, because each graphene layer attenuates the SE signal, making the analysis layer dependent.[163] Thus, an initial analysis can be performed without the need to transfer the graphene.[162]

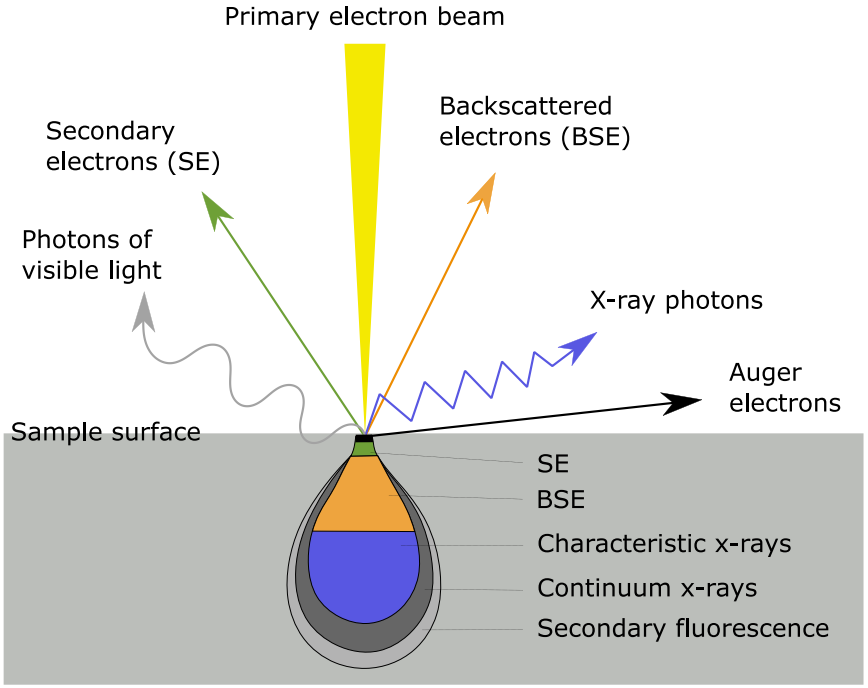

Figure 10. Various interaction mechanisms of the sample due to irradiation with an incident electron beam. Image modified after Goldstein *et al.*[162]

2.3.4 Electrical Characterisation

The field-effect transistor (FET) is a type of transistor that controls the charge carrier current flow along the channel by the bias voltage which is applied to its gate terminal. As a result, the conductivity of the channel is modulated. As a unipolar transistor, electrons or holes are alternatively used as charge carriers depending on the channel being n- or p-type, respectively. A FET is originally a four-terminal device, with source (S), drain (D), gate (G) and body (B, bulk or substrate), however, S and B are typically internally connected which creates a three-terminal device. Among various types of field-effect transistors after the first FET device, the metal-oxide-semiconductor (MOS) structure is the most widely used, resulting in the so-called MOSFET.

A MOSFET traditionally consists of a MOS capacitor and two heavily doped regions, namely the S and the D. These are typically either a p- or n-doped semiconductors, which supply and drain electrons, respectively. Additionally, the gate is separated from the body by a thin insulating layer of oxide, generating the MOS capacitor. In order to control the current flow of the channel, a high enough gate voltage is required, which is typically noted as threshold voltage, V_{th}. As a consequence, an electric field forms through the oxide and results in an inversion layer in the semiconductor, the so-called channel. The flow of the current in the channel can be modulated by the variation of the gate voltage.[164]

In this thesis, all electrical characterisations were performed using backgated GFETs, which are derived from the MOSFET structure. The bottom layer of the SiO_2/Si substrate is a heavily doped polysilicon and is used as a gate electrode to apply gate bias voltage (V_{gs}). The top SiO_2 layer is used as a gate dielectric layer for the introduction of an electric field. Transferred graphene onto the SiO_2/Si substrate behaves as a channel with source (S) and drain (D) electrodes placed on top as shown in Figure 11. Drain-to-source current (I_{ds}) is modulated by the induced electric field through the gate (G) dielectric layer, and consequently the graphene channel conductivity changes.

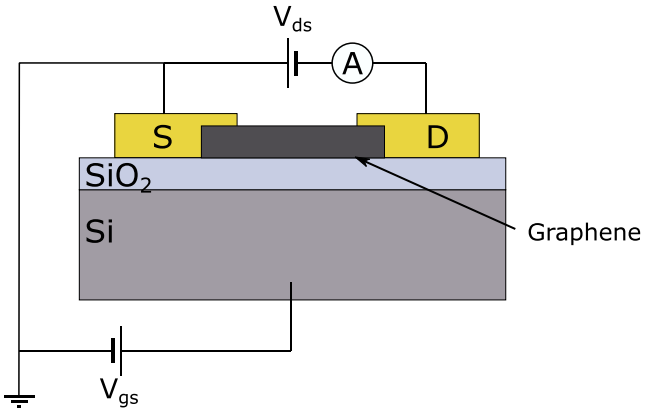

Figure 11. Schematic cross-section of a GFET. Graphene is placed on top of an insulating SiO_2 layer, separating it from the Si substrate that is used as the backgate. Source (S) and drain (D) electrodes on top of graphene.

Using GFETs, different characterisations can be performed out of which the following parameters can be generated: resistance, carrier mobility and Dirac voltage of the sample. Therefore, GFETs are operated in two different configurations, measuring output characteristics and transfer characteristics. The application of a drain-to-source bias voltage, V_{ds}, on the electrode results in a measurable current, I_{ds}, through the graphene channel (output characteristics). Exemplary I_{ds}-V_{ds} curves of a GFET at different V_{gs} are displayed in Figure 12a), presenting linear characteristics in all regions. This relation is typical for

ohmic contacts (Au/Ni/Graphene), which is usually the case for the semi-metallic graphene, which allows for the resistance, R, calculation using Ohm's law:

$$R = \frac{V}{I} = \rho\frac{L}{A} = (\sigma\frac{A}{L})^{-1} = G^{-1} \tag{4}$$

With ρ, σ and G being the resistivity, conductivity and conductance, respectively. L and A denote the length in m and area in m^2 of the sample, respectively.

The second operational mode of GFET is the transfer curve, where a constant V_{ds} is applied and the voltage of the backgate V_{gs} swept. The resulting current and, thus, the conductance can be modulated. The minimum of that curve is the CNP or Dirac point of the graphene device (see Figure 12b) and the voltage at that point is typically referred to as Dirac voltage, V_{Dirac}. The field-effect charge-carrier mobility μ can be calculated, when the capacitance of the oxide layer per unit gate area C_{Ox} in Fm^{-2} and the graphene channel length L and width W are known:

$$\mu = \frac{1}{C_{SiO_2}}\frac{L}{W}\frac{\delta I_{ds}}{\delta V_{gs}}\frac{1}{V_{ds}} \tag{5}$$

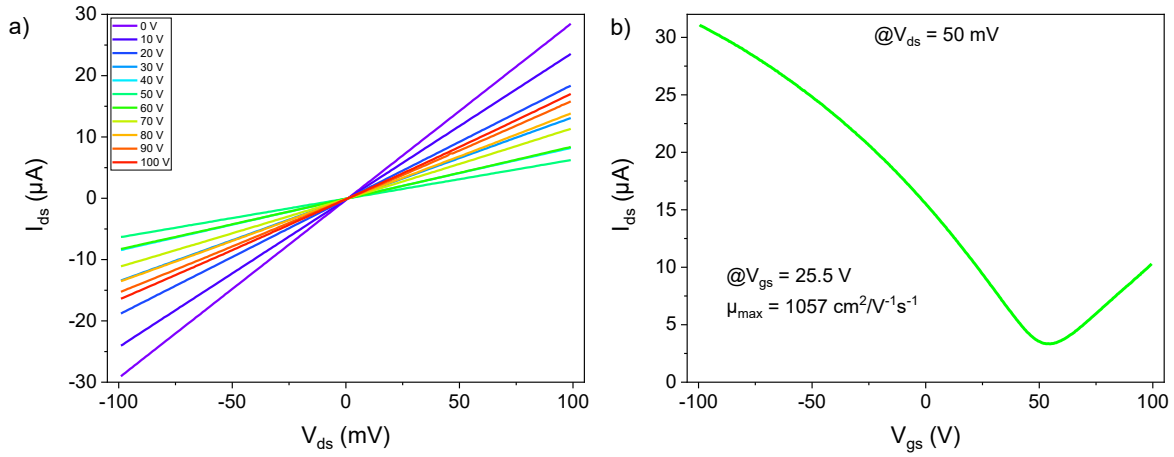

Figure 12. a) Output characteristics at cascading gate voltages, b) transfer characteristics at V_{ds} of 50 mV with a V_{Dirac} of 25.5 V and calculated field-effect mobility of 1057 cm^{2}V^{-1}s^{-1}.

3 Experimental Methods

In the following sections, all fabrication stages from CVD graphene growth to the GFET are presented and the functionalisation approaches to obtain a specific biosensor are explained. Additionally, the application of the characterisation methods with respective parameters is described.

3.1 Fabrication of a Graphene Field-Effect Transistor

3.1.1 Chemical Vapour Deposition

The tube furnace for graphene CVD growth is depicted in Figure 13a). It consists of a 40 mm wide quartz tube in the centre of the furnace, which elevates the temperature by surrounded heating coils. Four gases are connected, namely Ar, H_2, CH_4 and O_2, and all gas pipes join in one single line before entering the tube. A schematic image of the gas introduction pipe system is depicted in Figure 13d). From left to right (direction towards furnace), each gas pipe is equipped with a valve, behind which the mass flow controller (MFC) is positioned to control the flow rate of each gas. The Ar supplying pipe splits up and has a second line going through a fine dosing valve (Figure 13c). For safety reasons, an overpressure valve is mounted at the pump. The minimum pressure reached by the system is approximately 2×10^{-3} mbar.

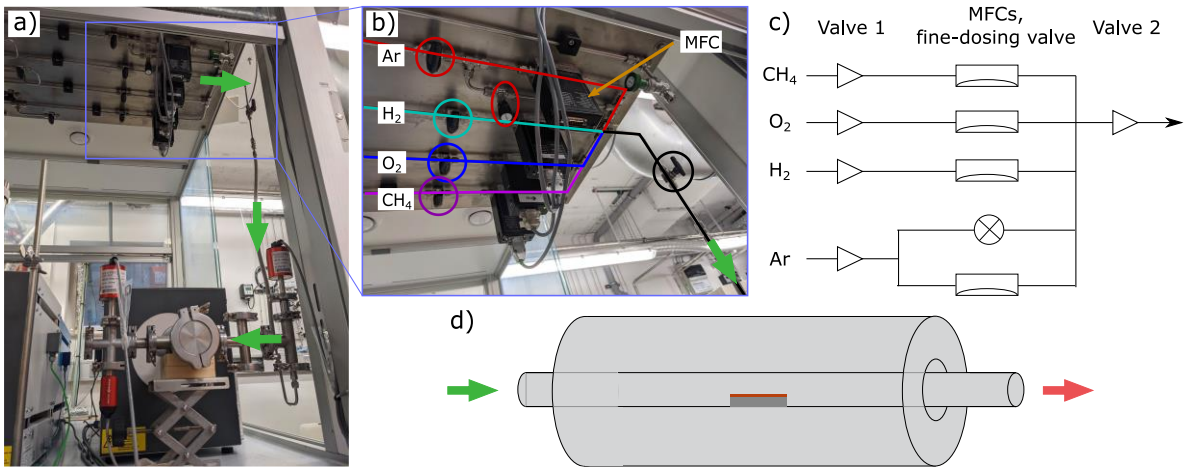

Figure 13. Photographic images of the CVD furnace a) from the front and b) close-up of gas supplying pipes, MFCs and valves (encircled). Schematics of c) the gas introduction configuration and d) the CVD furnace.

The 25 µm thin Cu foil (Alfa Aesar, ordered at Merck) has 99.8% purity on metal basis, which means that elements such as carbon are not included in the specification. The usual Cu foil shape used in this work is a 6×10 cm^2 rectangle (Figure 14a), which is folded twice at the longitudinal axis to increase the Cu foil surface to gain a reasonable output per process (Figure 14b). The folded Cu foil is place onto a quartz boat, which is then transferred into the centre of the CVD tube (Figure 14c).

Some internal leaks were found in the MFCs, which can lead to corruption of the growth process. To prevent this and avoid dangerous explosive mixtures when switching from oxygen to hydrogen (or vice versa), all gas pipes are kept evacuated if not needed. Thus, the MFCs are opened to allow a flow rate of 10-20 sccm (standard cubic centimetres per min) while the valves are closed, until no gas is left. This is performed in the beginning of each process and after each step when the respective gas was used.

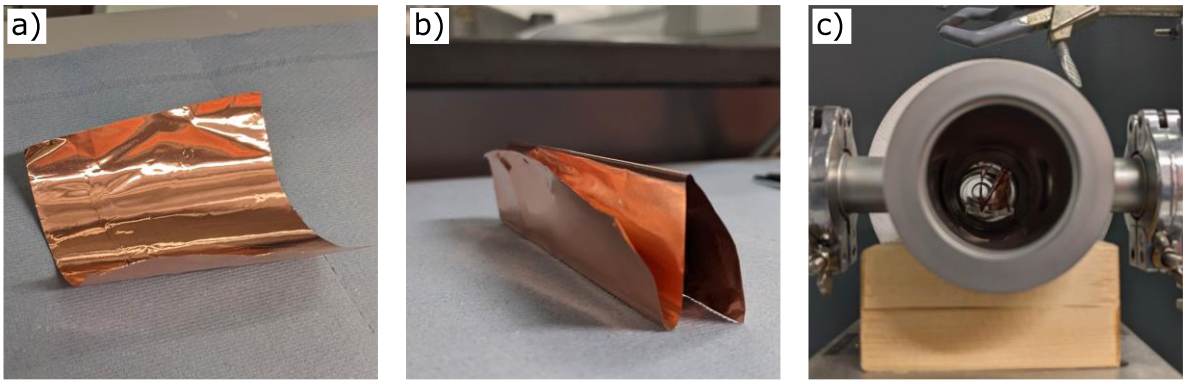

Figure 14. Preparation of the Cu foil from a) cut rectangular, b) folded twice longitudinally, c) placed in the centre of the furnace on a quartz boat.

The CVD chamber is cleaned by purging it three times with Ar after evacuating all pipes. Therefore, the chamber is filled with Ar and then pumped down to base level three times to remove residual molecules in the tube. During this work, the CVD growth process was tuned several times. The standard process will be described in the following and the ranges indicated in the brackets.

While the furnace ramps at 15 °C/min to 1060 °C, a gas flow of Ar at typically 0.5 mbar (in between 0.03-0.11 mbar) partial pressure and additional 80 sccm H_2 (40-100 sccm) is set, to obtain a reducing atmosphere. The stability and accuracy of the temperature ramping were tested using a thermocouple in multiple measurements, which resulted in a stable temperature ramp within the desired range of the process. Once the temperature is reached, H_2 is shut off and O_2 flown at 2.8 sccm (2.8-5 sccm) for 15 min (9-18 min) to deplete the Cu foil of intrinsic carbon. Subsequently, O_2 was shut off and H_2 was introduced again at a rate of 80 sccm (40-100 sccm) for 90 min (60-120 min), to obtain an oxide-free Cu-surface in the reducing atmosphere.[165] Subsequently, 5 sccm CH_4 (1.2-20 sccm) for 10 min (10—40 min) was added to the H_2 flow. For cooling, 1.2 sccm CH_4 (0-1.2 sccm)/80 sccm H_2 (40—100 sccm) was set. During the whole process, the chamber pressure was kept at around 1—1.5 mbar.

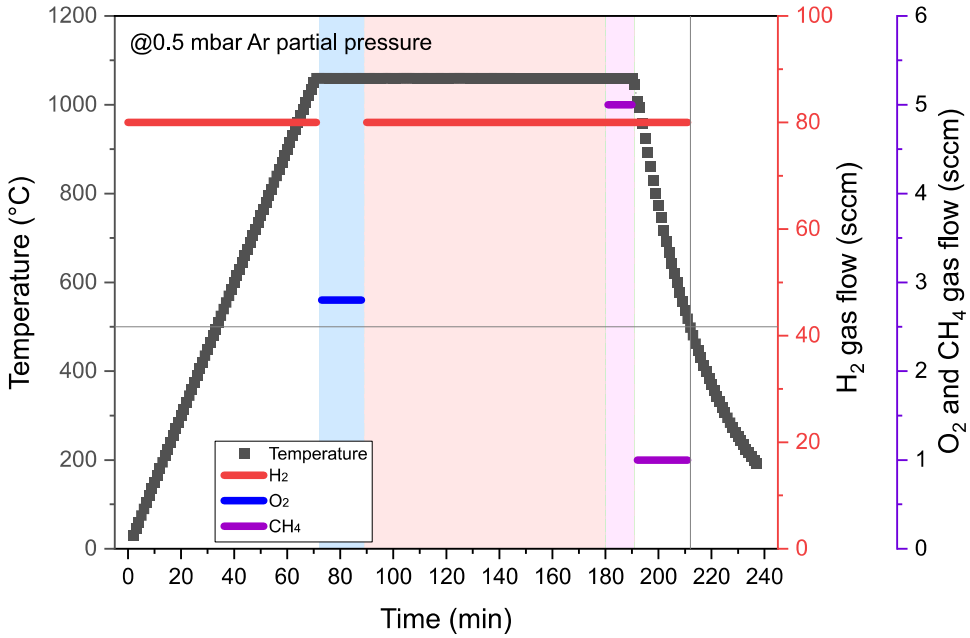

Figure 15. Schematic diagram for the typical CVD growth process. The temperature is ramped at 15 °C/min to 1060 °C (black). H_2 (red), O_2 (blue) and CH_4 (purple) gas flows are displayed as well. The oxidation stage serves to deplete the Cu foil from intrinsic carbon (blue background) and formed oxide products are reduced by the following H_2 treatment (red background). The graphene growth time is shown in the violet background.

3.1.2 Graphene Transfer

3.1.2.1 Conventional Graphene Transfer and Functionalisation

The graphene grown on a Cu substrate is required to be transferred onto a suitable insulating substrate for further application and integration.

In the following, the protocol for the conventional transfer is explained (Figure 16).[51,87] A protection layer for graphene during the transfer is required, which stabilises the graphene together when the Cu foil underneath it is etched. In this work, Allresist AR-PC 504 based on poly(methyl methacrylate) (PMMA) is used in a sevenfold dilution with chlorobenzene. Less residue was found when using low PMMA concentrations[86] and the concentration used here was tested to produce the cleanest and most intact graphene after transfer, which was evaluated in several tests. The polymer layer is spin-coated (B.L.E. Delta 10) onto the graphene-Cu stack in a two-step process with 500 rpm (rounds per min) for 5 s and subsequent 3200 rpm for 60 s. Subsequently, the PMMA-spun coat sample is baked for 10 min at 120 °C on a hotplate to minimise the residual solvent concentration. After cutting

off the outermost edges of the PMMA/graphene/Cu stack to avoid the edge bead effect, the sample is trimmed into pieces of desired size and approximately 7×0.5 mm^2 of PMMA/graphene/Cu strips are prepared for the following GFET production. These are set floating on a. approximately 0.5 M ammonium persulfate (APS) solution. In this thesis, the APS solution is prepared using 2 mol of 96% H_2SO_4, 2 mol of 25% NH_3, 1 mol of 30% H_2O_2 and subsequently filled up to 1 l with deionised (DI) water. The samples are floating on the APS solution to etch way the backside Cu foil, typically for 2-5 h. If the Cu layers were not completely removed, a second batch is applicable using 0.1 M of APS solution. After the entire Cu foil was removed completely, the samples are transferred into a DI water beaker by placing them on a target (glass or SiO_2/Si) substrate and releasing them again in the new beaker. This method is conducted at least twice, to remove any remaining APS from the sample. As a final step, 10×10 mm^2 SiO_2/Si substrates are used to fish out the channels, ideally such that the PMMA/graphene channel is placed in the centre of the quadratic chip. The substrates (Si-Mat, p++ type with boron dopants, resistivity <0.005 Ω cm, single-side polished, 525 ± 25 µm thickness with 300 nm SiO_2) were previously washed by consecutive acetone cleaning, isopropanol (IPA) rinsing and dry N_2 blowing to remove organic contaminants, which possibly exist on the substrate surfaces. The samples are placed in a vacuum desiccator at approximately 800 mbar overnight to stably adhere the transferred PMMA/graphene channel onto the SiO_2/Si substrate by dehydration. The samples are then placed in two successive acetone baths, each for at least 0.5 h, to strip the PMMA layer. After subsequent IPA rinse and N_2 dry, the samples are ready for further processing. It was taken care that the PMMA layer was only on graphene for one night, as it has been found that the resulting graphene shows more residues on its surface otherwise. However, polymeric residues remain inevitably on graphene after transfer because they are difficult up to impossible to entirely be removed.[98,112,166] A lot of research went into optimising the transfer procedure and the charge carrier mobilities of more cleaner CVD graphene in the optimised and improved transfer methods were found to compete with conventional mechanically-exfoliated graphene.[60,68,113]

All chemicals were purchased by Merck Sigma-Aldrich, unless stated otherwise. The DI water was always taken from a Merck Millipore® system with the resistivity of ~18 MΩ cm.

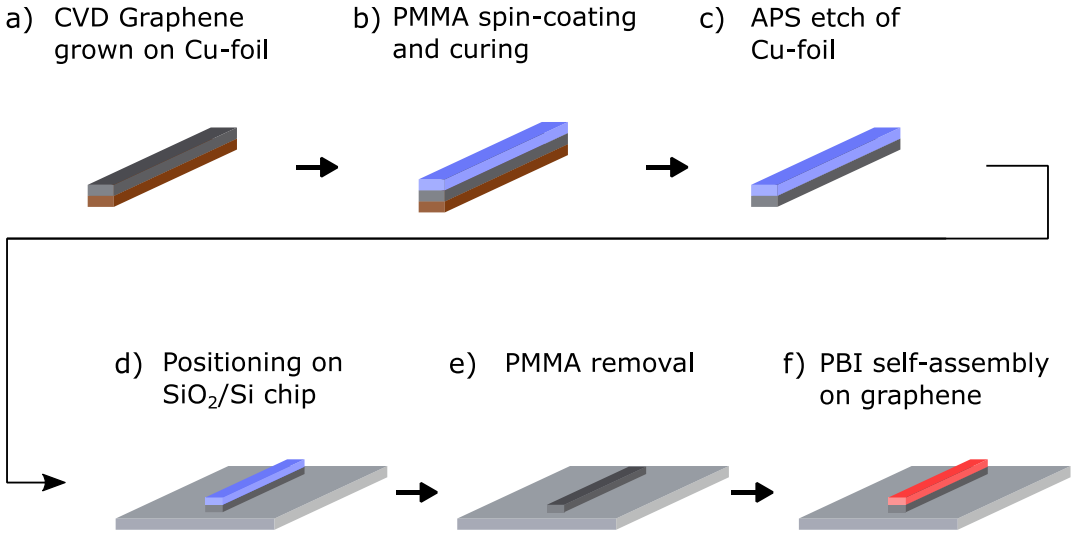

Figure 16. Process flow of the conventional transfer and functionalisation of a) CVD grown graphene channels. b) PMMA is spin-coated onto graphene, c) the Cu foil is etched using APS, d) after DI water washing the samples are placed on SiO_2/Si substrates, e) PMMA is removed using acetone, f) PBI functionalisation.

Functionalisation with PBI

The perylene bisimide (PBI) molecules generally exist in the powdery form, which then is diluted with DI water to obtain 0.1 mM solutions. The transferred graphene is annealed at 200 °C in 100 mbar of N_2 atmosphere to get rid of undesired adsorbates on the graphene surface, and after complete cooling, the sample is incubated in the PBI solution for 5-10 min. Afterwards, the sample is repeatedly rinsed in DI water to remove excessive PBI molecules from the graphene surface, for 10 min in general.[51] After a final DI water wash, the sample is carefully dried in N_2.

3.1.2.2 Functional Layer Transfer

To guarantee most homogeneous functionalisation of the graphene, the least contamination of its surface prior to functionalisation must be obtained.[51] As-grown pristine graphene on Cu foil has an almost perfectly clean surface right after unloading from the CVD furnace. However, the graphene surface directly contacts the PMMA during the conventional transfer method as aforementioned, which causes the issue of polymeric residue on the graphene surface because perfect PMMA removal is still challenging even though many and different resist removers/strippers have consistently proposed up to this day.[167,168] These polymeric residues hinder the homogeneous self-assembly of the PBI molecule on graphene as they already occupy parts of the graphene surface prior to functionalisation. For more homogenous functional group formation, the key point is the process procedure

rearrangement to keep the intact graphene surface from the graphene growth furnace. Therefore, graphene straight from the CVD furnace is functionalised with the PBI, and subsequently transferred onto SiO_2/Si using the polymer-assisted method (see Figure 17).[169] This minimises surficial contamination issue of the PMMA and adsorbates on the graphene surface in the laboratory environment, e.g. gaseous molecules/pollutants in air or from carrier boxes.[170] This was the birth of the functional layer transfer (FLaT) method to achieve homogeneous formation of PBI molecules on graphene.[169]

The FLaT comprises the same traditional transfer steps as described in the previous section, section 3.1.2.1, but arranged in a different process order (see Figure 17). The as-grown CVD graphene on Cu foil is immersed into PBI solution at the instant it is taken out of the tube furnace. Following the same functionalisation procedure, after 5-10 min of functional molecule incubation, the sample is washed in DI water three times and dried off by N_2 blow. Subsequently, the graphene transfer is carried out: Starting from spin-coating and curing PMMA on the sample, cutting the PMMA-graphene-Cu stack in the desired shapes, etching the underlying Cu with APS, washing the samples in DI water at least twice, dry overnight in a vacuum desiccator, and removing the PMMA the next day by cleaning twice with acetone, washing with IPA and drying with N_2. Note that for visualisation purposes larger graphene sheets were used for the FLaT process in Figure 17. For comparison, a graphene channel is displayed on the bottom right.

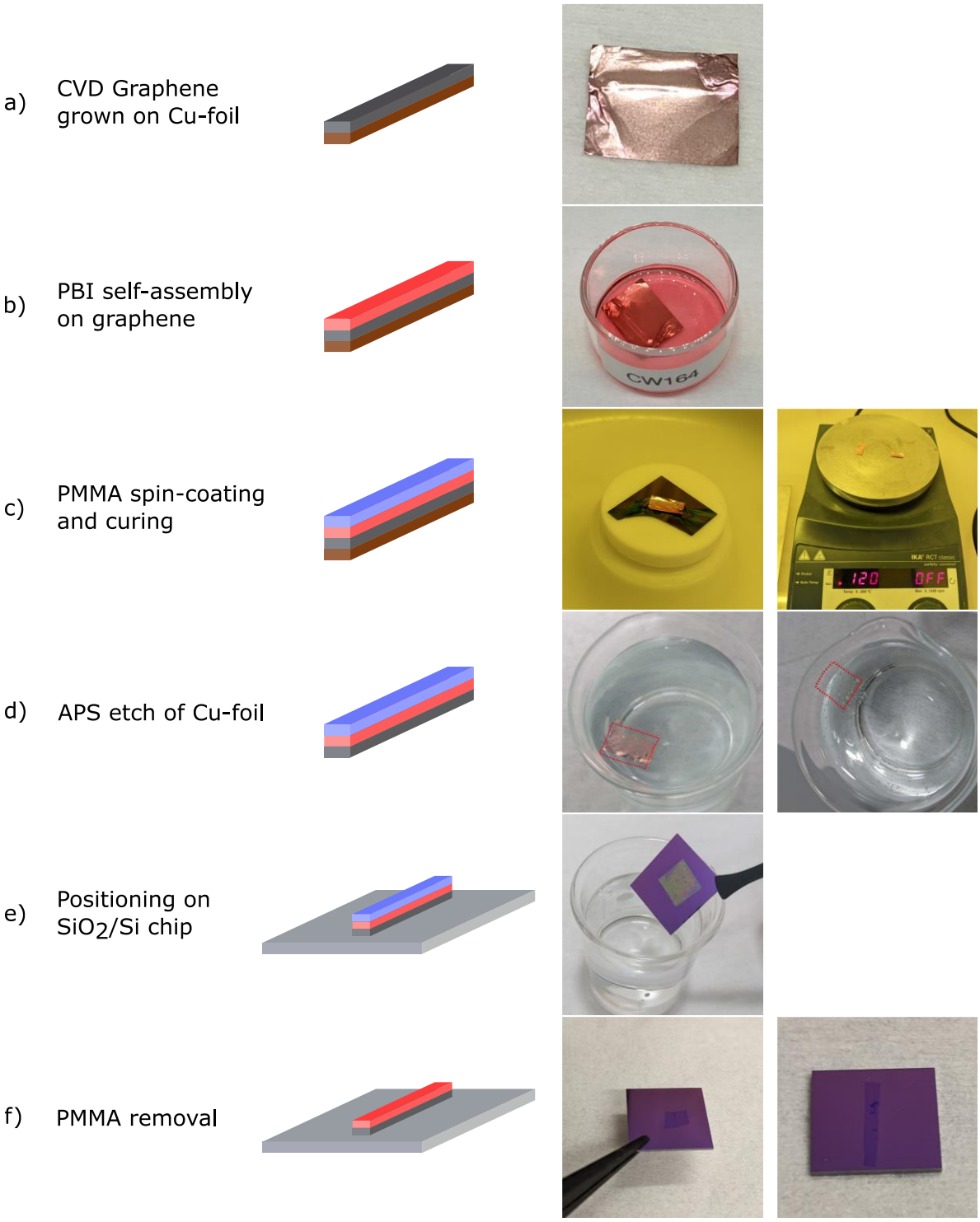

Figure 17. Process flow of FLaT starting with a) clean graphene on Cu foil from the furnace, b) PBI self-assembly on graphene, c) spin-coating of PMMA, d) APS etch of Cu foil, e) positioning of the sample on SiO_2/Si substrate, f) PMMA removal. Photographic images of the respective transfer steps on the right.

3.1.3 Structuring

For electrical measurements of transferred graphene, metallic electrodes are deposited in the configuration of the FET structure. In this work, a metal shadow mask is used to define electrodes of serial channels as shown in Figure 18, because it is advantageous to evade additional resist residue problem from the structuring lithography process and facile to apply as the device size is macroscopic enough. Twelve electrodes are aligned parallel across a long graphene stipe as channel, resulting in eleven individual devices in a row, since one device consists of two neighbouring electrodes, respectively D and S. A thin Ni layer for intimate electrical contact with graphene and reliable adhesion onto SiO_2 surface, and gold (Au) as electrode material are successively deposited *via* thermal evaporation through the windows in the shadow mask. The resulting electrodes have dimensions of 0.2 mm width with a spacing of 0.2 mm. Each electrode is connected to one contact pad of 2×2 mm^2.

The unfunctionalised and functionalised graphene channels on the SiO_2/Si substrate are annealed at 300 °C and 150 °C for 30 min in N_2, respectively, to remove adsorbed species from the graphene surface. Subsequently, each sample is mounted onto a dummy wafer for metallisation and the metal shadow mask covers the top of the sample. Although metal evaporation is supposed to be more anisotropic than sputtering, the deposited metal is likely to bridge over the SiO_2 layer on the side of the substrate. This results in undesirable leakage current *via* an electrical short, especially when the shadow mask was slightly skewed on the substrate. Therefore, all edges of the substrate were sealed with Kapton® tape in this thesis (see Figure 18c), after metal deposition and the shadow mask detachment). Afterwards, the 15×15 mm^2 metal shadow mask is attached onto the substrate, so that the parallel electrodes align with the graphene channel underneath. At vacuum levels of approximately 2×10^{-5} mbar, first 20 nm Ni and subsequently 60 nm Au are evaporated at deposition rates of ~0.2 and 0.6 Å/s, respectively. The substrate holder is rotating at 10 rpm for uniform metal thickness.

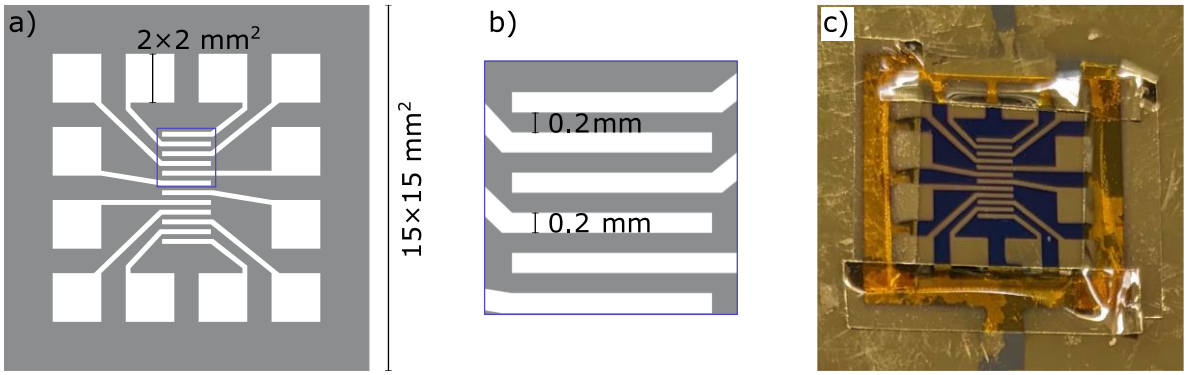

Figure 18. a) Schematic image of the metal shadow mask with twelve electrodes, aligned parallel to each other in the centre of the 15×15 mm^2 mask. Each electrode as well as the distance between them is 0.2 m. Magnified area in b). c) GFET with taped edges after metal deposition and shadow mask detachment.

3.2 Specific Functionalisation to Realise Biosensor

3.2.1 Materials

Two different perylene molecules (PBI and PTA) are used in this work, which act as linkers used for antibody coupling. Both molecules share the perylene core, and while the PTA has four additional carboxylic end groups, the PBI is characterised by two long side chains with six carboxylic end groups.

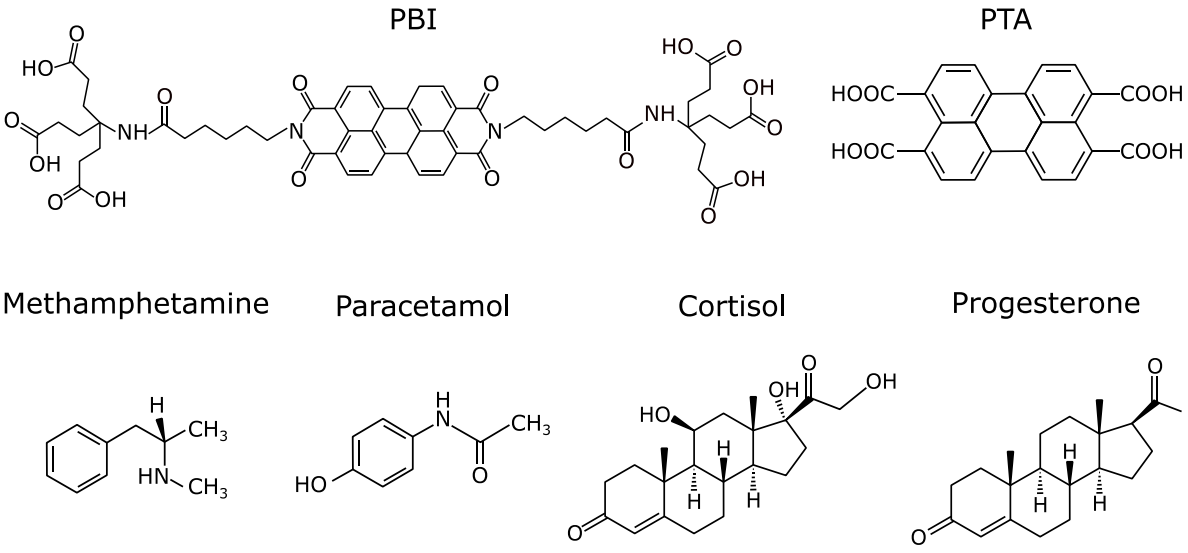

Figure 19. Chemical structures of the molecules used in this thesis.

In this work, the unit for the concentrations is chosen to be µg/ml. However, in purely biological studies, the unit thereof is typically given in molarities. Therefore, both units will be used in this chapter, and the unit µg/ml is used in the remaining part of the thesis.

EDC and NHS solutions are prepared separately because after their combination, the resulting solution is instable over a prolonged period. 100 mM 2-(N-morpholino)ethanesulfonic acid (MES) was dissolved in DI water and its pH was adjusted to pH 6.0 using NaOH. 40 mM EDC and 100 mM NHS were each dissolved in MES buffer solution (all purchased from Merck). Just before application, 500 µl of each solution were combined and 1000 µl MES added, resulting in the final EDC/NHS solution.

The monoclonal anti-methamphetamine antibody (methamphetamine-AB, EastCoast Bio, Inc.) and polyclonal anti-mouse antibody (AB2, Jackson ImmunoResearch Laboratories Inc.) were dissolved in 10 mM phosphate buffered saline (PBS) of pH 7.1 and in 10 mM sodium phosphate and 250 mM NaCl of pH 7.6, respectively, and were used as received. Both antibody types are in the order of 150-160 kDa and were produced in a mouse and donkey host, respectively. The antibody stock solutions of 10 µg/ml (67 mM) were prepared by adding 50 mM 4-(2-hydroxyethyl)-1-piperazineethanesulfonic acid (HEPES, Merck) buffer of pH 7.2 to them. The methamphetamine-AB concentration of 1 µg/ml (6.7 mM) is believed to fully saturate the surface, however, tests will be carried out to investigate it. In chapter 5 Development of a Reliable Biosensor Platform, SEM measurements will be discussed for which AB2 were coupled to gold nanoparticles (AuNP). Their diameter is 40 nm and the optical density of the 100% AB2-AuNP in solution is 5.7 OD. The AB2-AuNP conjugate was solved in bicine buffer. Calculations show the theoretical density of the methamphetamine-ABs on the surface, if the complete space is occupied:

$$\rho_{meth-AB} = \frac{A_{total}}{A_{meth-AB}} = \frac{10^{-12}}{10^{-9} * 14^{-9}} = 7143 \quad (6)$$

With the total area of 1 µm² and the dimensions of an IgG antibody lying in a flat position on the surface of 10x14 nm².

The anti-cortisol (17) Fab antibody (cortisol-Fab) was found in the VTT steroid specific antibody library, which is displayed on bacteriophages by using cortisol-3 CMO (Sigma) conjugated alkaline phosphatase carrier protein. The same selection and screening methods reported earlier were applied.[171] Cortisol-Fab was cloned in the pKKTac production vector which is containing a six histidine tag.[172] For the production, Escherichia coli bacterial strain RV308[171] were used and subsequently purified with metal affinity and Protein G chromatography according to manufacturer's instructions (Cytiva).[173] The affinity

determination of cortisol-Fab for cortisol was performed by Biacore T200 instrument (Cytiva) with Sensor Chip CM5 functionalised with cortisol 3-CMO -BSA (USBiological). Using the Affinity in solution-method, the affinity of cortisol-Fab for cortisol was found to be 7 nM. Cortisol-Fab is 48 kDa in dimension and was used in 2 µg/ml (42 mM) solutions. Fab-fragments are generally believed to be in the order of 7 nm×5 nm×4 nm in dimension.[174] Following equation (6), the theoretical density of cortisol-Fabs can be calculated to be 4000/µm².

The methamphetamine standard solution of 10 µg/ml (M, Lipomed AG, hydrochloride salt, aq.) was diluted to the desired concentrations with DI water. Methamphetamine has a mass of 120 Da. Paracetamol (Merck) in DI water has a mass of 151 Da and was also used in the concentration of 10 µg/ml (66 µM).

The stock solution of the cortisol-Fab (48,000 g/mol) of 2.46 mg/ml was solved in PBS buffer with pH 7.3. For the desired concentration, the stock solution was diluted in HEPES buffer, prepared by solving 1.19 g HEPES salt (260.3 g/mol, Merck) in 100 ml DI water. However, the pH value of this buffer was not stabilised. The resulting buffer will be referred to as HEPES-prep in this work, since it is of different origin than the previously used one.

The small molecule cortisol (hydrocortisone, Merck) with a molar mass of 362.46 g mol^{-1} was dissolved in HEPES-prep buffer and used in a concentration of 10 µg/ml (28 µM). Progesterone was diluted in 2% DMSO (in HEPES-prep buffer) and applied in a concentration of 10 µg/ml (31 µM). All molecules mentioned in this paragraph were provided by VTT, Finland.[173] The chemical structure of all small molecules used in this work are displayed in Figure 19.

3.2.2 Application

All perylene functionalised graphene samples are annealed at 150 °C in N_2 for 30 min to remove unwanted adsorbed molecules (Figure 20a). After an as short time as possible, 60 µl EDC/NHS solution is applied on the samples and incubated for 15 min (Figure 20b). Subsequently, the samples are rinsed with DI water for approximately 45 s. The remaining droplet is soaked away with a clean-room tissue without touching and damaging the graphene. This will leave the surface slightly moist but no water droplet remains. It cannot be entirely excluded that neither some water film remains on the surface, nor that the sample is completely dry. This step will be simply referred to as drying in the following. Due to the instability of the activated carboxylic groups, 60 µl of the desired antibody solution is applied directly afterwards (Figure 20c). The incubation times for the different antibody

solutions varies between them, being 30 min for methamphetamine-AB and cortisol-Fab, and 10 min for AB2 with and without conjugation to AuNP. A second DI washing step followed by the subsequent drying of the sample.

Samples with methamphetamine-AB coupled to the PBI *via* EDC/NHS chemistry will be referred to as methamphetamine biosensor platform in this work. This notation applies accordingly to the other antibodies as well.

Directly after the antibody coupling to the perylene on graphene, 60 µl of the AB2-AuNP solution or either one of the small molecules is applied (Figure 20d). The incubation times varied, being 4 or 6 min for methamphetamine, 4 min for paracetamol, 6 or 10 min for cortisol and 6 min for progesterone. Subsequently, DI water rinse and sample drying followed.

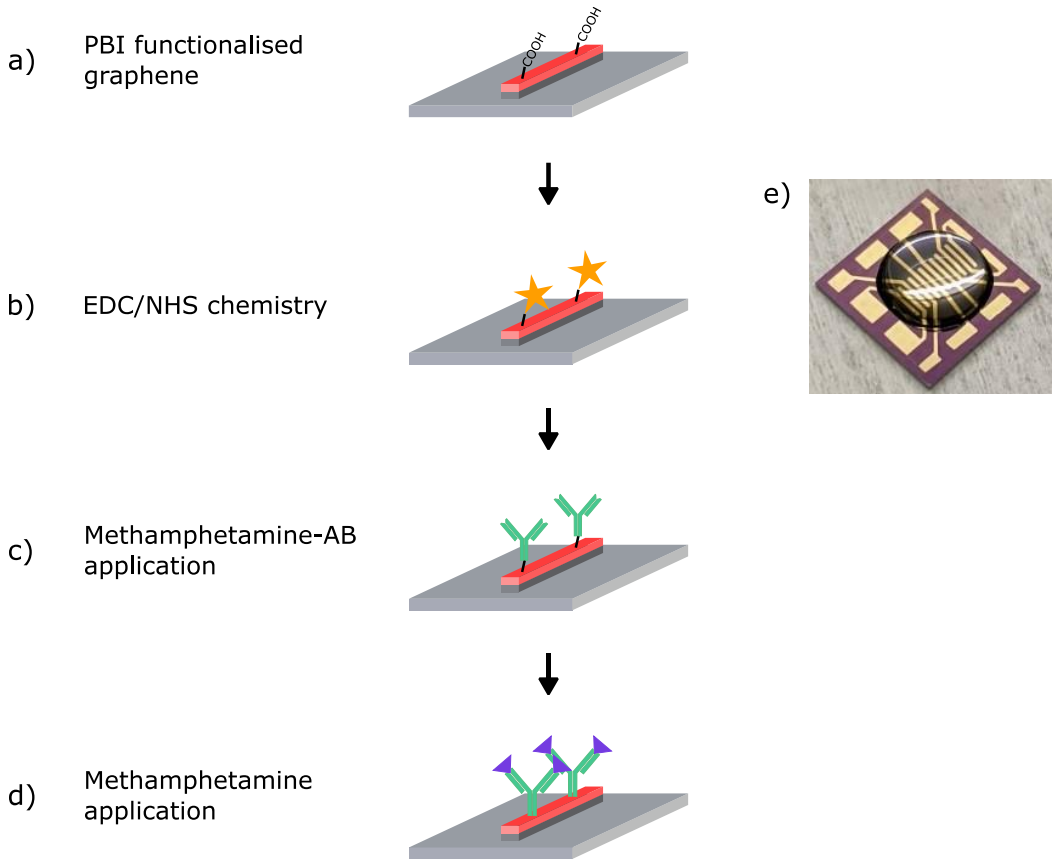

Figure 20. Illustration of the functionalisation steps to realise a graphene-based methamphetamine biosensor. a) PBI functionalised graphene, b) EDC/NHS chemistry with preparation for amine coupling, c) coupling of methamphetamine-AB to the PBI resulting in the methamphetamine biosensor platform, d) methamphetamine exposure. e) GFET during functionalisation with 60 µl EDC/NHS solution (b).

3.3 Characterisation Techniques

3.3.1 Raman Spectroscopy

A WITec alpha300 R Raman spectroscope operated with the Control FIVE 5.1 software (version 5.1.13.69, WITec GmbH, Germany) was used for all Raman characterisation in this work. For analysis, the Project FIVE software (version 5.1.8.64, WITec GmbH, Germany) was used.

If not stated otherwise, a laser with a wavelength of 532 nm (2.33 eV) was used for excitation, of which the power varied from 2 mW for unfunctionalised to 0.2 mW for functionalised graphene. Each single spectrum is integrated for an acquisition time of 10 s and accumulated twice. Typically, the grating is 600 g/mm. For Raman spectroscopy on Cu foil the 50x objective and for analysis on flat SiO_2/Si substrates the 100x objective was used.

All Raman maps consist of 4,356 single spectra equally distributed over an area of 100×100 µm^2. Each single spectrum of unfunctionalised graphene, PBI functionalised graphene and PTA functionalised graphene is integrated for 2 s, 3 s and 5 s, respectively. The laser power was selected to be 1 mW, 0.2 mW and 0.2 mW, respectively. The True Surface feature of the system allowed for an automated precise focus adjustment throughout the large-area scans. The Raman maps were analysed using the above-mentioned software, using the filters to extract peak intensity, FWHM and peak positions. Intensity ratios in the form of I_a/I_b were calculated in the software where the value of each pixel from map (a) is divided by the value of the same pixel of map (b). The resulting changes in intensity ratios is calculated by applying following equation:

$$\Delta\frac{I_a}{I_b} = \left(\left(\frac{I_a}{I_b}\right)_2 - \left(\frac{I_a}{I_b}\right)_1\right)/\left(\frac{I_a}{I_b}\right)_1 * 100 \tag{7}$$

The ratio $\left(\frac{I_a}{I_b}\right)_1$ is the value produced first, e.g. before a treatment was performed. For ΔFWHM(2D), a typical subtraction is carried out:

$$\Delta FWHM(2D) = FWHM(2D)_2 - FWHM(2D)_1 \tag{8}$$

The wavenumber ranges for the filters applied are as follows: 1265-1335 cm^{-1} (P1), 1345-1415 cm^{-1} (P2), 1532-1582 cm^{-1} (P3), 1582-1632 cm^{-1} (G), 2630-2730 cm^{-1} (2D).

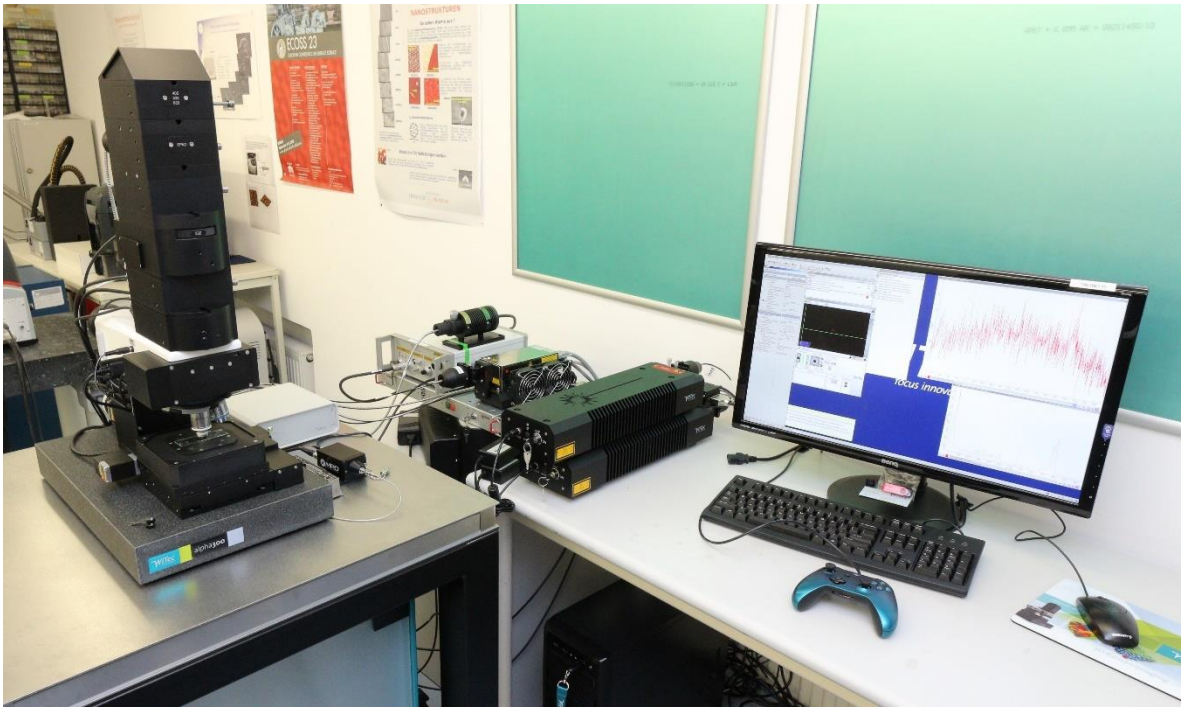

Figure 21. An Alpha300 R (WITec) Raman spectroscope with the optical column on the left and lasers in the centre.

3.3.2 Atomic Force Microscopy

The AFM images were acquired using the nanoIR2 AFM-IR (Anasys Instruments), operated with the Analysis Studio software (version 3.15.7381, Bruker Inc., USA), or a Jupiter XR AFM (Asylum Research-Oxford Instruments). The former was used for the AFM measurements in Figure 31 and in Figure 51, and the latter for Figure 59. Standard tapping (PR-EX-T125-10) probes with resonant frequencies of 200-400 kHz were used. The topography and height profile analysis was carried out in Gwyddion software (version 2.52, General Public License).

Unfunctionalised and functionalised graphene samples were annealed at 300 °C and 150 °C for 30 min, respectively, prior to AFM measurements.

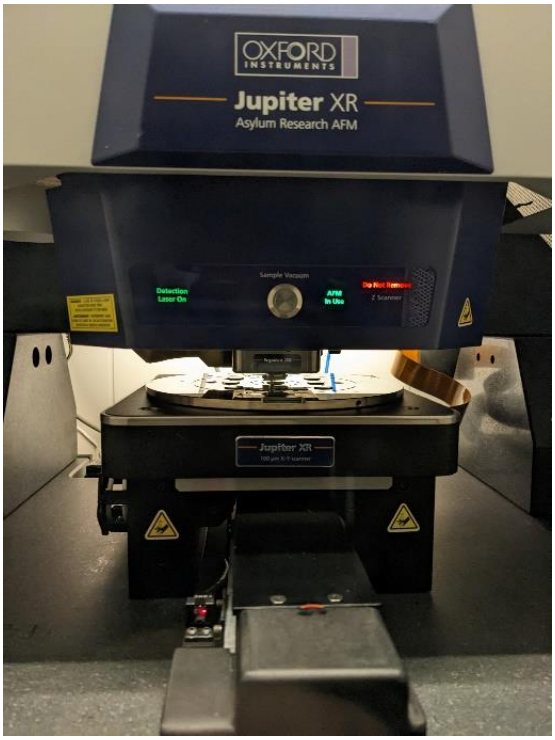

Figure 22. Close-up image of the Jupiter XR atomic force microscope (Asylum Research-Oxford Instruments) during operation.

3.3.3 Scanning Electron Microscopy

A JEOL JSM-6700F and CLARA (Tuscan) SEM was operated at 2, 5 kV or 10 kV acceleration voltage with a working distance of 7 mm to obtain SEM images. The SE detector was used to obtain topographical images.

Figure 23. A JSM-6700F (JEOL) scanning electron microscope.

3.3.4 Electrical Characterisation

The electrical measurements were performed in a mechanical probe station (Rucker&Kolls 681A semiautomatic wafer probe station) with source measure units (Agilent E5270B measurement mainframe and E5281B precision medium power source meter unit modules) controlled by LabVIEW™ (National Instruments, USA). For data analysis and visualisation, ORIGIN 2020 (OriginLab® Cooperation, USA) was used.

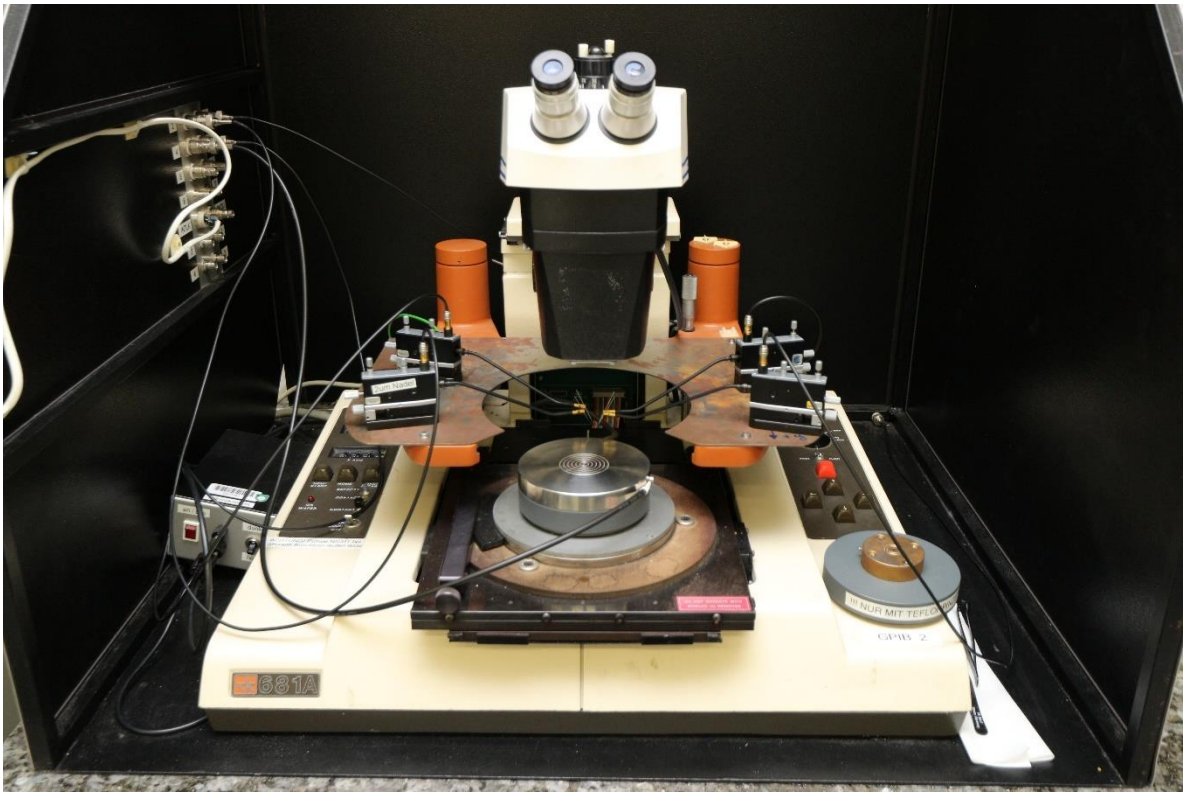

Figure 24. Electrical measurement setup consisting of four micromanipulators with fine needle probes, a metallic vacuum chuck on the motorised stage for wafer sample mounting and an optical microscope.

The GFET sample is placed on the metal sample stage and each single graphene channel out of the 11 GFETs per chip is individually probed using the micromanipulators, which were positioned to connect two neighbouring electrodes. Typically, the output characteristics were measured by sweeping V_{ds} from -100 mV to 100 mV at a floating backgate. For transfer characteristics, V_{ds} was kept at 10 mV and V_{gs} was swept from -100 V to 100 V.

To realise biosensors, the GFETs are functionalised. The resulting response due to the functionalisation is determined by measuring the electrical parameters of the same device before and after the process. This is a necessary step for the investigation of the true biosensor performance because the initial GFET characteristics differ considerably from each other. Since all samples are handmade in this thesis and slight differences during processing may occur, the final devices are likely to have differences in the electrical performance. In Figure 25a), the I_{ds}-V_{ds} curves of two individual FLaT functionalised GFETs are displayed in green and blue. The solid lines indicate the respective initial resistance values of 1216.3 Ω and 399.5 Ω for GFET1 and GFET2, respectively. Therefore, the changes in their electrical characteristics are calculated and will be compared in this work, rather than absolute values.

The preferrable parameter to compare the output characteristics of highly crystalline 2D materials is sheet resistance, because the thickness is ambiguous to decisively define in very thin films, such as monolayered or layered materials. This is especially useful for comparing the electrical properties of thin films, as the sheet resistance remains constant regardless of film size. It compensates for the device dimensions by including L and W in the calculation (see equation (4), enabling a direct comparison of different devices made of the same material. However, the following equation demonstrates that resistance changes, ΔR, have the same result as sheet resistance changes, ΔR_S:

$$\Delta R_S = \frac{R_{S,func} - R_{S,0}}{R_{S,0}} * 100 = \frac{R_{func} * \frac{A}{L} - R_0 * \frac{A}{L}}{R_0 * \frac{A}{L}} * 100 = \frac{R_{func} - R_0}{R_0} * 100 = \Delta R \quad (9)$$

With $R_{S,0}$ and $R_{S,func}$ being the sheet resistance before (FLaT functionalised graphene) and after functionalisation, respectively. Equivalent notation for R_0 and R_{func}, respectively. Due to simplicity reasons, ΔR will be used in this work.

The ΔV_{Dirac} is calculated as:

$$\Delta V_{Dirac} = V_{Dirac,func} - V_{Dirac,0} \quad (10)$$

Analogous to the resistance symbols, $V_{Dirac,0}$ and $V_{Dirac,func}$ describe the ΔV_{Dirac} before (FLaT functionalised graphene) and after functionalisation, respectively.

The dashed lines in Figure 25 show the electrical data of the same devices after functionalisation. In both cases, a resistance decrease can be seen by the steepening of the curve. In numbers, the ΔR are -20.7% and -33.5% for GEFT1 and GFET2, respectively. Similarly, in Figure 25b), the ΔV_{Dirac} are 5.5 V and 42.5 V, respectively.

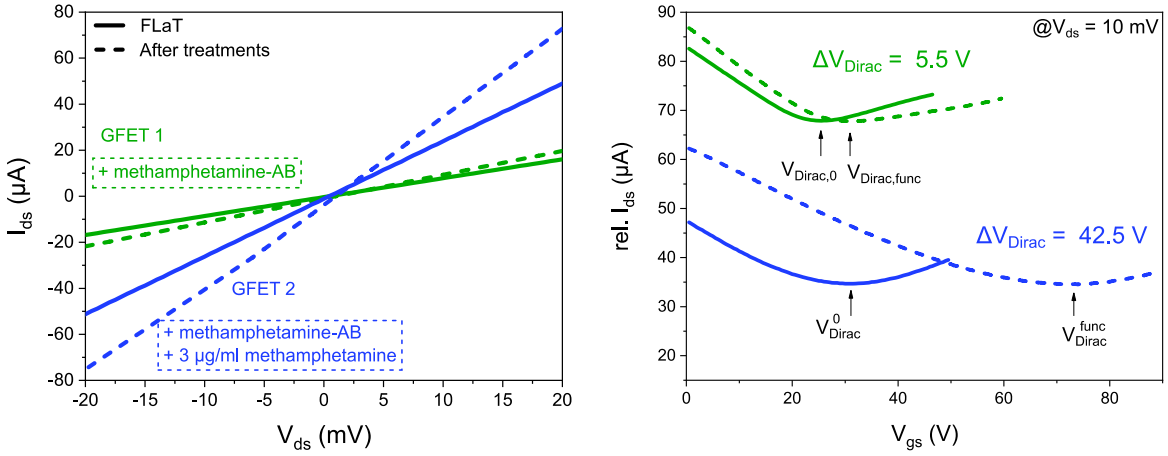

Figure 25. a) I_{ds}-V_{ds} and b) I_{ds}-V_{gs} curves for two samples, respectively. In both plots, the characteristic for FLaT graphene is indicated by the solid line, and after respective treatment in dashed line. Methamphetamine-AB was coupled to the PBI of GFET1 (green), resulting in a slight resistance decrease (a) and an increase in V_{Dirac} of 5.5 V. Similarly, methamphetamine-AB coupling and subsequent methamphetamine exposure (blue) resulted in strong resistance decrease and V_{Dirac} increase of 42.5 V.

The specific functionalisation for the biosensor fabrication consists of three parts (Figure 26):

Stage 0: FLaT GFET,

Stage 1: antibody coupling to the functionalised graphene (biosensor platform)

Stage 2: subsequent analyte exposure (biosensor).

Electrical characterisation is performed before (Stage 0) and after the functionalisation processes (Stage1 or 2). However, no measurement is conducted on the same sample in between (Stage 1) and (Stage 2), as the samples are functionalised in one flow. Therefore, the resulting shifts in electrical parameters are notated as ΔR_{AB} and $\Delta V_{Dirac,AB}$ for biosensor platforms (Stage 0-1), and as ΔR_{AB+An} and $\Delta V_{Dirac,AB+An}$ for biosensors (Stage 0-2). In most sections in this chapter, the analysis of the actual signal change due to the analyte is desired (Stage 1-2). Since this is not directly measurable, the change due to the analyte is estimated using a different approach, which is described in the following.

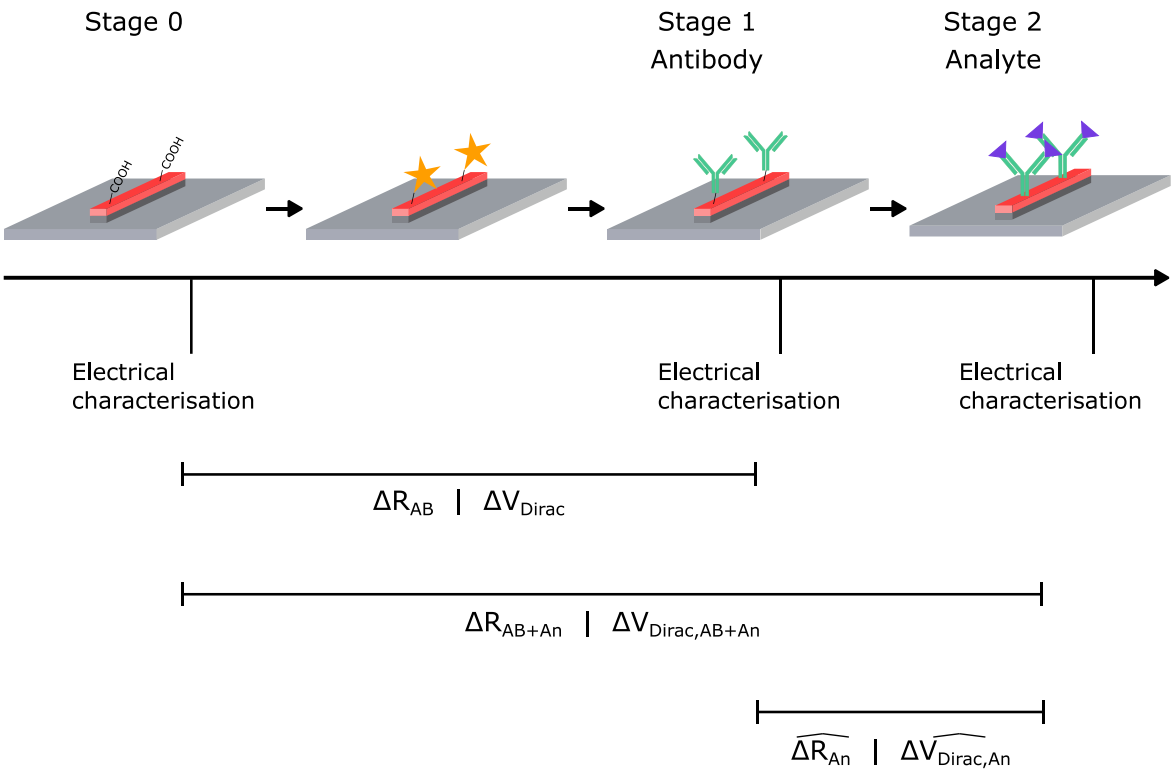

Figure 26. Schematic process flow of functionalisation and the respective time-frame of electrical measurements. Parameters to be derived during measurements are noted in the illustration.

At least one biosensor platform sample (solely antibody on GFET) was measured simultaneously to a biosensor batch (antibody + antigen on GFET). The resulting ΔR_{AB} and $\Delta V_{Dirac,AB}$ of all biosensor platforms of one batch are averaged and stated as $\overline{\Delta R_{AB}}$ and $\overline{\Delta V_{Dirac,AB}}$. Then the contributions of the analyte, $\widehat{\Delta R_{An}}$ and $\widehat{\Delta V_{Dirac,An}}$, are extracted as following equations, respectively:

$$\widehat{\Delta R_{An}} = \Delta R_{AB+An} - \overline{\Delta R_{AB}} \tag{11}$$

$$\widehat{\Delta V_{Dirac,An}} = \Delta V_{Dirac,AB+An} - \overline{\Delta V_{Dirac,AB}} \tag{12}$$

For each functionalisation batch, the averaged biosensor platform values are subtracted from each individual GFET value (equation (11) and (12)), thus a change smaller deviating from 0% and 0 V can be attributed to the impact of the analyte.

4 Graphene Surface Modification with Perylene Bisimide

Graphene is characterised by a variety of excellent properties that are suitable for numerous applications. All properties are the result of its unique structure with carbon atoms arranged in a honeycomb lattice. One drawback is the lack of selectivity towards adsorbing molecules. In general, all kinds of molecules are prone to adsorb on graphene, however, the all-carbon nature of the material does not grant any selectivity towards specific molecules, which is especially required for sensing applications. Therefore, functionalisation of the graphene with linker molecules that provide selectivity towards target molecules is required.

In this chapter, the effect of the functionalisation of graphene with the perylene derivative PBI is closely investigated using Raman spectroscopy, AFM, SEM and electrical measurements. Additionally, the stability of the functionalisation towards elevated temperatures under nitrogen atmosphere is tested. This is especially important when it comes to back-end of line processes, where the functionalised graphene might be integrated into more complex electronic systems that requires the use of higher temperatures.

4.1 Experimental Details

The CVD growth of graphene followed the typical procedure described in section 3.1.1 Chemical Vapour Deposition, and the subsequent transfer protocol can be found in detail under section 3.1.2 Graphene Transfer.

The Raman spectra of unfunctionalised CVD grown graphene on Cu foil were acquired using laser wavelengths of 404 nm and 532 nm (Figure 28). For the former, the integration time was 10 s and 3 accumulations, for the latter 10 mW, 20 s and 2 accumulations. The laser power of the 404 nm laser cannot be specified directly, since there is no direct feedback to exactly measure it. Therefore, the laser power was tuned such that the resulting spectrum had a sufficient signal-to-noise ratio.

For Figure 29, the PBI was diluted in DI water to obtain a 0.1 mM solution, which was drop-casted onto a clean SiO_2/Si substrate and allowed to dry in. The CVD grown graphene on Cu foil was immersed into the PBI solution for 5 min for the PBI self-assembly on

graphene and subsequently DI water washed. The same procedure is performed for the FlaT graphene, where the functionalised graphene is subsequently transferred to a clean SiO_2/Si substrate.

The Raman spectra in Figure 29 were mainly acquired using the laser with 532 nm excitation wavelength and are the average of large-scale Raman maps, consisting of several individual spectra. For the dried-in PBI on SiO_2/Si substrate, 0.4 mW, 10 s and 2 accumulations were used; and the spectrum was background subtracted using a polynomial fit in the 9^{th} order. The parameter for PBI functionalised graphene on Cu foil were 1 mW, 10 s and 1 accumulation. The PBI FlaT graphene was analysed using 0.2 mW, 10 s and 2 accumulations with the 532 nm, and 60 s and 2 accumulations at a laser power estimated to be below 4 mW for the 404 nm laser. All following Raman spectra were performed using solely the laser with 532 nm excitation wavelength.

The unfunctionalised sample in Figure 30 and Figure 31 was analysed using Raman spectroscopy and AFM, was then annealed at 200 °C in N_2, subsequently functionalised with the PBI and analysed again. The Raman maps originate from the same location on the sample.

The Raman spectra in Figure 33 were taken using laser powers of 0.1 mW, 0.2 mW, 0.3 mW, 0.5 mW and 1 mW and integration times of 5 s, 10 s and 20 s each. All spectra of one laser power were acquired at the same location to keep the conditions equal. This is especially important to ensure the same laser focus of the laser on the sample. Therefore, the focus for the three spectra on each location is the same. The intensity of the Si peak at 520 cm^{-1} increases with laser power and integration time but is not damaged by it. Therefore, the Si peak can be assumed a constant in the Raman spectra at the same location and is used to normalise the Raman spectra. All Raman spectra taken at the same location are normalised to the intensity of their Si peaks, which can be seen in Figure 27. PBI fLaT graphene was measured at the same location at 0.3 mW laser power with integration times of 5 s (black), 10 s (red) and 20 s (green). The Raman signal was normalised to the Si peak, resulting in an excellent overlap of Si peaks in the inset.

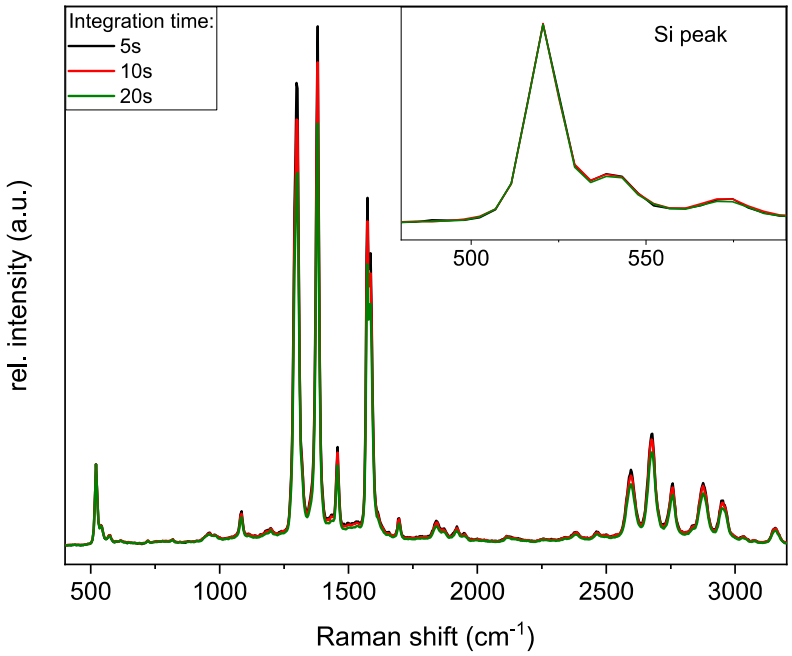

Figure 27. Raman spectra of PBI FLaT graphene using 0.3 mW laser power and different integration times (0.5 s, 10 s and 20 s in black, red and green, respectively). Magnification of the Si peak in the inset.

For Figure 37, unfunctionalised graphene is transferred *via* the conventional method and subsequently structured to obtain a GFET. After initial Raman spectroscopy and electrical measurements of the unfunctionalised GFETs, the samples are immersed in 0.1 mM PBI solution for functionalisation and subsequently DI water washed. Additional electrical characterisation are carried out and the changes in electrical parameters detected.

4.2 Results and Discussion

4.2.1 Characterisation of CVD Grown Graphene on Cu foil

In this work, all samples are based on CVD grown graphene and a detailed analysis thereof is required. A first quality assessment of the graphene can be performed directly on the growth substrate using optical microscopy, SEM or Raman spectroscopy. The graphene itself is not easily visible on the Cu foil, since a monolayer graphene only absorbs 2.3% of the incident light. Only by variations in layer number, cracks within the graphene sheet, grain boundaries or similar inhomogeneities, the graphene can be visualised. This makes it especially difficult to detect a high quality and continuous monolayer. SEM is an important tool to investigate the graphene quality on Cu foil in high magnification and resolution. The

surface sensitive SE allow for an easy distinction between the graphene and the underlying Cu to visualise possible cracks or voids in the graphene sheet. Additionally, grain boundaries between graphene domains, as well as a decisive analysis of the number of graphene layers is easily possible.[175]

The SEM image in Figure 28a) shows graphene on the Cu foil after the typical CVD growth process. The diagonal line from the top left to the bottom right is a Cu grain boundary and the narrow dark lines distributed over the image correspond to graphene grain boundaries. The domain size of the graphene varies from several micrometres to approximately 15 µm. The few bright spots can be attributed to contamination from the furnace. The Cu foil is covered by a continuous monolayer of graphene, where no cracks or additional graphene layers are visible. For comparison, an SEM image with a multilayer graphene flake will be discussed in Figure 34, where the contrast difference in the SEM image is correlated to the number of graphene layers.

One step of the typical CVD process includes the Cu foil depletion of intrinsic carbon by O_2 introduction (see 3.1.1 Chemical Vapour Deposition). This step was found to be necessary to obtain better control over the growth process and decrease the nucleation density. Figure 28b) shows a Cu foil after a CVD process, where all typical steps (oxidation, subsequent reduction) were performed except the following methane flow. Since no carbon source was additionally introduced and the Cu foil is mostly depleted of carbon, no graphene layer forms. Some dark spots are visible on the foil which can be attributed to some carbon or beginning graphene formation, but the vast majority of the surface is plain Cu. Therefore, the oxidation process depleting the Cu foil of carbon is very efficient and the following graphene growth using methane flow corresponds to a controlled CVD process.

To analyse the graphene on Cu foil after the typically used CVD growth process, Raman spectroscopy is performed. The Cu foils cause a strong background in the Raman signal when excited with a 532 nm laser (2.33 eV), due to the surface plasmon emission of Cu.[176,177] Therefore, a laser with a wavelength of 404 nm (3.07 eV) is commonly chosen for detailed Raman spectroscopy of graphene on Cu. For comparison, a representative Raman spectrum acquired with each of the two lasers is displayed in Figure 28c). Note that the background is subtracted for the spectrum using the 532 nm laser.

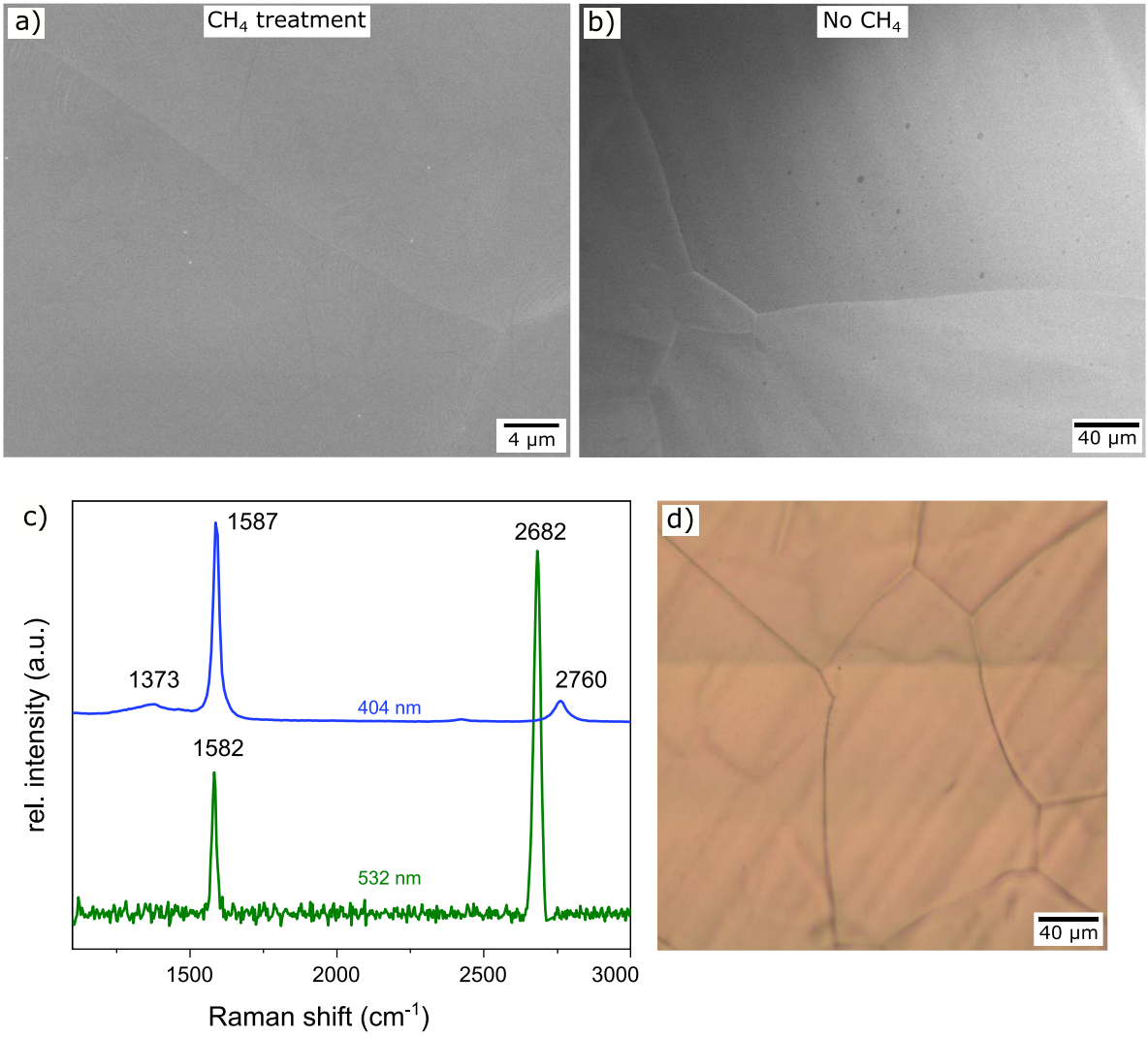

Figure 28. SEM images of Cu foils after different CVD processes a) with CH_4 introduction and b) without CH_4 during the process. Continuous graphene layer, with grain boundaries visible (a) in comparison to small and scattered graphene spots on the Cu foil (b). c) Raman spectra of high-quality monolayer graphene on Cu foil acquired with laser of different wavelengths: 404 nm (blue) and 532 nm (green). Peak positions of D, G and 2D peaks are noted in the image. The I_{2D}/I_G decreases drastically and the ω(2D) shifts to higher wavenumbers with increasing laser energy. d) Optical image of the graphene on Cu foil after the typical CVD growth process, comparable to the SEM in a).

Both Raman spectra show the G and 2D peaks typical for graphene. While the G peak position is comparably the same for both laser wavelengths, the peak parameters concerning the D and 2D peaks differ between them. The peak position $\omega(D_{532nm})$ at approx. 1350 cm^{-1} [137] shifts to higher wavenumbers with excitation wavelength, resulting in a $\omega(D_{404nm})$ of approx. 1370 cm^{-1}.[178,179] Similarly, the $\omega(2D_{532nm})$ and $\omega(2D_{404nm})$ are located at approx. 2682 cm^{-1} [74,127] and 2760 cm^{-1}, respectively, with a notable position shift between

them.[176,180] Additionally, the intensities of the peaks vary with excitation energy. For the 532 nm laser, the intensity ratio I_{2D}/I_G is in the order of 2 as described in section 2.3.1.2 Raman Spectrum of Graphene. This ratio decreases significantly using higher excitation wavelengths (approximately 0.3 in Figure 28c).[176,181] The FWHM(2D) increases from approximately 28 cm^{-1} in monolayer graphene to approximately 40 cm^{-1} over the range of 532 nm to 404 nm excitation wavelength. Overall, the spectrum of the graphene using the typical CVD growth process shows a high-quality monolayer with no distinctive D peak, a reasonable FWHM(2D) of 28 cm^{-1} and an I_{2D}/I_G of approximately 2, as derived from the spectrum using 532 nm excitation energy.

The optical image of the analysed graphene on Cu foil is depicted in Figure 28d), where the Cu grains are distinctly visible. Due to the properties of graphene, a monolayer thereof cannot easily be identified by eye and must be detected through other means such as Raman spectroscopy. The longitudinal marks in the Cu foil have their origin in the rolling of the Cu foil in the manufacturing process.

CVD grown graphene on Cu foil can easily be investigated using a combination of SEM imaging and Raman spectroscopy. The quality of the graphene including the continuity of the graphene sheet as well as the distribution of graphene grain boundaries and the graphene layer number are distinctly visible by SEM. The typical CVD growth process results in a coninuous graphene monolayer with domains of several micrometres in size. Additional Raman spectroscopy supports these findings and reveals a high quality monolayer graphene with a FWHM(2D) of approximately 28 cm^{-1}.

4.2.2 Characterisation of PBI Functionalisation of Graphene

Biosensors are expected to possess a high level of selectivity towards the substance being analysed. This is commonly achieved by using antibodies, which recognise their respective antigen. However, pristine graphene does not provide selective functionalisation with antibodies on its surface and a linker molecule is necessary to deliver the selectiveness between graphene and the antibodies. Perylene molecules serve as the linker molecules in this work and are characterised using Raman spectroscopy in the following. The Raman spectra in Figure 29a) show differently functionalised PBI samples, with magnification of the spectra in Figure 29b). Note that the spectra are normed to the respective highest perylene peak.

A solution of PBI in DI water was deposited onto a Si substrate via drop-casting and allowed to dry. The resulting solids after water evaporation consist of PBI molecules, which were

analysed using a 532 nm wavelength laser. Several distinct peaks can be identified that are typically found in a perylene Raman spectrum (Figure 29a, purple): 1302 cm^{-1},1381 cm^{-1}, 1457 cm^{-1}, 1574 cm^{-1}, 1582 cm^{-1} and 2680 cm^{-1}.[155,156] The last two peaks correlate with the graphene peaks (G and 2D, respectively) at the same wavenumbers. This is in agreement with what has been observed previously.[51,182] Additionally, the peak at approximately 1700 cm^{-1} was found to be attributed to imide bending, which is present in the chemical structure of the PBI.[182] For a closer look on the Raman peaks of the perylene molecules, refer to the detailed work of Chiang *et al.*[183] who combined theoretical time-dependent density functional theory and experimental tip-enhanced Raman spectroscopy. At this increased resolution, several prominent peaks were found to split into doublets. The exact analysis of the perylene peaks goes beyond the scope of this work and will not be investigated further.

Graphene on Cu foil is functionalised with the PBI by immersion in its solution. The resulting Raman spectrum (pink) is displayed in Figure 29a). Even though similar acquisition parameters as of pristine graphene on Cu foil are used (see Figure 28c), the spectrum appears much smoother and has a larger signal-to-noise ratio. This is the result of the GERS effect, which applies to self-assembled perylene molecules on graphene (refer to 2.3.1.1 Graphene-Enhanced Raman Spectroscopy). Additionally, the absence of a fluorescent background demonstrates the strong quenching effect of the graphene. The perylene peak intensities are increased and the signal-to-noise ratio becomes stronger. The high intensities of the perylene P1 and P2 peaks in contrast to the G peak reveal successful functionalisation of the graphene with a high packing density of the PBI molecules.[51]

PBI functionalised graphene on Cu foil is subsequently transferred onto a SiO_2/Si substrate using the FLaT approach and analysed with the 532 nm laser as well as the 404 nm laser. A Raman map of 100×100 μm^2 is acquired with a total of 4,356 single spectra arranged in an x-y grid (532 nm). The average of all spectra is displayed in Figure 29a) in red. The same peaks as described for the pure PBI are found and are located at the same wavenumbers. Interestingly, a qualitative analysis of the peaks in the magnification in Figure 29b) indicates highly similar peaks with similar intensities, FWHMs and peak positions. This will be investigated in more details in Figure 36.

Additionally, a second PBI FLaT sample is investigated, where the 404 nm laser is used (Figure 29a, blue). Interestingly, no perylene peaks show, which indicates that no Raman modes exist, which can be excited at that frequency. A Raman spectrum of the exact same sample acquired with the 532 nm laser is displayed in Figure A1, which shows successfully functionalised graphene with the typical perylene peaks. Using the 404 nm laser, solely the

underlying graphene is visible with the typical characteristics as described in the previous section. The ω(2D) is found at 2754 cm^{-1}, the FWHM(2D) is 37 cm^{-1} and the I_{2D}/I_G ratio is approximately 0.5. All values are comparable to the unfunctionalised graphene discussed in Figure 28c).

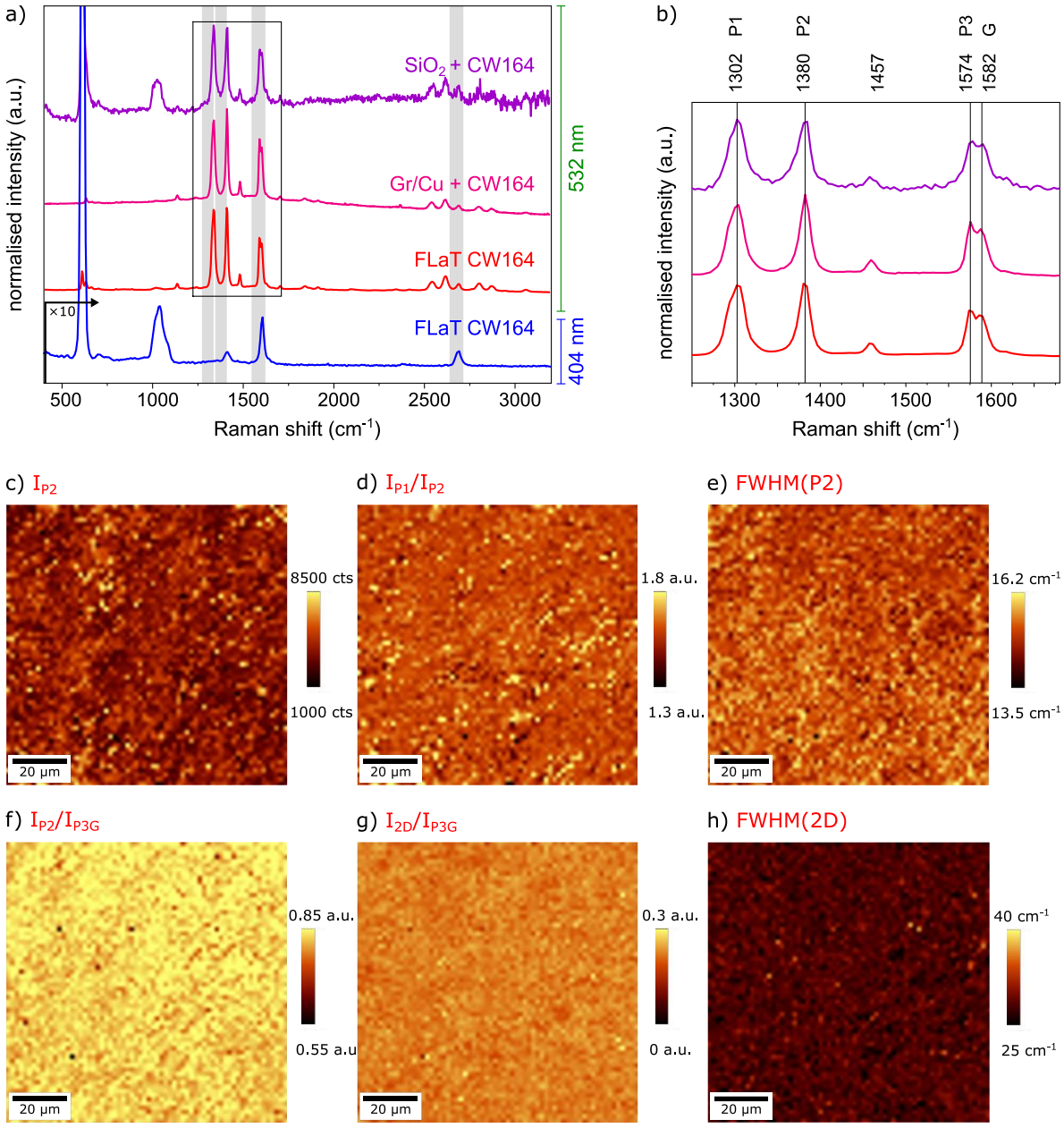

Figure 29. Raman spectroscopy of PBI on different substrates, investigated using the 532 nm and the 404 nm Raman laser. a) PBI solution dried in on Si (purple), the PBI as SAM on graphene on Cu foil (pink), average spectrum of a 100×100 μm^2 Raman scan of PBI FLaT graphene on SiO_2/Si using the 532 nm laser (red), and FLaT graphene using the 404 nm laser (blue). b) magnified wavenumber region of a) with peak positions indicated. c-h) Raman maps of the same scan as in a-b)

of the FLaT graphene imaged at 532 nm, with different filters applied (grey background in a). All show homogeneous PBI distribution over the entire area.

The large-scale Raman maps in Figure 29c-h) are derived from the same data set as the red spectrum in Figure 29a). Here, different wavenumber regions are selected to be displayed, which are marked as grey background in Figure 29a). The perylene peak P2 is of similar intensity over the entire area, although slight variations can be observed at specific locations. The intensity ratios of the P1 to the P2 peak, I_{P1}/I_{P2}, as well as the FWHM(P2) show a homogeneous distribution with mean values of 0.97 and 14.9 cm^{-1}, respectively. The ratios I_{P2}/I_{2D} and of I_{P2}/I_{P3G} show homogeneous Raman signals, with values of approximately 2.8 and 0.22. Similarly, the FWHM(2D) is uniform with a mean value of 30.7 cm^{-1}.

The successful functionalisation of graphene with the PBI is evident, both for graphene on the Cu foil as well as after transfer. The typical perylene peaks are visible at the same wavenumbers as in the pure PBI spectrum on SiO_2/Si substrate, with a much stronger signal-to-noise ratio due to the GERS effect when present as SAM on graphene. The distribution of the perylene on FLaT graphene is homogeneous on a large scale, as evidenced by the Raman maps.

Raman spectra of unfunctionalised (black, Unfunc.), conventionally functionalised (orange, Conv. func.) and FLaT (red) graphene are displayed in Figure 30a), with a magnified spectrum of the FLaT graphene in Figure 30b).[173] For better comparison, the same data of FLaT graphene were used in Figure 29 and Figure 30. Each Raman spectrum is averaged over several spectra taken to obtain a Raman map, which are displayed in Figure 30c-e). Note that in this section, the data acquired for the unfunctionalised and conventionally functionalised images originate from the same location on the same sample before and after PBI functionalisation, respectively. In contrast, the FLaT sample was first functionalised with the PBI and transferred subsequently. For details on the transfer protocol refer to 3.1.2 Graphene Transfer.

The spectrum of unfunctionalised graphene shows a high-quality monolayer with no distinctive D peak and an I_{2D}/I_G of approximately 2, which is comparable to what has been discussed in Figure 28. Both PBI functionalised graphene samples show prominent Raman peaks attributed to the PBI at approximately 1304 cm^{-1} and 1381 cm^{-1}.[155,156] Successful functionalisation of the graphene and a high packing density of the PBI molecule are found.[51] The peak intensities of PBI functionalised compared to unfunctionalised graphene are increased due to the GERS effect, as described in the previous section. Interestingly, the

Raman spectra of conventionally functionalised and FLaT graphene are highly similar and a high packing density for the conventionally functionalised graphene cannot be excluded using Raman spectroscopy. This might arise from the annealing step prior to PBI functionalisation and the fact that the laser spot is too large to investigate the spatial distribution of single molecules. All analysed samples stem from the same CVD growth batch and can, therefore, be expected to have similar graphene characteristics, which were described for the unfunctionalised sample.

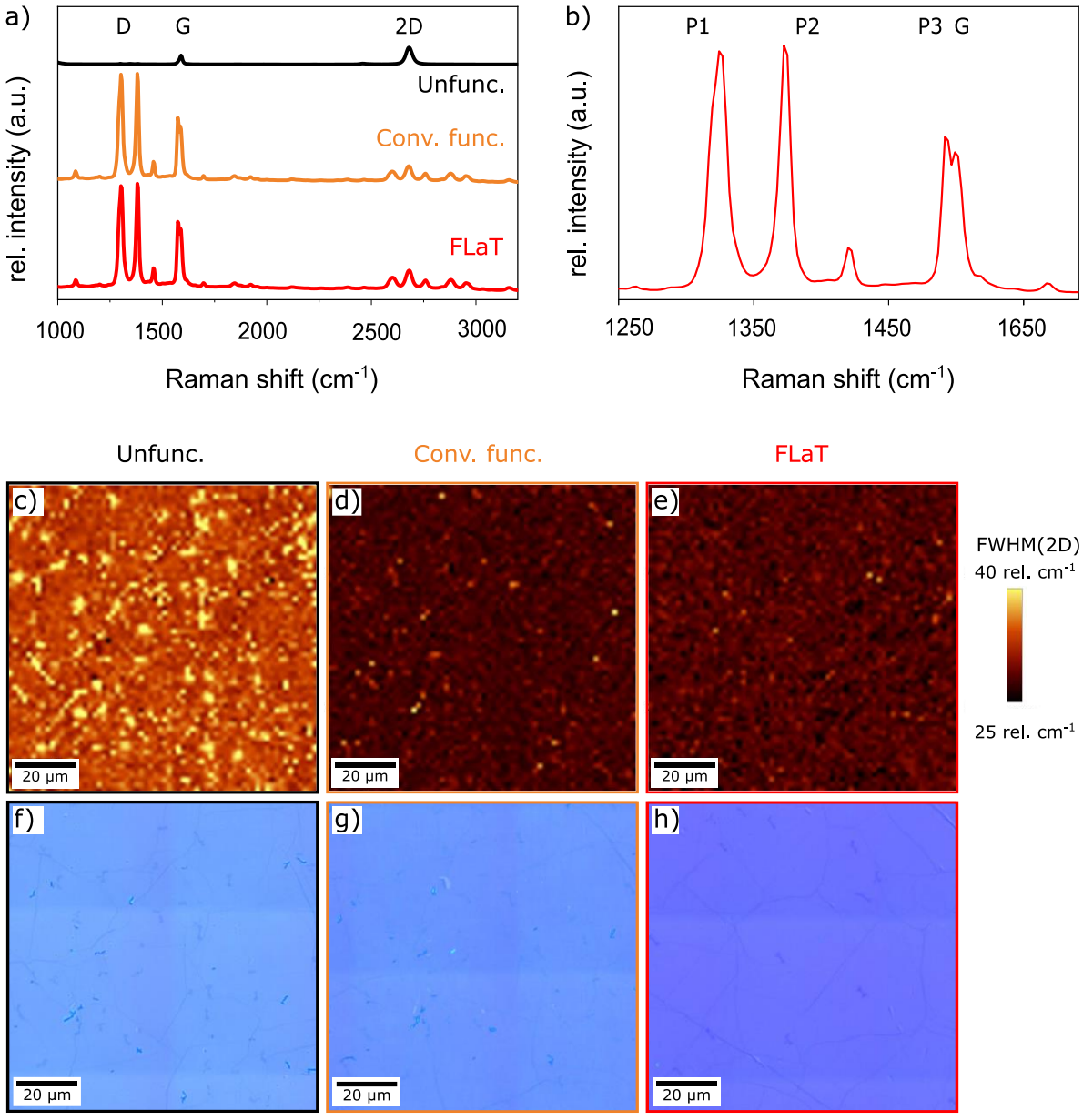

Figure 30. a) Raman spectra of unfunctionalised (black), conventionally functionalised (orange) and FLaT (red) graphene with the magnified spectrum of the FLaT sample in b). c-e) 100×100 µm² Raman maps of the FWHM(2D) at 2700 cm⁻¹ of unfunctionalised, conventionally functionalised and FLaT graphene, respectively, showing monolayer

graphene and a homogeneous PBI functionalisation, respectively. Same colour scale for all maps. f-g) Respective optical images.[173]

The Raman maps in Figure 30c-e) show the FWHM(2D) over an area of 100×1000 µm², with respective optical images displayed in Figure 30f-g).[173] The colour scale on the right side applies to all maps in this Figure. The unfunctionalised graphene (Figure 30a) has an average FWHM(2D) of 33.3 cm^{-1} and is characterised by primarily monolayer graphene with patches of bilayer graphene (yellow), supporting the pervious observation. The FWHM(2D) of approximately 30 cm^{-1} of the conventionally functionalised and FLaT samples with very little deviation indicate a highly homogeneous PBI coverage on the graphene. Additionally, the PBI functionalisation stabilises the FWHM(2D) to a slightly lower value than found in unfunctionalised graphene.

The same samples were investigated using AFM. The resulting large-area AFM scans of the unfunctionalised, conventionally functionalised and FLaT graphene are displayed in Figure 31a-c), respectively.[173] The scale bar is valid for all AFM scans in Figure 31. Each sample was thoroughly washed in acetone and IPA, and subsequently annealed in N_2 atmosphere to clean the samples.

Wrinkles and folds are visible on all samples, which are the consequence of mainly the transfer process. The white spots indicate higher situated features and can be attributed to polymeric residues on the surface. They are numerous in Figure 31a), become less in Figure 31b) and are almost non-existent in Figure 31c). This observation is quantified in the surface roughness, S_a, analysis over the scanned areas. It is largest for unfunctionalised graphene with an S_a of 0.99 nm. Interestingly, after annealing and subsequent PBI functionalisation of that same sample, the S_a is reduced to 0.85 nm (conventionally functionalised). In comparison, the surface of the FLaT sample appears smooth and clean, with few larger features on the surface. Here, the S_a is lowest with a value of 0.44 nm. This can be attributed to the pristine and exceptionally clean graphene surface before PBI functionalisation, which has been stated before.[169] During the short time between the CVD growth process and the PBI self-assembly on the graphene surface, very few pollutants and adsorbing species were able to contaminate the graphene. Thus, the self-assembly of the PBI on graphene proceeded undisturbed and homogeneously.

In Figure 31d-f), step edges from (functionalised) graphene to the SiO_2/Si substrate are shown. The height profiles are derived along the respective white dotted lines displayed in the images, and are visualised in Figure 31g). The unfunctionalised graphene (black) layer height of 0.9 ± 0.2 nm corresponds well with previous reports of transferred monolayer

graphene.[166,184] The height profiles of conventionally functionalised and FLaT graphene are similar with 2.3 ± 0.2 nm and 2.5 ± 0.2 nm, respectively.[173] In a previous study, it was found that perylene molecules selectively adsorb on 2D material surfaces and not on the SiO_2 surface.[170] As a consequence, the step height of the sample surface to the substrate is the combined height of graphene and the PBI layer. Taking the monolayer graphene height into account, the PBI layer height on FLaT graphene is approximately 1.5 nm. Previous publications of Tilmann *et al.*[170] and Wirtz *et al.*[185] have measured perylene monolayer heights of 1 nm and 1.2 nm, respectively. The perylene molecules used in their studies had smaller side chains than the PBI used in this work, which is likely to result in a smaller overall height.[170,185] Thus, the PBI monolayer height of 1.5 nm is reasonable.

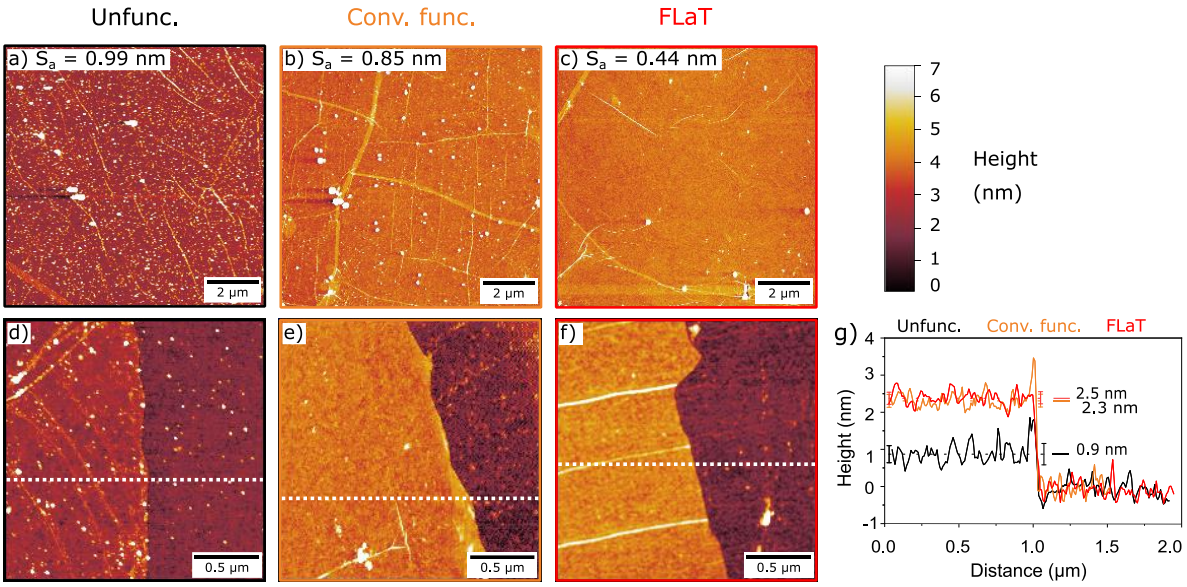

Figure 31. AFM images of a, d) unfunctionalised (black), b, e) conventionally functionalised (orange) and c, f) FLaT (red) graphene. The large-scale scans in the top row show decreasing surface roughness S_a from a-c). The height profiles in g) were derived along the white dotted line of the step edges from the (functionalised) graphene to the SiO_2/Si substrate (d-f). Same height scale for all images. The unfunctionalised graphene is identified as monolayer with a height of 0.9 nm, and the PBI layer height can be derived to be approximately 1.5 nm.[173]

To complete the characterisation of unfunctionalised, conventionally functionalised and FLaT graphene, SEM images of each sample type are displayed in Figure 32a-c), respectively. A darkening in the grey scale indicates an increased amount of graphene layers or other components, since the SE detector is used. In this configuration, each graphene layer attenuates the signal further, resulting in darkening of the image with increasing layer amount (see 2.3.3 Scanning Electron Microscopy). Therefore, the light grey, which covers the majority in all images, indicates monolayer graphene. The darker grey shows the

locations of bilayer graphene patches, which are commonly observed in CVD growth. Additionally, on all images, wrinkles and folds in the graphene can be seen. All samples have a very similar appearance, which is reasonable, and only the underlying graphene is visualised. Furthermore, organic molecules are easily destroyed when bombarded with electrons, which is why no sample was used for further measurements after SEM imaging.

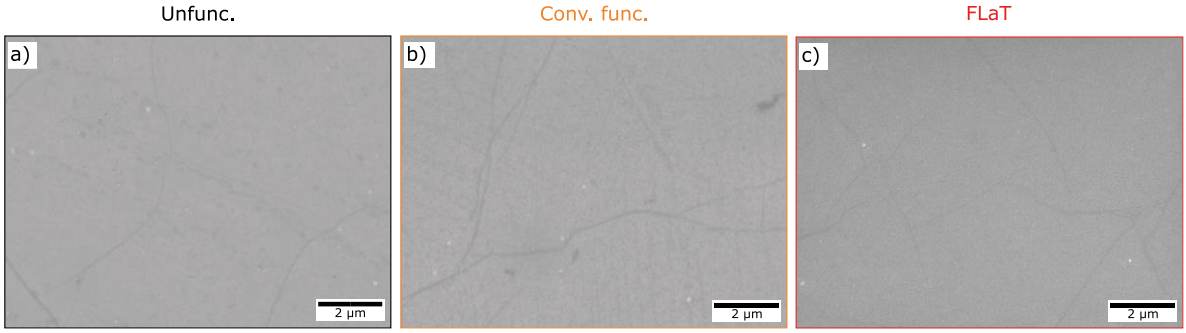

Figure 32. a-c) SEM images of unfunctionalised, conventionally functionalised and FLaT graphene on SiO_2/Si substrate, respectively. Some wrinkles and grain boundaries (dark lines) with an otherwise clean surface are visible. Domain size is roughly 5-10 µm.[173]

Transferred monolayer graphene was identified to have a high structural quality, with only few bilayer sites observable. However, it is characterised by a large surface roughness with numerous polymeric residues due to its direct contact to PMMA during transfer. Even though thorough acetone washing as well as annealing in N_2 were applied, the residues were not entirely removed. After PBI functionalisation, the surface roughness decreased slightly and a good PBI functionalisation was observed. However, the smoothest surface is obtained by FLaT transfer of graphene, taking advantage of the clean graphene surface after CVD growth. The cleanliness of graphene prior to functionalisation plays a crucial role in the development of a homogeneous noncovalent surface functionalisation. The PBI self-assembly resulted in a high packing density on the graphene and only very few residues due to the subsequent transfer process remain. Thus, in the following sections, only FLaT graphene will be applied. This homogeneous PBI SAM on graphene is highly beneficial for the following functionalisation steps, granting an exceptional starting point due to its homogeneous distribution.

4.2.3 Detailed Raman Spectroscopy Analysis of PBI FLaT Graphene

4.2.3.1 Optimisation of Raman Spectroscopy Parameters

Raman spectroscopy proves to be highly useful in order to examine the success and quality of the PBI functionalisation of graphene. The Raman laser locally introduces a high amount of energy on the surface to be examined, which can be destructive to organic molecules such as the PBI. In Figure 33a-e), the effect of the Raman laser on the PBI functionalisation at different laser powers (0.1 mW to 1 mW) and integration times (5 s to 20 s) is inspected. The Raman spectra of same laser powers are taken in the same location to ensure equal conditions, especially in terms of the laser focus on the sample (Figure 33f). The focus influences the peak intensities strongly, which can be neglected under the chosen circumstances. It was ensured that the respective locations were at least 30 µm away from each other to prevent one Raman spectrum to affect the remaining spectrum locations.

The Raman signal of the PBI is evident in all spectra presented in Figure 33a-e). Independent of the integration time used, the three spectra in Figure 33a) at the same laser power of 0.1 mW completely overlap with each other. This suggests that the PBI SAM on graphene remains intact as no signal reduction is observable. While the Raman spectra of 5 s and 10 s integration time in Figure 33b) overlap and imply an intact PBI SAM, the spectrum using 20 s integration time already shows a slightly lower intensity.

The simplest explanation theory for this behaviour is the perylene packing density on the surface and the influence on the peak contributions. Since the Raman signal indicates the packing density of the PBI on graphene (2.3.1.3 Raman Spectrum of a Perylene Bisimide Derivative), a higher packing density results in a higher perylene peak intensity. A decrease in the Raman signal can be correlated to a decrease of the PBI presence, when the remaining conditions are kept constant. Also, perylene peaks superimpose graphene's peaks and following a decrease in perylene peak contribution, the contribution from the graphene's peaks increases. Therefore, a change in peak characteristics can be explained by a partial destruction of perylenes due to the laser.

Starting from Figure 33c), a gradual destruction of the perylene molecules can be observed, which increases both with integration time and laser power. This is most significant at 1 mW laser power in Figure 33e), where the peak intensities decrease significantly using 10 s (red) integration time and even more significantly at 20 s (green).

A deeper investigation is performed by correlating the peak intensities and the FWHM(2D) to the laser powers and integration times used. Since the Si peak intensity is assumed to

stay the same for monolayer graphene samples, the relative changes of the P2 peak to the Si peak are taken as a measure of perylene destruction. The I_{P2}/I_{Si} ratio stays approximately constant for 0.1 mW and 0.2 mW laser power, independent of the integration time. With increasing laser power as well as increasing integration time from 0.3 mW onwards, the ratio decreases significantly. The minimum of -34% is reached for 1 mW laser power and 20 s integration time. Similarly, the I_{P2}/I_{2D} ratio decreases and the FWHM(2D) increases with increasing laser power.

The laser power of 0.2 mW can be assumed to be non-destructive to the perylene, while a notable Raman signal decrease is observed for higher laser powers. To obtain the maximum Raman signal at no significant PBI destruction, for all following Raman measurements of functionalised graphene a laser power of 0.2 mW with 10 s integration time is chosen.

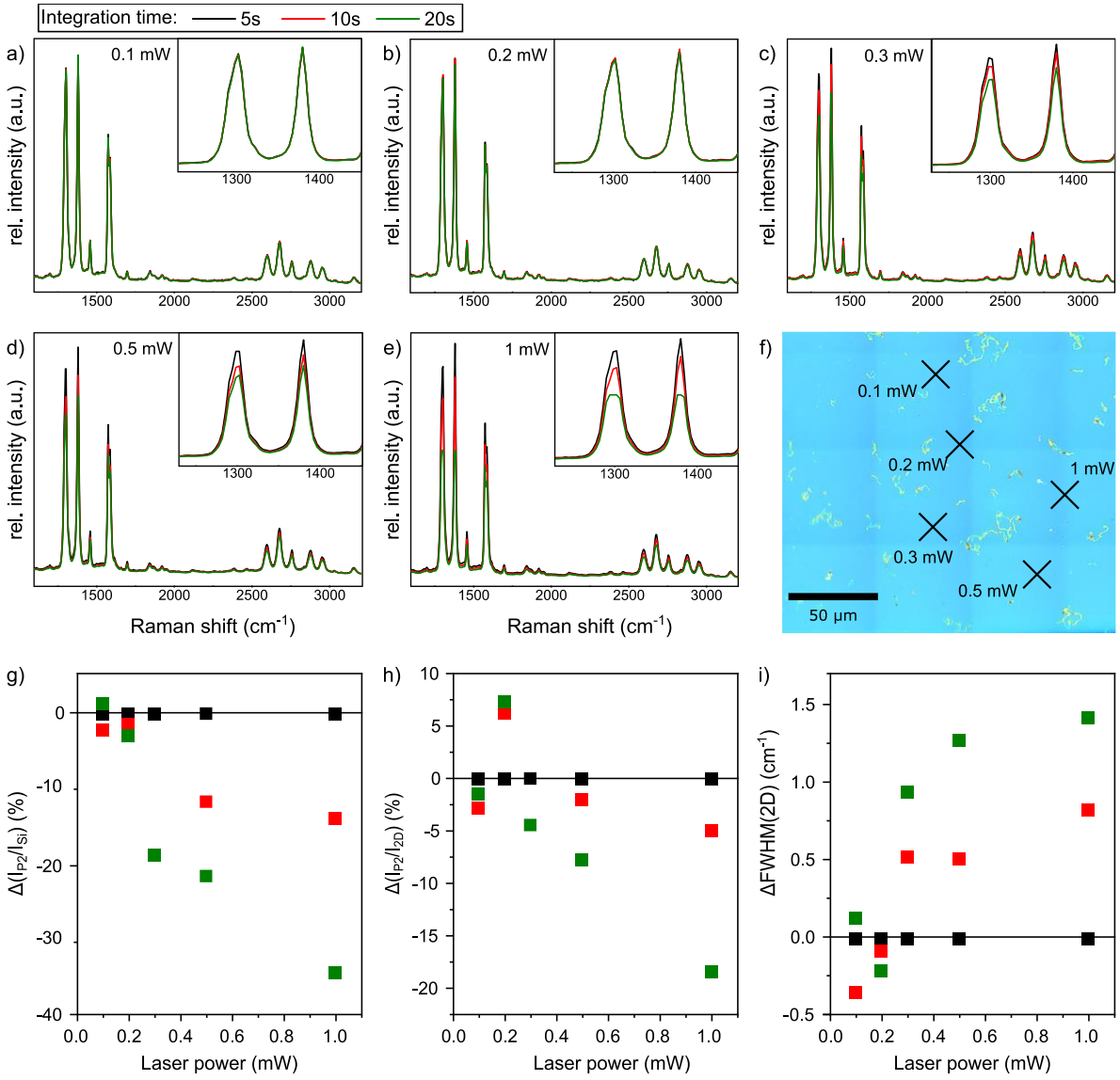

Figure 33. Influence of laser power and integration time on the PBI functionalised graphene. a-e) 0.1 mW to 1 mW laser power, respectively, at integration times of 5 s (black), 10 s (red) and 20 s (green). Peaks P1 and P2 magnified in the insets. f) optical image of the PBI graphene with locations of Raman spectra indicated. g-h) Relative peak intensity ratios of I_{P2}/I_{Si} and I_{P2}/I_{2D}, respectively, i) relative FWHM(2D) change.

4.2.3.2 Raman Signal Dependency on Graphene Layer Number

The Raman spectra of unfunctionalised graphene change significantly due to the graphene layer number, especially with regards to the I_{2D}/I_G and FWHM(2D), as discussed in section 2.3.1.2 Raman Spectrum of Graphene. Since the PBI functionalisation of graphene has a strong effect on the Raman signal, Raman spectroscopy data of PBI FLaT graphene in relation to the graphene layer number are investigated and are displayed in Figure 34. To

obtain a graphene sample with large multilayer flakes, the CVD growth process was adjusted and a ratio of 40:20 sccm H_2:CH_4 for 30 min was introduced during the growth process, while the remaining steps were kept constant. This high methane concentration resulted in multilayer graphene flakes with dimensions of approximately 25-40 µm², with the innermost core being 3 layered graphene, as detected by both SEM imaging and optical microscopy. The SEM image shows monolayer graphene on the majority of the sample, with multilayers in the centre (Figure 34a). The SE detector of the SEM can resolve single graphene layers, where the signal is attenuated with each layer. Therefore, the innermost spot is trilayer graphene, with a bilayer surrounding it and monolayer graphene covering the remaining surface. The CVD grown graphene was subsequently transferred using the PBI FLaT approach. An area of 10×10 µm² is investigated, with the multilayer graphene flake in the centre, as is visible in the optical image (Figure 34b). A false-colour image visualises the approximate areas of same layer number (Figure 34c). Note that it is not the same multilayer flake as in Figure 34a), because SEM imaging of PBI functionalised graphene likely leads to a destruction of the PBI molecules. However, the analysed sample stem from the same growth process.

The entire 10×10 µm² area is mapped using Raman spectroscopy and one single spectrum is taken from the scan on each of the trilayer types (Figure 34d), with monolayer graphene in red, bilayer graphene in purple and trilayer graphene in blue. A vertical offset of the spectra is applied to visualise them more clearly. All spectra show the typical perylene peaks. Even though the spectra look similar, an increased 2D peak intensity is already seen in the trilayer graphene spectrum. Interestingly, the Raman spectrum of 3-layered graphene is significantly noisier than the other two spectra and also has a slightly increased background. This might be an indication, that the coupling of the PBI to the graphene becomes less with graphene layer number.

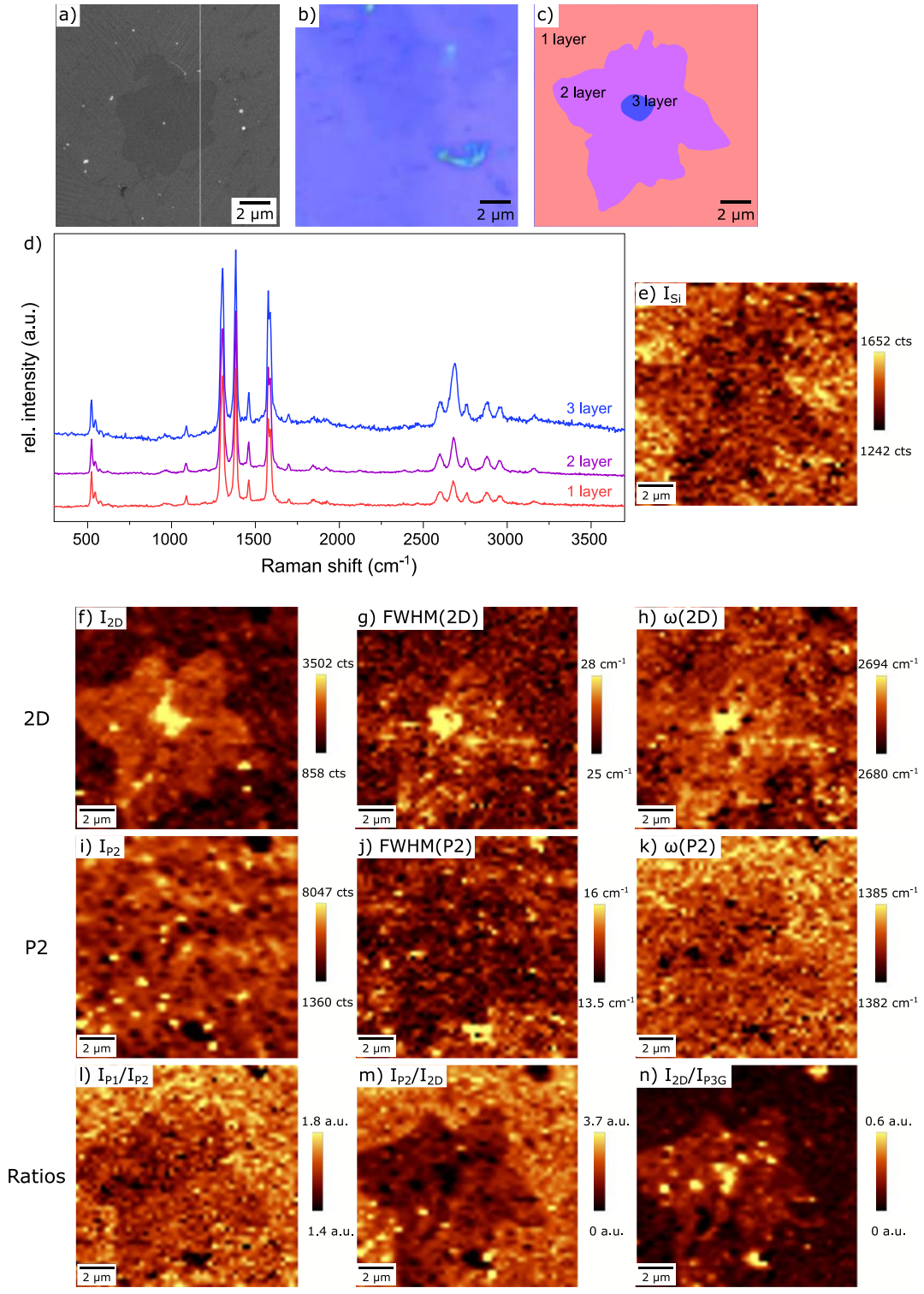

Figure 34. a) SEM image of a multilayer graphene flake on Cu foil, b) optical image of a 10×10 µm² area of PBI FLaT graphene with a multilayer graphene flake in the centre of the same growth process as in a). c) False-colour map of b). d) Exemplary Raman spectra of a monolayer (red), bilayer (violet) and trilayer (blue) graphene. d-f) Raman spectroscopy maps of the same are imaged in a). A signal dependence on layer number can be seen in the majority of Raman maps.

Several filters are applied on the Raman map, out of which selected maps are displayed in Figure 34e-n). Additional Raman maps with different filters can be found in Figure A3. As a reference, the I_{Si} map at 520 cm^{-1} is shown, where the signal attenuation with increasing graphene layer number is observed, as would be expected. Especially in the Raman maps related to the 2D peak, a strong signal change due to the number of layers is visible, where the intensity, FWHM and ω increase with increasing layer number. This is a reasonable result, since the 2D peak is the most indicative peak to derive the layer number in unfunctionalised graphene. The distinction of the layer numbers in the I_{2D} is clear, with higher intensity of the 2D peak indicating a higher layer number (Figure 34f). However, this quantity cannot be used in comparison with Raman maps of other samples, as the settings of each Raman spectroscope and the surrounding conditions influence the absolute peak intensities. The average values of the FWHM(2D) are revealed to be 30 ± 2 cm^{-1}, 34.0 ± 4 cm^{-1} and 45.5 ± 1.5 cm^{-1} for mono-, bi- and trilayer graphene, respectively (Figure 34g). The value for monolayer graphene is comparable to what was observed in Figure 29. Additionally, the ω(2D) indicates a shift to higher wavenumbers for increasing layer number, but the distinction between mono- and bilayer is challenging (Figure 34h). The mentioned behaviour of the 2D peak parameters with layer number is similar to what would be expected for unfunctionalised graphene. Interestingly, the graphene signal is still detectable, despite the superposition of the PBI with the graphene peaks.

The perylene peak P2 alone does not show any reliable changes with graphene layer number. While the FWHM(P2) and the ω(P2) both create the impression to decrease with increasing layer number, the signal is not clear enough to draw definitive conclusions (Figure 34j-k, respectively). Interestingly, even though the individual perylene peak intensities do not show any signal difference by themselves, in the combination of I_{P1}/I_{P2} the signal is inversely proportional to the graphene layer number. The signal is strongest for monolayer graphene with 0.98 (0.97 in Figure 29) and decreases to ~0.90 for trilayer (Figure 34l). Since the intensities of the peaks are influenced by the focus, a comparison between this analysis and previous ones are challenging. As expected, the intensity of the I_{P2}/I_{2D} decreases with increasing layer number (Figure 34m). Respectively, the intensity of I_{2D}/I_{P3G} increases with layer number (Figure 34n), resulting in approximately 0.35 up to 0.60 for monolayer and trilayer graphene, respectively. The comparison of the Raman characteristics of the monolayer graphene between the two samples discussed (Figure 29 and Figure 34) shows a very strong correlation between the values observed.

The data obtained in this section reveal the possibility to derive the graphene layer number from PBI FLaT graphene. Like unfunctionalised graphene, the 2D peak is affected most

thoroughly by the layer number. Therefore, the observation of the intensity, FWHM and ω of the 2D peak are most interesting to derive the layer number. Additionally, the intensity ratio of the perylene peaks P1 to P2 show a signal change with layer number. Interestingly, the deviation from mono- to bilayer is most pronounced using the perylene peaks, while it is not significant using the 2D peak. However, no overall change in characteristics between bi- and trilayer graphene can be observed using solely the perylene peaks, while it is most significant using the 2D peak. This analysis presented here is mostly qualitative and a more detailed analysis is required to allow a precise statement on the correlation of Raman spectroscopy parameters and the layer number of graphene.

4.2.3.3 Temperature Stability

Organic molecules are usually vulnerable to changes from ambient conditions such as too much energy induced by a laser as discussed in section 4.2.3.1 Optimisation of Raman Spectroscopy Parameters, but also heat in general. To investigate the response of PBI FLaT graphene to elevated temperatures, the samples were exposed to various temperatures at 150 mbar in N_2 atmosphere for 1 h. Exemplary Raman spectra for each treatment are displayed in Figure 35. Similar to the previous section, the spectra are normed to the Si peak at ~520 cm^{-1} to better visualise changes in the peak intensities. The Raman spectra of each sample before annealing can be found in Figure A2, which all show successfully functionalised graphene, as described before.

The Raman signal mirrors the interaction of the PBI with the graphene. In entirely intact PBI FLaT graphene, the FWHM(2D) is relatively constant, as was discussed in Figure 29 and Figure 34. In comparison, unfunctionalised graphene commonly has a larger FWHM(2D), which was revealed to be approximately 33 cm^{-1} (Figure 30). Therefore, with decreasing influence of the PBI, the FWHM(2D) is expected to converge to the value of unfunctionalised graphene, and, thus, to increase. The Raman spectrum after annealing the sample at 400 °C is not altered in comparison to pre-annealed PBI FLaT graphene, which is indicated by the equally high perylene peaks. The I_{P2}/I_{Si} as well as the FWHM(2D) have not significantly changed (Figure 35b, c). With increasing annealing temperature, the intensity of the perylene peaks decreases drastically. Already at 450 °C, the I_{P2}/I_{Si} is decreased by 22% and the FWHM(2D) by 4.5 cm^{-1}. An even stronger perylene peak intensity decrease can be observed for treatments from 500 °C onwards. After annealing at 525 °C, the spectra show extremely small peaks. In both I_{P2}/I_{Si} and FWHM(2D) analysis, the parameters have changed significantly due to annealing.

To the extent of the Raman analysis performed here, annealing of the PBI FLaT graphene at temperatures including 400 °C does not appear to affect the functionalisation significantly. However, for higher temperatures, the PBI molecules begin to degrade continuously, with the extent of degradation increasing with higher temperatures. This analysis was based on the intensity ratio of the P2 to the Si peak and not between the perylene peaks themselves. However, the relative increase of the FWHM(2D) is a strong indication of a smaller influence of the PBI on the Raman spectra. Typically, organic molecules do not survive temperatures of 400 °C for such a prolonged period as was investigated here. Remarkably though, the PBI on graphene are assumed to be relatively stable under these conditions.

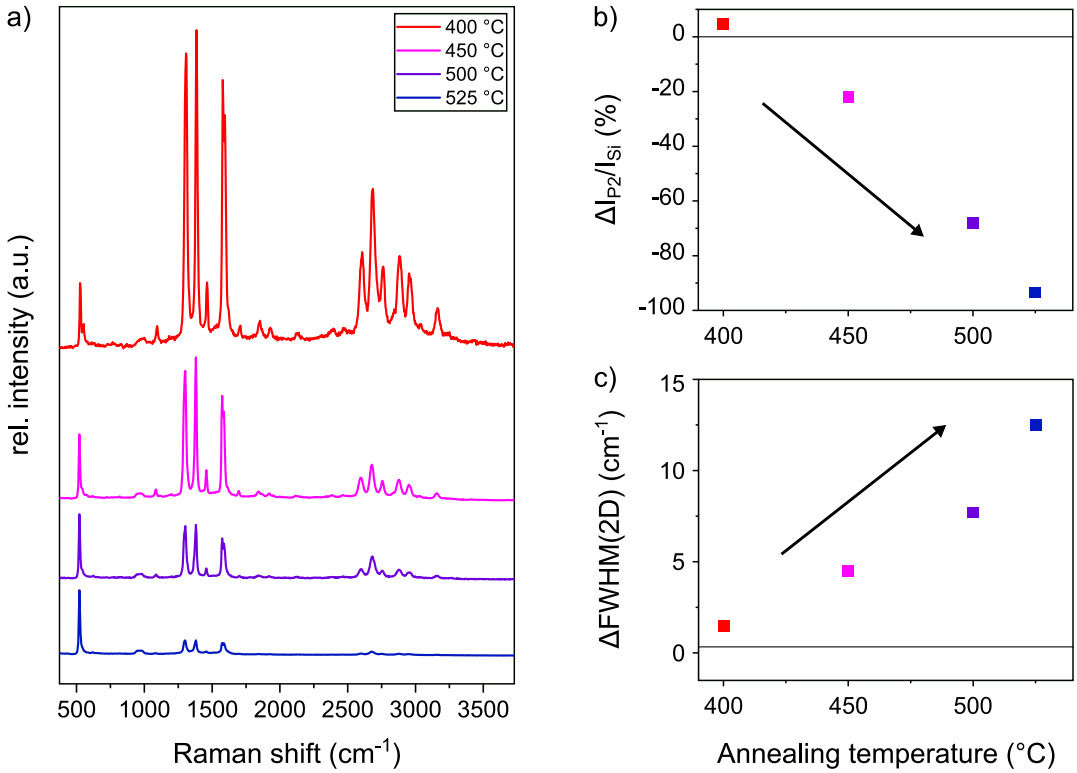

Figure 35. a) Raman spectra of PBI FLaT graphene after annealing at temperatures from 400 °C to 525 °C (red to blue). Relative changes in the Raman spectra of before and after annealing at given temperatures, with b) $\Delta I_{P2}/I_{Si}$ and c) ΔFWHM(2D).

4.2.3.4 Substrate Influence on the Raman Characteristics

In this chapter, Raman spectroscopy of the PBI on different substrates was performed, including in solid form on SiO_2/Si, as SAM on graphene on Cu foil, and as SAM on transferred graphene (both conventionally functionalised and FLaT). All Raman data included in this section were separately discussed in Figure 29, Figure 30 and Figure 34, and

more details on the samples can be found in the respective section. All data stem from the average Raman spectrum of large-area Raman maps, and subsequent filters are applied to study one aspect of the spectrum. The results are summarised in Figure 36.

To narrow down the analysis to the most informative and significant parameters identified, the selected parameters are either P2 peak or 2D peak related. The I_{P1}/I_{P2} appears to be primarily substrate-independent and remains relatively unchanged across all samples (Figure 36a). However, while the intensity ratio is approximately 0.97 across the majority of samples, the self-assembled PBI on graphene/Cu has a slightly decreased ratio of approximately 0.96. Additionally, with increasing graphene layer number of the FLaT samples, the I_{P1}/I_{P2} decreases to 0.96 (bilayer) and then strongly to 0.90 for trilayer graphene.

Similarly, while the I_{2D}/I_{P3G} is relatively constant for all substrates but the PBI on graphene/Cu, more graphene layers increase the ratio significantly from approximately 0.35 to ~0.6 for trilayer graphene. This is the opposite effect of what would be expected for unfunctionalised graphene, where the ratio typically decreases with increasing layer number. A possible explanation is the change in coupling effect of the PBI to the graphene with increasing layer number. This evaluation of this effect is beyond the scope of this thesis and needs to be investigated in future experiments. The value of PBI SAM on graphene on Cu foil is very low with an I_{2D}/I_{P3G} of 0.2. This sample shows the most deviation from the mean values in almost all of the here discussed analysis.

The FWHM(P2) and the ω(P2) remain unchanged due to the PBI being on different substrates, expect for the PBI on graphene/Cu, which shows a decreased and increased value, respectively (Figure 36b). While the graphene layer number does not affect the ω(P2), a slightly decreased FWHM(P2) with increased graphene layer number is observed. However, the differences are very small and might be within the error. No graphene peak except the D peak at 1350 cm^{-1} exists in the wavenumber range of the P2 peak and no change in P2 peak related parameters is reasonable. The D peak only exists for defective graphene and, if no defects exist, no increase thereof is expected.

Both the FWHM(2D) and the ω(2D) are primarily independent on substrate but significantly change with increasing graphene layer number (Figure 36c). This response to layer number increase is partially expected for unfunctionalised graphene as well, where the differences between monolayer and bilayer are strongest and subsequent layer addition is not as easily tracked. However, the PBI on SiO_2/Si substrate has a slightly smaller FWHM(2D) of approximately 27.5 cm^{-1}.

This analysis indicates that the majority of Raman characteristics is independent of the substrate, which means that the parameters are mainly influenced by the PBI itself. This was revealed by comparing the peak intensity ratios, FWHM and position values of different samples.

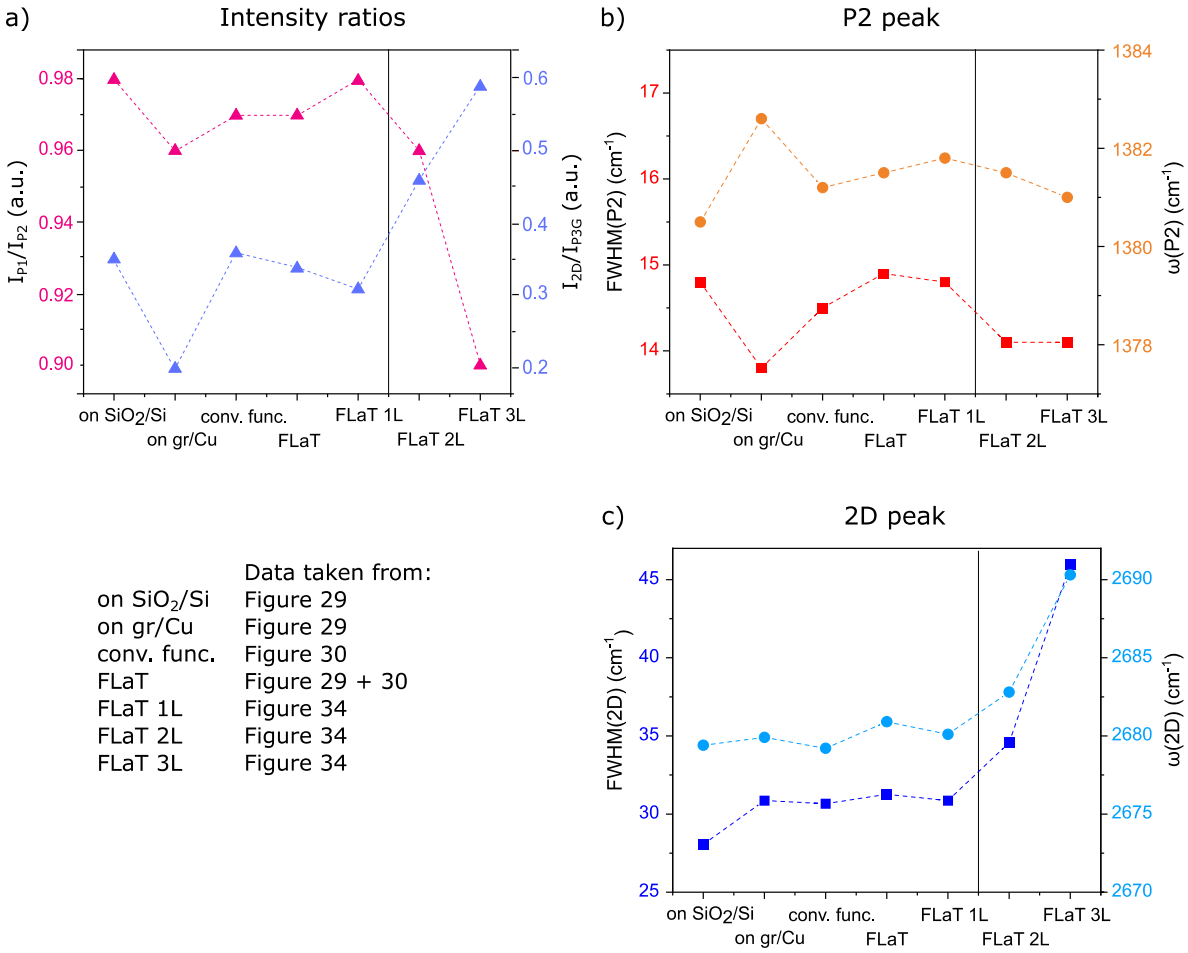

	Data taken from:
on SiO_2/Si	Figure 29
on gr/Cu	Figure 29
conv. func.	Figure 30
FLaT	Figure 29 + 30
FLaT 1L	Figure 34
FLaT 2L	Figure 34
FLaT 3L	Figure 34

Figure 36. Combined Raman spectroscopy results of the PBI on various substrates. A) intensity ratios I_{P1}/I_{P2} and I_{2D}/I_{P3G}, b) P2 peak characteristics FWHM(P2) and ω(P2), c) 2D peak characteristics FWHM(2D) and ω(2D). Changes mostly in 2D-peak related parameters due to graphene layer number. However, FWHM(P2) might indicate a substrate-related charge rather than layer number related. The data were previously discussed in several sections of this chapter, to which they are referred to.

4.2.4 Electrical Characteristics

The modification of the graphene surface can cause a change in several properties of graphene, resulting from the interaction of the molecule with graphene. Noncovalent functionalisation is commonly considered to not be detrimental to graphene's chemical structure and, thus, to its electrical properties. However, charge transfer is a common,

sometimes desired, effect of this type of functionalisation, where the π-system of graphene interacts with the molecule. This may cause changes in the measurable electrical properties of graphene. The majority of research in this work is done with the PBI as functionalising molecule on graphene. In Figure 37, the changes in electrical response of GFETs due to the functionalisation with the PBI are shown. An unfunctionalised GFET was electrically analysed, subsequently functionalised with the PBI and characterised again. The changes in the resistance, Dirac voltage and charge carrier field-effect mobility are displayed in Figure 37a-c), respectively. Each individual device is represented as a black diamond. The average of all values is displayed as a red square with the respective standard deviation.

The ΔR decreases by -34.7 ± 9.1% due to PBI functionalisation, while the ΔV_{Dirac} increased by 14.6 ± 4.0 V. Both results indicate a p-type doping effect of the PBI on graphene. This is in accordance with findings from Marcia *et al.*[186] who stated an electron deficiency of the PBI core. As a result of that, the PBI core is a p-type dopant to graphene.

While the ΔR and ΔV_{Dirac} data suggest a relatively defined change in parameters, the mobility analysis is not as clear. Due to PBI functionalisation, the $\Delta\mu$ stays approximately the same, with a slight change of -1.9 ± 16.1%. However, the standard deviation is extremely large, which indicates a not as reliable result as for the other two measurements. Summarising, the functionalisation with PBI is not detrimental to the electrical properties of graphene, with a R decrease, V_{Dirac} increase and an unchanged mobility observed.

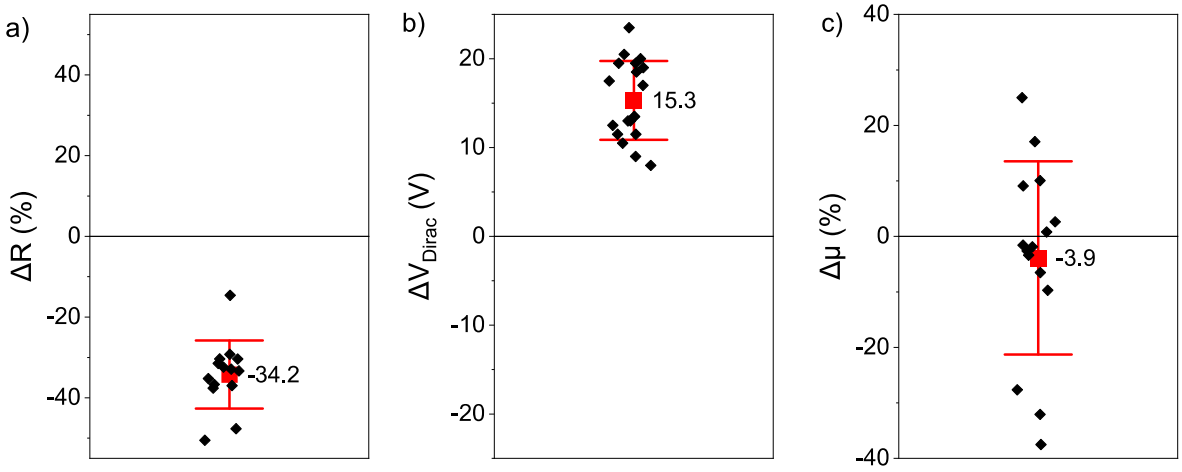

Figure 37. a-c) ΔR, ΔV_{Dirac} and $\Delta\mu$ due to functionalisation of GFETs with PBI. Each diamond represents one device. The mean value (red square) is labelled, with the respective standard deviation.

4.3 Conclusion

In this chapter, a comprehensive investigation of the CVD grown graphene, the PBI molecules, and the noncovalent functionalisation of graphene with the PBI was conducted using various techniques such as SEM, Raman spectroscopy, AFM, and electrical measurements. The optimised CVD growth method typically performed in this work successfully produces a high-quality and continuous monolayer graphene with a domain size of 5-15 µm, as revealed by SEM. This is supported by Raman spectroscopy, showing the typical graphene peaks in the defect-free monolayer arrangement, which is derived mainly from the absence of the D peak and the characteristics of the FWHM(2D). This applies to both the graphene on Cu foil and after its transfer onto SiO_2/Si substrate using the conventional wet-chemical transfer process.

Raman spectroscopy of the pure, solid PBI molecule on SiO_2/Si substrate revealed several high intensity Raman peaks, which are typical for perylenes. Two of those peaks superimpose the graphene G and 2D peaks at the same wavenumbers.

The majority of samples in this work is prepared using the FLaT approach, where the graphene on Cu foil is noncovalently functionalised with the PBI directly after CVD growth by immersion in a water-based PBI solution. This is followed by a wet-chemical transfer of the functionalised graphene onto a SiO_2/Si substrate, where the polymer PMMA serves as supporting layer and is removed subsequently. Both the as-functionalised graphene on Cu foil as well as after the complete FLaT show the typical perylene peaks with a high signal-to-noise ratio. The overall peak intensities are much higher than in comparison to unfunctionalised graphene and pure PBI molecules under similar Raman spectroscopy settings. This indicates a strong coupling between the PBI and graphene molecular systems, enhancing the Raman signal and quenching possible fluorescence, which is called the GERS effect.

This PBI functionalisation of the graphene surface prior to the wet-chemical transfer onto SiO_2/Si substrate is of exceptional importance. The graphene surface has the highest cleanliness directly after CVD growth, which is the perfect starting point for a homogeneous self-assembly of the PBI with high packing density of the molecules. This is mirrored not only in large-scale Raman spectroscopy maps, but also in the detailed AFM analysis. This technique reveals a smooth PBI monolayer on FLaT graphene of approximately 1.5 nm height with a low surface roughness of 0.44 nm, in contrast to the increased roughness of conventionally functionalised graphene. In that case, the graphene was first transferred, and functionalised with the PBI after the removal of the PMMA. This approach does not provide

a highly clean graphene surface to begin with and the molecules are not able to self-assemble as homogeneously on the surface as determined for the FLaT.

The noncovalent functionalisation of the graphene was found to be non-destructive to the graphene lattice, as derived from the prevailing consistent mobility. However, the functionalisation induced a resistance decrease and simultaneous V_{Dirac} increase, which can be attributed to a p-type doping of the PBI.

Raman spectroscopy of PBI FLaT graphene was optimised by testing the integrity of the PBI layer by using different acquisition parameters, such as laser powers and integration times. The highest signal at no significant PBI destruction due to the Raman laser was discovered to be 0.2 mW at 10 s integration time. These settings were used in all further Raman characterisation of perylene functionalised graphene. Additionally, Raman spectroscopy revealed the stability of PBI FLaT graphene up to and including 400 °C for 1 h in nitrogen atmosphere. With increasing temperatures from there on, the Raman peak intensities decreased significantly and the FWHM(2D) increased, suggesting a stronger influence of the underlying graphene to the Raman signal. This temperature stability allows the FLaT approach to be investigated for example in back-end-of-line applications, where elevated temperatures are often required to integrate devices.

The PBI Raman peaks superimpose the graphene peaks, making an analysis of the graphene layer number challenging. Interestingly, the 2D peak is still very informative and similar characteristics as for unfunctionalised graphene can be revealed, with increasing FWHM and peak position of the 2D peak with increasing layer number. Since also the intensity of the 2D peak increases with layer number, all intensity ratios including this peak can be taken into account for the analysis. Additionally, the intensity ratio of the P1 to the P2 peak gives rise to the layer number. Several PBI Raman characteristics with respect to their dependence on the underlying substrate are compared, including intensity ratios, FWHM and peak positions. The substrate used does not influence the perylene peaks strongly, which is derived from the similar characteristics for the majority of substrates.

5 Development of a Reliable Biosensor Platform

5.1 Introduction

A bioanalytical sensor is a device which is used to detect, measure and monitor biological molecules. It usually combines physical, chemical and biological components in order to detect and analyse a specific type of molecule. To ensure not only qualitative analysis, quantitative methods have to be investigated. Thus, labelling methods are widely applied and used most often so far. This includes the labelling of either a second antibody or the antigen, if applicable, with e.g. a fluorescent dye, molecules or nanoparticles. If the labelled molecules bind to the sensor surface, the sensor response can be quantified. As an example, the intensity of the measured fluorescence gives quantitative information on the labelled molecule concentration. In this chapter, the second antibody is labelled with gold nanoparticles (AuNPs) instead of a fluorescent dye. The working principle is similar and instead of the intensity of fluoresce, the number of gold nanoparticles is quantified.

For a long time it has been known that the antibody-antigen coupling mechanism is exceptionally specific and that low cross-reactivities can be achieved.[124] Furthermore, it has been found that the covalent bonding of antibodies to specific sites on the substrate, rather than random adsorption thereof, improves the density of the antibody distribution.[121] While this is highly beneficial for the detection of antigens, a homogeneous underlying anchoring layer is required to bind antibodies homogeneously as well. Secondly, covalent bonding of antibodies to the substrate involves random orientation of antibodies, which is due to their large amount of functional groups distributed over their whole surface.[121]

The preparation of anchoring functional groups on the graphene can easily be done by the physisorption of molecules on the graphene surface.[58,121] Thus, molecules with an aromatic core and additional functional groups are prone as anchoring molecules. The aromatic core serves as the stabilising part of the molecule on graphene *via* noncovalent π-π-interaction. The head-groups are solution-faced and contain functional groups for further chemistry.[121] Thus, the molecule 1-pyrenebutanoic acid succinimidyl ester (PBASE) has been widely applied as linker molecule in numerous publications.[29,58,187–189] Perylene molecules fulfil these requirements as well but have not been used as much. STM analysis showed that perylenes

produce a homogeneous anchoring layer through self-assembly on graphene.[51] This is supported by the Raman spectroscopy and AFM analysis performed in the previous chapter, where a homogeneous layer of the self-assembled PBI molecules on graphene was revealed. This characteristic feature will be exploited in the following chapters.

This chapter outlines the different development stages to create a graphene-based biosensor platform for the detection of specific molecules. The noncovalent PBI functionalised described in the previous chapter is complemented by the use of antibodies to enhance the specificity of the biosensors. The exemplarily chosen methamphetamine-AB is immobilised on the PBI functionalised graphene and the density of the antibodies' receptor sites is investigated. Therefore, a second antibody (AB2) is conjugated with gold nanoparticles (AB2-AuNP), which produces markers visible by SEM. Their density is used to draw conclusions on the underlying antibody layer.

5.2 Experimental Details

Typically, the PBI functionalised graphene samples in this chapter are transferred using the FLaT approach. Unfunctionalised graphene is prepared using the conventional transfer method, and subsequent PBI functionalisation thereof results in the conventionally functionalised graphene. For details on the transfer protocols, refer to 3.1.2 Graphene Transfer.

5.2.1 Surface Functionalisation

The protocol in 3.2 Specific Functionalisation to Realise Biosensor demonstrates the general surface modification steps for further functionalisation of the PBI functionalised graphene. In the general approach, the methamphetamine-AB is coupled to the carboxylic groups of the PBI using EDC/NHS chemistry, resulting in the methamphetamine biosensor platform. Subsequently, AB2-AuNP is applied and the AB2 binds to the methamphetamine-AB (see Figure 38). The incubation times are 15 min for EDC/NHS, 30 min for methamphetamine-AB and 10 min for AB2-AuNP coupling. Note that for direct comparison all functionalisation steps are carried out equally for unfunctionalised samples.

Different methamphetamine-AB concentrations (0.5 µg/ml, 2 µg/ml, 6 µg/ml and 10 µg/ml and AB2-AuNP concentrations (0.5%, 20%, 40%, 60% and 100%) were used throughout this chapter. If not specifically stated, the highest concentrations of each antibody solution were applied (10 µg/ml and 100%, respectively).

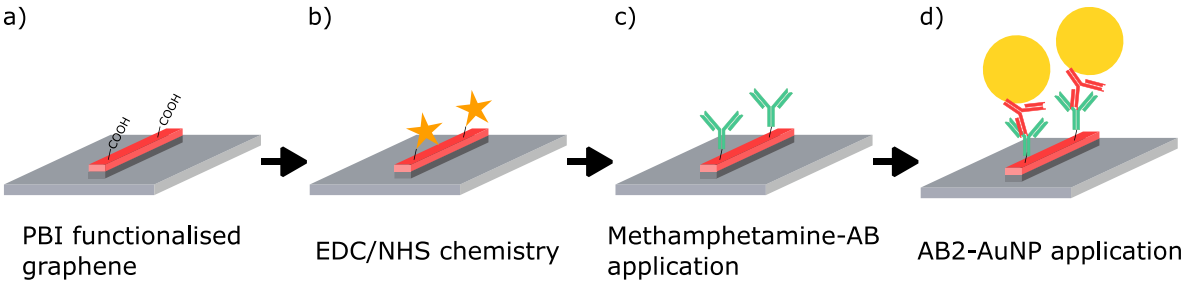

Figure 38. Schematic display of the functionalisation steps for the graphene biosensor development. a) PBI functionalised graphene, b) EDC/NHS chemistry for the preparation of amine coupling, c) coupling of methamphetamine-AB to the PBI resulting in the methamphetamine biosensor platform, d) AB2-AuNP application.

5.2.1.1 Details on the Washing Procedures

For section 5.3.1 Investigation of the Washing Procedure, 20% or 100% AB2-AuNP were applied onto the methamphetamine biosensor platform, produced by using 10 µg/ml methamphetamine-AB. Subsequently, different final washing procedures were tested on two samples each: In scenario 1) the samples were thoroughly washed with DI water for approximately 1 min. In scenario 2), the samples were washed with DI water for approximately 15 s, immersed in a 50 mM HEPES solution for 5 min, and then rinsed with DI water. In scenario 3), the samples were washed with DI water for approximately 15 s, immersed in a 50 mM HEPES bath, sonicated for 30 s, and then rinsed with DI water. The unbound molecules are expected to most effectively be removed from the surface when in contact with a buffer solution that grants optimal conditions for the antibodies. After all washing steps, any remaining water droplets were removed with a clean-room tissue. The following respective abbreviations will be used: (1)-Water, (2)-HEPES, (3)-US.

For the analysis of Figure 44, PBI FLaT samples were functionalised with 2 µg/ml methamphetamine-AB and 100% AB2-AuNP. 50 mM NaCl was dissolved in 50 mM HEPS buffer solution. After the AB2-AuNP application, the samples were rinsed with either 1 ml or 2 ml NaCl enriched HEPES buffer, and a subsequent DI water wash. As a control, thorough DI water washing was applied as described in the previous section. All samples were dried using the typical approach while the single exceptional sample was dried using N_2 blowing as a control sample.

5.2.2 SEM Imaging

After functionalisation, each sample was imaged using SEM at magnifications of 10,000x and 20,000x. The images were acquired in different locations with several 100 µm distance

between each other, to obtain statistics over the whole sample. Out of each image, the amount of AuNP and/or amount of AuNP clusters was derived.

5.2.2.1 Determination of AuNP and AuNP Cluster Density

To obtain the number of AuNP, the program ImageJ was used. Thus, the image to be analysed (see Figure 39a) needs to be properly prepared. Therefore, a brightness threshold is selected to differentiate between the grey levels belonging to the newly defined 'black' or 'white'. With the 'watershed' task, particles stuck together to form one big shape are recognised by the program and separated for further analysis (see Figure 39b). For the particle count, the minimum and maximum size of the particles in pixel² to be analysed can be chosen. In this work, an empirically derived minimum size of 15 pixel² is selected for the analysis on 20,000x images. In the example displayed in Figure 39c), a total of 374 particles are counted by ImageJ (National Institutes of Health, USA), which are outlined in red after the image processing. In comparison, the count by hand resulted in a total of 383. Due to the excellent accordance of almost 98% and the benefit of a much quicker counting time, all nanoparticle counts were performed using ImageJ.

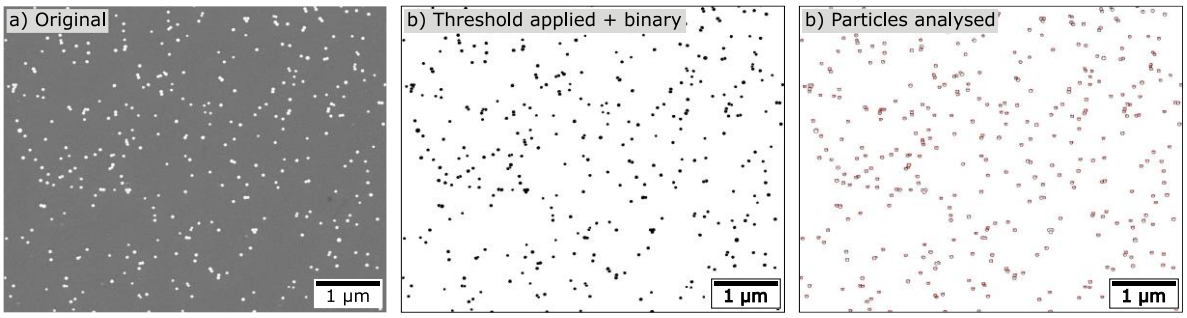

Figure 39a) Original SEM image, b) after threshold applied and watershed, c) final particle count, resulting in 374 particles.

An AuNP cluster is defined to be five or more accumulated AuNPs, as can be seen in the centre of Figure 40. To extract the AuNP and AuNP cluster densities, their respective numbers per area were derived and normed to X/100 µm².

5.3 Results and Discussion

To develop a homogeneous and reliable biosensor platform, all graphene surface modification steps are optimised from the starting point. Thus, an intense study using Raman spectroscopy and SEM imaging is performed on unfunctionalised, conventionally

functionalised and FLaT graphene upon surface modification. The necessity of the individual functionalisation steps will be discussed, as well as the required concentrations thereof.

5.3.1 Influence of Functionalisation Steps on Receptor Density

5.3.1.1 Gold Nanoparticle Dimension

In Figure 40, a high magnification SEM image of an AuNP cluster (centre) and several individual AuNPs is displayed. The sizes of the AuNPs are measured and their dimensions given are presented in the image as well. Out of the 14 measurements, the average AuNP diameter is calculated to be 40.3 $\pm$ 3.8 nm. This is in good agreement with the theoretical value of 40 nm.

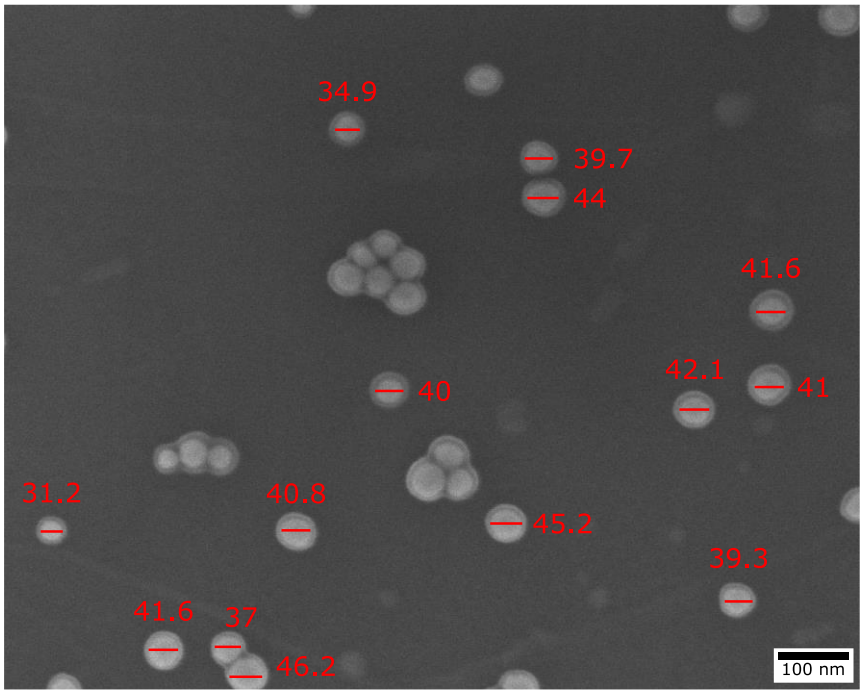

Figure 40. High magnification SEM image of AuNPs with measured particle sizes in nm of roughly 40 nm.

5.3.1.2 Gold Nanoparticle Cluster Formation due to Functionalisation Steps

The surfaces of three PBI FLaT graphene samples were functionalised differently, and one exemplary SEM image each is displayed in Figure 41. For better visualisation, the functionalisation steps performed on each sample are written in each image.

In Figure 41a), PBI functionalised graphene after solely AB2-AuNP application is displayed. The AB2 cannot couple to anything specific and, thus, the unbound AB2-AuNP are removed.

In very few cases, the AB2-AuNP unspecifically adsorbs on the surface, resulting in very few bright spots on the SEM images, that can be attributed as AuNP.

Second, methamphetamine-AB was applied onto PBI functionalised graphene with subsequent AB2-AuNP application. Note that no EDC/NHS coupling occurred previously to activate the carboxylic groups of the PBI and, therefore, no methamphetamine-AB coupling to the PBI can occur (Figure 41b). This results in unspecifically adsorbed molecules on the surface, which are most likely not distributed in a smooth antibody monolayer but aggregated clusters. Onto these clusters, numerous AB2-AuNP can bind, building up the visible accumulations. The variable region of the AB2 can bind to the constant region of the methamphetamine-AB, making this a specific mechanism. Numerous clusters are visible, out of which several exceed 1 µm in size. It can be observed that the methamphetamine-AB have not been removed entirely and form some molecule accumulations onto which the AB2-AuNP can bind. This is neither homogeneous nor reliable.

The fully functionalised sample (Figure 41c) consists of PBI FLaT graphene with methamphetamine-AB coupled to the carboxylic functions of the PBI, and subsequent AB2-AuNP exposure. Very few small AuNP clusters can be seen, out of which none is the range of the clusters seen in Figure 41b). The homogeneity of the underlying PBI SAM is the starting point for the homogeneous antibody layer formation. The AB2-AuNP is primarily a visualisation of the methamphetamine-AB layer. Therefore, the smaller and fewer the AuNP clusters are identified, the more homogeneous is the methamphetamine-AB layer.

Summing up, without the possibility of methamphetamine-AB coupling to the PBI, aggregates form on the surface. Thus, the necessity of all steps within the developed procedure to form a sensor platform is demonstrated.

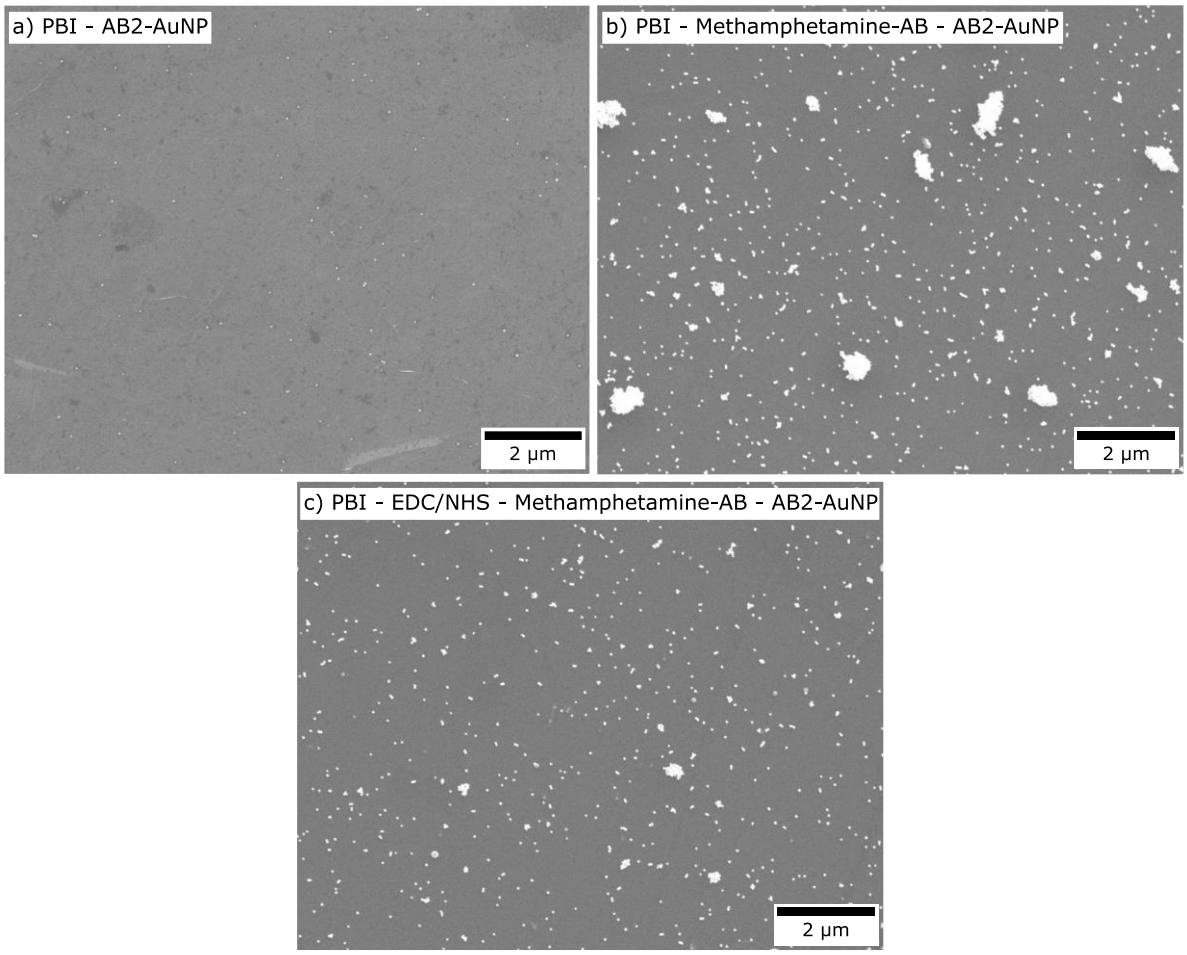

Figure 41. SEM images of differently functionalised graphene samples with their respective treatment steps written in the image.

5.3.1.3 Raman Analysis of Surface Functionalisation

Two samples before and after the surface functionalisation with antibodies, which are equivalent to the ones in Figure 41a) and b), were investigated using Raman spectroscopy. The solid black lines in Figure 42a) and b) depict the Raman spectra of FLaT and unfunctionalised graphene, respectively. The PBI functionalised graphene shows high intensity perylene peaks, indicating an excellent GERS effect as well as high packing density of the PBI molecules, as was discussed in the previous chapter. In detail, FWHM(2D) is approximately 30 cm^{-1}, the ω(2D) 2681 cm^{-1} and the I_{2D}/I_{P3G} approximately 0.4. Furthermore, the characteristics attributed to the PBI are a FWHM(P2) of 13.7 cm^{-1}, ω(P2) 1383 cm^{-1} and the I_{P1}/I_{P2} 0.91.

In the spectrum of unfunctionalised graphene, the typical G and 2D peaks are well visible, with their peak positions of 1598 cm^{-1} and 2696 cm^{-1}, respectively, marked by the vertical

lines in the inset (Figure 42b). Both the FWHM(2D) of 31.7 cm^{-1} and their intensity ratio I_{2D}/I_G of approximately 2 imply monolayer graphene. Furthermore, the very small D peak indicates good quality graphene. Both the PBI functionalised and the unfunctionalised sample originate from the same CVD growth as well as transfer batch, which is why very similar characteristics of the samples can be assumed. The spectra are in good agreement to the analysis performed in Figure 28 and Figure 29.

Both samples were then treated with the same functionalisation procedure, applying EDC/NHS chemistry, methamphetamine-AB and AB2-AuNP subsequent to one another, with washing steps in between to remove unbound molecules. Two Raman spectra of each sample were acquired, which are displayed as dotted, coloured lines in Figure 42. The Raman spectra of PBI functionalised graphene before and after treatments are extremely similar with no significant change in peak positions, FWHM or intensity ratios observable. This indicates strong coupling between the antibodies and the PBI functionalised graphene. A slight increased background is visible after functionalisation, which is most likely the consequence of some few molecules, whose structural system is not coupled to that of graphene, as discussed in the previous section.

In contrast, the Raman spectra after treatments in Figure 42b) show a highly increased background that can be attributed to fluorescence, which is especially strong in the dark green spectrum. This is an indication of the presence of molecules on the graphene surface that do not fulfil the requirements of the GERS effect, because otherwise a quenching of the fluorescence would be observed. No D peak is introduced through treatments, indicating no destruction of the graphene lattice. The G peak in the orange Raman spectrum became broader and possibly multiple peaks can be fitted. Additionally, the peak positions of both G and 2D peaks are red-shifted, resulting in 1590 cm^{-1} and 2686 cm^{-1}, respectively. This can be attributed to the influence of AuNP on the graphene surface, which induces tensile strain and, thus, a peak position shift to higher frequencies.[148] Since a strong fluorescence can be observed, the molecules are believed to not couple to the graphene, indicating random and possibly multilayer adsorption rather than actual binding.

The functionalisation with PBI, subsequent coupling of antibody to the carboxylic groups *via* EDC/NHS chemistry and final antibody-antibody binding is a necessary reaction chain to functionalise the sensor homogeneously and allow for good assembly on the graphene.

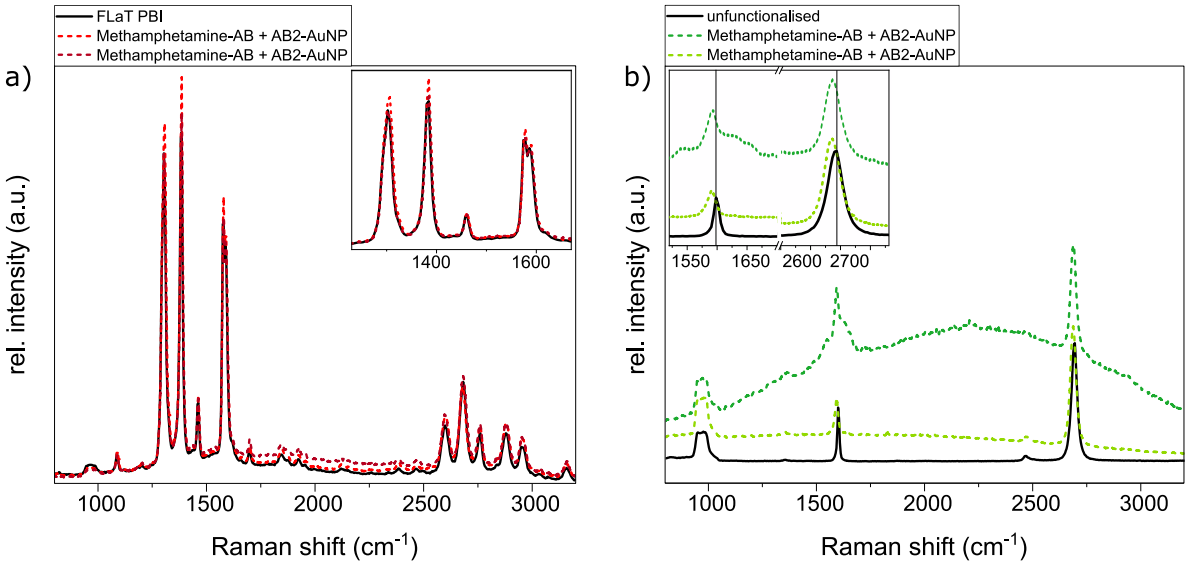

Figure 42. Raman spectra of a) PBI functionalised graphene and b) unfunctionalised graphene (black solid) and after methamphetamine-AB coupling and AB2-AuNP exposure (coloured dotted lines). Magnifications in the insets with the vertical lines in b) indicating the peak positions of the unfunctionalised graphene.

5.3.2 Investigation of the Washing Procedure

The effect of different washing procedures on the density and distribution of AuNP clusters was investigated and is displayed in Figure 43. The medium for washing is expected to have an effect on removing unbound molecules from the surface. Antibodies are most efficiently solved in buffer solution such as HEPES buffer, and are expected to be removed more easily when the sample is washed with the buffer. All samples are equally treated methamphetamine biosensor platforms with subsequent AB2-AuNP application in 20% or 100% (5.2.1 Surface Functionalisation). This was followed by one out of three washing procedures:

(1) Thorough DI water rinse of approximately 1 min (orange),

(2) 30 s DI water rinse + 5 min incubation in HEPES buffer + DI water wash (pink),

(3) 30 s DI water wash + 30 s ultrasonication (US) in HEPES buffer + Di water wash (purple).

Each procedure was performed on two samples each (for details refer to 5.2.1.1 Details on the Washing Procedures). In addition, every sample was imaged using SEM in multiple locations to obtain statistics. In Figure 43a), 10, 8 and 8 (20% AB2-AuNP) and 6, 7 and 7 (100% AB2-AuNP) individual measurements were taken, counted from left to right.

Similarly, 7, 7 and 7 (20% AB2-AuNP) and 7, 6 and 6 (100% AB2-AuNP) images, from left to right, make up Figure 43b).

The application of 20% (triangles) AB2-AuNP onto the methamphetamine biosensor platform results in 327 ± 44 AuNP/100 µm², 374 ± 131 AuNP/100 µm² and 371 ± 188 AuNP/100 µm² after washing procedures (1)-(3), respectively (Figure 43a). The number of nanoparticles is very similar for all washing procedures. The main difference lies in the standard deviation, which is significantly smaller for (1)-Water. After (2)-HEPES, the standard deviation is 3 times, and after (3)-US even 4 times larger. Note that all values are listed in Table A1.

This result is partly mirrored for samples with 100% (squares) AB2-AuNP application, with the standard deviations of (2)-HEPES and (3)-US being more than 3 times and 4 times larger, respectively, than (1)-Water. However, the number of AuNP/100 µm² are much higher for (2)-HEPES bath and (3)-US, with 794 ± 72 AuNP/100 µm², 1087 ± 241 AuNP/100 µm² and 1314 ± 478 AuNP/100 µm² for washing procedures (1)-(3), respectively.

Summarised, the number of AuNP/100 µm² after pure DI water wash is smaller but, most importantly, much more homogeneous than for any of the other procedures tested.

In Figure 43b), the number of AuNP clusters/100 µm² is displayed. An AuNP cluster is defined to be five or more AuNP accumulated. The different washing procedures after 20% (triangles) AB2-AuNP incubation do not seem to have a significant impact on cluster formation, being almost zero in all cases (see Table A2 for details).

The data points after 100% AB2-AuNP exposure are presented as squares. For each data point, two exemplary SEM images are displayed with each AuNP cluster encircled in red for better visibility. In contrast to the low concentration AB2-AuNP, the cluster density varies significantly for the different washing procedures. The (1)-Water procedure results in 30 ± 3 clusters/100 µm² (Figure 43c and d). The low standard deviation and, thus, large homogeneity can clearly be seen in the SEM images, which show very similar amounts of AuNP as well as AuNP clusters. The samples after (2)-HEPES have 39 ± 31 clusters/100 µm² on the surface (Figure 43e and f). The two SEM images do not show similar cluster distribution, where one image has a much higher cluster density than the other, while the AuNP single particle density is slightly less (Figure 43d and e, respectively). The samples after (3)-US had 50 ± 22 clusters/100 µm² on the surface (Figure 43g and h). Here, extreme inhomogeneity is visible, with Figure 43g) being filled

with single AuNP but not as many clusters. In contrast, the surface in Figure 43h) has fewer AuNP and more clusters.

As can be seen in Figure 43, the washing procedure has an immense effect on the AuNP cluster formation. Next to the unwanted high cluster density for (2)-HEPES and (3)-US washing, their standard deviations are extremely large. Thus, it can be assumed that these processes are not following an ordered procedure but rather random adsorption. It is unclear why this occurs since most sensors work as such that the unbound molecules are removed by rinsing in the same solution as used for application. Thus, the washing procedure needs to be investigated further. The most homogeneous surfaces are obtained by using purely DI water wash. Even though this procedure did not result in the most AuNP on the surface, the homogeneity is extremely important for biosensors.

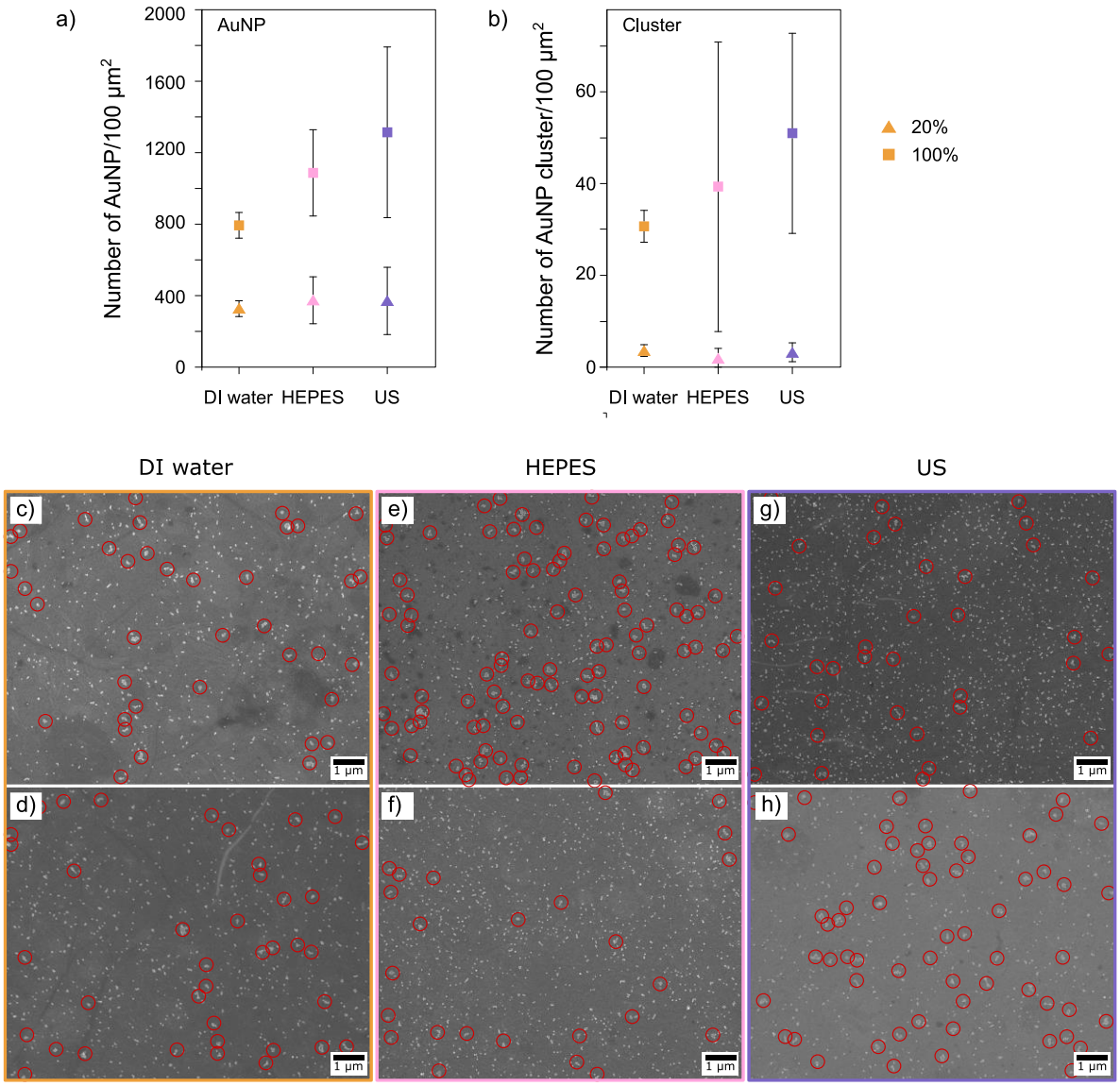

Figure 43. a) AuNP/100 µm² and b) AuNP clusters/100 µm² for methamphetamine biosensor platforms after 20% (triangles) and 100% (squares) AB2-AuNP exposure and different washing procedures: (1) DI water wash (orange), (2) 5 min HEPES (pink), (3) 30 s ultrasonic bath (purple). Each data point consists of several SEM images acquired from two equally treated samples. Respective SEM images of 100% AB2-AuNP application in c-h), two images each for comparison. c) and d) homogeneous with similar amount of AuNP and AuNP clusters. Less AuNP and more AuNP clusters in e) than in f). Opposite for g) and h), respectively.

First attempts were made to investigate the washing procedure further. Instead of only immersing the samples into HEPES buffer solution after the last treatment step as was done in the previous section, the samples were now rinsed with 1 ml NaCl enriched HEPES buffer. The increased salt concentration in the buffer solution is believed to dissolve the antibodies

better because it is a more natural environment. Therefore, the antibodies are removed more easily and are less prone to stick to the graphene surface. In total, 5, 3, 5, 10 and 5, 4, 3, 14 individual measurements were done from left to right in Figure 44a) and b), respectively.

PBI FLaT graphene was functionalised with 2 µg/ml methamphetamine-AB and subsequently with 100% AB2-AuNP. Different washing procedures were conducted after each functionalisation step (see 5.2.1.1 Details on the Washing Procedures) and are displayed in Figure 44.

The typical process washing the samples thoroughly with DI water is displayed on the right. The values of 701 ± 62 AuNP/100 µm^2 and 14.1 ± 3.3 cluster/100 µm^2 for nanoparticle and cluster density, respectively, are in the same order of magnitude as the previous measurements in this chapter. The remaining samples were either washed once (light red background) or twice (red background) with NaCl enriched HEPES buffer solution. After drying of the samples, the average AuNP density was found to be 910 ± 113 and 783 ± 28 AuNP/100 µm^2, respectively. The cluster density is 13.6 ± 2.5 and 12.6 ± 2.2 cluster/100 µm^2, respectively. These results indicate an increased AuNP concentration at similar cluster density when NaCl enriched HEPES buffer is used. This environment is, therefore, considered beneficial for usage in the biosensor functionalisation process. While the majority of the data in this study were acquired using the previous process, where solely DI water was used to remove unbound molecules, these results were discovered towards the end of the thesis. Since they show a significant improvement, I highly suggest using the NaCl enriched HEPES for biosensor functionalisation in future work.

One sample was dried using a dry N_2 flow instead of the clean-room tissue. This sample is characterised by a huge variation is both AuNP density and cluster density. As a consequence, no N_2 drying is recommended for obtaining homogeneous and reliable biosensors.

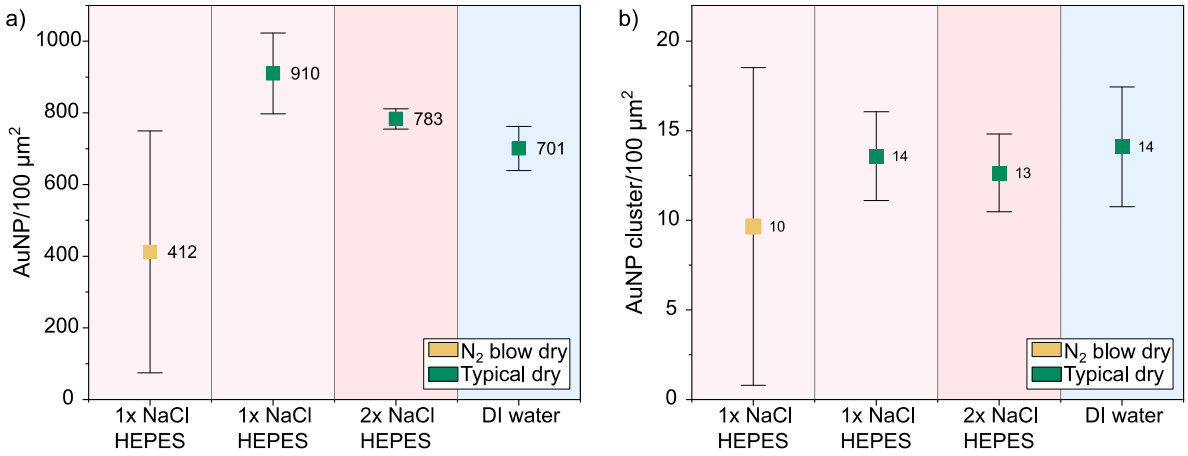

Figure 44. a) number of AuNP/100 µm² and b) number of AuNP cluster/100 µm² for differently washed methamphetamine biosensor platforms that were exposed to 100% AB2-AuNP. The samples were either washed with NaCl enriched HEPES buffer (red background) or with DI water (blue background) and subsequently either dried using a N_2 blowing (orange) or using the typical approach (petroleum).

5.3.3 Density of Receptor Sites on Biosensor Platform

In order to verify the homogeneous distribution of the receptor sites of the methamphetamine-ABs on the functionalised graphene, the AB2-AuNP were attached to the methamphetamine biosensor platform. Using SEM, the AuNP on different samples were imaged and calculated to obtain information about the AuNP density. Statistical analysis of the distribution of the AB2-AuNPs was performed and is displayed as the number of AuNP/100 µm² in Figure 45. Figure 45 includes the data of 18 individual samples: 15 FLaT, two conventionally functionalised and 1 control sample. Several SEM images were taken on each sample, making up the data points and accounting for the standard deviation. For the FLaT PBI samples, a total of 7, 29, 7 and 10 images were used for 0.5%, 20%, 40% and 100% AB2-AuNP, respectively. 29 and 7 images were used for the data points of conventionally functionalised and the control sample, respectively.

The PBI functionalised graphene was treated with EDC/NHS chemistry and following 10 µg/ml methamphetamine-AB application. Subsequently, the methamphetamine biosensor platform was subjected to AB2-AuNP in various concentrations (0.5%, 20%, 40% and 100%) on FLaT samples (Figure 45, red) and in 100% on conventionally functionalised samples (Figure 45, orange). As the control measurement, AB2-AuNP (100%) was applied onto FLaT graphene without EDC/NHS treatment and methamphetamine-AB coupling

(Figure 45, black). Thorough DI water washing was performed in between the functionalisation steps.

Each data point in Figure 45 comprises the data of several SEM images from which the number of AuNPs per unit area was calculated. Note that no AuNP clusters are counted in. With 98 ± 13 AuNP/100 µm², the lowest AuNP concentration is from AB2-AuNP (control measurement) on the PBI functionalised surface. Without methamphetamine-AB coupled to the PBI, there are no receptor sites where the AB2-AuNP can specifically bind to, resulting in low AB2-AuNP attachment.

In contrast to this, the methamphetamine biosensor platform provides specific binding sites for AB2 and shows a significantly increased number of AuNPs: 46 ± 53 AuNP/100 µm², 386 ± 65 AuNP/100 µm², 642 ± 85 AuNP/100 µm² and 798 ± 76 AuNP/100 µm² for 0.5%, 20%, 40% and 100% AB2-AuNP, respectively. This results in an increase in the number of attached AuNPs with increasing concentration, which can be correlated with a hyperbolic fit (Figure 45).

$$y = \frac{m}{x - \frac{m}{c}} + c \tag{13}$$

Previous publications suggested a hyperbolic fit to investigate saturation curves and was therefore chosen here as well.[190–193] This function was empirically derived to ensure the function going through the origin at (0,0). The values for m and c for the fitting function are selected to be -32,128 and 1058, respectively. The goodness of fit is determined by the R^2 value of 0.9883, which is a reasonable outcome. This dependency suggests a relation of the number of AuNPs with the concentration of AB2-AuNPs and confirms the successful binding mechanism of the two antibodies. Simultaneously, it verifies the specific binding of the methamphetamine-AB to the activated carboxyl functionality of the PBI functionalised graphene without which the methamphetamine-ABs would not reside on the surface.

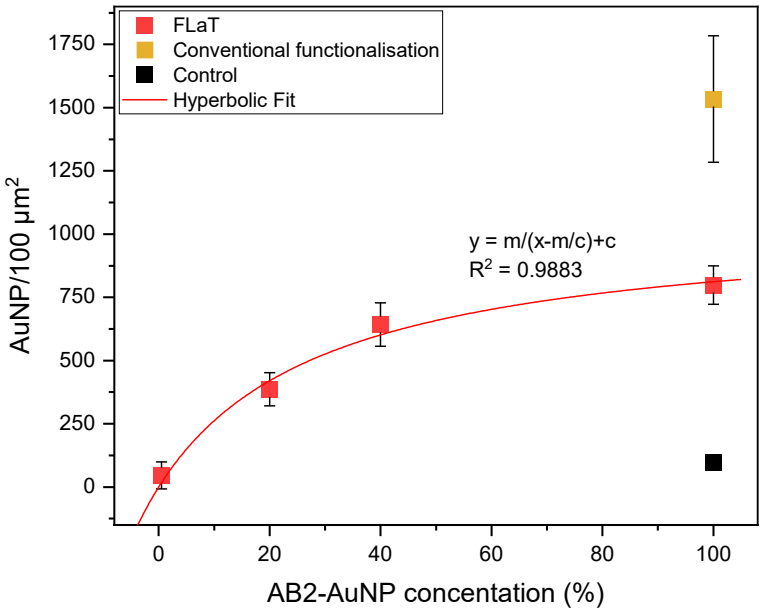

Figure 45. AuNP/100 µm² over AB2-AuNP concentration. FLaT PBI graphene show a hyperbolic fit with AB2-AuNP concentration (red). Conventionally functionalised graphene has larger AuNP density on the surface but shows a much stronger error bar (orange). An unfunctionalised control is visible in black.

The number of AuNPs for conventionally functionalised samples of 1,534 ± 250 AuNP/100 µm² is much larger than the 798 ± 76 AuNP/100 µm² of FLaT samples. However, the standard deviation of conventionally functionalised samples is more than 3x larger compared to FLaT graphene. This results in a lower homogeneity within each conventionally functionalised sample but also between samples. Following this, the FLaT appoach was demonstrated to benefit over conventional functionalisation in terms of reliability and homogeneity.

5.3.4 Antibody Concentration Variation

A number of PBI graphene samples were functionalised with either 2 µg/ml (violet) or 10 µg/ml (red) methamphetamine-AB. Each sample was subsequently exposed to 0.5%, 20%, 60% or 100% AB2-AuNP. In Figure 46a-h), exemplary SEM images of differently treated graphene samples are displayed. The SEM images are arranged in an array, respective to the methamphetamine-AB (rows) and AB2-AuNP (columns) concentrations used. AuNP clusters are marked by the red circles. The cluster density increases from left to right, as well as from top to bottom in each row. The samples treated with 2 µg/ml methamphetamine-AB and an increasing concentration of AB2-AuNP are shown in the top row, with the number of AuNP clusters of 0, 1, 15 and 22 for Figure 46a-d), respectively.

Figure 46e-h) show similar results, with the cluster amounts being 0, 3, 17 and 23, respectively. The distances between clusters are approximately 0.5-4 µm. In both cases, the cluster density increases with increasing AB2-AuNP concentration. This suggests an excess of AB2 molecules that aggregate upon themselves. Additionally, the cluster size increases with AB2-AuNP concentration.

The individual data points in Figure 46i) consists of measurements on six individual SEM images, apart from the 2 µg/ml methamphetamine-AB and 100% AB2-AuNP data point, which is derived of five images. For the calculation of the AuNP density calculation, 22 individual images were used. The optimised washing procedure from Figure 43 was implemented here, using a thorough DI water wash of approximately 1 min. Note that the total amount of AuNP did not vary significantly with methamphetamine-AB.

For both methamphetamine-AB concentrations, the cluster density is 0 cluster/100 µm^2 for 0.5% AB2-AuNP, and increases with increasing AB2-AuNP concentration. At the highest AB2-AuNP concentration (100% AB2-AuNP), the cluster density is largest with 18.2 ± 5.5 cluster/100 µm^2 for 2 µg/ml and 30.2 ± 4.4 cluster/100 µm^2 for 10 µg/ml methamphetamine-AB. At the same time, the density of individual AuNP is very similar with 756 ± 68 AuNP/100 µm^2 for 2 µg/ml and 798 ± 76 AuNP/100 µm^2 (see previous section) for 10 µg/ml methamphetamine-AB, respectively.

Even though the amount of AuNP is similar, the cluster density varies a lot with both methamphetamine-AB and AB2-AuNP concentration. This indicates a relatively specific AB2 attachment to individual receptor sites of the methamphetamine-AB, but a rather inhomogeneous cluster formation. As a consequence, the washing procedure needs to be optimised to better remove the unbound and aggregated AuNP clusters.

Since a higher methamphetamine-AB does not increase the receptor density and additionally worsens the cluster density, a concentration of 2 µg/ml methamphetamine-AB will be used in further measurements.

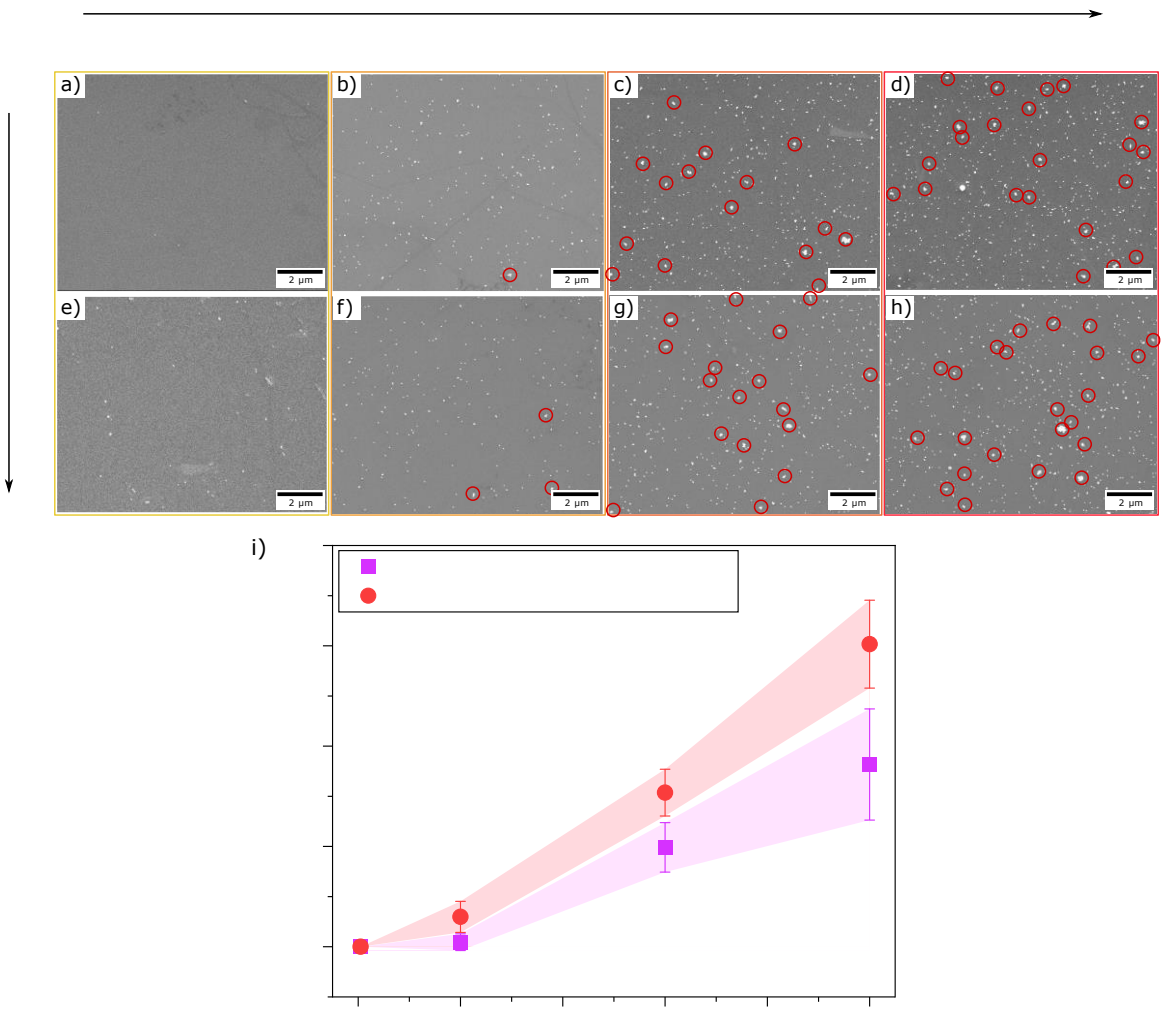

Figure 46. SEM images of PBI functionalised graphene, treated with different concentrations of methamphetamine-AB (rows) and AB2-AuNP (columns). With increasing concentrations, the amount and size of AuNP-clusters enlarges. Same scale for all images. AuNP cluster density for samples treated with 2 µg/ml (violet) or 10 µg/ml (red) methamphetamine-AB and AB2-AuNPconcentrations of 0.5%, 20%, 60% or 100%.

5.4 Conclusion

In this chapter, detailed Raman spectroscopy and SEM analysis were used to investigate and verify the various stages involved in the production of a homogeneous methamphetamine biosensor platform. The necessity of the immunochemical functionalisations within the developed procedure is demonstrated using Raman spectroscopy and the comparison of AuNP cluster densities derived from SEM imaging. The cluster density gives insight in the

homogeneity and reproducibility of the surface functionalisations. Several investigations confirm that AuNP cluster formation occurs when 1) there is no PBI on the graphene surface or 2) no EDC/NHS chemistry to activate the carboxylic groups in order to bind methamphetamine-AB to the PBI. Furthermore, clusters arise when there is a too excessive concentration of antibodies applied, out of which the unbound molecules are not effectively removed from the surface. This issue was targeted and an analysis of different washing procedures confirmed that thorough DI water washing removes unbound molecules most reliably. However, AuNP cluster formation afterwards is still notable and adds inhomogeneity to the measurements. The first investigation to use NaCl-enriched HEPES buffer solution resulted in a positive outcome with an increased AuNP density and similar cluster density compared to DI water washed samples. This needs to be investigated and optimised in further measurements to obtain sensor surfaces solely specifically bound molecules. Nonetheless, a significant improvement of homogeneity on the AuNP density as well as on the cluster density has been obtained. An optimisation protocol for the setup may involve a longer continuous rinsing of DI water or NaCl-enriched HEPES, or the implementation in a flow cell. The latter has disadvantages such as a larger setup is required and the sensor functionalisation cannot take place in point of care situations. Additionally, the measurements would be required to take place in liquid environment as opposed to the dry one discussed in this work. It must be noted that some aggregation of AuNP already in the conjugate solution is common and some AuNP clusters already exist prior to incubation on the sample. The quantitative analysis of the number of clusters, however, is a challenging and required additional equipment and is time consuming. Therefore, the cluster density comparison of samples functionalised with the same conjugate solution is used.

Additionally, the methamphetamine-AB concentration of 2 µg/ml was found to be optimum, as sensors functionalised therewith result in both high receptor density as well as low cluster density and will be used in further analysis. Finally, the homogeneity between two functionalisation approaches was investigated. The FLaT method was found to produce a much more homogeneous AuNP distribution than the conventionally functionalised one, which was tested on several locations on one sample as well as between several individual samples. Concluding, the most homogeneous and reproducible methamphetamine biosensor platform results from FLaT graphene as starting material, and subsequent specific methamphetamine-AB coupling to the activated carboxylic functions of the PBI.

6 Electrical Analysis of Biomarker Detection

The labelling of molecules for biosensing applications is a highly utilised way of quantifying a molecule. However, the labelling itself requires an extra step to the sensor development, which is tedious, more expensive and might add cross-reactivities to the sensor performance. Therefore, label-free biosensors were developed and have been investigated worldwide. A prominent example of a label-free, quantitative biosensor is the functionalised GFET. Not only are GFETs characterised by having quick response times,[39,194] easy operation without the need for complicated tools,[188] and real-time monitoring,[46,49,189] GFETs are also highly sensitive.[58,72,195] Next to the CVD grown graphene used in this work, also GO, rGO and exfoliated graphene have been used as biosensors. Islam *et al.*[39] have implemented exfoliated graphene to produce GFETs for the detection of Human immunodeficiency virus (HIV) and related diseases. Even though the sensor was highly sensitive, the publication did not provide statistics. This is a critical issue in using exfoliated materials due to the scalability issue and difficulty to produce a larger number of equivalent samples. Other publications rely on GO or rGO for the development of a GFET biosensor, such as Kim *et al.*[196] for the detection of prostate cancer or Thakur *et al.*[194] for the sensing of Escherichia coli bacteria. GO and rGO are interesting as material for biosensors due to their numerous functionalities and ease of binding further molecule to the crystal lattice. However, they produce disturbances in the crystal lattice and, therefore, do not exploit the exceptional electronic properties pristine graphene has. These can be achieved by CVD grown graphene and a noncovalent functionalisation thereof, as has been investigated in the previous sections. CVD grown graphene has been widely used as biosensor, such as for pathogen detection,[55,197] disease recognition,[38] and many more.[41,189,198–200] This type of graphene is an excellent choice due to its scalability, ease to functionalise and the undisturbed lattice structure because the electronic properties keep intact.

This chapter presents an analysis of biosensors with the focus on electrical characterisation. The response of the developed biosensor platforms with respect to analyte exposure is discussed, and the specificity and reliability in detecting antigens investigated. The specific case of methamphetamine and its antibody is examined in detail.

6.1 Experimental Details

In this thesis, PBI FLaT graphene on 10×10 mm^2 SiO_2/Si substrate is structured resulting in a GFET array of 11 channels with a global backgate electrode per sample (Figure 47). Either methamphetamine-AB or AB2 are coupled specifically *via* amine coupling to the carboxylic groups of the PBI using EDC/NHS crosslinking mechanism. The specific antigen is coupled to the respective antibody. For control measurements, the biosensor platform is exposed to placebo molecules. The functionalisation protocol can be found in full detail in section 3.2 Specific Functionalisation to Realise Biosensor.

If not specifically indicated, all measurements were performed in a semi-dry state. Thus, after functionalisation and washing of the samples, the remaining liquid is soaked away by a clean-room tissue. This likely leaves a minimal liquid film on the surface. The effect of the remaining film is experimentally investigated in section 6.2.1 Electrical Characterisation of GFETs.

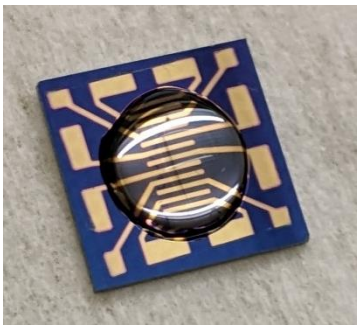

Figure 47. Noncovalently functionalised graphene channel across the twelve parallel electrodes, composing a GFET array with eleven devices per chip. 60 µl EDC/NHS solution was drop-casted onto the sample, which covers every individual device.

6.1.1 Characterisation

The AFM measurements of the methamphetamine biosensor were performed within 1 day of treatment.

In this chapter, the resistance change, ΔR, and Dirac voltage shift, ΔV_{Dirac}, of GFETs resulting from various functionalisations are investigated. Each data point (represented as a black diamond) typically corresponds to a single device. The average of all devices of the same treatment are averaged and displayed as column, with the resulting standard deviation visualised as the whisker.

6.1.2 Procedure for Time-Dependent Analysis

Figure 48a) shows a photograph of a GFET sample, in which one device (a methamphetamine biosensor platform) is probed by two micropositioners and a liquid droplet containing 10 µg/ml of methamphetamine is located on top. The device was measured in the backgated configuration every 40 s for 6 min after the solution was applied by sweeping the V_{gs} from -100 V to 100 V at a constant V_{ds} of 10 mV. The resulting transfer curves are displayed in Figure 48b). Subsequently, the biosensor was rinsed by DI water to remove unbound analyte and then measured again 1 h after dry-off.

Obtaining comprehensive electrical data from current flow through aqueous solution can be challenging, as evidenced by the missing data points (1st, 2nd, and 6th runs) in Figure 48b). To derive the V_{Dirac} from each transfer characteristic curve, the measured data points are filtered using the adjacent averaging method with a window size of 10 data points, which is used to interpolate a fitted curve. The representative transfer curve smoothing resulting in a 4th order polynomial fit is shown in Figure 48c).

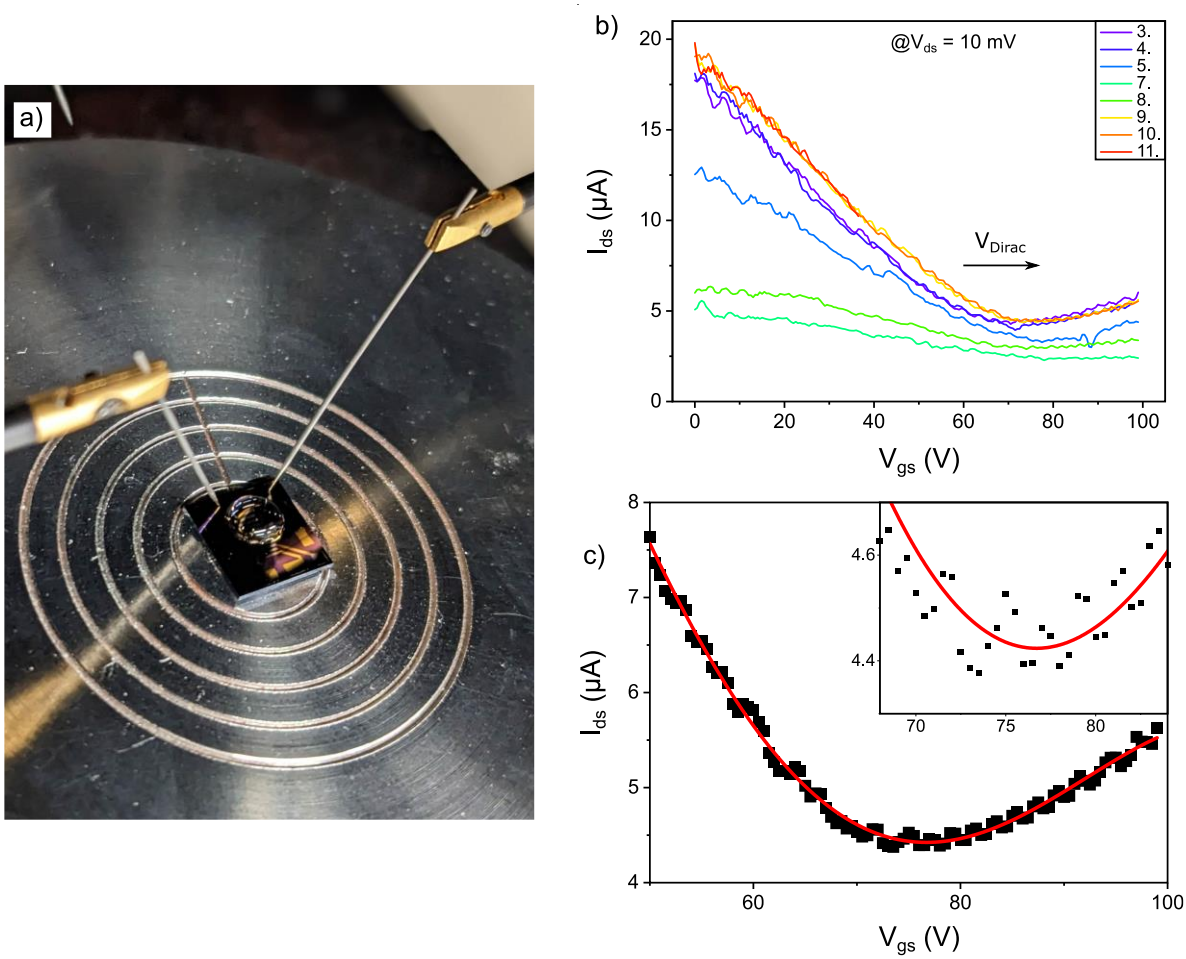

Figure 48. a) Photograph of the GFET sample during electrical characterisation, with droplet on surface. b) Transfer characteristics of the same device measured in intervals of 40 s for 6 min while droplet on sample. c) A transfer characteristic curve (red curve) of the 10th measurement data (black squares) after smoothing and application of a polynomial fit. Inset: close-up of the minimum of the transfer curve, indicating a V_{Dirac} of 75.5 V.

6.1.3 Sample Preparation for Stability Investigation

Two methamphetamine biosensor samples (S1 and S2) are measured electrically (Figure 57, green). Subsequently, 60 µl HEPES (50 mM) buffer is applied onto S1, while S2 remains pristine. The HEPES buffer is intended to keep the sample surface from drying. Individual covers are placed onto both samples and they are left in a fume hood for approximately17 h (see Figure 56a). Afterwards, S1 is washed with DI water and dried. 10 µg/ml methamphetamine is applied to both samples. After the incubation time of 6 min, the samples are DI water washed, dried and electrically characterised. All data derive actual changes by methamphetamine binding from the calculations of equation (11) and (12) as shown in Figure 57 (purple).

6.2 Results and Discussion

6.2.1 Electrical Characterisation of GFETs

Graphene is very sensitive to its surrounding environment and its electronic system is influenced strongly. In ambient conditions, graphene is naturally p-doped, resulting from the numerous molecules interacting with the graphene. Water, which is commonly found as humidity, is the most abundant and strongest dopant in laboratory conditions.[201] Additionally, gases such as O_2, NO_2, CO_2 and many more can behave as a p-dopant to graphene. This chemical doping behaviour is observed in electrical measurements, e.g. as Dirac voltage shift towards positive V_{gs} regime.[202] All GFETs in this work are electrically characterised in atmospheric conditions at room temperature and likely show some kind of doping effects due to the aforementioned reasons. Additionally, both the antibody as well as the small molecules are diluted in aqueous solutions and all samples are washed with DI water after their incubation. The subsequent drying with a dry N_2 flow resulted in a strongly inhomogeneous distribution of markers on the graphene surface (see Figure 44). Therefore, the removal of the remaining water droplet by soaking it away with a lint-free cleanroom wipe is conducted. However, this is not sufficient to entirely dehydrate the sample surface and a small water film is highly likely to remain on the surface. Therefore, the influence of the DI water on the electrical measurements needs to be investigated in a time-resolved experiment.

A GFET is measured every 4 s in the I_{ds}-V_{ds} configuration for a total of 29 min. The resulting resistance values are displayed in Figure 49. The first measurements are performed in the initial dry state of the device (black). Subsequently, 50 µg/ml of DI water is applied onto the sample and measured for the following 16 min. A steep R increase is observed in the beginning. After the maximum R is measured after approximately 5 min, R subsequently decreases. The saturation regime is expected as R change gradually attenuates but the DI water droplet is removed before a plateau appears. A drastic R drop is observed due to the water loss; however, this incomplete dehydration still leaves the graphene surface moist. In the following 14 min, the water evaporates from the surface and the graphene dries continuously. The tendency of R decrease during drying has not reached a plateau, which is why a continued R decrease can be assumed. The ΔR of the last measurement to the initial measurement is relatively small with only 7.3%. However, the contribution of water molecules on the surface needs to be considered regarding the processing time between functionalisation and measurement.

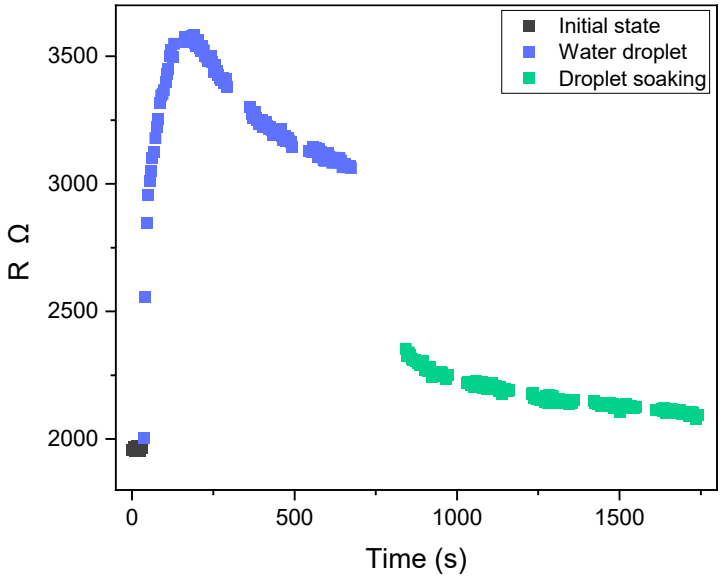

Figure 49. Resistance over time of one device in the initial dry state (black), upon DI water exposure (blue) and after the droplet was removed (green).

It is difficult to quantise the influence from the remaining water on the surface and estimate its doping intensity. To overcome this issue, a different approach is adopted: A set of 10-30 samples undergo chemical treatment simultaneously and are electrically measured in the same intervals following the functionalisation process to reduce sample variations. Hence, the potential effect of residual water will be disregarded, as the time taken for evaporation from the moist surface is assumed to be roughly the same for all samples. This requires several functionalisation batches as only a limited number of samples can be processed simultaneously. However, since every sample consists of 11 devices, a large number of devices per functionalisation batch can be processed.

Every set of samples has a minimum of one reference sample, which is functionalised with antibodies, but no small molecules are applied subsequently (biosensor platform). The resistance and ΔV_{Dirac} changes of all biosensor platform devices in a sample batch are averaged, resulting in the denoted shifts of $\overline{\Delta R_{AB}}$ and $\overline{\Delta V_{Dirac,AB}}$, respectively. Subsequently, the $\overline{\Delta R_{AB}}$ and $\overline{\Delta V_{Dirac,AB}}$ are subtracted from the ΔR_{AB} and $\Delta V_{Dirac,AB}$ of each device. This identifies the deviation of each device from the mean of all devices. For details on the calculations, refer to section 3.3.4 Electrical Characterisation.

Figure 50 shows the electrical characterisation of PBI FLaT GFETs after methamphetamine-AB coupling using EDC/NHS chemistry. The as-described calculation was performed on every device and the result is depicted accordingly as a black diamond. The whisker represents the respective standard deviation. The methamphetamine-AB functionalisation

tends to have a low standard deviation in both resistance and ΔV_{Dirac} measurements (± 3.7% and ± 2.9 V, respectively). Thus, the methamphetamine biosensor platform can be assumed to be highly reliable.

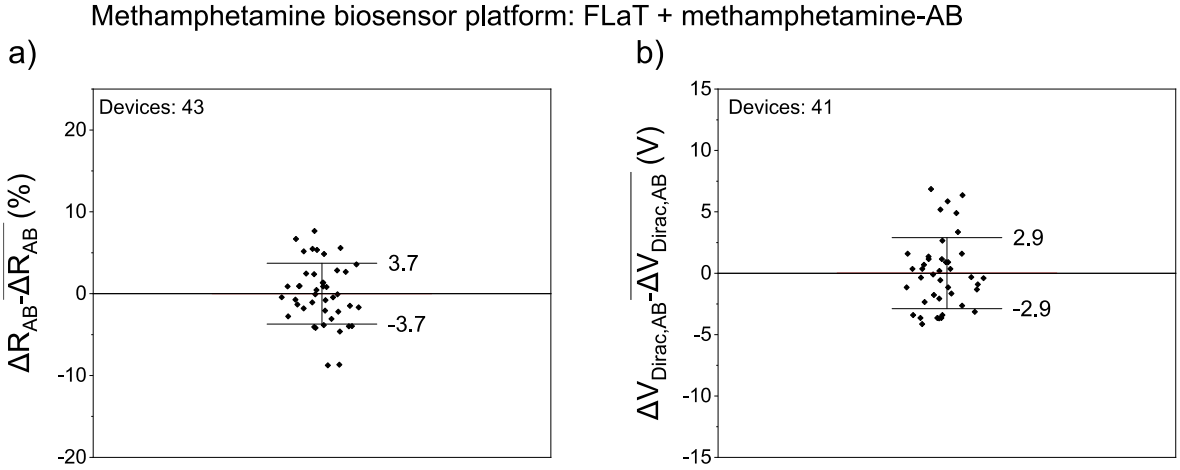

Figure 50. Electrical characterisation of methamphetamine biosensor platforms, showing the deviations from the mean $\overline{\Delta R_{AB}}$ (a) and $\overline{\Delta V_{Dirac,AB}}$ (b). Each device is displayed as a black diamond and the standard deviation is illustrated by the whisker.

In the following sections, the electrical changes due to small molecule application is traced using the same calculation approach. Since the equations include the $\overline{\Delta R_{AB}}$ and $\overline{\Delta V_{Dirac,AB}}$ values, their standard deviation is important to correlate the signal changes. Therefore, their respective standard deviation is plotted in the following figures as a grey background. This improves the visualisation of comparing the displayed values with regard to the biosensor platforms on which their calculation is based.

6.2.2 Specific Detection of Methamphetamine

6.2.2.1 Surface Analysis of a Methamphetamine Biosensor

Figure 51a) displays the topography of FLaT graphene after coupling 2 µg/ml methamphetamine-AB to the PBI, and subsequent 3 µg/ml methamphetamine exposure. The surface of the sample is characterised by some almost parallel arranged wrinkles and folds, which are also found on FLaT graphene without AB immobilisation (Figure 30). Even though the majority of the surface between those wrinkles has a smooth appearance, the surface roughness S_a is 1.1 nm over the whole scanned area (Figure 51a). This rather large value focuses the attention on the several protrusions, indicated by the white spots on the

surface. These protrusions appear irregularly in distances of approximately 1 µm to each other and have a significant height. They can either be attributed to residues from the transfer process or to antibody accumulations. Since the FLaT graphene surface is smoother with a surface roughness S_a of 0.44 nm (Figure 30), it is unlikely that the entirety of the protrusions in Figure 51a) results from the transfer process alone. Thus, it is considered that the protrusions partly happened at later stages of the functionalisation processes using methamphetamine-AB.[203,204] Additionally, antibody accumulations were already found in the analysis in Figure 46, too. Although polymeric residues could attribute somewhat to the protrusions as well as possible antibody accumulations, the functionalised graphene surface is extremely homogeneous in general. This indicates a smooth and specific coupling procedure of antibody to the PBI.

As previously stated, the perylene molecules selectively assemble on the 2D-material surface. Since the coupling process of antibody to PBI molecules is highly specific, it can be assumed that the antibodies are only located on the functionalised graphene surface. The profile in Figure 51b) reveals a height of 7.6 ± 0.2 nm (blue) from the methamphetamine biosensor to the substrate.[173] From the height profiles with and without methamphetamine-AB functional group, the antibody height is estimated to be approximately 5.1 nm, which is in agreement with literature.[203,204] The size of the methamphetamine can be neglected here due to their relatively insignificant dimension of 120 Da (see 3.2.1 Materials). Due to the asymmetric dimensions of antibodies, their orientation on graphene can be estimated. In several studies, the flat-on immobilisation of antibodies resulted in roughly 5 nm antibody height, which is in agreement with the measurements in this section.[121,205] In this case, the longitudinal antibody axis is well aligned along the surface, with one Fab-fragment slightly more in the air than the other one.[121] Since antibodies have numerous amine groups distributed over their surface, an immobilisation in random orientation is highly likely as reported before.[125,206,207] If the antibodies are in different orientations on the surface, the surface roughness naturally increases, which can partly be accounted for here.

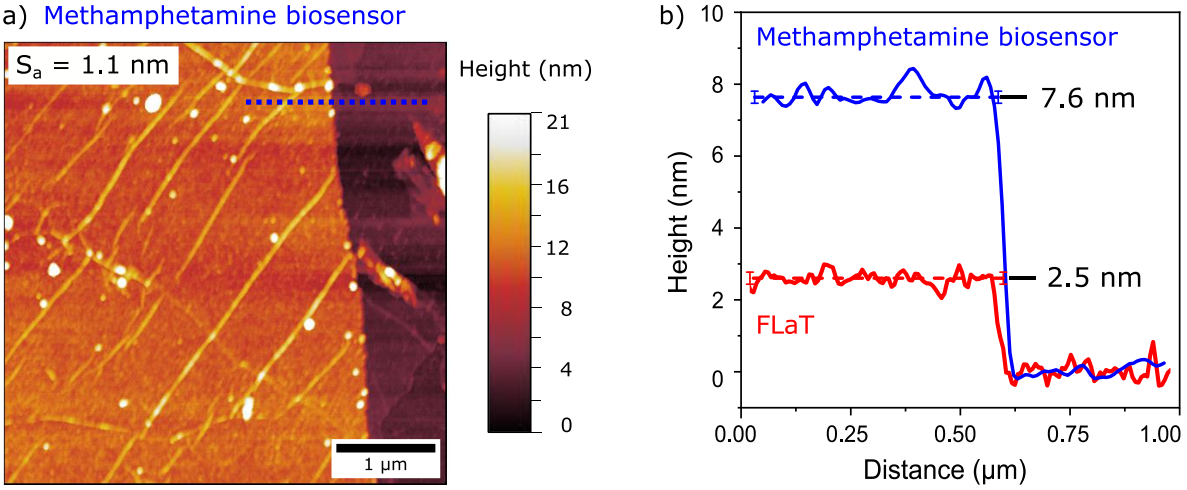

Figure 51. a) AFM topographic map of a methamphetamine biosensor. The height profile is taken along the dashed blue line in a) and is displayed in b), together with the profile of FLaT graphene (red). An antibody monolayer of 5.1 ± 0.2 nm is measured with a homogeneous distribution on the surface.

6.2.2.2 Impact of the Anti-Methamphetamine Antibody Concentration

The electrical analysis of methamphetamine biosensors is performed on numerous samples for various antibody concentrations. Complementary to Figure 46, the influence of the methamphetamine-AB concentration on the biosensor performance is investigated. In the measurements using AuNPs as markers, it was found that the methamphetamine-AB concentration did not show a strong correlation with functional group density on the surface. However, slightly increased number of AuNP clusters indicating antibody accumulations was found in the higher concentration of methamphetamine-AB functionalisation. Therefore, the influence of methamphetamine-AB concentrations on the electrical measurements is addressed in this section, which is derived by ΔR and ΔV_{Dirac}.

The carboxylic groups of the PBI on FLaT graphene are activated through EDC/NHS chemistry. Subsequently, 0.25 µg/ml, 1 µg/ml, 2 µg/ml or 10 µg/ml methamphetamine-AB is coupled to the PBI, after which 10 µg/ml methamphetamine is applied. The shifts in electrical parameters due to the functionalisation with both antibody and analyte are measured, denoted as ΔR and ΔV_{Dirac}. To obtain the influence on electrical parameters of solely the analyte, the mean shifts of the biosensor platforms, $\overline{\Delta R_{AB}}$ and $\overline{\Delta V_{Dirac,AB}}$, are subtracted from these values, following equations (11) and (12). The resulting $\widehat{\Delta R_{An}}$ and $\widehat{\Delta V_{Dirac,An}}$ specify the estimated change of electrical parameters of the analyte only. For details on the calculations, refer to section 3.3.4 Electrical Characterisation.

The resulting $\widehat{\Delta R_{An}}$ and $\widehat{\Delta V_{Dirac,An}}$ are displayed in Figure 52a) and b), respectively. The number of individual devices in Figure 52a) is 14, 16, 41 and 44, and 11, 8, 47 and 44 in Figure 52b). Each individual device is represented as a single diamond. The values of all samples with the same methamphetamine-AB concentration are averaged and plotted as one column with its respective standard deviation. Since these values are calculated by taking $\overline{\Delta R_{AB}}$ and $\overline{\Delta V_{Dirac,AB}}$ into account, their standard deviation is also illustrated in the graph as a box with grey background. If the data points fall within this marked background, the devices did not detect any analyte.

The biosensor platforms with low AB concentrations (0.25 µg/ml and 1 µg/ml) do not result in any significant $\widehat{\Delta R_{An}}$ upon exposure to methamphetamine (Figure 52a). On the other hand, biosensors with high AB concentrations (2 µg/ml and 10 µg/ml) show a noteworthy decrease in $\widehat{\Delta R_{An}}$ (-27.4 ± 13.1% and -23.1 ± 16.6%, respectively), of which the former has a slightly larger $\widehat{\Delta R_{An}}$ with a simultaneously smaller standard deviation. A similar tendency is observed in the V_{Dirac} measurements (Figure 52b). These results suggest that there is only little methamphetamine binding in the lowest AB-concentration biosensors, while the high-concentration AB biosensors show a clear response to methamphetamine. This proportional tendency suggests that increasing the concentration of methamphetamine-AB on the PBI graphene surface leads to a greater amount of methamphetamine binding, up to a certain AB concentration. The result of using 0.25 µg/ml methamphetamine-AB indicates that this concentration is too low for effective antibody formation on the surface, and is, thus, unsuitable for biosensing. On the one hand, the $\widehat{\Delta R_{An}}$ for biosensors using 1 µg/ml methamphetamine-AB is close to 0%, but an increase of 24.8 ± 3.0 V in $\widehat{\Delta V_{Dirac,An}}$ is visible in Figure 52b), suggesting that more methamphetamine is able to bind in comparison to lower concentrations. The highest $\widehat{\Delta V_{Dirac,An}}$ of 39.8 ± 7.8 V is obtained by using 2 µg/ml methamphetamine-AB, indicating that this concentration provides the most effective antibody formation and highest methamphetamine binding. As a consequence, 2 µg/ml of AB concentration is optimal to obtain large signal changes upon methamphetamine exposure.

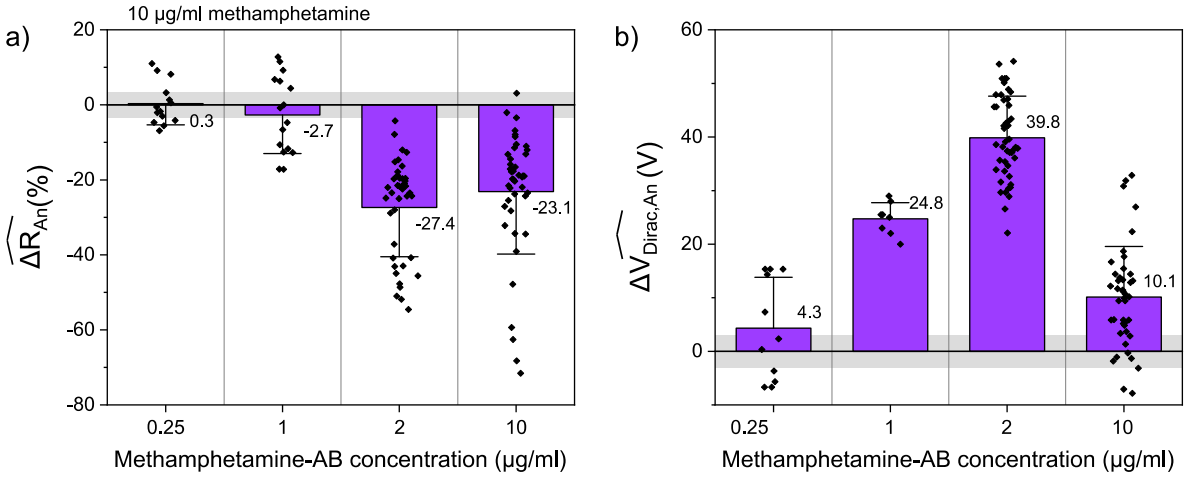

Figure 52. The effect of methamphetamine-AB concentration variation on the biosensor performance. a) $\widehat{\Delta R_{An}}$ and b) $\widehat{\Delta V_{Dirac,An}}$ for 0.25 µg/ml, 1 µg/ml, 2 µg/ml and 10 µg/ml methamphetamine-AB, from left to right. Each device is represented by a black diamond, with all devices per treatment comprised in one column. The height and whisker represent the mean value and standard deviation, respectively. The grey box indicates the standard deviation of the $\overline{\Delta R_{AB}}$ and $\overline{\Delta V_{Dirac,AB}}$ values used for calculation. The biosensors functionalised with 2 µg/ml methamphetamine-AB result in the strongest changes in both $\widehat{\Delta R_{An}}$ and $\widehat{\Delta V_{Dirac,An}}$. The samples were electrically measured after the removal of the liquid droplet.

6.2.2.3 Specific and Concentration-Dependent Detection of Methamphetamine

In order to evaluate the effect of different methamphetamine concentrations on the biosensor platform, a range of analyte concentrations were tested. Specifically, the PBI FLaT methamphetamine biosensor platforms were exposed to varying amounts of the small molecule, namely 0.3 µg/ml (light blue), 3 µg/ml (dark blue) or 10 µg/ml (violet) methamphetamine. The resulting $\widehat{\Delta R_{An}}$ and $\widehat{\Delta V_{Dirac,An}}$ are displayed in Figure 53a) and b), respectively. The design of the figure is adapted from Figure 52. For the columns in Figure 53a) from left to right, 43, 45, 48, 20 and 19 individual devices were used. Likewise, the data in Figure 53b) from left to right are made up by 39, 33, 39, 18 and 20 devices. The same devices were used for Figure 53c) and d), respectively.

Since all acquired data are normed to the biosensor platform, all changes in $\widehat{\Delta R_{An}}$ and $\widehat{\Delta V_{Dirac,An}}$ indicate a response to solely the analyte. A clear concentration-dependent relation of both $\widehat{\Delta R_{An}}$ and $\widehat{\Delta V_{Dirac,An}}$ over the concentration range 0.3-10 µg/ml methamphetamine is observed. Specifically, the $\widehat{\Delta R_{An}}$ decreased to -39.9% and the $\widehat{\Delta V_{Dirac,An}}$ increased to 39.2 V in the same range.[173] These distinct concentration-dependent responses in both $\widehat{\Delta R_{An}}$

and $\Delta\widehat{V_{Dirac,An}}$ demonstrate the successful detection of methamphetamine by the biosensor. All GFETs commonly show a positive shift of the V_{Dirac} after the respective treatments, indicating p-type doping. Graphene is naturally p-doped in ambient conditions and remains sensitive to majority charge carrier density changes, which results in the observed $\widehat{\Delta R_{An}}$ decrease and $\Delta\widehat{V_{Dirac,An}}$ increase.[202]

To assess the selectivity of the methamphetamine biosensor, cross detection with the placebo paracetamol is carried out. This molecule is chosen as a nonspecific control due to its similar size compared to methamphetamine (see 3.2.1 Materials). The addition of 10 µg/ml paracetamol onto the GFETs after methamphetamine-AB coupling does not alter the electrical parameters, which can be seen for both $\widehat{\Delta R_{An}}$ and $\Delta\widehat{V_{Dirac,An}}$. This result verifies the specificity of the methamphetamine biosensors towards the explicit detection of methamphetamine through methamphetamine-AB.[173]

The x-axis of analytic concentration in Figure 53a) and b) is not linear, which may lead to misunderstandings of the limit of detection (LOD) and concentration relation. Therefore, a hyperbolic fit is applied to the data Figure 53a) and b) and is displayed in Figure 53c) and d), respectively. Its shape is determined by equation (13) as previously stated. The hyperbolic fit is chosen because they have been previously suggested to fit saturation curves.[190–193] This function ensures that the fitted curve goes through the origin at (0,0). The values for m and c for the fitting function are expected to be 3.68 and -34.87 (Figure 53c), respectively, and −18.67 and 40.13 (Figure 53d), respectively. The R^2 coefficient indicating the goodness of fit is 0.9935 and 0.9931, respectively. Since the fit only consists of 4 data points, the significance of the result should not be overestimated. After a strong signal increase, a flattening of the curve can be observed in both graphs. With caution, this can be interpreted as a saturation curve with the saturation being almost reached with 10 µg/ml methamphetamine. Furthermore, it can be inferred that the LOD has not been met using 0.3 µg/ml methamphetamine concentration applied here.

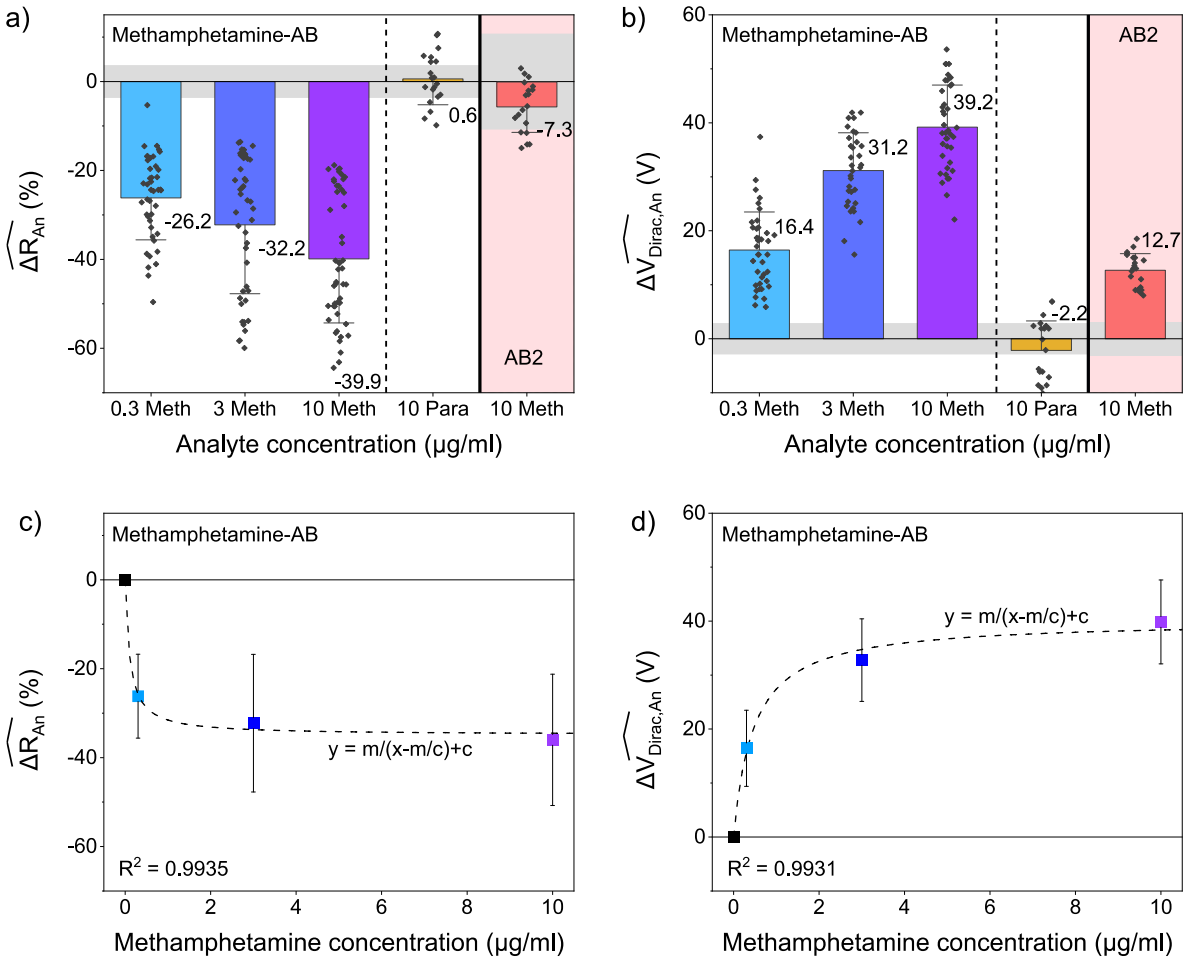

Figure 53. a, b) Average $\widehat{\Delta R_{An}}$ and $\widehat{\Delta V_{Dirac,An}}$ values of methamphetamine biosensor platforms after exposure to different concentrations of methamphetamine (light blue, dark blue, violet) or paracetamol (orange), respectively. Design adapted from Figure 52. Concentration-dependent response of the biosensors towards methamphetamine is observed, with no cross-reactivity towards paracetamol. Cross-reactivity tests by applying methamphetamine onto the AB2 biosensor platform (red) show small influence of the methamphetamine, which can be attributed to unspecific adsorption onto the functionalised graphene.[173] c) and d) hyperbolic fits of methamphetamine biosensor responses with same data as in a) and b), respectively. The samples were electrically measured after the removal of the liquid droplet.

Additional experiments were conducted to investigate the specificity of the functionalisation method. The antibody AB2 was coupled to the PBI to result in an AB2 biosensor platform. Note that the AB2 was not conjugated with AuNP in this chapter. The coupling process works similarly as for methamphetamine-AB, since both antibodies exhibit amine groups necessary for the crosslinking chemistry. Onto the AB2 biosensor platform, 10 µg/ml

methamphetamine was applied. Note that the AB2 does not have any receptor sites for the methamphetamine molecule and should function as a non-binding control. The standard deviations of the AB2 biosensor platform, as calculated from $\overline{\Delta R_{AB}}$ and $\overline{\Delta V_{Dirac,AB}}$, are displayed in the grey background.

The methamphetamine exposure onto the AB2 resulted in a $\widehat{\Delta R_{An}}$ of -7.3 ± 7.4% and $\widehat{\Delta V_{Dirac,An}}$ of 12.7 ± 3.1 V. However, the $\widehat{\Delta R_{An}}$ data are well within the standard deviation range of the $\overline{\Delta R_{AB}}$ (grey background), and no evident sensing signal is detected from this result. Note that the $\widehat{\Delta R_{An}}$ and $\widehat{\Delta V_{Dirac,An}}$ of methamphetamine onto the AB2 biosensor platform is at the same concentration.

From these data, a contribution from the methamphetamine cannot be excluded completely. Even though the AB2 is a non-specific antibody to the methamphetamine, adsorption of the antigen needs to be considered. As discussed in the previous chapter, the washing procedure in between functionalisation steps has not been fully optimised yet and needs to be investigated in future experiments. Furthermore, unspecific adsorption on graphene is a frequently occurring problem, which was noticed in previous publications.[29,57,67,208] As a consequence, unbound molecules may reside on the surface, e.g. inducing charge transfer to the sample. Nevertheless, the influence of methamphetamine on the AB2 biosensor platform is negligibly small in comparison to the influence on the methamphetamine biosensor platform.[173]

6.2.3 Comparison of FLaT to Conventional Functionalisation Approach

In this work, all samples have been prepared using the FLaT method. The publications of Berner *et al.*[51] and Winters *et al.*[169] demonstrated a clear benefit of this approach over the conventional functionalisation process. They used several methods including STM, Raman spectroscopy and contact angle measurements to underline their results.[51,169] The packing density of the PBI molecules was found to be highest on the cleanest possible graphene without contamination from the PMMA during conventional transfer. Supporting this, the AFM scans and surface roughness analysis performed in this work show a cleaner and more homogeneous surface after FLaT transfer (see Figure 31).

For a more detailed comparison of those types of transfer, two methamphetamine biosensor platforms are prepared using the FLaT method and six samples *via* the conventional functionalisation approach. The detection of methamphetamine is addressed using electrical characterisation. The same protocol was performed on all samples, with the coupling of the methamphetamine-AB on the PBI, and exposing the samples subsequently to 10 µg/ml

methamphetamine. The resulting $\widehat{\Delta R_{An}}$ and $\widehat{\Delta V_{Dirac,An}}$ are displayed in Figure 54a) and b), respectively.[173] Each individual sample is presented as one data point. Since one sample consists of 11 devices, the standard deviation is represented by the whisker and visualises the variation between individual devices of the same sample. In this statistical analysis, the reproducibility of samples as well as the homogeneity within samples is accounted for. In Figure 54a) and b), the number of individual devices per data point/sample are 6, 5, 10, 6, 7, 10, 7, 10, and 4, 4, 11, 7, 8, 3, 10, 10, respectively.

In Figure 54, the FLaT biosensors (purple squares) show a distinct $\widehat{\Delta R_{An}}$ decrease and $\widehat{\Delta V_{Dirac,An}}$ increase due to methamphetamine binding with small deviations between samples. This indicates a high homogeneity using FLaT graphene, which is in agreement with the result that was already demonstrated in Figure 45. It is obvious that the standard deviations of the $\widehat{\Delta R_{An}}$ and $\widehat{\Delta V_{Dirac,An}}$ values of the conventionally functionalised samples (black circles) are much larger than of the FLaT biosensors, especially in the $\widehat{\Delta R_{An}}$ measurements. The average values differ significantly from device to device and from sample to sample. Note that the missing data point (fourth from the left in conventional functionalisation) in Figure 54a) corresponds to an outlier out of displayed range. In the $\widehat{\Delta V_{Dirac,An}}$ measurements the sample-to-sample variation is considerably higher while the variation between each device on the same sample is relatively less. Furthermore, the overall change in electrical properties of the conventionally functionalised GFETs upon methamphetamine exposure is less (~25%) than of the FLaT GFETs (~60%) in most devices. Especially with respect to $\widehat{\Delta V_{Dirac,An}}$, FLaT GFETs show an approximately 4 times stronger response.[173]

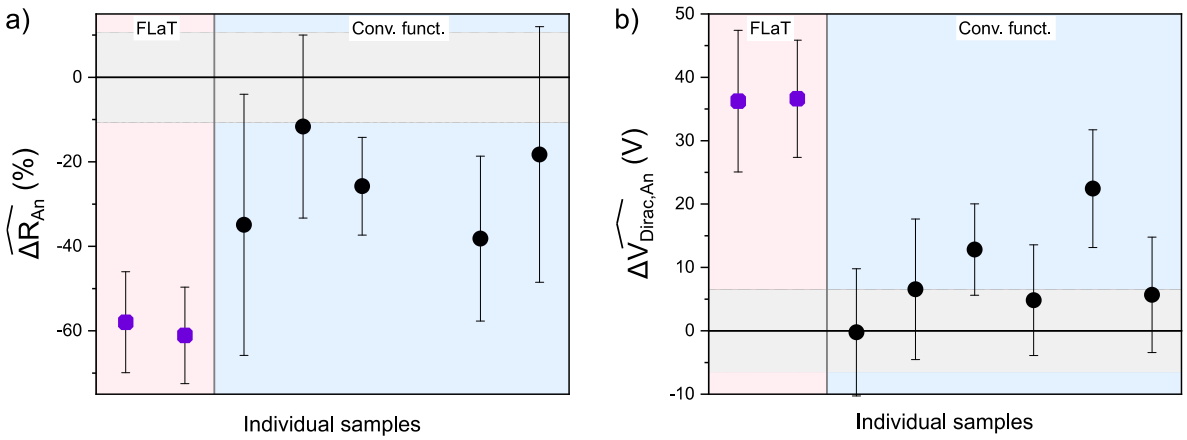

Figure 54. Electrical measurements of FLaT (purple squares) and conventionally functionalised (black circles) samples showing a) $\widehat{\Delta R_{An}}$ and b) $\widehat{\Delta V_{Dirac,An}}$ results. Each of the 8 samples is depicted as one data point with the standard deviation resulting from the individual devices per sample. Grey background as in Figure 52. The FLaT GFETs show lower standard deviations than the conventionally

functionalised ones.[173] The samples were electrically measured after the removal of the liquid droplet.

6.2.4 Investigation of the Methamphetamine Binding Time

To investigate the binding time of the small molecule methamphetamine on its biosensor platform, a time-dependent electrical analysis is performed. 10 µg/ml methamphetamine was applied onto a functionalised PBI FLaT methamphetamine biosensor platform, after which the device was electrically characterised every 40 s for 6 min. The respective transfer curves are displayed in Figure 48. The derived V_{Dirac} values are plotted over time in Figure 55 (squares). The light violet coloured region indicates the time range in which the methamphetamine solution dwells on the surface. A large and prompt V_{Dirac} increase caused by methamphetamine binding is observed after the analyte application. Afterwards, the V_{Dirac} gradually increases and tends to be stabilised at a relatively constant value of 75−76 V. Therefore, it concludes that approximately the methamphetamine binding generally takes 4 min to complete in this condition.

The measured sample is processed further as follows the aforementioned procedure and then re-measured after approximately 1 h. Since a V_{Dirac} (star) of 76.5 V is measured, the methamphetamine binding consequently increases V_{Dirac} by approximately 28.5 V, which is in agreement with previously measured devices at the same methamphetamine concentration (see Figure 53).

The V_{Dirac} increase in the beginning of the measurement is most likely not only attributed to the methamphetamine binding alone. Since the exposure to pure DI water also non-negligibly influences the resistance of the device (Figure 49), it may also affect the Dirac voltage. However, the ΔV_{Dirac} of 28.5 V in the pre- to post-treatment in Figure 55 is comparable to what has been observed for similar devices and, therefore, suggests a valid experiment. The incubation time of methamphetamine lies in between 2.5 min and 4 min in the tested conditions.

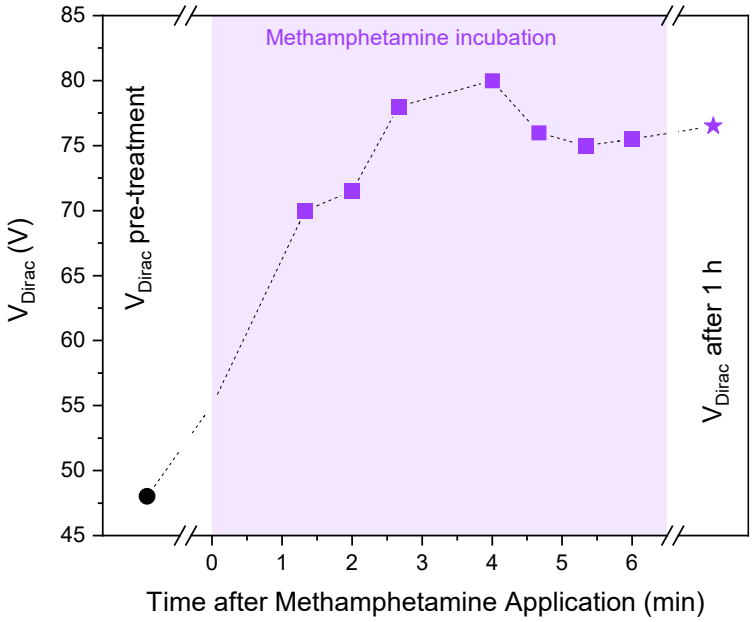

Figure 55. V_{Dirac} shift of a methamphetamine biosensor platform over time during methamphetamine exposure (coloured region). The ΔV_{Dirac} before methamphetamine application (black circle) and after 1 h post-treatment (star) of 28.5 V indicate successful functionalisation.

6.2.5 Lifetime of Biosensors

6.2.5.1 Stability of Methamphetamine Biosensor Platform

Two PBI samples (S1 and S2) were functionalised with 2 µg/ml methamphetamine-AB using crosslinking chemistry and then electrically characterised. In Figure 57, $\overline{\Delta R_{AB}}$ and $\overline{\Delta V_{Dirac,AB}}$ values are displayed in green and each data point of S1 (square) and S2 (circle) stands for average values out of 7 and 10 individual devices, respectively. After the electrical measurements, 50 mM HEPES buffer solution was applied onto S1 while S2 was left untouched as a control sample. Onto each sample, a cover glass was placed and both samples were then stored in air for 17 h. The buffer solution on S1 dried in with the buffer remnants visible in Figure 56b). For details on the protocol, see section 6.1.3 Sample Preparation for Stability .

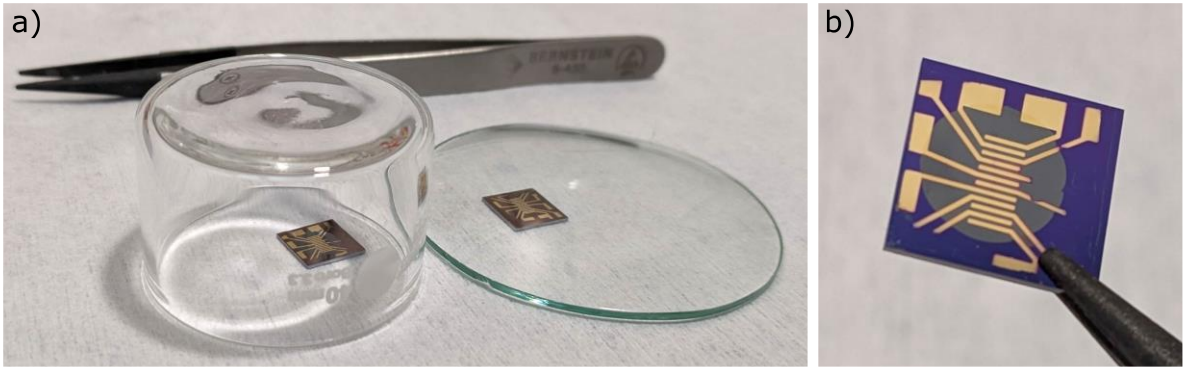

Figure 56. a) S1 and S2 are individually protected by a glass cover over night. b) S1 with a stain left by the dried HEPES buffer droplet after 17 h in atmosphere.

After the over-night storage, S1 was DI water washed to remove dry residues from the buffer solution, then both samples were exposed to 10 µg/ml methamphetamine. The $\widehat{\Delta R_{An}}$ and $\widehat{\Delta V_{Dirac,An}}$ are displayed in purple colour in Figure 57a) and b), respectively. The methamphetamine exposure decreased the resistance down to -40.4 ± 4.3% and −54.2 ± 5.8% for S1 and S2, respectively. This tendency is comparable to what has been observed in Figure 53. Likewise, it increased the V_{Dirac} to 33.1 ± 5.2 V and to 40.3 ± 5.0 V, respectively.

It is not clearly observable whether the buffer solution completely dried out or whether some liquid remained to help stabilise the underlying antibodies. The results indicate that the antibodies might have survived the treatment, which would be interesting for applications. Long-term stability and reliability are important criteria in sensor applications. Prior to validity investigation of industrialisation and possible mass-production, the lifetime and storage conditions of the sensor platforms need to be addressed. The possibility of storing this methamphetamine biosensor platform in air for at least 17 h and still be able to functionalise it with methamphetamine afterwards would be a huge benefit and promises a practical sensor model.

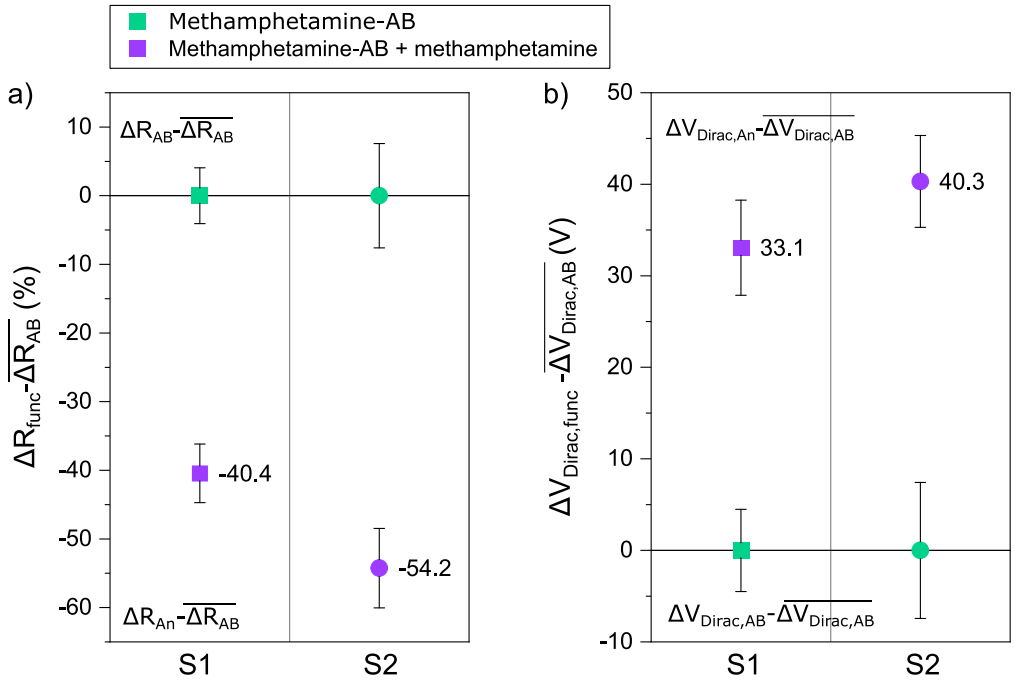

Figure 57. a) $\widehat{\Delta R_{func}}$ and b) $\widehat{\Delta V_{Dirac,func}}$ for S1 (square) and S2 (circle) after different functionalisations. Methamphetamine biosensor platform in green and after storage and subsequent 10 µg/ml methamphetamine exposure in purple. The samples were electrically measured after the removal of the liquid droplet.

6.2.5.2 Lifetime of Methamphetamine Biosensors

Several methamphetamine biosensors were initially realised by coupling 2 µg/ml methamphetamine-AB to the PBI functionalised graphene, which were subsequently exposed to different methamphetamine concentrations. The resulting ΔR and ΔV_{Dirac} are displayed as squares in Figure 58a) and b), respectively. These shifts result from solely taking into account the pre- and post-functionalisation values, following equations (9) and (10). Note that one data point stems from one sample consisting of several individual devices, resulting in the displayed standard deviation. In Figure 58a), 10, 10, 11 and 11 devices were used per data point (from left to right); and data of 10, 10, 10 and 11 devices were acquired in Figure 58b). The methamphetamine biosensor platform is shown in green, and the samples after methamphetamine exposure in concentrations of 0.3 µg/ml, 3 µg/ml and 10 µg/ml in light blue, dark blue and purple, respectively.

ΔR and ΔV_{Dirac} commonly show an apparent dependency on concentration as discussed in the section 6.2.2 Specific Detection of Methamphetamine. The data for the highest methamphetamine concentration (10 µg/ml) do not align with this relation, showing the same ΔR value and lower ΔV_{Dirac} value as the neighbouring data point with 3 µg/ml. This suggests that the sample is not of the same quality as the others, but it is highly difficult to

elaborate the reason. The Raman spectrum (Figure A4) of that particular sample before functionalisation with antibodies reveals the success of PBI functionalisation with a high packing density of the graphene. Thus, the issue most probably occurred during subsequent surface functionalisations. Either the crosslinking chemistry may not have been sufficiently performed, or the methamphetamine was not fully bound to its antibody.

After a long-term storage in N_2 for almost 7 months (208 days), the samples still keep the concentration dependency (Figure 58, stars). However, it has become less than what was observed pre-storage: the initial ΔR (74.3%) and ΔV_{Dirac} (43.3 V) between samples of 3 µg/ml and 0 µg/ml methamphetamine have decreased down to 33.7% and 27.5 V, respectively (dotted lines in Figure 58).

Interestingly, the differences in ΔR and ΔV_{Dirac} between pre- and post-storage of the same sample decrease with increasing methamphetamine concentration. This is more obvious for the biosensor platform (51.0% and 40.9 V, green line), while a smaller gap is observed for 3 µg/ml methamphetamine (10.4% and 25.1 V, blue line).

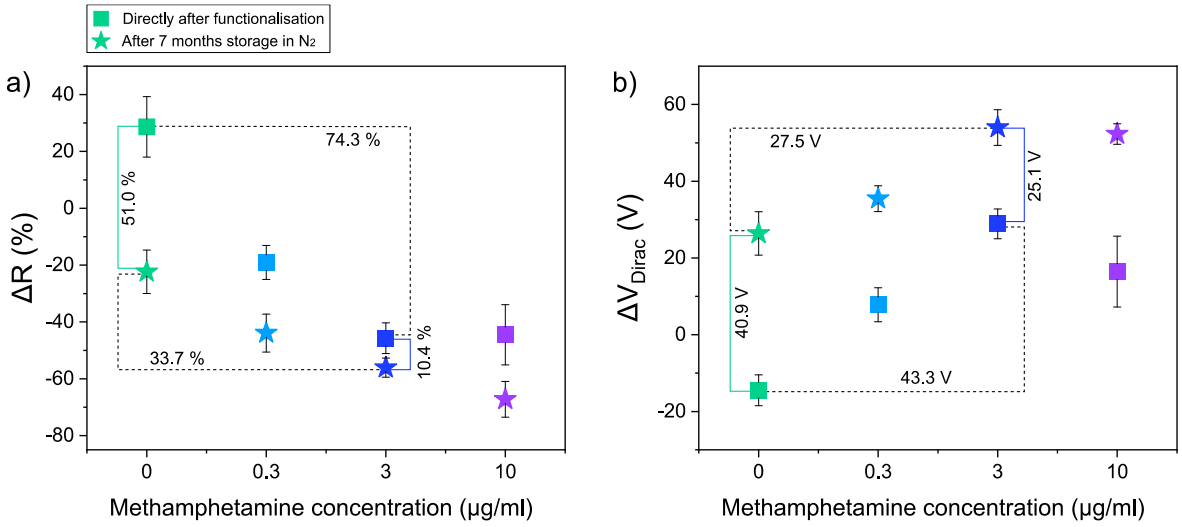

Figure 58. a, b) ΔR and ΔV_{Dirac}, respectively, for methamphetamine biosensor platforms after exposure of different methamphetamine concentrations. The data points of the same colour represent the same sample directly after functionalisation (square) and after subsequent storage in N_2 for ~7 months (star). Values within the plots are ΔR and ΔV_{Dirac}, respectively, between the data points connected by the lines.

Several factors interact during storage in N_2 gas at room temperature, which might influence the electrical characteristics and account for the variation between pre- and post-storage. These include the dehydration of the sample surface, possible denaturation of the antibodies, which might lead to a breaking of the antibody-antigen bonds, oxidation, contamination

from the sample container[209] or neighbouring samples. Nitrogen itself is a relatively inert gas and is unlikely to react with graphene at room temperature. Any small amount of nitrogen molecules that do adsorb onto the surface of graphene during storage would induce slight n-type doping of the samples. The surface dehydration also would result in a slight n-type doping of the sample, as water is a p-dopant. However, since the initial amount of water on the surface is small (see 6.2.1 Electrical Characterisation of GFETs), the complete drying is not likely to change the electrical properties significantly.

While graphene is expected to remain stable under N_2, biomolecules such as antibodies are likely affected. Antibodies will denature without a matrix surrounding them, unfold and lose their tertiary structure. This brings the functional groups and captured methamphetamine into closer contact with the graphene surface, possibly contributing more significantly to the observed changes in ΔR and ΔV_{Dirac}. However, the argument is weakened by the fact that the most significant deviation due to storage is observed for the methamphetamine biosensor platform. Since methamphetamine is a small molecule, it may evaporate from the surface under certain conditions due to its low molecular weight. Since all samples were stored in the same sample box, evaporated methamphetamine might have been transported and deposited on other samples, explaining the increased change in the methamphetamine biosensor platform. Additionally, the decrease of ΔR and increase of ΔV_{Dirac} with methamphetamine concentration after storage is smaller, which might be explained by the averaging of the methamphetamine across all samples.

The doping behaviour of graphene during storage is influenced by a complex interplay of factors related to the graphene itself, the storage environment, and any prior treatment or exposure history.

6.3 Outlook – Cortisol Detection with Noncovalently Functionalised GFETs

First attempts have been made to apply the functionalisation and biosensor preparation process to a second antibody-antigen system, namely cortisol. The main differences in comparison to the previously discussed methamphetamine biosensors are the use of a Fab-fragment instead of a whole antibody, and a differently prepared HEPES buffer, which will be called HEPES-prep in the following. A Fab-fragment consists of one out of two arms of a Y-shaped antibody that essentially recognises and binds specific antigens (see Figure 5). Since there are numerous amine groups on one Fab-fragment, the immobilisation using crosslinking chemistry works equally as for regular antibodies. The Fab-fragment is

significantly smaller in size than the antibody and a larger number of them can theoretically immobilise on the surface. This enables more binding sites for antigens. The HEPES-prep was prepared by solving 1.19 g HEPES powder in 100 ml DI water to obtain a 50 mM solution and no additional pH stabilisation was conducted.

6.3.1 Surface Analysis

A Raman spectroscopy investigation is performed from PBI FLaT graphene to the final cortisol biosensor and the resulting spectra are displayed in Figure 59a), with magnified wavenumber region in Figure 59b). PBI FLaT graphene (red) shows the typically found PBI peaks, which have been discussed previously (Figure 29). Subsequent functionalisation with 2 µg/ml cortisol-Fab (purple) did not result in a significant change in the Raman spectrum, however, a shoulder on the P1 peak towards lower wavenumbers newly arises. Additionally, the P3 to G peak ration increases. These observations are equally made for the fully functionalised cortisol biosensor (blue) after subsequent 10 µg/ml cortisol application.

After a storage in an N_2 flow box for 4 months, AFM measurements of the cortisol biosensor were performed to examine the sample surface. Details can be found at 3.3.2 Atomic Force Microscopy. AFM scans across the functionalised graphene to the SiO_2/Si substrate were performed in different locations of the sample and two exemplary images are displayed in Figure 59d) and e). The height profiles across the edge were taken along the coloured dashed lines and are displayed in Figure 59f). The height profile of the cortisol biosensor indicates a sample height of 4.6 nm. After the subtraction of the PBI FLaT graphene height of 2.5 nm, the cortisol-Fab height is estimated to 2.1 nm. This is in good agreement with values of Fab-fragments reported in literature.[203,210] The functionalised graphene surface is characterised by several wrinkles and some cracks, which complicates a defined surface roughness analysis.

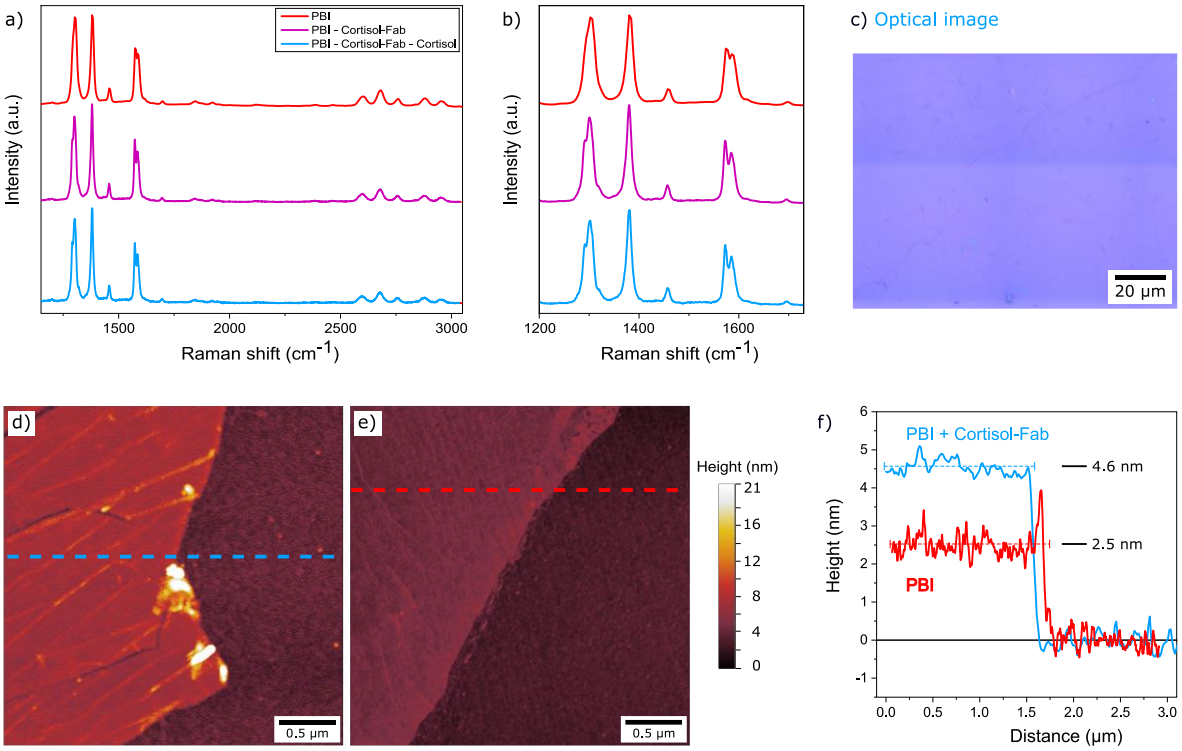

Figure 59. a) Raman spectroscopy characterisation of a PBI FLaT graphene (red), after cortisol-Fab binding (purple) and after additional cortisol exposure (blue). Raman spectra in the magnified wavenumber range in b). c) Optical image from the surface of the fully functionalised cortisol biosensor. d-e) AFM scans across the edge of a cortisol biosensor to the substrate, with dashed lines indicating the height profiles displayed in f). The biosensor layer height is 4.6 nm.

It was found that in a few areas on the sample the profile height was only 2.5 nm, which is exactly the height of PBI FLaT graphene. Since the scratch in the functionalised graphene film was performed directly before the AFM measurement, the substrate is expected to be free of cortisol-Fab molecules. Therefore, it must be assumed that cortisol-Fab binding was not entirely successful.

As the most reasonable scenario, the crosslinking chemistry to bind the Fab-fragments to the PBI might have not worked as anticipated. The PBI functionalisation of graphene was definitely successful (see Raman spectra in Figure 59a-b) and the carboxylic groups of the PBI exist. The actual crosslinking step using EDC/NHS chemistry might not have worked entirely due to either (i) deficient EDC/NHS solution, (ii) insufficient cortisol-Fab concentration, (iii) damaged Fab-fragments:

(i) The EDC/NHS solution is prepared separately for every functionalisation batch. The solution is instable over a prolonged period of time (see section 3.2 Specific Functionalisation to Realise Biosensor), which was considered during the

functionalisation. Each EDC/NHS solution was discarded after 10 min to avoid the solution becoming inefficient by time. However, further insight into the stability of EDC/NHS solutions might be helpful to investigate this issue. The EDC/NHS solution for methamphetamine-AB coupling was provided in a MES buffer at pH 6, while the EDC/NHS solution used for cortisol-Fab binding was prepared using unstabilised HEPES-prep buffer or DI water. These solutions were not specifically optimised to obtain a certain pH and a deviation from pH 6 is highly likely. However, the pH value of EDC/NHS solution is critical for its efficiency, since the ratio of NH_2:NH_3 groups on the antibody or fab-fragment gives the reactivity of the crosslinking chemistry. A deviation of the ideal ratio results in an only partly successful activation of the carboxylic groups.

(ii) A calculation of the necessary cortisol-Fab concentration required to saturate the functionalised graphene surface is performed as follows. For the calculations, several assumptions have to be made. It is known that the cortisol-Fab has a molecular weight of 48 kDa. The molecule is required to be folded in its tertiary state to detect cortisol molecules. Therefore, a radius, r_{Fab}, of approximately 3 nm can be assumed for the folded Fab-fragment.[211–213] Additionally, it is assumed that all cortisol-Fab molecules bind to the surface at the same time and use the space provided in an optimal way.

a) Cortisol-Fab area, A_{Fab}:

$$A_{Fab} = \pi * r_{Fab}^2 = 2.8 \times 10^{-17} m^2 \tag{14}$$

b) Particle number, N, of cortisol-Fab:

$$N = n * N_A = \frac{m}{M} * N_A = \frac{c * V}{M} * N_A = 1.5 \times 10^{12} \tag{15}$$

With the concentration, c, of 2 µg/ml, volume, V, of 60 µl, molar mass, M, of 48 kDa, and the Avogadro constant, N_A.

c) Theoretical area, A_{th}, that is covered by cortisol-Fab:

$$A_{th} = A_{Fab} * N = 42 \times 10^{-6}\, m^2 \tag{16}$$

d) Graphene surface area, A_{gr}, covered by 60 µl droplet:

$$A_{gr} = L * W = \ 28 \times 10^{-6}\, m^2 \tag{17}$$

with L and W of 7 mm and 4 mm, respectively, when all devices per chip are combined.

Comparing the graphene surface area of 28×10^{-6} m^2 with the area all cortisol-Fab molecules can theoretically cover of 42×10^{-6} m^2, an excess of cortisol-Fab molecules is evident. There are a lot of assumptions involved for the estimation, therefore, the derived numerical value may be slightly inaccurate, but it still remains in the same order of magnitude. Therefore, it is assured that a sufficient amount of cortisol-Fab is applied.

(iii) Biomolecules are highly instable in conditions that deviate from their ideal ones. Therefore, buffered solutions of a certain pH are typically employed to obtain a higher biomolecule stability. The HEPES-prep buffer solution was not adjusted and it cannot be guaranteed that the resulting pH value is the ideal one for the cortisol-Fab. A wrong pH value can cause the biomolecules to degrade and lose their ability to capture target molecules. Additionally, the storage of 4 months in N_2 atmosphere is not ideal to retain the 3D structure of the molecules due to likely denaturation of biomolecules in these non-ideal conditions. Interestingly however, some areas do show the expected height of Fab-fragments of approximately 2.1 nm, which might indicate that some molecules possibly do retain their volume and maybe their structure. Nevertheless, the surface of the cortisol-Fab biosensor platform in shorter time scales after functionalisation must be examined in future works.

In summary, the cortisol-Fab concentration is calculated to be sufficient to cover the entire graphene area. As a result, it concludes that a deficient EDC/NHS or cortisol-Fab solution is possibly the dominant cause because the buffer solution did not have the ideal pH value. A not fully functionalised surface with cortisol-Fab can be assumed to be the consequence. In consideration of an incomplete functionalisation with the cortisol-Fab, individual channels and/or entire samples may have more cortisol-Fab bound to the PBI functionalised graphene than others. This remarkably increases the inhomogeneity of the samples, which is investigated using electrical measurements in the following section.

6.3.2 Electrical Detection of Cortisol

The electrical measurements shown in Figure 60 are the equivalent of cortisol biosensor platforms to the previously described methamphetamine biosensor platforms in Figure 50. In short, for each cortisol biosensor platform, the ΔR_{AB} $\Delta V_{Dirac,AB}$ are calculated. The deviation of each device from the mean value ($\overline{\Delta R_{AB}}$ and $\overline{\Delta V_{Dirac,AB}}$, respectively) is calculated. For details on the calculations, refer to section 3.3.4 Electrical Characterisation.

The functionalisation with cortisol-Fab results in larger standard deviations of ± 11.5% and ± 8.7 V for resistance and ΔV_{Dirac} measurements, whereas the standard deviations of electrical measurements for methamphetamine biosensor platforms were ± 3.7% and ± 2.9 V, respectively.

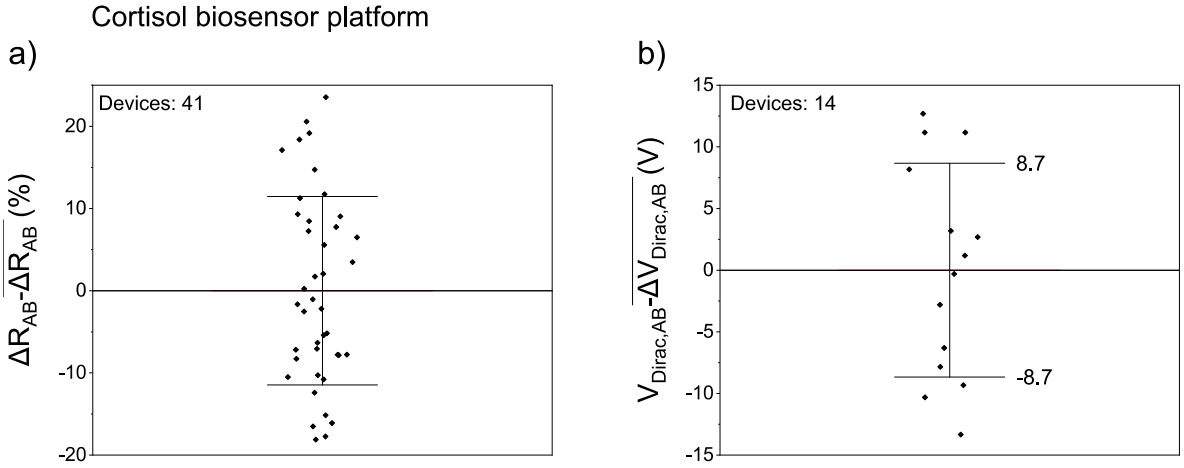

Figure 60. Electrical characterisation of cortisol biosensor platforms, showing the deviations from the mean $\overline{\Delta R_{AB}}$ (a) and $\overline{\Delta V_{Dirac,AB}}$ (b). Each device is displayed as black diamond and the standard deviation is illustrated by the whisker.

Figure 61 depicts the results of the electrical measurements conducted for cortisol detection, including control measurements to examine the functionalisation principles and selectivity of the biosensor. As in the previous section, the role of antibody binding to the carboxylic groups of the perylene was investigated using both PBI functionalised and unfunctionalised graphene, displayed against a red and white background, respectively. EDC/NHS solution and subsequent cortisol-Fab (brown box) were applied, and the presence of a functional cortisol biosensor platform was confirmed by the application of 10 µg/ml cortisol (brown diamonds). Cross-reactivity tests were conducted using the placebo progesterone instead of cortisol (grey diamonds). Both molecules belong to the group of steroids and, thus, have a similar chemical structure. From left to right, the number of devices in Figure 61a) is 25, 27, 7 and 18, while 51, 33, 2 and 1 device was used in Figure 61b).

The majority of devices of the cortisol biosensor shows a significant $\widehat{\Delta R_{An}}$ increase of 23.6 ± 21.8% and a $\Delta \widehat{V_{Dirac,An}}$ decrease of -23.4% ± 13.4 V. In the case of PBI functionalised graphene, the cortisol-Fab couples to the carboxylic groups of the PBI and the electrical analysis reveals a fully working cortisol biosensor. Additionally, the direction of the shifts indicates n-type doping behaviour by cortisol as is in agreement with previous reports.[173,214,215]

The unfunctionalised graphene cannot realise a cortisol biosensor platform as the cortisol-Fab does not bind to the surface. The subsequent exposure to cortisol does not result in any significant $\widehat{\Delta R_{An}}$ and no cortisol binding can be detected. Interestingly, the $\Delta V_{Dirac,An}$ result needs to be carefully examined because the opposite direction of Dirac voltage shift by cortisol on its cortisol-Fab is observed.

Onto PBI functionalised graphene, 10 µg/ml cortisol was applied directly. In both electrical characterisations, completely opposite responses (negative $\widehat{\Delta R_{An}}$ and positive $\Delta V_{Dirac,An}$) were reproduced unlike the working cortisol biosensors. Up to now it creates the impression that the cortisol is n-type doping for biosensors and p-type doping after pure application. This shift is in the same range as for unfunctionalised graphene. Only one sample was used to obtain these results, which is why it should be investigated more thoroughly before a final statement can be made.

The chemical structure of progesterone is very similar to cortisol (see Figure 19). Thus, optimisation of cortisol biosensors is necessary to avoid cross-reactivity. A cortisol biosensor platform was exposed to 10 µg/ml progesterone, of which the individual devices are presented as grey diamonds. A strong cross-reactivity can be observed for ΔR measurements with the signal being almost as strong as for cortisol biosensors. On the other hand, an immaterial increase was monitored in ΔV_{Dirac} measurements.

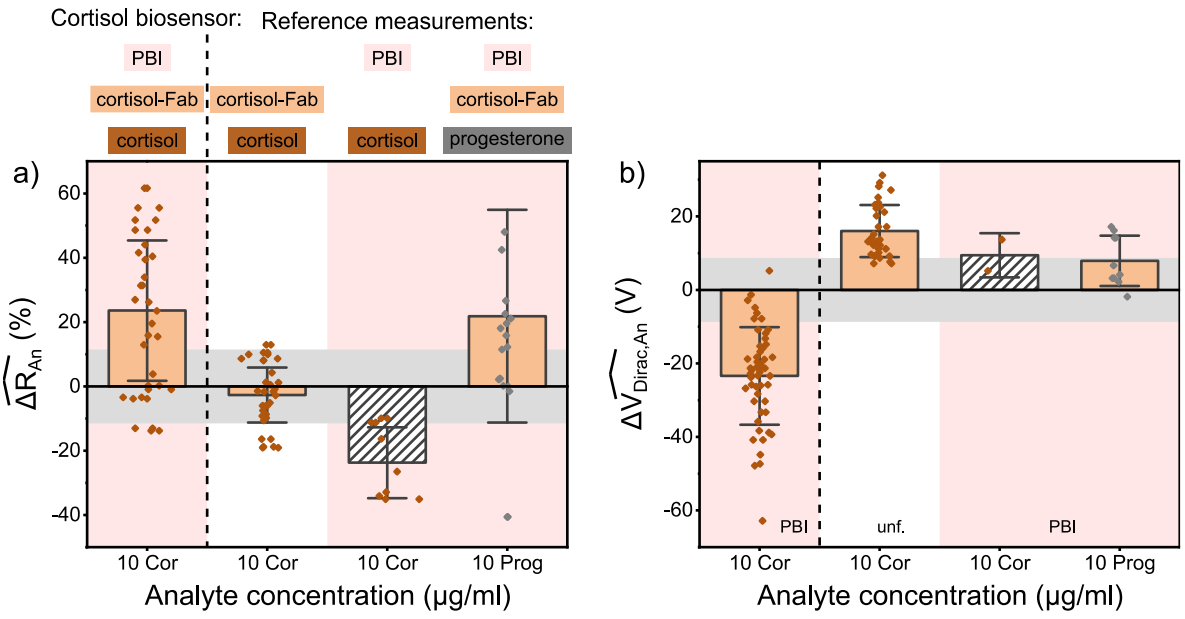

Figure 61. $\widehat{\Delta R_{An}}$ and $\Delta V_{Dirac,An}$ for cortisol biosensors developed from PBI FLaT graphene and control measurement. Each data point stems from one device and the box averages all devices of one concentration with the standard deviation in the whisker. All data are normed to the cortisol biosensor platform (grey background). From left to right: cortisol biosensor (10 µg/ml cortisol) and control

samples. PBI functionalised graphene (red background) and unfunctionalised samples were exposed to different chemicals: EDC/NHS chemistry and cortisol-Fab (brown box), cortisol (brown diamonds) or progesterone (grey diamonds). The samples were electrically measured after the removal of the liquid droplet.

The inhomogeneity in AFM measurements is reflected in the electrical characteristics, directly impacting the device yield. In addition, the $\widehat{\Delta R_{An}}$ and $\Delta V_{\widehat{Dirac,An}}$ results of the control measurements show less reproducibility. This entire characterisation should be performed again using a pH stabilised buffer solution for both EDC/NHS and cortisol-Fab solutions, and also it is suggested to analyse the biosensors soon after functionalisation and in liquid. So far, the stability of the molecule in N_2 atmosphere has not been fully disclosed yet in spite of its importance. As cortisol in a concentration of 10 µg/ml was detected by the noncovalently functionalised GFETs, it is demonstrated the detection mechanism works as well, and the specificity and overall performance of the sensors are expected to be improved after further optimisation.

6.4 Conclusion

In this chapter, noncovalently functionalised GFETs are investigated as a homogeneous and reliable biosensor platform. Using the FLaT process, CVD grown graphene is functionalised with PBI molecules and subsequently transferred to SiO_2/Si substrates. This ensures the most homogeneous self-assembly of the PBI on the graphene. EDC/NHS crosslinking chemistry is used to selectively bind antibodies onto the carboxylic functional groups of the PBI. The homogeneous PBI distribution is reflected to the anti-methamphetamine antibody layer, resulting in a homogeneous and smooth antibody surface with a surface roughness of 1.1 nm and an antibody layer height of 5.1 nm. It reveals the antibody orientation to be in a lying position rather standing upright.

In order to detect antigens, the electrical responses caused by the binding of the antigen to the antibody are analysed. The results demonstrate that an antibody concentration of 2 µg/ml is optimal for the formation of a homogeneous antibody layer and the subsequent detection of methamphetamine. This concentration yields the strongest and most reliable electrical response upon methamphetamine exposure. Using lower methamphetamine-AB concentration, the sensor surface is not efficiently covered by antibodies, which is derived from the insufficient methamphetamine detection with decreasing antibody concentration.

The electrical response of methamphetamine biosensor platforms to different concentrations of methamphetamine is found to be concentration-dependent. The highest tested

concentration of 10 µg/ml is assumed to be close to the saturation level of the biosensors based on a hyperbolic fit, while the lowest concentration of 0.3 µg/ml is still within the effective sensing range and no limit of detection is reached. The absence of a specific signal upon exposure of the placebo paracetamol to the methamphetamine biosensors indicates a highly specific methamphetamine biosensor. However, a small cross-reactivity is observed for AB2 biosensor platforms at the highest concentration of methamphetamine exposure and further study is required.

In line with the previous chapter, electrical measurements were carried out to explore the variance in sensing behaviour between the FLaT and conventionally functionalisation methods. The uniformity observed among the samples as well as between individual devices on a single sample indicates a higher level of reproducibility and reliability of FLaT graphene. Furthermore, FLaT devices tend to show a stronger response, thus enhanced sensitivity and accuracy are potentially promised in biosensing applications. In conclusion, these results claim that FLaT graphene is advantageous for the development of high-performance biosensors.

Stability and lifetime of both the methamphetamine biosensor and its platform are examined. The methamphetamine biosensors do not show any remarkable time-dependent sensor performance deterioration even after a long-term storage in N_2 for approximately 7 months. In the follow-up measurements, the biosensor platforms are stable for at least 17 hours in ambient conditions and methamphetamine detection was still possible. This implies the potential application of the sensors in field work, where it may not be feasible to conduct the functionalisation procedure.

7 Adaptation of a New Perylene Derivative

The biosensors developed and tested in the previous chapters are based on the noncovalent functionalisation of graphene with the PBI. This molecule serves as linker molecule between graphene and the subsequently applied antibodies. The main requirements of the PBI are 1) noncovalent functionalisation of the graphene in order to preserve its natural lattice structure and benefit from graphene's properties, and 2) selectively couple antibodies to its functional groups. These demands can not only be fulfilled by the PBI but a wide range of other molecules, as has been proven by several groups so far.[29,50,58,187–189] In the specific case of the functionalisation technique used in this work, carboxylic end groups of the linker molecule are required for antibody binding. Therefore, a newly synthesised perylene molecule with carboxylic end groups is investigated in this chapter. The benefit of using this new perylene molecule is that the lateral dimension is smaller and, theoretically, a larger number of the molecules can self-assemble on the graphene surface. This, in turn, opens up the possibility of increased biomolecule attachment and resulting sensitivity.

7.1 Experimental Details

7.1.1 Synthesis

The synthesis route for the water soluble Perylene-3,4,9,10-tetracarboxylate (PTA, Figure 62b) developed by Narayan *et al.*[95] was adapted in this work to obtain large quantities of the p-doping perylene molecule. It is derived from the perylene tetracarboxylic dianhydride (PTCDA, Merck, Figure 62a), which is an n-type organic semiconductor.[216] The similar structure of PTA to graphene, combining the planar structure and the conjugated π-system, ensures good adhesion and noncovalent functionalisation *via* π-π-stacking of graphene, as described before (see 2.2.1 Noncovalent functionalisation).

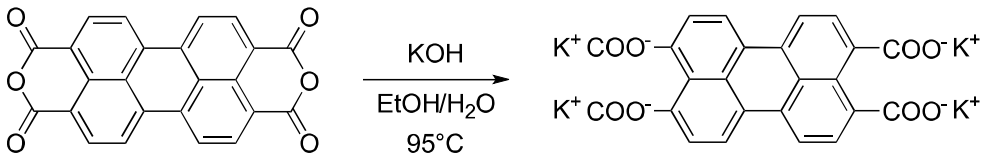

Figure 62. Chemical structures of a) PTCDA and b) PTA potassium salt.

In a 500 ml flask, 1 g PTCDA powder was dispersed in 100 ml ethanol (Merck). A 0.5 M aqueous KOH solution was prepared by mixing 4.2 g KOH powder (Merck) in 150 ml DI water, which was subsequently added to the PTCDA-ethanol solution. The flask was placed directly above a pot filled with mineral oil, and a distillation column was mounted on the flask. The temperature of the oil bath was increased to 145 °C until the reflux started. During the 6 h reflux and subsequent cooling to room temperature, a magnetic stirring bar kept running (Figure 63a) and b), respectively). To aid the precipitation process of the yellow PTA potassium salt powder, excess ethanol is added, because the PTA is not soluble in that solvent. The solution was filtered using a trap and vacuum pump to simultaneously dry the solids (Figure 63c). Subsequently, the solids were redissolved in 300 ml of 50/50 water/ethanol, which was heated to ~85 °C for better dissolution. The PTA dissolves while the red PTCDA remains solid and is captured during filtering (Figure 63d) and e) in side and top view, respectively). Upon cooling, PTA precipitates and is dissolved in 50/50 water/ethanol for a second time. As the reaction from PTCDA to PTA might have an intermediate derivative, it has to be ensured that only the fully-reacted PTA is filtered out. The fully-reacted molecule is more soluble in water due to its 4 carboxylic functionalities. Thus, 30 ml water was added to ensure complete dissolution of the fully-reacted PTA and leave the half-reacted PTA precipitated. After a renewed filtering, the half-reacted PTA will be left in the filter and the fully-reacted PTA remains dissolved. This solution was then dried with a rotary evaporator at 150 rpm, 150 mbar and 40 °C for the first several minutes and at 250 rpm, 80mbar and 55 °C for the remaining process (Figure 63f). The PTA was washed in DI water several times during which the potassium exchanges with hydrogen. Out of the 1 g PTCDA, around 800 g fully-reacted PTA were obtained.

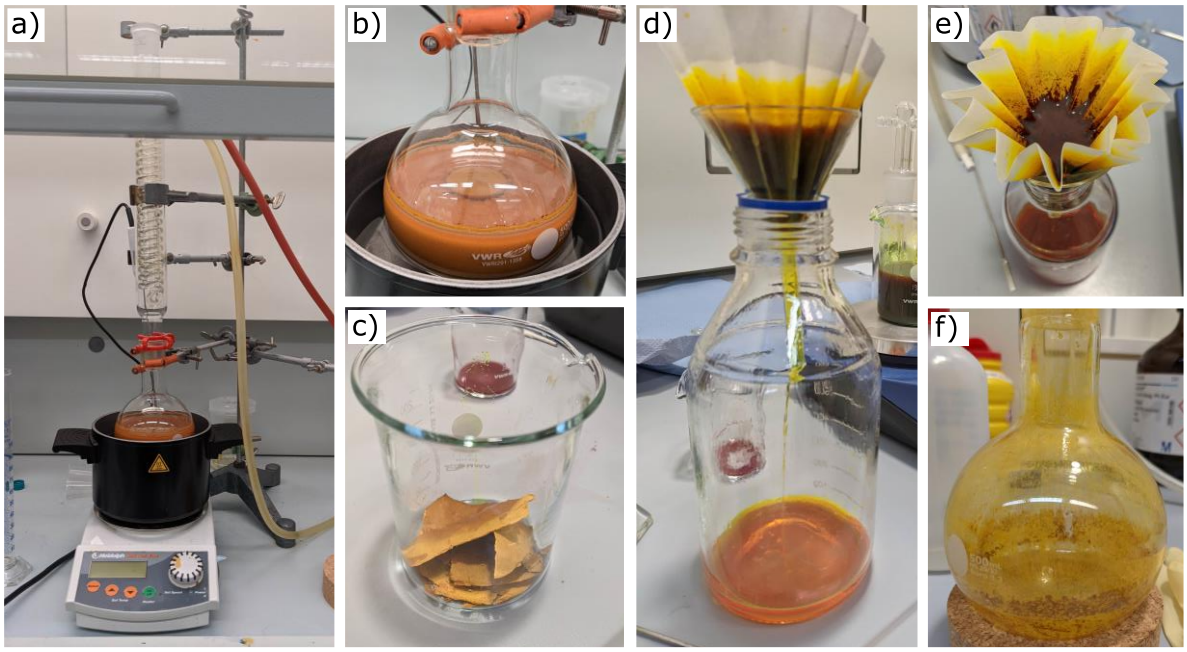

Figure 63. PTA synthesis route. a) 6 h reflux of PTCDA+KOH, b) after cooling to RT, c) solid material after filtering and drying, d) and e) filtering of the redissolved solids in side and top view, respectively, f) final PTA product after drying with a rotary evaporator.

7.1.2 Sample Preparation

The PTA solution for functionalisation is prepared by dissolving the PTA molecule in DI water to obtain a 0.1 mM solution. The solution is either drop-casted onto the desired substrate or the graphene is immersed into its solution. Typically, the sample is thoroughly washed with DI water after functionalisation.

PTA functionalised graphene on 10×10 mm^2 SiO_2/Si substrates is prepared *via* the FLaT method. In section 7.2.2 Comparison of the Perylene Derivatives for the Improvement of the Biosensor Performance, PBI FLaT graphene will be used as comparison. The functionalisation and transfer protocol is described in section 3.1.2 Graphene Transfer in more detail, with either PTA or PBI as perylene molecule. The following functionalisation steps are carried out using the protocol described in 3.2 Specific Functionalisation to Realise Biosensor. Note that the same stabilised buffer solutions are used as in the majority of this work (except for measurements for cortisol detection, which was clarified in chapter 6.3 Outlook – Cortisol Detection with Noncovalently Functionalised GFETs).

7.1.3 Characterisation Techniques

7.1.3.1 Raman Analysis

The Raman spectrum in Figure 66a) was taken using 10 mW laser power, 20 s integration time and 2 accumulations. In Figure 66d), the Raman spectrum was stitched using a 1800 g mm^{-1} grating, 0.2 mW laser power, 10 s integration time and 1 accumulation.

7.1.3.2 Fourier-Transform Infrared Spectroscopy

Fourier-transform infrared spectroscopy (FTIR) is a physical analysis method that uses IR radiation and belongs to the methods of molecular spectroscopy. When a substance is irradiated with IR radiation, certain frequency ranges are absorbed. The absorption bands are visible in the measured spectrum and can be assigned to energy states in molecules. The position of the absorption bands is characteristic for the respective bonds and gives insight in the functional groups of the molecule. Therefore, a structure elucidation and identification of materials is possible. Restrictively, it has to be noted that only in the case of IR-active molecules an interaction between electromagnetic radiation and the molecule occurs. The measurement is carried out in the spectral range from 7800 cm^{-1} to 350 cm^{-1} with attenuated total reflection crystal plates made of diamond.

A Nicolet iS10 FTIR Spectrometer (Thermofisher Scientific) was used by Dr. Mathias Köberl for the measurements in the range of 400 cm^{-1} to 4000 cm^{-1}.

7.2 Results and Discussion

7.2.1 Characterisation of Synthesised PTA

To investigate the success of the synthesis, the PTCDA reactant and PTA product will be compared in terms of their solubility and FTIR signal. Additionally, PTA FLaT graphene is analysed more thoroughly with Raman spectroscopy, AFM and electrical characterisation, in order to study the influence of the perylene molecule on graphene.

7.2.1.1 Solubility

To investigate the solubility of both the PTCDA and the PTA in different solvents, the molecules were mixed with either chloroform, dimethyl sulfoxide (DMSO), DI water, acetone

or methanol. Since perylenes are dyes, their colour is instantly visible when the molecule is dissolved. Therefore, the colour and transparency of solvent-molecule solutions as well as the resulting homogeneity of the solution are taken as an indication of solubility success.

After molecule addition to the solvents, the vials were left for 14 days to better monitor solubility (Figure 64). The molecules might be solved in parts directly after mixing but reaggregate after a while and form precipitants. The first obvious indication is the colour difference of the molecules. While the PTCDA is dark red, the PTA has a strong yellow colour. This is in agreement with what has been observed by Narayan *et al.*[95] PTCDA is partly soluble in DMSO, with precipitate on the bottom of the vial. It is insoluble in all other investigated solvents. The picture for PTA is different, being well soluble in DI water, with no precipitation occurring. Therefore, the PTA is dissolved in DI water to obtain PTA solution for graphene functionalisation. Furthermore, the molecule is partly soluble in methanol and almost insoluble in DMSO.

The solubility of molecules in different solvents is an indication of the functionalities of the molecules and the similarity between them. In the case of PTCDA and PTA, the molecules show a differing solubility behaviour, indicating a change in the chemical structure during the synthesis. Since PTCDA is insoluble in DI water and PTA is water soluble, PTA must have gained functional groups that enable the solubility in water. This, as well as the colour change of the molecules, is a strong indication of the success of the synthesis, as the PTA has carboxylic groups that make the molecule water soluble.

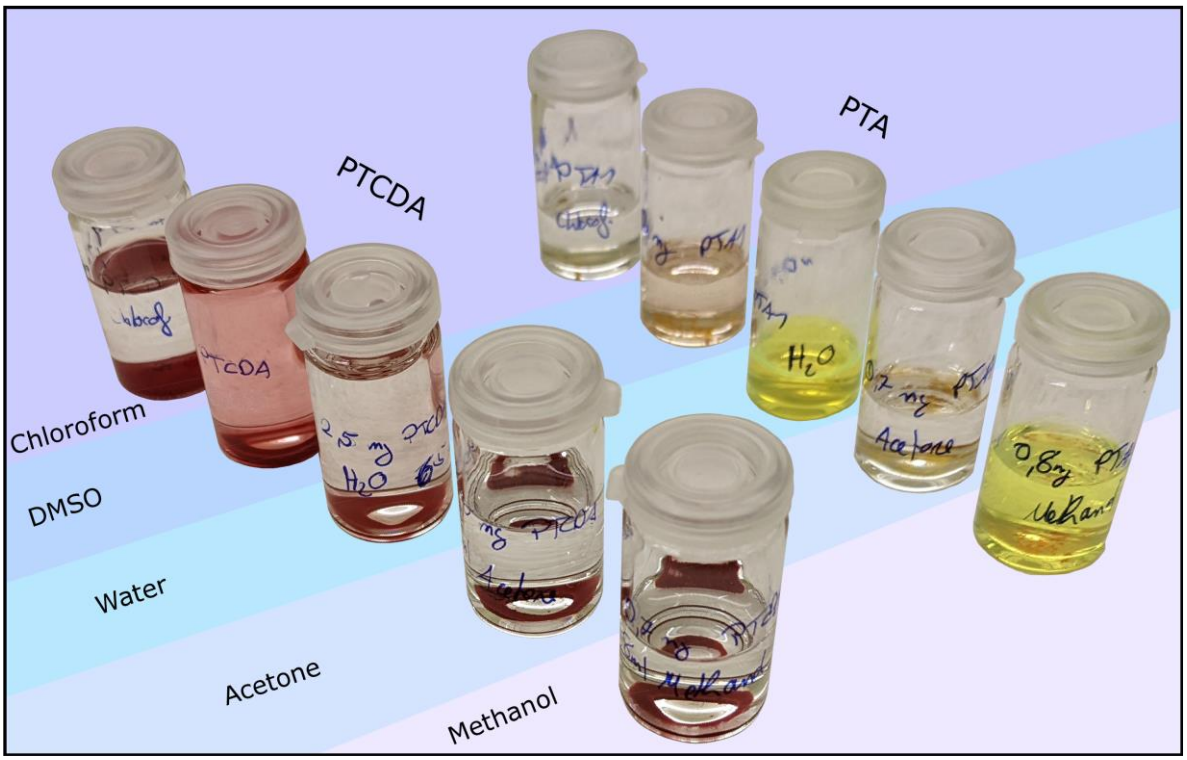

Figure 64. PTCDA (left) and PTA (right) mixed in different solvents 14 days after mixing. Solvents from back to front: chloroform, DMSO, DI water, acetone, methanol.

7.2.1.2 Fourier-Transform Infrared Spectroscopy

FTIR analysis on PTCDA and PTA powders were performed and the resulting transmittance is displayed in Figure 65. The spectrum and most distinct peaks of the PTCDA were compared to the data in the Spectral data base for Organic Compounds (SDBS)[217] and a high agreement is observed. Please refer to the Figure A5 for further details.

The spectra of PTCDA and PTA differ strongly from one another, which is a first indication that the chemical structure of the materials are different. The aromatic C-H vibrations of the perylene backbone are visible in the PTCDA spectrum around 3100 cm^{-1} but are overlaid by residual water in the PTA spectrum. The main similarities of both molecules in the fingerprint region are the aromatic C=C vibrations at 1588 cm^{-1} and 1585 cm^{-1}.[95,218,219]

The PTCDA structure has two anhydride groups, which are hydrolysed to carboxylic groups in the PTA. Therefore, several anhydride peaks can only be found in the PTCDA spectrum. These include the strong C-O-C bands[156,220] at 1012 cm^{-1}, 1118 cm^{-1} and 1294 cm^{-1} and the strong C=O stretching vibrations from 1730-1770 cm^{-1}.[156,219,220] The exact wavenumber was

found to shift slightly depending on the substrate.[221] In general, C=O stretching modes can be observed from 1700 cm^{-1} onwards.[156] No peaks above 1587 cm^{-1} are found in the PTA spectrum.

Vibrations of the COO^--group are published to be found around 1558 cm^{-1} and 1414 cm^{-1}.[95] In the PTA spectrum, both peaks are strong at positions of 1548 cm^{-1} and 1409 cm^{-1}. While the latter peak is observed in the PTCDA spectrum as well, there is no peak at the former wavenumber. Therefore, the carboxylic group was successfully produced through hydrolysis of the anhydride group.[156] Refer to the literature for more details on the FTIR peaks.[156,219,220] The C-H bands of the perylene structure in the region below 900 cm^{-1} follow a similar pattern in both spectra.

From the FTIR analysis, the success of the synthesis from PTCDA to PTA can be understood. The anhydride bands from 1000-1300 cm^{-1} and 1730-1770 cm^{-1} are present throughout the PTCDA spectrum and are absent in the PTA one. Furthermore, new peaks that are assigned to carboxylic groups arose.

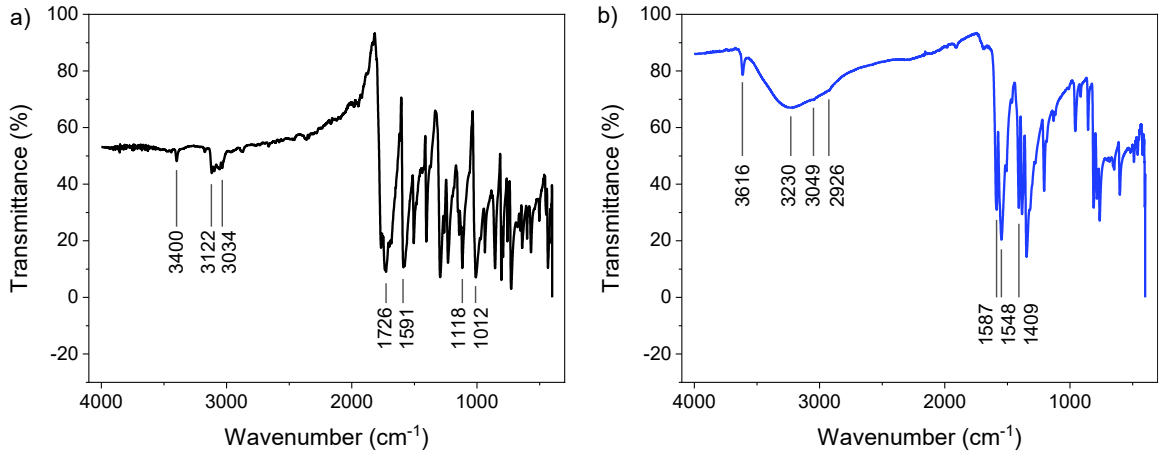

Figure 65. IR spectra of a) PTCDA and b) the fully reacted PTA with the wavenumbers of distinct peaks indicated.

7.2.1.3 Raman Spectroscopy

For a closer look on the characterisation of the PTA molecule, Raman spectroscopy was performed on the pure molecule as well as on PTA functionalised graphene. Derived from Figure 64, the PTA fully dissolves in DI water and a respective 0.1 mM PTA solution is used for functionalisation.

The PTA solution is drop-casted on a blank SiO_2/Si chip, building multiplayers of the molecule. After the water evaporation, Raman spectroscopy on a visible molecule

accumulation is acquired and is displayed in Figure 66a), with magnified wavenumber region in the inset. The location of the spectrum taken is marked in the optical image of the dried PTA (Figure 66b). Characteristic Raman peaks of the perylene core can be found in the wavenumber range 1250 cm^{-1} to 1730 cm^{-1}, with the peak positions of all distinct peaks noted in the image.[182] The strongest peak at 1574 cm^{-1} results from the C-C stretching vibration.[156] The remaining peaks are of similar intensities at wavenumbers of 1286 cm^{-1}, 1319 cm^{-1},1352 cm^{-1} and 1384 cm^{-1} and correspond primarily to in-plane ring "breathing", ring bending and stretching vibrations.[156,222] The Raman signal is not sufficiently clear to distinguish Raman peaks in the high wavenumber region.

For the investigation of the influence of the PTA on graphene, the 2D material was functionalised with the PTA and transferred using the FLaT approach. A 100×100 μm^2 Raman map is acquired, and the average of all single spectra is displayed in Figure 66c). The inset shows the magnified wavenumber region from 1250-1730 cm^{-1}. The Raman peaks are of high intensity, especially in comparison to the spectra from Figure 66a) and show a clear Raman signal without the appearance of a fluorescent background. This reflects the presence of strong coupling between the PTA molecules and the graphene and the resulting quenching of the fluorescence. Similar to what was discussed in section 4.2.2 Characterisation of PBI Functionalisation of Graphene for the Raman spectroscopy of the PBI, the perylene peaks superimpose the graphene Raman peaks.[182] The peaks in the wavenumber range 1200—1700 cm^{-1} are specific to the perylene core, while the peaks found at 2500 cm^{-1}—3300 cm^{-1} can be attributed to the perylene end groups.[182] More specifically, the high-intensity peaks at ~1300 cm^{-1} and ~1381 cm^{-1} correspond to in-plane ring "breathing", and the peak at ~1454 cm^{-1} to ring deformation vibrations. The peaks for in-plane C-C stretching vibrations can be found at 1571 cm^{-1} and 1591 cm^{-1}.[156] Several peaks are observed in the high wavenumber region with peak positions of 2598 cm^{-1}, 2640 cm^{-1}, 2680 cm^{-1} and 2756 cm^{-1} (Figure 66d).

The peak positions of the solid perylenes and the respective FLaT graphene are very similar and differ only by approximately 3 wavenumbers, which is comparably small. Therefore, the same mechanisms of Raman mode origin can be assumed. Interestingly, instead of the two peaks at 1284 cm^{-1} and 1311 cm^{-1} observable in Figure 66a), only one peak is listed at 1299 cm^{-1} in the PBI FLaT graphene spectrum. Therefore, the two peaks in the solid PTA spectrum are likely to have resulted in a peak overlapping. For absolute comparison of the Raman peaks, a more detailed analysis is required.

Selected Raman spectroscopy maps of the PTA FLaT graphene are displayed in Figure 66e-g) and the respective optical image can be found in Figure A6). Different filters are applied

on the maps to investigate different Raman characteristics. Note that the wavenumber ranges for the filters include the most distinct peaks and are highlighted in grey in Figure 66c). The perylene P1 peak is existent over the entire mapped area (Figure 66e). Some patches are of higher intensity than others but the PTA can be found everywhere, as is additionally indicated by the histogram. The intensity ratio I_{P1}/I_{P3} is very homogeneous, with an average value of 1.2 ± 0.1. It is evident that the areas with different intensity in the I_{P1} map are calculated out here, which indicates a similar distribution of intensities of the P3 peak (Figure A7). Therefore, the differences are ruled out in the intensity ratio map. The FWHM(2D) is very homogeneous over the mapped area and averages at 28.3 ± 1.9 cm^{-1}.

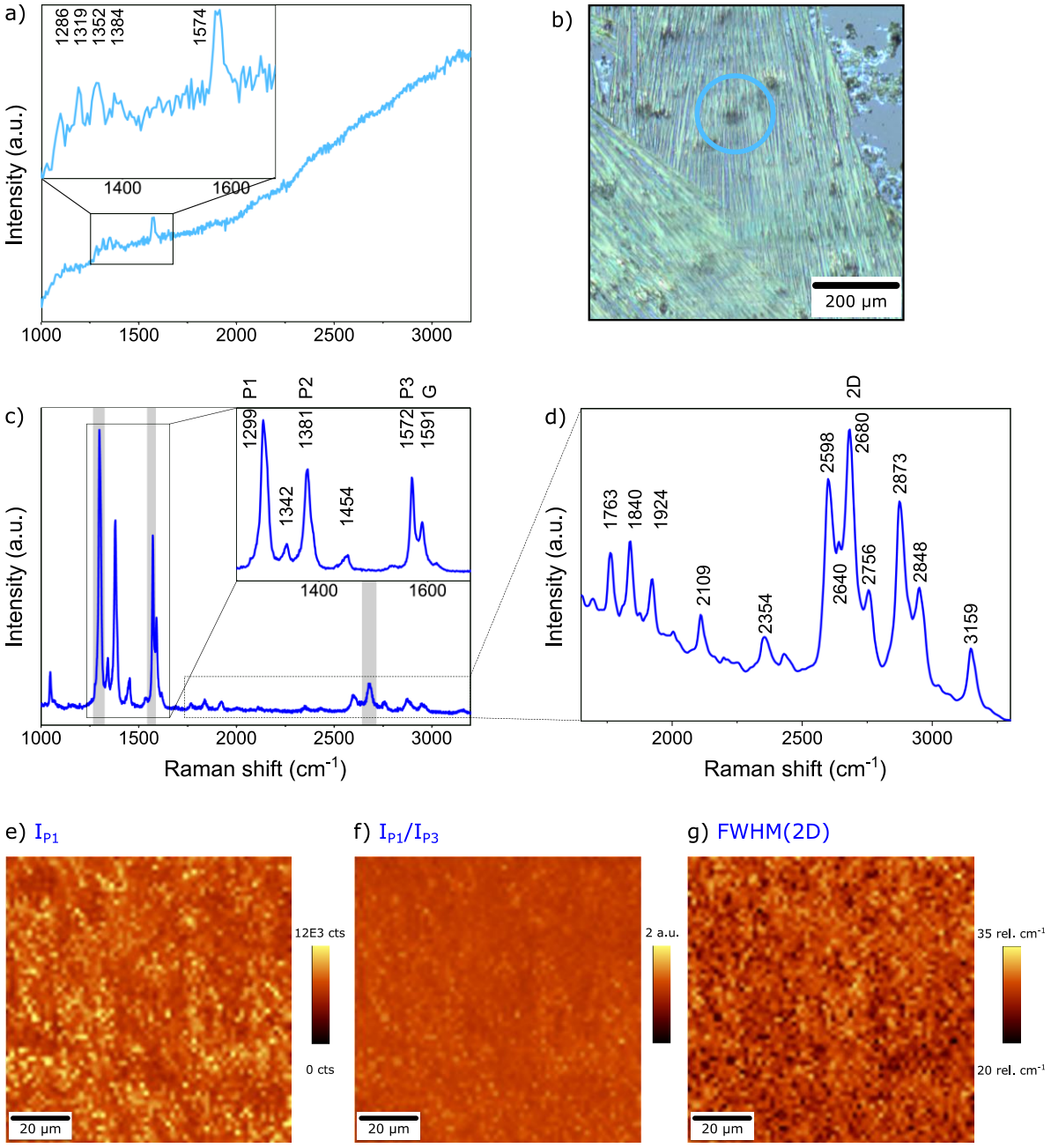

Figure 66. a) Raman spectrum of solid PTA on a SiO_2/Si substrate (light blue) with respective optical image in b). c) Average Raman spectrum of a 100×100 µm² map of PTA FLaT graphene with the magnified wavenumber region in the inset. d) Magnified wavenumber range of a PTA FLaT graphene single spectrum. The grey shaded areas in c) indicate the wavenumber regions of the Raman maps in e-g). The Raman maps show homogeneous distribution of the molecule over the entire area. Some lower intensity areas are visible in e), which are absent in f) and g).

For both PBI (Figure 29) and PTA (Figure 66) perylenes, a full Raman spectroscopy analysis in their solid form and after the functionalisation of graphene using the FLaT approach is

performed. In the following, the characteristics of the respective Raman signals of the perylenes will be compared.

The most striking differences lie in the comparably lower intensities of the peaks at ~1380 cm^{-1} (P2) and at 1590 cm^{-1} (G) for the PTA FLaT graphene. This is already evident in the spectra of solid perylene on Si substrate, where no graphene is involved. Additionally, several small peaks arise in the PTA Raman spectrum, which are not encountered in the spectrum of the PBI. They can be found at approximately 1345 cm^{-1}, 1763 cm^{-1} and 2640 cm^{-1} in the PTA FLaT graphene spectrum. Since these peaks neither exist in the Raman spectrum of unfunctionalised graphene, they are most likely the result of the perylene PTA itself.

In Figure 67, a variety of Raman maps for the two perylene FLaT graphene samples is shown, with intensity ratios of Raman peaks on the left (Figure 67a-d), and FWHM and ω(P1) maps on the right (Figure 67e-h). For better comparison, the colour scales are equal for both perylenes and are positioned between the respective maps. Additional Raman maps can be found in Figure A7.

In both Raman spectra, the P1 peak at ~1302 cm^{-1} is of highest intensity compared to the other perylene peaks. At the respective wavenumber, no graphene peaks exists and it only appears with high intensity if the perylene is in close contact with the graphene, enabling the GERS effect. Therefore, this peak is indicative of the success of perylene functionalisation. The Si peak intensity attenuation is influenced by the overlying layers and when the layers on top of Si are distributed homogeneously, the Si peak intensity should not vary. This is apparent in the maps of the Si peak (see Figure A7). Therefore, the intensity ratio of P1 to the Si peak, I_{P1}/I_{Si}, is an indication of homogeneity of the functionalised sample. Figure 67a) shows the Raman maps of the I_{P1}/I_{Si} for both perylenes, with PBI on the left and PTA on the right. The intensity ratio is very homogeneous over the entire area for both perylenes and lies in the same order of magnitude of approximately 4.5 a.u. Therefore, the P1 peak can be taken as quality measure and will be used for peak intensity comparison in the following.

The ratio I_{P1}/I_{P3G} is similar for the PBI and PTA on graphene, with an average of 1.6 ± 0.1 and 1.2 ± 0.1, respectively. However, the ratio I_{P2}/I_{P3G} is much smaller for the PTA graphene, indicating that the P2 is significantly smaller than the P1 peak, which supports the previous findings of Figure 66c). The 2D peak intensity of the PTA is approximately half of the 2D peak intensity of the PTA, which is expressed by a doubled I_{P1}/I_{2D} ratio.

The FWHM(P1) and FWHM(P2) are approximately equal for the PTA on graphene. While the FWHM(P2) of the PBI is in the same order, its FWHM(P1) is significantly larger (Figure 67e) and f). Both perylenes on graphene show a highly similar FWHM(2D), with average values of approximately 28.2 cm^{-1}. This value is smaller than what was observed for unfunctionalised graphene (see Figure 30). Therefore, a contribution of the perylenes to the peak is evident. Additionally, the ω(P1) are similar with approximately 1302 cm^{-1} and no significant change between the two perylenes is observed. Interestingly, while the Raman peak intensities differ between spectra of the two different perylenes, the peak positions equal one another.

The PBI molecules have nitrogen atoms on the sides of the perylene core and bind long side chains. Furthermore, the PBI has six carboxylic groups while the PTA only has four. These differences in the chemical structure are likely to contribute to the differences of the Raman spectra. Overall, the homogeneity of the functionalisation is very similar and depending on the parameter, the uniformity of distribution across the measured area changes. For example, most of the intensity ratios are more homogeneous for the PTA molecule, while the FWHM tend to be more homogeneous for the PTA functionalisation.

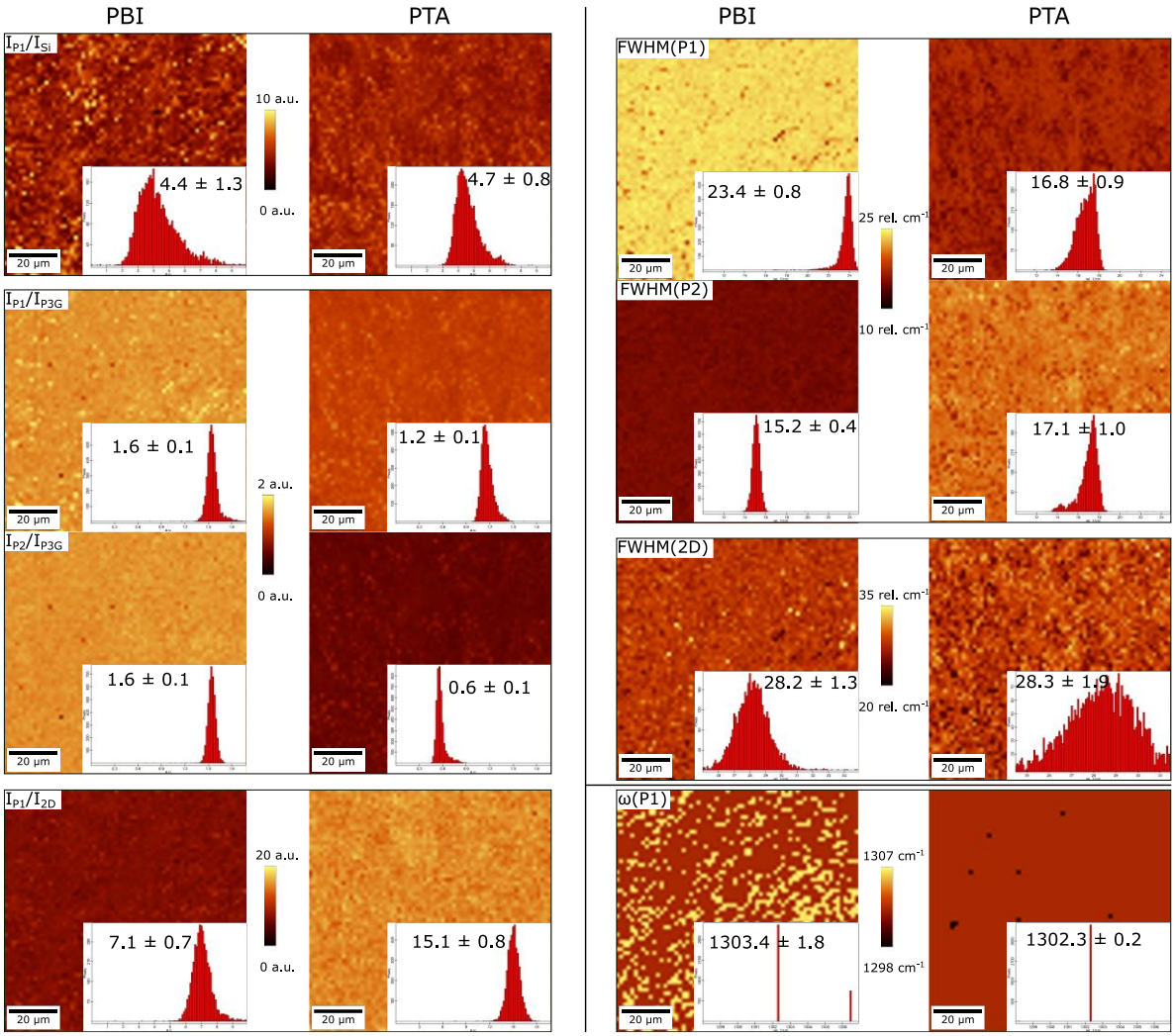

Figure 67. Raman maps of the PBI and PTA FLaT graphene samples. Different filters are applied with the colour scales remaining the same. Left: Intensity ratios, right: FWHM and ω(P1). Histograms are displayed in the images with respective average value and its standard deviation.

7.2.1.4 Atomic Force Microscopy

Graphene was functionalised with the PTA and transferred using the FLaT approach. An AFM analysis of the resulting surface is displayed in Figure 68. In the 10×10 µm² area, wrinkles in the graphene sheet and a few small protrusions on the surface are visible (Figure 68a). The surface roughness S_a over the entire area is calculated to be 0.37 nm, supporting the smooth and homogeneous appearance of the functionalised graphene. A height profile across a graphene-to-substrate edge was performed to investigate the layer height of the functionalised graphene. For better comparison to AFM characterisation of the PBI FLaT graphene (Figure 31), the height scale in all AFM images was adapted and set to 7 nm. The profile taken along the dashed blue line in Figure 68b) indicates a layer height of

2.0 ± 0.2 nm (Figure 68c). The conventionally transferred graphene height was previously found to be 0.9 ± 0.2 nm (Figure 31). Therefore, the PTA height on graphene is calculated to be 1.1 nm. This value is reasonable considering that the PBI is a larger molecule with a layer height of 1.5 nm. A tear, which is located roughly 0.25 µm to the left of the edge, can be correlated to a dip in the height profile.

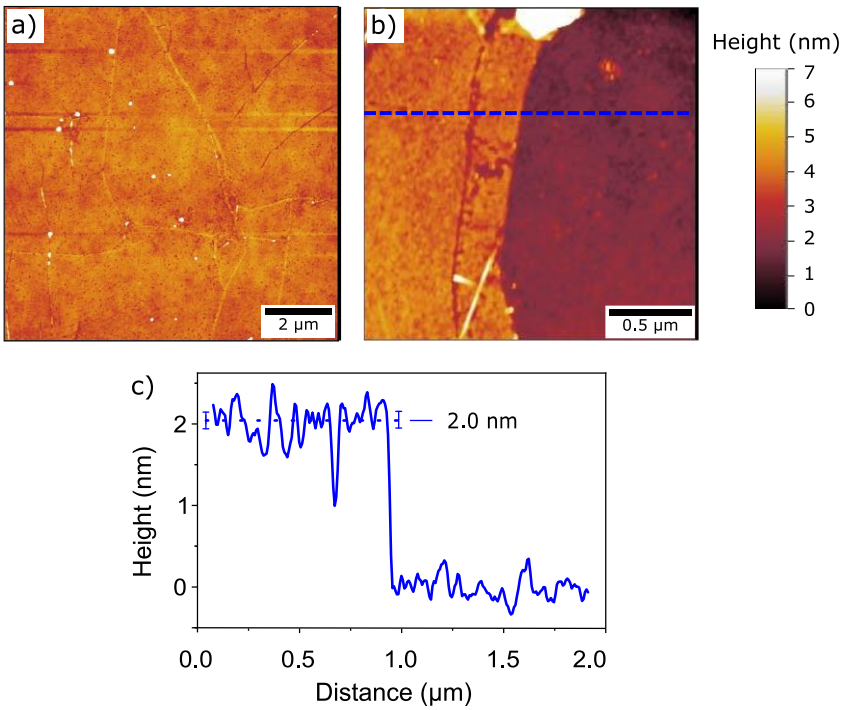

Figure 68. a) 10×10 µm² AFM image of PTA FLaT graphene with smooth and homogeneous surface, b) 2×2 µm² AFM image of the PTA FLaT graphene across an edge to the substrate, c) height profile along the dashed blue line in b), indicating a PTA graphene height of 2.0 ± 0.2 nm.

7.2.1.5 Electrical Characterisation

The impact of the PTA on the electrical parameters of GFETs was investigated. Therefore, a conventionally transferred graphene was analysed in both I_{ds} - V_{ds} and I_{ds} - V_{gs} configurations. Subsequently, the samples were functionalised with the PTA by immersing them into the PTA solution and were characterised again. The resulting changes in resistance, V_{Dirac} and mobility are displayed in Figure 69a-c), respectively. Figure 69a-c) contains 7, 6 and 5 individual data points, respectively.

Interestingly, in comparison to the PBI functionalised graphene, the changes due to the PTA are relatively small. Both ΔR and ΔV_{Dirac} values accumulate near 0% and 0 V, respectively, with a very small standard deviation. However, the µ decreases by 8.2% due to PTA

functionalisation. Likewise, the standard deviation is small, which indicates a good agreement between the samples and a reliable functionalisation.

While a strong p-type doping effect of the PBI on graphene can be observed, no doping for the PTA is detected by purely I_{ds}-V_{ds} and I_{ds}-V_{gs} measurements. To investigate the true doping behaviour, more intense measurements must be conducted.

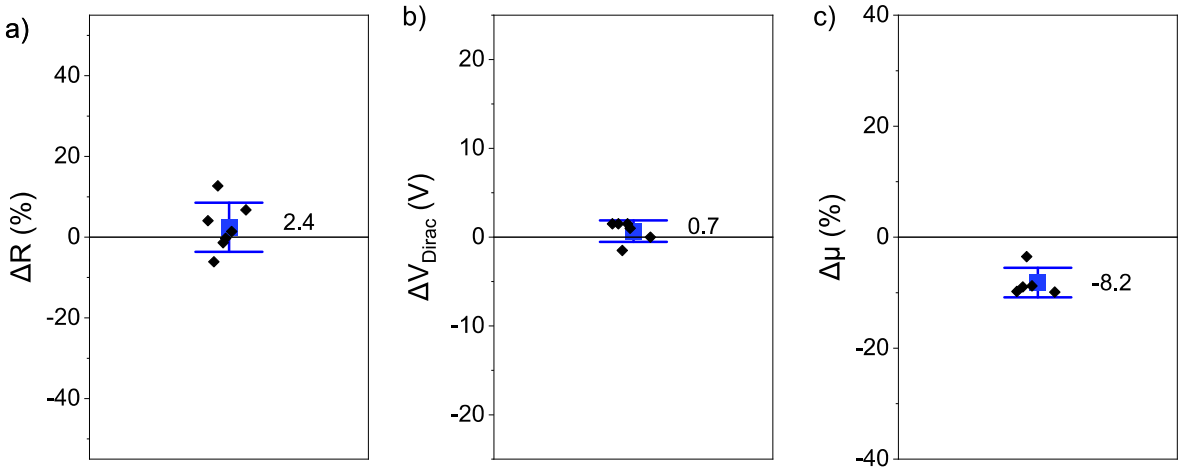

Figure 69. Characterisation of the influence of PTA on the electrical parameters of graphene, with ΔR, ΔV_{Dirac} and $\Delta\mu$ in a-c), respectively.

7.2.2 Comparison of the Perylene Derivatives for the Improvement of the Biosensor Performance

7.2.2.1 Density of Gold Nanoparticles and Clusters

In the previous chapters, all biosensor work has been accomplished using the PBI as linker molecule on graphene. The PBI molecule is characterised by longer and wider side chains which, on one hand, might be preferrable for antibody binding. However, its lateral size is larger than that of the PTA, resulting in a possibly smaller molecule density on the surface. This might have an impact on the antibody density, which are subsequently bound to the perylene. However, since the antibody size is much larger compared to both perylene molecules, the effect might not be large. Nevertheless, the PTA statistically provides a higher cross-linking possibility of the amine groups of the antibodies to the carboxylic groups of the perylenes. Therefore, a study of the receptor density is executed and will be discussed here.

The samples investigated in this section are prepared *via* the FLaT approach using either PBI or PTA as perylene for graphene functionalisation. Subsequently, methamphetamine-AB in a concentration of 2 µg/ml are coupled to the carboxylic groups of the perylene

molecules using EDC/NHS chemistry. The resulting samples are exposed to various concentrations of AB2-AuNP (0.5%, 20%, 60% and 100%) and analysed using the SEM. These AB2 antibodies are conjugated with gold nanoparticles, which can be detected in SEM. The AuNP and AuNP cluster per unit area are calculated as described previously (5.2.2.1 Determination of AuNP and AuNP Cluster Density). Note that for this section, an entirely new sample batch is produced and not the previously discussed data reused. For exact density values, please refer to Table A12 and Table A13. The data points in Figure 70a) consist of 14, 16, 10 and 1 individual SEM images for PBI samples and 10, 10, 10 and 10 for PTA samples after 0.5%, 20%, 60% and 100% AB2-AuNP application, respectively. Equivalently, 6, 6, 6 and 3 individual SEM images for PBI samples and 6, 6, 6 and 6 for PTA samples were used to obtain Figure 70b). Each functionalisation was performed on two samples, out of which the SEM images were taken. The same samples were used for both analysis.

Figure 70a) shows the AuNP density for PBI (red) and PTA (yellow) FLaT graphene. The density increases with AB2-AuNP concentration for both sample types. While the AuNP density is similar in the low AB2-AuNP concentration regime, it diverges as the concentration increases. The PTA samples have the highest AuNP density at 100% AB2-AuNP with 1142 ± 122 AuNP/100 µm^2. In contrast, the AuNP density of PBI FLaT graphene is 837 ± 117 AuNP/100 µm^2 at the same concentration. This value is highly comparable to previous observations with 95% agreement (refer Figure 45), which supports the previously demonstration of achieving a controllable functionalisation process. Since all samples included in this section were prepared at the same time, the conditions can be assumed equal. Therefore, the increased AuNP density for PTA functionalised samples implies a greater methamphetamine-AB density and, therefore, a higher perylene density.

Figure 70b) displays the density of AuNP clusters, which increases as the AB2-AuNP concentration increases. The cluster density is approximately zero for concentrations up to 20% AB2-AuNP, but it increases to18.2 ± 5.5 and 15.1 ± 4.2 AuNP cluster/100 µm^2 for PBI and PTA graphene, respectively. The cluster density of PTA graphene appears to be slightly smaller than that of PBI graphene, but the difference is not significant enough to draw any definitive conclusions.

In summary, it is possible to use the PTA molecule for biosensor applications. The self-assembly of the PTA on the graphene might even result in a larger molecule density, which is derived from indirect measurements. The AuNP density on the functionalised surface is a measure of the density of the underlying methamphetamine-ABs, which, in turn, are bound to the perylene molecules. Since the PTA and PBI graphene samples were functionalised at

the same time in the same conditions, a comparison of the resulting AuNP density is reasonable. A larger AuNP density for PTA functionalised graphene was found, indicating a higher number of receptor sites on the biosensor platform. This supports the idea that smaller molecules self-assemble in a higher density on the sensor surface, allowing for more linker molecules to be available for antibody coupling. A higher number of antibody receptor sites may lead to a larger sensitivity as more target molecules can bind, making PTA functionalised biosensors likely more suitable for sensing applications than the PBI.

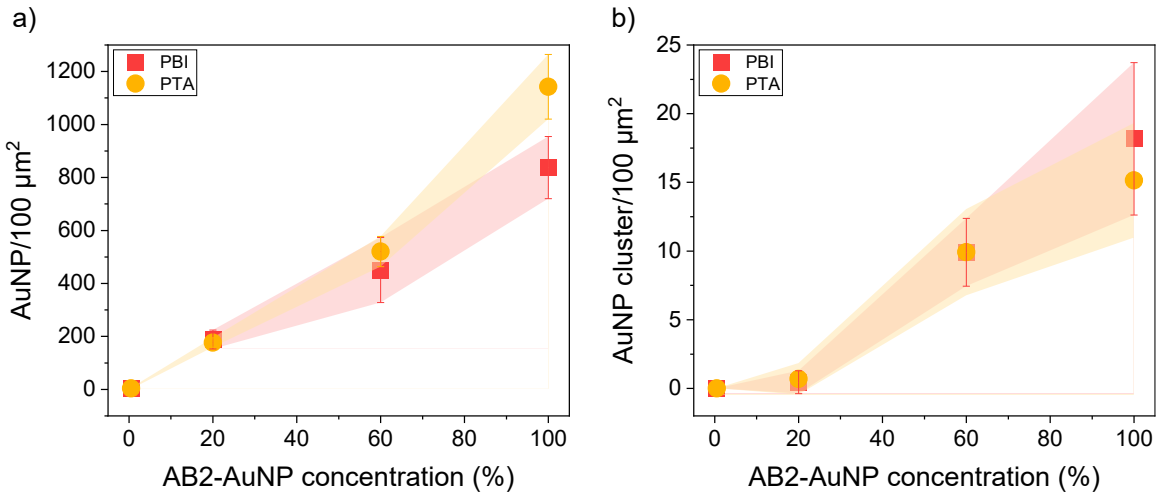

Figure 70. a) The number of AuNP/100 µm² and b) the number of AuNP clusters/100 µm² for PBI (red) and PTA (yellow) FLaT graphene. All samples were coupled to methamphetamine-AB and subsequently exposed to AB2-AuNP in various concentrations. A higher AuNP density is observed on the PTA functionalised samples.

7.2.2.2 Detection of Biomarkers

This section will examine the sensing capabilities of PTA functionalised graphene further, as compared to PBI. Electrical measurements are conducted, which are similar to those shown in Figure 53. Either PBI or PTA is used as perylene molecule for the FLaT of graphene, followed by coupling of methamphetamine-AB in 2 µg/ml concentration to the carboxylic groups of the perylenes. Subsequently, a concentration of 0.3 µg/ml methamphetamine is applied. The resistance and V_{Dirac} values are measured before and after functionalisation to derive the ΔR and ΔV_{Dirac}, respectively. From these data, the average $\overline{\Delta R_{AB}}$ and $\overline{\Delta V_{Dirac,AB}}$ from the respective biosensor platforms are subtracted. The resulting $\widehat{\Delta R_{An}}$ and $\widehat{\Delta V_{Dirac,An}}$ estimate the change in electrical parameters due to solely the analyte, methamphetamine. For details on the procedure, refer to Figure 26 and the equations (9)-(12).

The $\widehat{\Delta R_{An}}$ and $\widehat{\Delta V_{Dirac,An}}$ are displayed in Figure 71a) and b), respectively. Each individual device is displayed as diamond, and the average of all devices per treatment are averaged in one column with its standard deviation as whisker. Note that the PBI values are copied from Figure 53. The standard deviation of the respective $\overline{\Delta R_{AB}}$ and $\overline{\Delta V_{Dirac,AB}}$ values used for calculation are displayed as grey and orange background for the individual perylene molecule. This is significantly larger for PTA samples. The device number of each sample from left to right in Figure 71a) is 43 and 22. Respectively, in Figure 71b) the device numbers are 39 and 9.

Notably, the PTA functionalised GFETs exhibit higher average $\widehat{\Delta R_{An}}$ and $\widehat{\Delta V_{Dirac,An}}$ values than the PBI functionalised GFETs at the same methamphetamine concentration. Single devices of the PTA GFETs even reach values as high as the maximum values for 10 µg/ml methamphetamine (see Figure 53). The $\widehat{\Delta V_{Dirac,An}}$ looks more promising for the PTA, with a significantly larger mean value than for the PBI. However, the standard deviation of PTA GFETs is larger as well, which is especially significant in the $\widehat{\Delta R_{An}}$ measurements.

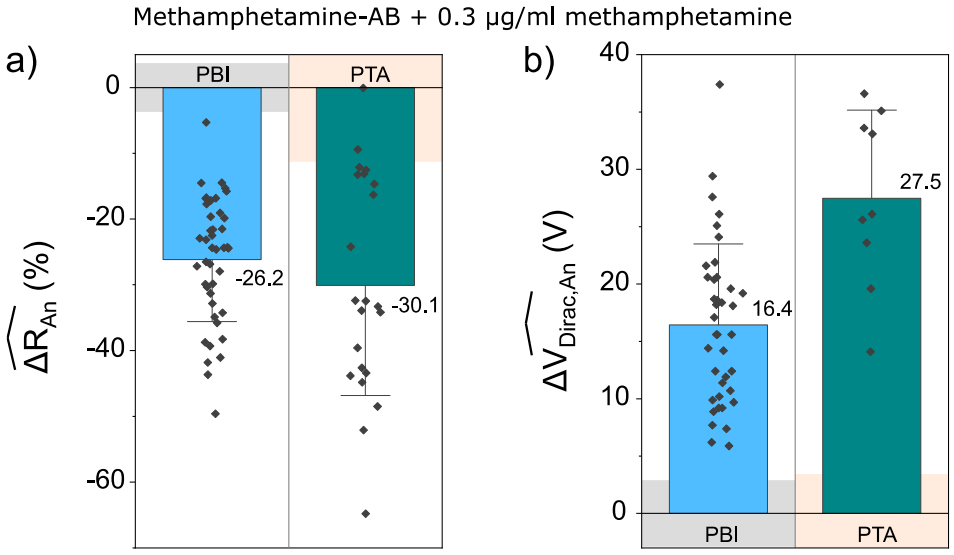

Figure 71. a) and b) Average standardised $\widehat{\Delta R_{An}}$ and $\widehat{\Delta V_{Dirac,An}}$ values of methamphetamine biosensors, respectively. The FLaT of graphene was either performed using the PBI (light blue) or the PTA (petroleum). The data of the PBI functionalised column is copied from Figure 53. Each device is represented by a black diamond, with all devices per treatment comprised in one column. The height and whisker represent the mean value and standard deviation, respectively. The grey background indicates the standard deviation of the $\overline{\Delta R_{AB}}$ and $\overline{\Delta V_{Dirac,AB}}$ values used for calculation. The samples were electrically measured after the removal of the liquid droplet.

To summarise, the PTA functionalisation of graphene results in biosensors with a higher sensitivity for methamphetamine compared to PBI functionalised sensors, as observed in both $\widehat{\Delta R_{An}}$ and $\widehat{\Delta V_{Dirac,An}}$. However, the deviation between results from different devices is larger and appears to be less reliable. The Raman spectroscopy analysis in Figure 67 indicates that the PTA is distributed slightly less homogeneous on the graphene surface than the PBI. This possibly results in a less reliable sensing of small molecules due to less homogeneous antibody coupling. Furthermore, the number of PTA-functionalised GFETs characterised here is relatively small and should be investigated further in future measurements.

7.3 Conclusion and Outlook

This chapter provides a complete investigation of the perylene derivative PTA, covering its synthesis, the self-assembly on graphene, and the performance of the resulting biosensor. Various characterisation techniques are employed to confirm the success of the synthesis. The differentiation from the reactant PTCDA was demonstrated by the colour change from red (PTCDA) to yellow (PTA) as well as solubility tests in seven different solvents. Most essential is the solubility of PTA in DI water, in which the PTCDA is insoluble. This is enabled by the newly formed carboxylic groups of the PTA, which do not exist in the PTCDA. FTIR analysis confirms the presence of these carboxylic groups, with the disappearance of anhydride groups observed in the PTCDA spectrum and new peaks assigned to carboxylic groups in the PTA spectrum. The correlation of both analysis techniques validates the successful synthesis of the PTA and the existence of the desired carboxylic groups.

Raman spectroscopy demonstrates the functionalisation of graphene with the PTA, showing high intensity perylene peaks. A full comparison of the two perylene derivatives PBI and PTA is conducted using Raman spectroscopy. All main perylene peaks existing in the PBI spectrum can also be found in the Raman spectrum of the PTA. The main differences are the lower intensities of some perylene peaks for the PTA and different FWHM of peaks P1 and P2. Nevertheless, all peak positions are the same. The topography of PTA FLaT graphene is characterised by a smaller surface roughness of 0.37 nm, which is lower than for the PBI FLaT graphene. Height profile measurements using AFM indicate a PTA monolayer height of 1.1 nm.

The biosensor performance was investigated with respect to the two different perylene molecules PBI and PTA. The FLaT graphene was further functionalised with methamphetamine-AB, and the receptor density was studied using AuNP. The AuNP

density on the methamphetamine biosensor platform reflects the receptor sites available for coupling with antibodies, which supports the assumption of smaller molecules self-assembling in higher density on the sensor surface. This leads to a larger number of available perylene linker molecules for antibody coupling and a larger number of antibody receptor sites, resulting in increased sensitivity for detecting target molecules. Therefore, PTA functionalised biosensors may be better suited for sensing applications than PBI.

Although the functionalisation of graphene with PTA does not significantly alter the electrical characteristics of graphene, it is found to slightly decrease the mobility. In the electrical characterisation of methamphetamine biosensors, the PTA functionalised GFETs were demonstrated to have higher sensitivities towards methamphetamine than PBI functionalised GFETs. The signal change upon methamphetamine exposure is stronger for both resistance and V_{Dirac} measurements.

8 Concluding Remarks and Outlook

This thesis presents a comprehensive investigation of the development and characterisation of reliable and specific graphene-based biosensors. All intermediate steps are presented, starting from the CVD growth of graphene, over the noncovalent functionalisation with perylene molecules, to the specific functionalisation using antibodies, and the final testing of the biosensor. Each development step involves a full characterisation of the materials using various techniques including Raman spectroscopy, SEM, AFM and electrical measurements, if applicable.

The graphene, which is produced using the optimised CVD growth process, is revealed to be of high quality, with minimal defects and a continuous, large-scale monolayer. To take advantage of the pristine, uncontaminated surface directly after CVD growth, the noncovalent functionalisation of the graphene is performed directly on the growth substrate. The surface has not yet been in contact with neither direct pollutants, such as PMMA during the transfer process, nor indirect pollutants including airborne polymers from sample carriers, e.g. Gel-Pak®. As a result, the perylene molecules can self-assemble in a homogeneous monolayer on the graphene, which is determined using several techniques. After the subsequent wet-chemical transfer, which finalises the Functional Layer Transfer of graphene, a homogeneous PBI SAM on graphene is quantitatively inspected by AFM. The surface roughness of 0.44 nm is measured over a large area and the height profile demonstrates a reasonable PBI monolayer height of 1.5 nm. Raman spectroscopy shows the typical perylene peaks of the PBI FLaT graphene. These are also identified on solid PBI on SiO_2/Si substrate and on the PBI on graphene on the Cu foil prior to the transfer. Small to no differences in the Raman spectra between the different sample types are observed. However, it is found that with a perylene SAM on graphene, the intensity of the resulting Raman signal is enhanced due to the GERS effect, which is caused by the coupling of the perylene molecules with the graphene. Despite the superposition of perylene and graphene peaks, the graphene layer number can be analysed, which is mainly possible by taking the 2D peak into account. Several tests on the PBI SAM on graphene suggest a high temperature stability of up to 400 °C, which may be interesting for PBI graphene implementation into integrated devices.

Onto the stable and homogeneous PBI FLaT graphene, methamphetamine-ABs are coupled using EDC/NHS crosslinking chemistry, resulting in the methamphetamine biosensor platform. This causes a surface roughness increase to 1.1 nm and the antibody height is revealed to be approximately 5.1 nm. These results imply that the antibodies reside slightly tilted on the surface, rather than completely flat, because of the presence of numerous functional groups on the antibodies for binding, which are distributed over its entire surface. The density of antibody receptor sites is scoped through a second antibody, AB2, that is conjugated with gold nanoparticles, AuNPs, which appear as bright spots in the SEM. The AB2 binds with its variable region to the constant region of the methamphetamine-AB. The nanoparticles appear as bright spots in the SEM, and their density and aggregation can be correlated to the performance and homogeneity of the AB layer, respectively. The methamphetamine-AB concentration is optimised and the necessity of the various functionalisation steps demonstrated. First attempts for the optimal procedure to remove unbound molecules are conducted. While pure DI water washing results in a good reliability, the test results suggest an effective cleaning process by using NaCl enriched HEPES buffer. Last, the AuNP density correlates with different concentrations of the AB2-AuNP and it is successfully interpolated to show a fitted curve, possibly including the saturation regime.

The biosensor performance is evaluated using the PBI FLaT graphene which is structured in the GFET configuration with twelve electrodes, resulting in eleven individual devices. The methamphetamine biosensor platform is optimised with respect to the antibody concentration, and subsequently tested using its specific antigen methamphetamine. The methamphetamine binding time is identified to be maximum 4 min, as observed in the time-dependent analysis of the Dirac voltage. Additionally, a clear concentration-dependent response of electrical parameters in different methamphetamine concentrations is identified, with approximately 40% resistance change and 39 V shift in the Dirac voltage after the application of 10 µg/ml methamphetamine. The correlation between analyte concentration and electrical response is successfully interpolated using a hyperbolic curve fit and it enables the estimation even in close-to-saturation regime. In this work, the lowest concentration of 0.3 µg/ml is easily detectable, indicating that the LOD has not been met using this concentration. Additionally, the biosensor is tested for cross-reactivity by applying the placebo molecule paracetamol onto methamphetamine biosensor platforms. No significant change in electrical parameters is observed and indicates a highly specific methamphetamine biosensor. However, a small cross-reactivity is found when the AB2 biosensor platform is tested using methamphetamine, which is unspecific to the AB2. At 10 µg/ml, the resistance and Dirac voltage changes are approximately 7% and 13 V, respectively. Nevertheless, these values are significantly lower than what is observed in methamphetamine biosensors.

Additional experiments are carried out to identify the stability and lifetime of the methamphetamine biosensor platform. After methamphetamine-AB functionalisation, the antibodies stay functional for over 17 h in ambient conditions and are still able to detect methamphetamine. It will be interesting to further investigate the duration of the biosensor platform stability without the degradation of the antibodies, as well as to determine the exact conditions under which this is possible. Additionally, completed methamphetamine biosensors are electrically analysed again after a long-term storage in N_2 and the methamphetamine concentration dependency is still observable with electrical parameters.

The principle of the biosensor is investigated using a second antibody-antigen system, cortisol. Herein, the cortisol is detectable using the cortisol-Fab fragment instead of the entire antibody. It is revealed that the cortisol biosensor platform has less surface roughness than observed for the methamphetamine biosensor platform with a cortisol-Fab height of approximately 2.1 nm. Although the cortisol concentration of 10 µg/ml is detected using the biosensor, a larger deviation between the individual devices is found. Additionally, some degree of cross-reactivity with the unspecific molecule progesterone is found. Both molecules are highly similar, since they originate from the same group as steroids. Since the resistance and Dirac voltage changes show different aspects, an in-depth study is necessary to reveal the origin of the variances. A possible starting point for future investigations is the careful selection of the medium and especially its pH value in which both EDC/NHS and the antibodies are solved in.

A full comparison between the two transfer processes is performed and analysed with the previously named characterisation techniques. While the samples are not distinguishable using Raman spectroscopy, the AFM analysis shows a clear distinction between the transfer processes with a cleaner, smoother surface as quantified by surface roughness measurements. Subsequent antibody coupling and AB2-AuNP application result in a larger AuNP density on the surface, which means a larger receptor density. However, the large deviation between the different samples and also on different locations of one sample suggests an inhomogeneous distribution of the AuNP, indicating a less reliable process. This is investigated in more detail with electrical measurements, where several GFETs of both transfer processes are functionalised as methamphetamine biosensor platforms and subsequently exposed to methamphetamine. The conventionally transferred GFETs tend to show less response to the antigen and have less uniform performance between individual devices in contrast to FLaT device. Therefore, it concludes that the FLaT is superior in terms of homogeneity of functional group formation, potentially resulting in a more reliable sensor performance.

The majority of results is produced using the PBI molecule, which has imide groups at each side of the perylene core and long side chains at which ends three carboxylic groups each are located. It is already shown in this work that this perylene provides an excellent base for further antibody coupling and producing a reliable biosensor. A second perylene molecule, PTA, is investigated with respect to its biosensor performance. A full-scale characterisation from synthesis to quality inspection of the self-assembly on graphene is conducted using Raman spectroscopy, SEM, AFM, and additional electrical measurements evaluate the resulting biosensor efficiency. The successful synthesis produces a new perylene with different characteristics as the reactant, which is demonstrated by solubility experiments and FTIR analysis. The Raman spectra of PTA reveals the typical perylene peaks, both as powdery solid and as SAM on graphene. The key differences in the Raman spectra between PBI and PTA lie in the peak intensity ratios and the FWHM of the P1, P2 and 2D peaks, which is discovered through large-area Raman maps on FLaT graphene. AFM analysis reveals a slightly lower surface roughness of PTA and a smaller height profile than of PBI, which possibly attributes to the overall smaller dimensions and significantly shorter side chains of PTA. The investigation of the density of receptor sites proves a very similar outcome for both perylene FLaT graphene samples, with a slightly enhanced performance for PTA functionalised samples. As noticeable sensitivity improvement is found by PTA in additional electrical measurements of methamphetamine binding at 0.3 µg/ml, it is necessary to do more detailed investigation of the characteristics of the PTA molecule in sensor applications.

Overall, this thesis presents a full-scale investigation, from synthesis of the base material graphene, to its noncovalent functionalisation using two types of perylene molecules, the subsequent antibody functionalisation and the characterisation of the final biosensor performance. The presented results demonstrate that noncovalently functionalised graphene can be used as a versatile biosensor with specific detection of the target molecules.

References

[1] K. S. Novoselov, A. K. Geim, S. V. Morozov, D. Jiang, Y. Zhang, S. V. Dubonos, I. V. Grigorieva, A. A. Firsov, *Science* **2004**, *306*, 666–669.

[2] K.S. Novoselov, A.K. Geim, S.V. Morozov, D. Jiang, M.I. Katsnelson, I.V. Grigorieva, S.V. Dubonos, A.A. Firsov, *Nature* **2005**, *10*, 197–200.

[3] L. Lin, B. Deng, J. Sun, H. Peng, Z. Liu, *Chem. Rev.* **2018**, *118*, 9281–9343.

[4] A. K. Geim, *Science* **2009**, *324*, 1530–1534.

[5] M. Prechtl, S. Parhizkar, O. Hartwig, K. Lee, J. Biba, T. Stimpel-Lindner, F. Gity, A. Schels, J. Bolten, S. Suckow, A. L. Giesecke, M. C. Lemme, G. S. Duesberg, *Adv. Funct. Mater.* **2021**, *31*, 2103936.

[6] H. Li, G. Lu, Y. Wang, Z. Yin, C. Cong, Q. He, L. Wang, F. Ding, T. Yu, H. Zhang, *Small* **2013**, *9*, 1974–1981.

[7] A. Castellanos-Gomez, L. Vicarelli, E. Prada, J. O. Island, K. L. Narasimha-Acharya, S. I. Blanter, D. J. Groenendijk, M. Buscema, G. A. Steele, J. V. Alvarez, H. W. Zandbergen, J. J. Palacios, H. S. J. van der Zant, *2D Mater.* **2014**, *1*, 25001.

[8] A. Splendiani, L. Sun, Y. Zhang, T. Li, J. Kim, C.-Y. Chim, G. Galli, F. Wang, *Nano Lett.* **2010**, *10*, 1271–1275.

[9] R. Peierls, *Ann. I. H. Poincare* **1935**, *5*, 177–222.

[10] L. D. Landau, *Phys. Z.* **1937**, *11*, 26–35.

[11] A. M. Díez-Pascual, J. A. Luceño Sánchez, R. Peña Capilla, P. García Díaz, *Polymers* **2018**, *10*, 217.

[12] X. Huang, X. Qi, F. Boey, H. Zhang, *Chem. Soc. Rev.* **2012**, *41*, 666–686.

[13] P. O. Patil, G. R. Pandey, A. G. Patil, V. B. Borse, P. K. Deshmukh, D. R. Patil, R. S. Tade, S. N. Nangare, Z. G. Khan, A. M. Patil, M. P. More, M. Veerapandian, S. B. Bari, *Biosens. Bioelectron.* **2019**, *139*, 111324.

[14] M. A. Al Faruque, M. Syduzzaman, J. Sarkar, K. Bilisik, M. Naebe, *Nanomater.* **2021**, *11*, 2414.

[15] Z. Wang, C.-J. Liu, *Nano Energy* **2015**, *11*, 277–293.

[16] K. Chen, Q. Wang, Z. Niu, J. Chen, *J. Energy Chem.* **2018**, *27*, 12–24.

[17] C. Redondo-Obispo, T. S. Ripolles, S. Cortijo-Campos, A. L. Álvarez, E. Climent-Pascual, A. de Andrés, C. Coya, *Mater. Des.* **2020**, *191*, 108587.

[18] Y. Lin, K. Jenkins, D. Farmer (Ed.) *Development of Graphene FETs for High Frequency Electronics*, IEEE, **2009**.

[19] R. K. Gupta, F. H. Alqahtani, O. M. Dawood, M. Carini, A. Criado, M. Prato, S. K. Garlapati, G. Jones, J. Sexton, K. C. Persaud, C. Dang, U. Monteverde, M. Missous *et al.*, *2D Mater.* **2021**, *8*, 25006.

[20] S. Kabiri Ameri, R. Ho, H. Jang, L. Tao, Y. Wang, L. Wang, D. M. Schnyer, D. Akinwande, N. Lu, *ACS Nano* **2017**, *11*, 7634–7641.

[21] I. Meric, M. Y. Han, A. F. Young, B. Ozyilmaz, P. Kim, K. L. Shepard, *Nat. Nanotechnol.* **2008**, *3*, 654–659.

[22] Z. H. Ni, T. Yu, Y. H. Lu, Y. Y. Wang, Y. P. Feng, Z. X. Shen, *ACS Nano* **2008**, *2*, 2301–2305.

[23] M. Y. Han, B. Ozyilmaz, Y. Zhang, P. Kim, *Phys. Rev. Lett.* **2007**, *98*, 206805.

[24] S. J. Zhang, S. S. Lin, X. Q. Li, X. Y. Liu, H. A. Wu, W. L. Xu, P. Wang, Z. Q. Wu, H. K. Zhong, Z. J. Xu, *Nanoscale* **2016**, *8*, 226–232.

[25] Y. Y. Broza, X. Zhou, M. Yuan, D. Qu, Y. Zheng, R. Vishinkin, M. Khatib, W. Wu, H. Haick, *Chem. Rev.* **2019**, *119*, 11761–11817.

[26] E. Fernandes, P. D. Cabral, R. Campos, G. Machado, M. F. Cerqueira, C. Sousa, P. P. Freitas, J. Borme, D. Y. Petrovykh, P. Alpuim, *Appl. Surf. Sci.* **2019**, *480*, 709–716.

[27] Z. Jiang, B. Feng, J. Xu, T. Qing, P. Zhang, Z. Qing, *Biosens. Bioelectron.* **2020**, *166*, 112471.

[28] M. Kujawska, S. K. Bhardwaj, Y. K. Mishra, A. Kaushik, *Biosensors* **2021**, *11*, 433.

[29] I. Novodchuk, M. Bajcsy, M. Yavuz, *Carbon* **2021**, *172*, 431–453.

[30] K. Sarkar, G. Madras, K. Chatterjee, *RSC Adv.* **2015**, *5*, 50196–50211.

[31] V. Mirzaie, M. Ansari, S. N. Nematollahi-Mahani, M. Moballegh Nasery, B. Karimi, T. Eslaminejad, Y. Pourshojaei, *Drug Des. Devel. Ther.* **2020**, *14*, 3087–3097.

[32] H. S. Nalwa, *J. Biomed. Nanotechnol.* **2014**, *10*, 2421–2423.

[33] H. U. Aamot, I. S. Hofgaard, G. Brodal, O. Elen, B. Holen, S. S. Klemsdal, *World Mycotoxin J.* **2013**, *6*, 31–41.

[34] H. O. Arola, A. Tullila, A. V. Nathanail, T. K. Nevanen, *Toxins* **2017**, *9*.

[35] J. P. Meneely, M. Sulyok, S. Baumgartner, R. Krska, C. T. Elliott, *Talanta* **2010**, *81*, 630–636.

[36] L. Fan, Y. Hu, X. Wang, L. Zhang, F. Li, D. Han, Z. Li, Q. Zhang, Z. Wang, L. Niu, *Talanta* **2012**, *101*, 192–197.

[37] S. Wang, M. Z. Hossain, T. Han, K. Shinozuka, T. Suzuki, A. Kuwana, H. Kobayashi, *ACS omega* **2020**, *5*, 30037–30046.

[38] D. Kwong Hong Tsang, T. J. Lieberthal, C. Watts, I. E. Dunlop, S. Ramadan, A. E. Del Rio Hernandez, N. Klein, *Sci. Rep.* **2019**, *9*, 13946.

[39] S. Islam, S. Shukla, V. K. Bajpai, Y.-K. Han, Y. S. Huh, A. Kumar, A. Ghosh, S. Gandhi, *Biosens. Bioelectron.* **2019**, *126*, 792–799.

[40] O. Parlak, S. T. Keene, A. Marais, V. F. Curto, P. Samorì, *Sci. Adv.* **2018**, *4.* 2904.

[41] N. Gao, T. Gao, X. Yang, X. Dai, W. Zhou, A. Zhang, C. M. Lieber, *Proc. Natl. Acad. Sci. U.S.A.* **2016**, *113*, 14633–14638.

[42] E. C. Peterson, M. Gunnell, Y. Che, R. L. Goforth, F. I. Carroll, R. Henry, H. Liu, S. M. Owens, *J. Pharmacol. Exp. Ther.* **2007**, *322*, 30–39.

[43] Ľ. Švorc, M. Vojs, P. Michniak, M. Marton, M. Rievaj, D. Bustin, *J. Electroanal. Chem.* **2014**, *717-718*, 34–40.

[44] Kaoru Yagiuda, Akihide Hemmi, Satoshi Ito & Yasukazu Asano, *Biosens. Bioelectron.* **1996**, *11*, 703–707.

[45] E. C. Peterson, W. B. Gentry, S. M. Owens, *Adv. Pharmacol.* **2014**, *69*, 107–127.

[46] V. R. Samuel, K. Rao, *Biosens. Bioelectron.* **2022**, *11*, 100216.

[47] A. Jilani, M. H. D. Othman, M. O. Ansari, S. Z. Hussain, A. F. Ismail, I. U. Khan, Inamuddin, *Environ. Chem. Lett.* **2018**, *16*, 1301–1323.

[48] V. Georgakilas, J. N. Tiwari, K. C. Kemp, J. A. Perman, A. B. Bourlinos, K. S. Kim, R. Zboril, *Chem. Rev.* **2016**, *116*, 5464–5519.

[49] H. A. Alhazmi, W. Ahsan, B. Mangla, S. Javed, M. Z. Hassan, M. Asmari, M. Al Bratty, A. Najmi, *Nanotechnol. Rev.* **2022**, *11*, 96–116.

[50] M. Singh, M. Holzinger, M. Tabrizian, S. Winters, N. C. Berner, S. Cosnier, G. S. Duesberg, *J. Am. Chem. Soc.* **2015**, *137*, 2800–2803.

[51] N. C. Berner, S. Winters, C. Backes, C. Yim, K. C. Dümbgen, I. Kaminska, S. Mackowski, A. A. Cafolla, A. Hirsch, G. S. Duesberg, *Nanoscale* **2015**, *7*, 16337–16342.

[52] S. Mao, G. Lu, K. Yu, Z. Bo, J. Chen, *Adv. Mater.* **2010**, *22*, 3521–3526.

[53] S. Farid, X. Meshik, M. Choi, S. Mukherjee, Y. Lan, D. Parikh, S. Poduri, U. Baterdene, C.-E. Huang, Y. Y. Wang, P. Burke, M. Dutta, M. A. Stroscio, *Biosens. Bioelectron.* **2015**, *71*, 294–299.

[54] X. Wang, Z. Hao, T. R. Olsen, W. Zhang, Q. Lin, *Nanoscale* **2019**, *11*, 12573–12581.

[55] J. W. Kim, S. Kim, Y.-H. Jang, K.-I. Lim, W. H. Lee, *Nanotechnology* **2019**, *30*, 345502.

[56] F. Liu, Y. H. Kim, D. S. Cheon, T. S. Seo, *Sens. Actuators B: Chem.* **2013**, *186*, 252–257.

[57] J. A. Mann, T. Alava, H. G. Craighead, W. R. Dichtel, *Angew. Chem.* **2013**, *125*, 3259–3262.

[58] A. Béraud, M. Sauvage, C. M. Bazán, M. Tie, A. Bencherif, D. Bouilly, *Analyst* **2021**, *146*, 403–428.

[59] P. Tassin, T. Koschny, C. M. Soukoulis, *Science* **2013**, *341*, 620–621.

[60] D. de Fazio, D. G. Purdie, A. K. Ott, P. Braeuninger-Weimer, T. Khodkov, S. Goossens, T. Taniguchi, K. Watanabe, P. Livreri, F. H. L. Koppens, S. Hofmann, I. Goykhman, A. C. Ferrari *et al.*, *ACS Nano* **2019**, *13*, 8926–8935.

[61] X. Wang, L. Zhi, K. Müllen, *Nano Lett.* **2008**, *8*, 323–327.

[62] S. Bae, H. Kim, Y. Lee, X. Xu, J.-S. Park, Y. Zheng, J. Balakrishnan, T. Lei, H. R. Kim, Y. I. Song, Y.-J. Kim, K. S. Kim, B. Ozyilmaz *et al.*, *Nat. Nanotechnol.* **2010**, *5*, 574–578.

[63] S. Bharech, R. Kumar, *J. Mater. Sci.* **2015**, *2*, 70–73.

[64] J. Xie, Q. Chen, H. Shen, G. Li, *J. Electrochem. Soc.* **2020**, *167*, 37541.

[65] F. Schedin, A. K. Geim, S. V. Morozov, E. W. Hill, P. Blake, M. I. Katsnelson, K. S. Novoselov, *Nat. Mater.* **2007**, *6*, 652–655.

[66] Y. Huang, X. Dong, Y- Shi, C. M. Li, L.-J. Li and P. Chen, *Nanoscale* **2010**, *2*, 1485–1488.

[67] Y. Liu, X. Dong, P. Chen, *Chem. Soc. Rev.* **2012**, *41*, 2283–2307.

[68] K. S. Kim, Y. Zhao, H. Jang, S. Y. Lee, J. M. Kim, J. Ahn, P. Kim, J. Choi, B. H. Hong, *Nature* **2009**, *457*, 706–710.

[69] J. Wang, F. Ma, M. Sun, *RSC Adv.* **2017**, *7*, 16801–16822.

[70] H. C. Lee, W.-W. Liu, S.-P. Chai, A. R. Mohamed, A. Aziz, C.-S. Khe, N. M. S. Hidayah, U. Hashim, *RSC Adv.* **2017**, *7*, 15644–15693.

[71] M. Coroş, S. Pruneanu, R.-I. Stefan-van Staden, *J. Electrochem. Soc.* **2020**, *167*, 37528.

[72] P. Suvarnaphaet, S. Pechprasarn, *Sensors* **2017**, *17*, 2161.

[73] A. H. Castro Neto, F. Guinea, N. M. R. Peres, K. S. Novoselov, A. K. Geim, *Rev. Mod. Phys.* **2009**, *81*, 109–162.

[74] A. Jorio, *Raman spectroscopy in graphene related systems*, Wiley-VCH, Weinheim Germany, **2011**.

[75] Tsuneya Ando, *NPG Asia Mater.* **2009**, *1*, 17–21.

[76] D. P. DiVincenzo, E. J. Mele, *Phys. Rev. B* **1984**, *29*, 1685–1694.

[77] S. V. Morozov, K. S. Novoselov, M. I. Katsnelson, F. Schedin, D. C. Elias, J. A. Jaszczak, A. K. Geim, *Phys. Rev. Lett.* **2008**, *100*, 16602.

[78] S. H. Mir, V. K. Yadav, J. K. Singh, *ACS omega* **2020**, *5*, 14203–14211.

[79] F. Bonaccorso, Z. Sun, T. Hasan, A. C. Ferrari, *Nat. Photon* **2010**, *4*, 611–622.

[80] A. Zubiarrain-Laserna, P. Kruse, *J. Electrochem. Soc.* **2020**, *167*, 37539.

[81] R. R. Nair, P. Blake, A. N. Grigorenko, K. S. Novoselov, T. J. Booth, T. Stauber, N. M. R. Peres, A. K. Geim, *Science* **2008**, *320*, 1308.

[82] G. Jung, Z. Qin, M. J. Buehler, *Extreme Mech. Lett.* **2015**, *2*, 52–59.

[83] S. E. Choi, S.-S. Kim, E. Choi, J. H. Kim, Y. Choi, J. Kang, O. Kwon, D. W. Kim, *Sci. Rep.* **2021**, *11*, 9518.

[84] C. Wang, J. Wu, Y. He, Z. Song, S. Shi, Y. Zhu, Y. Jia, W. Ye, *Nano Lett.* **2020**, *20*, 166–175.

[85] N. Lindvall, A. Kalabukhov, A. Yurgens, *J. Appl. Phys.* **2012**, *111*, 64904.

[86] J. W. Suk, W. H. Lee, J. Lee, H. Chou, R. D. Piner, Y. Hao, D. Akinwande, R. S. Ruoff, *Nano Lett.* **2013**, *13*, 1462–1467.

[87] T. Hallam, N. C. Berner, C. Yim, G. S. Duesberg, *Adv. Mater. Interfaces* **2014**, *1*, 1400115.

[88] B. Zhuang, S. Li, S. Li, J. Yin, *Carbon* **2021**, *173*, 609–636.

[89] M. Yi, Z. Shen, *J. Mater. Chem. A* **2015**, *3*, 11700–11715.

[90] Y. Xu, H. Cao, Y. Xue, B. Li, W. Cai, *Nanomater.* **2018**, *8*, 942.

[91] J. Xu, Y. Wang, S. Hu, *Microchim Acta* **2017**, *184*, 1–44.

[92] M. Qi, Z. Ren, Y. Jiao, Y. Zhou, X. Xu, W. Li, J. Li, X. Zheng, J. Bai, *J. Phys. Chem. C* **2013**, *117*, 14348–14353.

[93] C. Chang, W. Chen, Y. Chen, Y. Chen, Y. Chen, F. Ding, C. Fan, H. Jin Fan, Z. Fan, C. Gong, Y. Gong, Q. He, X. Hong *et al.*, *Acta Phys-Chim. Sin.* **2021**, *37*, 2108017.

[94] Y. Hernandez, V. Nicolosi, M. Lotya, F. M. Blighe, Z. Sun, S. De, I.T. McGovern, B. Holland, M. Byrne, Y. Gun'ko, J. Boland, P. Niraj, G. S. Duesberg, S. Krishnamurti, R. Goodhue, J. Hutchison, V. Scardaci, A. C. Ferrari, J. N. Coleman, *Nat. Nanotechnol.* **2008**, *3*, 563–568.

[95] R. Narayan, J. Lim, T. Jeon, D. J. Li, S. O. Kim, *Carbon* **2017**, *119*, 555–568.

[96] G. Wang, B. Wang, J. Park, Y. Wang, B. Sun, J. Yao, *Carbon* **2009**, *47*, 3242–3246.

[97] J. A. Mann, W. R. Dichtel, *J. Phys. Chem. Lett.* **2013**, *4*, 2649–2657.

[98] M.-Y. Lin, C.-F. Su, S.-C. Lee, S.-Y. Lin, *J. Appl. Phys.* **2014**, *115*, 223510.

[99] M. Losurdo, M. M. Giangregorio, P. Capezzuto, G. Bruno, *Phys. Chem. Chem. Phys.* **2011**, *13*, 20836–20843.

[100] K. F. McCarty, P. J. Feibelman, E. Loginova, N. C. Bartelt, *Carbon* **2009**, *47*, 1806–1813.

[101] Daniel Dobkin, "Chemical Vapor Deposition Fundamentals", can be found under http://www.enigmatic-consulting.com/semiconductor_processing/CVD_Fundamentals/, **2016**.

[102] Y. Chen, X.-L. Gong, J.-G. Gai, *Adv. Sci.* **2016**, *3*, 1500343.

[103] M. H. Ani, M. A. Kamarudin, A. H. Ramlan, E. Ismail, M. S. Sirat, M. A. Mohamed, M. A. Azam, *J. Mater. Sci.* **2018**, *53*, 7095–7111.

[104] X. Li, W. Cai, J. An, S. Kim, J. Nah, D. Yang, R. Piner, A. Velamakanni, I. Jung, E. Tutuc, S. K. Banerjee, L. Colombo, R. S. Ruoff, *Science* **2009**, *324*, 1312–1314.

[105] C. Gong, G. Lee, B. Shan, E. M. Vogel, R. M. Wallace, K. Cho, *J. Appl. Phys.* **2010**, *108*, 123711.

[106] G. V. Troppenz, M. A. Gluba, M. Kraft, *J. Appl. Phys.* **2013**, *114*, 214312.

[107] P. Braeuninger-Weimer, B. Brennan, A. J. Pollard, S. Hofmann, *Chem. Mater.* **2016**, *28*, 8905–8915.

[108] J. Hu, J. Xu, Y. Zhao, L. Shi, Q. Li, F. Liu, Z. Ullah, W. Li, Y. Guo, L. Liu, *Sci. Rep.* **2017**, *7*, 45358.

[109] J. Kraus, L. Böbel, G. Zwaschka, S. Günther, *Ann. Phys.* **2017**, *529*, 1700029.

[110] C.-J. Chen, M. H. Back, R. A. Back, *Can. J. Chem.* **1976**, *54*, 3175–3184.

[111] X. Zhang, J. Ning, X. Li, B. Wang, L. Hao, M. Liang, M. Jin, L. Zhi, *Nanoscale* **2013**, *5*, 8363–8366.

[112] A. Pirkle, J. Chan, A. Venugopal, D. Hinojos, C. W. Magnuson, S. McDonnell, L. Colombo, E. M. Vogel, R. S. Ruoff, R. M. Wallace, *Appl. Phys. Lett.* **2011**, *99*, 122108.

[113] N. Petrone, C. R. Dean, I. Meric, A. M. van der Zande, P. Y. Huang, L. Wang, D. Muller, K. L. Shepard, J. Hone, *Nano Lett.* **2012**, *12*, 2751–2756.

[114] N. Mishra, J. Boeckl, N. Motta, F. Iacopi, *Phys. Status Solidi A* **2016**, *213*, 2277–2289.

[115] J. Plutnar, M. Pumera, Z. Sofer, *J. Mater. Chem. C* **2018**, *71*, 622.

[116] K. V. Emtsev, A. Bostwick, K. Horn, J. Jobst, G. L. Kellogg, L. Ley, J. L. McChesney, T. Ohta, S. A. Reshanov, J. Röhrl, E. Rotenberg, A. K. Schmid, D. Waldmann *et al.*, *Nat. Mater.* **2009**, *8*, 203–207.

[117] Y. Wang, Z. Ni, T. Yu, Z. Shen, H. Wang, Y. Wu, *J. Phys. Chem. C* **2008**, *112*, 10637–10640.

[118] H. Y. Mao, Y. H. Lu, J. D. Lin, S. Zhong, A. T. S. Wee, W. Chen, *Prog. Surf. Sci.* **2013**, *88*, 132–159.

[119] V. Georgakilas, M. Otyepka, A. B. Bourlinos, V. Chandra, N. Kim, K. C. Kemp, P. Hobza, R. Zboril, K. S. Kim, *Chem. Rev.* **2012**, *112*, 6156–6214.

[120] Y. Kanai, Y. Ohmuro-Matsuyama, M. Tanioku, S. Ushiba, T. Ono, K. Inoue, T. Kitaguchi, M. Kimura, H. Ueda, K. Matsumoto, *ACS sensors* **2020**, *5*, 24–28.

[121] N. G. Welch, J. A. Scoble, B. W. Muir, P. J. Pigram, *Biointerphases* **2017**, *12.* 02D301.

[122] A. V. J. Collis, A. P. Brouwer, A. C. R. Martin, *J. Mol. Biol.* **2003**, *325*, 337–354.

[123] H. Persson, J. Lantto, M. Ohlin, *J. Mol. Biol.* **2006**, *357*, 607–620.

[124] C. A. Ascoli, B. Aggeler, *BioTechniques* **2018**, *65*, 127–136.

[125] Y. Sun, H. Du, C. Feng, Y. Lan, *J. Solid State Electrochem.* **2015**, *19*, 3035–3043.

[126] A. Williams, I. T. Ibrahim, *Chem. Rev.* **1981**, *81*, 589–636.

[127] A. C. Ferrari, D. M. Basko, *Nat. Nanotechnol.* **2013**, *8*, 235–246.

[128] M. Hulman in *Graphene*, Elsevier, **2014**, pp. 156–183.

[129] C. V. Raman, K. S. Krishnan, *Nature* **1928**, *121*, 501–502.

[130] I. Childres, L. A. Jaureguir, W. Park, H. Cao, Y. P. Chen, *Raman Spectroscopy of Graphene and Related Materials*, New Developments in Photon and Materials Research, **2013**.

[131] E. B. Barros, M. S. Dresselhaus, *Phys. Rev. B* **2014**, *90*, 35443.

[132] S. Huang, X. Ling, L. Liang, Y. Song, *Nano Lett.* **2015**, *15*, 2892–2901.

[133] X. Ling, L. Xie, Y. Fang, H. Xu, *Nano Lett.* **2010**, *10*, 553–561.

[134] C. Muccianti, S. L. Zachritz, A. Garlant, C. N. Eads, B. H. Badada, A. Alfrey, M. R. Koehler, D. G. Mandrus, R. Binder, B. J. LeRoy, O. L. Monti, J. R. Schaibley, *J. Phys. Chem. C* **2020**, *124*, 27637–27644.

[135] S. Cortijo-Campos, R. Ramírez-Jiménez, A. de Andrés, *Nanomater.* **2021**, *11*, 644.

[136] M. S. Dresselhaus, A. Jorio, R. Saito, *Annu. Rev. Condens. Matter Phys.* **2010**, *1*, 89–108.

[137] F. Schedin, E. Lidorikis, A. Lombardo, V. G. Kravets, A. K. Geim, A. N. Grigorenko, K. S. Novoselov, A. C. Ferrari, *J. Mol. Struct.* **2010**, *1040*, 213–215.

[138] L. M. Malard, M. A. Pimenta, G. Dresselhaus, M. S. Dresselhaus, *Phys. Rep.* **2009**, *473*, 51–87.

[139] J. B. Wu, M. L. Lin, X. Cong, H. N. Liu, P. H. Tan, *Chem. Soc. Rev.* **2018**, *47*, 1822–1873.

[140] P. Poncharal, A. Ayari, T. Michel, J.-L. Sauvajol, *Phys. Rev. B* **2008**, *78*, 113407.

[141] T. M. G. Mohiuddin, A. Lombardo, R. R. Nair, A. Bonetti, G. Savini, R. Jalil, N. Bonini, D. M. Basko, C. Galiotis, N. Marzari, K. S. Novoselov, A. K. Geim, A. C. Ferrari, *Phys. Rev. B* **2009**, *79*, 424.

[142] A. C. Ferrari, J. C. Meyer, V. Scardaci, C. Casiraghi, M. Lazzeri, F. Mauri, S. Piscanec, D. Jiang, K. S. Novoselov, S. Roth, A. K. Geim, *Phys. Rev. Lett.* **2006**, *97*, 187401.

[143] A. C. Ferrari, *Solid State Commun.* **2007**, *143*, 47–57.

[144] J. Lee, E. K. Lee, W. Joo, Y. Jang, B.-S. Kim, *Science* **2014**, *344*, 286–289.

[145] V. N. Popov, P. Lambin, *Carbon* **2013**, *54*, 86–93.

[146] S. Heydrich, *Raman spectroscopy of nanopatterened graphene*, **2014**.

[147] Z. Ni, Y. Wang, T. Yu, Z. Shen, *Nano Res.* **2008**, *1*, 273–291.

[148] X. Zheng, W. Chen, G. Wang, Y. Yu, S. Qin, J. Fang, F. Wang, X.-A. Zhang, *AIP Adv.* **2015**, *5*, 57133.

[149] E. del Corro, M. Taravillo, V. G. Baonza, *Phys. Rev. B* **2012**, *85*, 33407.

[150] A. Das, S. Pisana, B. Chakraborty, S. Piscanec, S. K. Saha, U. V. Waghmare, K. S. Novoselov, H. R. Krishnamurthy, A. K. Geim, A. C. Ferrari, A. K. Sood, *Nat. Nanotechnol.* **2008**, *3*, 210–215.

[151] M. B. S. Larsen, D. M. Mackenzie, J. M. Caridad, P. Bøggild, T. J. Booth, *Microelectron. Eng.* **2014**, *121*, 113–117.

[152] C. Neumann, S. Reichardt, P. Venezuela, M. Drögeler, L. Banszerus, M. Schmitz, K. Watanabe, T. Taniguchi, F. Mauri, B. Beschoten, S. V. Rotkin, C. Stampfer, *Nat. Commun.* **2015**, *6*, 8429.

[153] Z. Ni, Y. Wang, T. Yu, Z. Shen, *Nano Res.* **2008**, *1*, 273–291.

[154] J. Zabel, R. R. Nair, A. Ott, T. Georgiou, *Nano Lett.* **2012**, *12*, 617–621.

[155] K. Akers, R. Aroca, A. M. Hor, R. O. Loutfy, *J. Phys. Chem.* **1987**, *91*, 2954–2959.

[156] R. Scholz, A.Yu. Kobitski, T.U. Kampen, M. Schreiber, and D.R.T. Zahn, *Phys. Rev. B* **2000**, *61*, 13659-13669.

[157] R. Aroca, R. E. Clavijo, *Spectrochim. Acta A* **1991**, *47*, 271–277.

[158] A. Dazzi, C. B. Prater, *Chem. Rev.* **2016**, *117*, 5146–5173.

[159] G. Binnig, C. F. Quate, and Ch. Gerber, *Phys. Rev. Lett.* **1986**, *56*, 930–934. 9.

[160] G. Meyer, N. M. Amer, *Appl. Phys. Lett.* **1988**, *53*, 1045–1047.

[161] N. A. Burnham, O. P. Behrend, F. Oulevey, G. Gremaud, P.-J. Gallo, D. Gourdon, E. Dupas, A. J. Kulik, H. M. Pollock, G. A. D. Briggs, *Nanotechnology* **1997**, *8*, 67–75.

[162] J. I. Goldstein, D. E. Newbury, J. R. Michael, N. W. Ritchie, J. H. J. Scott, D. C. Joy, *Scanning Electron Microscopy and X-Ray Microanalysis*, Springer New York, New York, NY, **2018**.

[163] K. Shihommatsu, J. Takahashi, Y. Momiuchi, Y. Hoshi, H. Kato, Y. Homma, *ACS omega* **2017**, *2*, 7831–7836.

[164] Chenming C. Hu, *Modern Semiconductor Devices for Integrated Circuits*, Pearson Education (US), **2009**.

[165] R. Chang, C. Lee, M. Lee, *Nanoscale* **2017**, *9*, 2324–2329.

[166] F. Qing, Y. Zhang, Y. Niu, R. Stehle, Y. Chen, X. Li, *Nanoscale* **2020**, *12*, 10890–10911.

[167] Z. Wu, X. Zhang, A. Das, J. Liu, Z. Zou, Z. Zhang, Y. Xia, P. Zhao, H. Wang, *RSC Adv.* **2019**, *9*, 41447–41452.

[168] Y.-C. Lin, C. Jin, J.-C. Lee, S.-F. Jen, K. Suenaga, P.-W. Chiu, *ACS Nano* **2011**, *5*, 2362–2368.

[169] S. Winters, N. C. Berner, R. Mishra, K. C. Dümbgen, C. Backes, M. Hegner, A. Hirsch, G. S. Duesberg, *Chem. Commun.* **2015**, *51*, 16778–16781.

[170] R. Tilmann, C. Weiß, C. P. Cullen, L. Peters, O. Hartwig, L. Höltgen, T. Stimpel-Lindner, K. C. Knirsch, N. McEvoy, A. Hirsch, G. S. Duesberg, *Adv. Electron. Mater.* **2021**, *7*, 2000564.

[171] A. Tullila, T. K. Nevanen, *Int. J. Mol. Sci.* **2017**, *18*.

[172] K. Takkinen, M. L. Laukkanen, D. Sizmann, K. Alfthan, T. Immonen, L. Vanne, M. Kaartinen, J. K. Knowles, T. T. Teeri, *Protein Eng.* **1991**, *4*, 837–841.

[173] L. von Lüders, R. Tilmann, K. Lee, C. Bartlam, T. Nevanen, K. Iljin, K. C. Knirsch, A. Hirsch, G. S. Duesberg, *Angew. Chem. Int. Ed.* **2023.** e202219024.

[174] K. Yoshimoto, M. Nishio, H. Sugasawa, Y. Nagasaki, *J. Am. Chem. Soc.* **2010**, *132*, 7982–7989.

[175] I. Jóźwik, *Electron. Mater.* **2016**, *44*, 11–16. 2.

[176] S. D. Costa, A. Righi, C. Fantini, Y. Hao, C. Magnuson, L. Colombo, R. S. Ruoff, M. A. Pimenta, *Solid State Commun.* **2012**, *152*, 1317–1320.

[177] A. Elhamid M., A. Elhamid, M. A. Hafez, A. M. Aboulfotouh, I. M. Azzouz, *J. Appl. Phys.* **2017**, *121*, 25303.

[178] S. Reich, C. Thomsen, *Philos. Trans. Royal Soc. A* **2004**, *362*, 2271–2288.

[179] F. Tuinstra, J. L. Koenig, *J. Chem. Phys.* **1970**, *53*, 1126–1130.

[180] H. Wang, J. You, L. Wang, M. Feng, Y. Wang, *J. Raman Spectrosc.* **2010**, *41*, 125-129.

[181] A. Eckmann, A. Felten, A. Mishchenko, L. Britnell, R. Krupke, K. S. Novoselov, C. Casiraghi, *Nano Lett.* **2012**, *12*, 3925–3930.

[182] N. V. Kozhemyakina, J. M. Englert, G. Yang, E. Spiecker, C. D. Schmidt, F. Hauke, A. Hirsch, *Adv. Mater.* **2010**, *22*, 5483–5487.

[183] N. Chiang, N. Jiang, L. R. Madison, E. A. Pozzi, M. R. Wasielewski, M. A. Ratner, M. C. Hersam, T. Seideman, G. C. Schatz, R. P. van Duyne, *J. Am. Chem. Soc.* **2017**, *139*, 18664–18669.

[184] A. Sidorenko, T. Krupenkin, A. Taylor, P. Fratzl, J. Aizenberg, *Science* **2007**, *315*, 487–490.

[185] C. Wirtz, T. Hallam, C. P. Cullen, N. C. Berner, M. O'Brien, M. Marcia, A. Hirsch, G. S. Duesberg, *Chem. Commun.* **2015**, *51*, 16553–16556.

[186] Mario Marcia, Andreas Hirsch, Frank Hauke, *FLatChem* **2017**, *1*, 89–103.

[187] N. I. Khan, E. Song, *Sensors* **2021**, *21*, 1335.

[188] Rajesh, Z. Gao, A. T. Charlie Johnson, N. Puri, A. Mulchandani, D. K. Aswal, *Appl. Phys. Rev.* **2021**, *8*, 11311.

[189] T. Murugathas, C. Hamiaux, D. Colbert, A. V. Kralicek, N. O. V. Plank, C. Carraher, *ACS Appl. Electron. Mater.* **2020**, *2*, 3610–3617.

[190] J. H. Jackson, C. R. MacCluer, *Bull. Math. Biol.* **2010**, *72*, 1315–1322.

[191] G. N. Wilkinson, *Biochem J.* **1961**, *80*, 324–332.

[192] G. Johansen, R. Lumry, *C. r. trav. lab. Carlsberg* **1961**, *32*, 185–214.

[193] W. W. Cleland, *Biochim. Biophys. Acta* **1963**, *67*, 104–137.

[194] B. Thakur, G. Zhou, J. Chang, H. Pu, B. Jin, X. Sui, X. Yuan, C.-H. Yang, M. Magruder, J. Chen, *Biosens. Bioelectron.* **2018**, *110*, 16–22.

[195] M. Kaisti, *Biosens. Bioelectron.* **2017**, *98*, 437–448.

[196] D.-J. Kim, I. Y. Sohn, J.-H. Jung, O. J. Yoon, N.-E. Lee, J.-S. Park, *Biosens. Bioelectron.* **2013**, *41*, 621–626.

[197] Y. Huang, X. Dong, Y. Liu, L.-J. Li, P. Chen, *J. Mater. Chem.* **2011**, *21*, 12358.

[198] Y. Ohno, K. Maehashi, Y. Yamashiro, K. Matsumoto, *Nano Lett.* **2009**, *9*, 3318–3322.

[199] M. B. Lerner, F. Matsunaga, G. H. Han, S. J. Hong, J. Xi, A. Crook, J. M. Perez-Aguilar, Y. W. Park, J. G. Saven, R. Liu, A. T. C. Johnson, *Nano Lett.* **2014**, *14*, 2709–2714.

[200] S. Xu, J. Zhan, B. Man, S. Jiang, W. Yue, S. Gao, C. Guo, H. Liu, Z. Li, J. Wang, Y. Zhou, *Nat. Commun.* **2017**, *8*, 14902.

[201] C. Melios, C. E. Giusca, V. Panchal, O. Kazakova, *2D Mater.* **2018**, *5*, 22001.

[202] S. Goniszewski, M. Adabi, O. Shaforost, S. M. Hanham, L. Hao, N. Klein, *Sci. Rep.* **2016**, *6*, 22858.

[203] S. Cheng, K. Hotani, S. Hideshima, S. Kuroiwa, T. Nakanishi, M. Hashimoto, Y. Mori, T. Osaka, *Materials* **2014**, *7*, 2490–2500.

[204] T. O. Paiva, K. Torbensen, A. N. Patel, A. Anne, A. Chovin, C. Demaille, L. Bataille, T. Michon, *ACS Catal.* **2020**, *10*, 7843–7856.

[205] M. Marciello, M. Filice, D. Olea, M. Velez, J. M. Guisan, C. Mateo, *Langmuir* **2014**, *30*, 15022–15030.

[206] J. Baniukevic, J. Kirlyte, A. Ramanavicius, A. Ramanaviciene, *Sens. Actuators B: Chem.* **2013**, *189*, 217–223.

[207] J. G. Vilhena, A. C. Dumitru, E. T. Herruzo, J. I. Mendieta-Moreno, R. Garcia, P. A. Serena, R. Pérez, *Nanoscale* **2016**, *8*, 13463–13475.

[208] F. Wu, P. A. Thomas, V. G. Kravets, H. O. Arola, M. Soikkeli, K. Iljin, G. Kim, M. Kim, H. S. Shin, D. V. Andreeva, C. Neumann, M. Küllmer, A. Turchanin *et al.*, *Sci. Rep.* **2019**, *9*, 20286.

[209] R. Tilmann, C. Bartlam, O. Hartwig, B. Tywoniuk, N. Dominik, C. P. Cullen, L. Peters, T. Stimpel-Lindner, N. McEvoy, G. S. Duesberg, *ACS Nano* **2023.** 3c01649.

[210] H. Kominami, K. Kobayashi, S. Ido, H. Kimiya, H. Yamada, *RSC Adv.* **2018**, *8*, 29378–29384.

[211] H. P. Erickson, *Biol. Proced. Online* **2009**, *11*, 32–51.

[212] nanoComposix, "Molecular Weight to Size Calculator", can be found under https://nanocomposix.com/pages/molecular-weight-to-size-calculator, **2023**.

[213] Fluidic Analytics, "How do you convert hydrodynamic (Stokes) radius to molecular weight?", can be found under https://www.fluidic.com/frequently-asked-questions/convert-hydrodynamic-radius-to-mw/, **2023**.

[214] M. Ku, J. Kim, J.-E. Won, W. Kang, Y.-G. Park, J. Park, J. Lee, J. Cheon, H. H. Lee, J.-U. Park, *Sci. Adv.* **2020**, *6.* eabb2891.

[215] N. N. M. Maidin, R. A. Rahim, N. H. A. Halim, A. S. Z. Abidin, N. A. Ahmad, Z. Lockman in *AIP Conf. Proc*, p. 20022.

[216] S. R. Forrest, *J. Phys.: Condens. Matter* **2003**, *15*, 2599–2610.

[217] *SDBSWeb: https://sdbs.db.aist.go.jp (National Institute of Advanced Industrial Science and Technology,date of access).*

[218] G. Salvan, C. Himcinschi, A. Y. Kobitski, M. Friedrich, H. P. Wagner, T. U. Kampen, D. Zahn, *Appl. Surf. Sci.* **2001**, *175-176*, 363-368.

[219] R. Kaiser, M. Friedrich, T. Schmitz-Hübsch, F. Sellam, T. U. Kampen, K. Leo, D. R. T. Zahn, *Fresenius J. Anal. Chem.* **1999**, *363*, 189–192.

[220] F. S. Tautz, S. Sloboshanin, J. A. Schaefer, R. Scholz, V. Shklover, M. Sokolowski, E. Umbach, *APS* **2000**, *61*, 933–947.

[221] S. Berger, K. Heimer, H. G. Mack, C. Ziegler, *Appl. Surf. Sci.* **2005**, *252*, 81–84.

[222] P. Aroca Jr., R. Aroca, G. J. Kovacs, R. O. Loutfy, *Langmuir* **1990**, *6*, 1050–1054.

Appendix

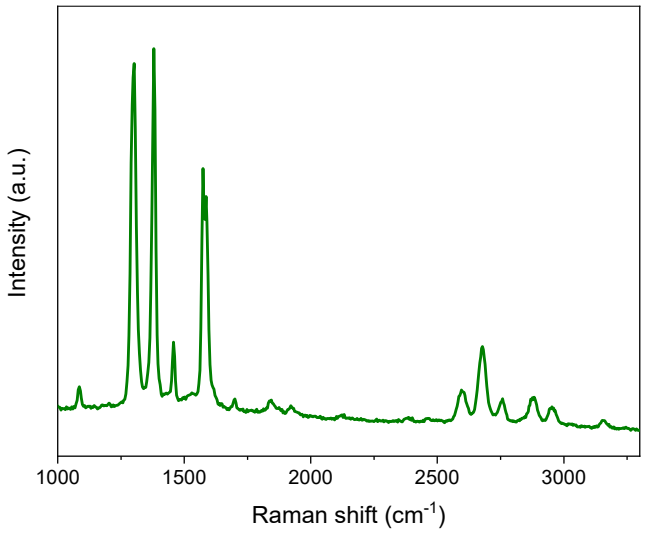

Figure A1. Raman spectrum of the sample which is displayed in Figure 29a) in blue. Spectrum acquired using 532 nm laser, 5 s integration time and 0.2 mW laser power showing high perylene packing density on graphene.

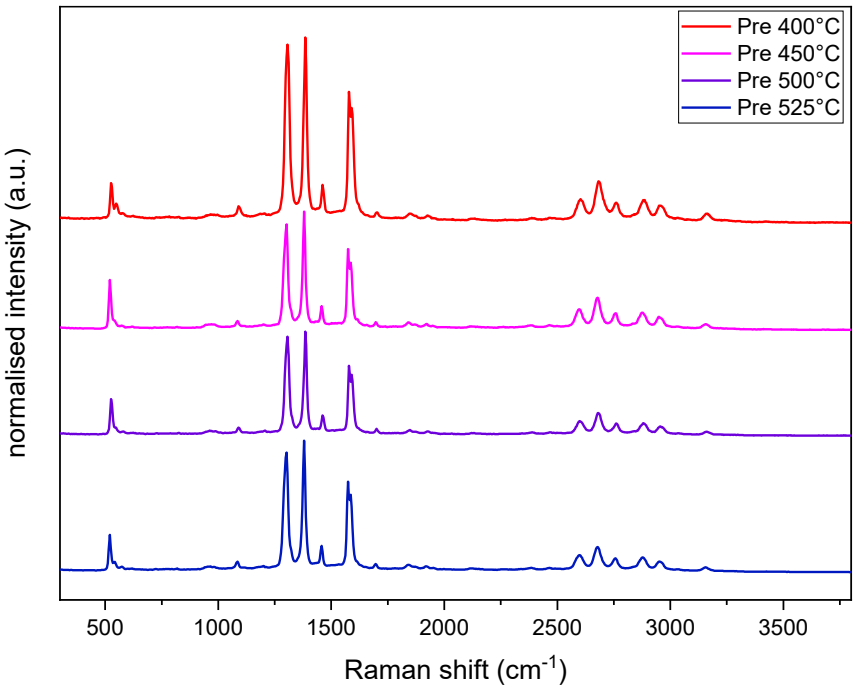

Figure A2. Normalised Raman spectra pre-annealing revealing successful PBI functionalisation of graphene with high packing density. Complementary data to Figure 35.

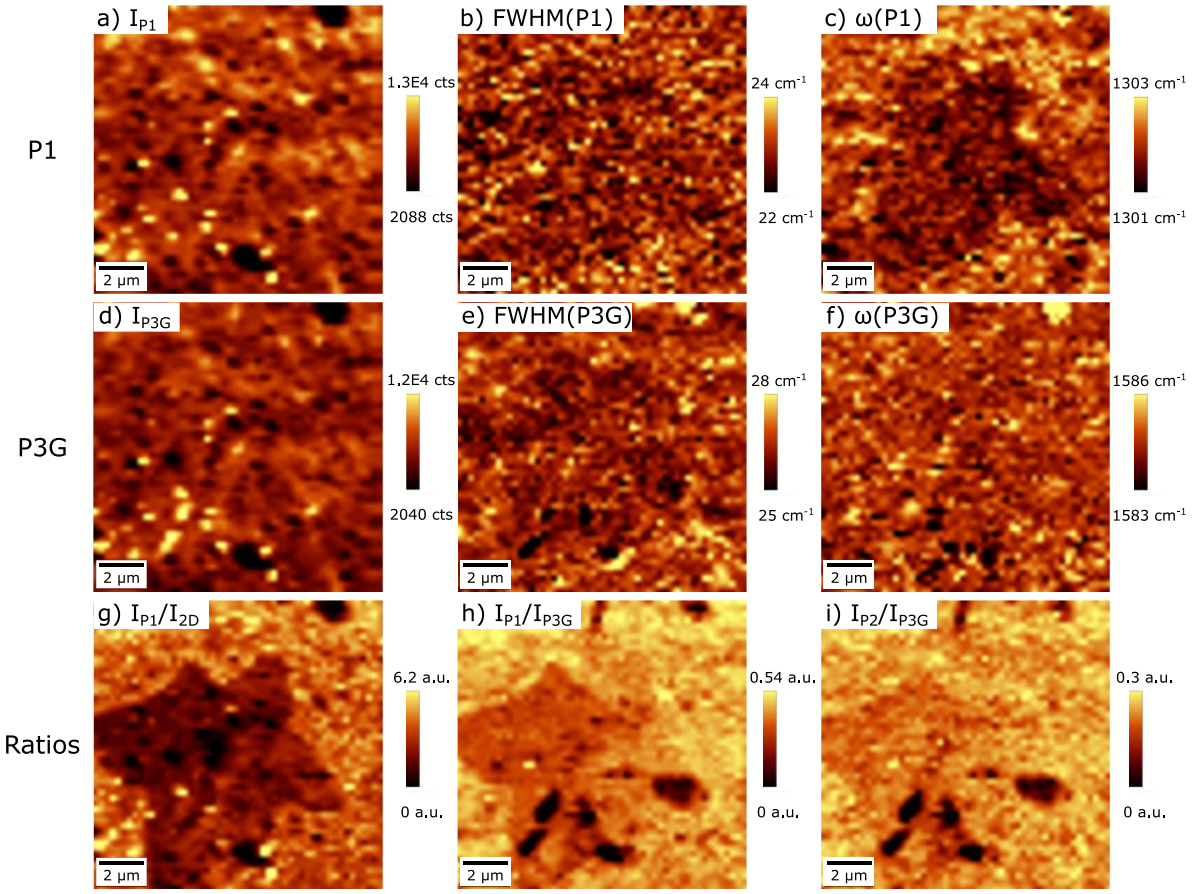

Figure A3. Additional Raman maps of the same scan as Figure 34.

Table A1. Number of AuNP/100 µm² for 20% and 100% AB2-AuNP application on the methamphetamine biosensor platform, after different washing procedures. Complementary to Figure 43a).

	DI water wash	5 min HEPES	30 s ultrasonication
20% AB2-AuNP	327 ± 44	374 ± 131	371 ± 188
100% AB2-AuNP	794 ± 72	1087 ± 241	1314 ± 478

Table A2. Number of AuNP clusters/100 µm² for 20% and 100% AB2-AuNP application on the methamphetamine biosensor platform, after different washing procedures. Complementary to Figure 43b).

	DI water wash	5 min HEPES	30 s ultrasonication

20% AB2-AuNP	4 ± 1	2 ± 2	3 ± 2
100% AB2-AuNP	30 ± 3	39 ± 31	50 ± 22

Table A3. Density of AuNP/100 µm² after application of different AB2-AuNP concentrations for several sample types: FLaT (control), methamphetamine biosensor platform and conventionally functionalised graphene with methamphetamine-AB coupling.

AB2-AuNP conc.	0.5%	20%	40%	100%
Control				98 ± 13
Methamphetamine biosensor platform	46 ± 53	386 ± 65	642 ± 85	798 ± 76
Conventionally functionalised + methamphetamine-AB coupling				1534 ± 250

Table A4. Average standardised $\widehat{\Delta R_{An}}$ and $\widehat{\Delta V_{Dirac,An}}$ values of methamphetamine biosensors after 10 µg/ml methamphetamine exposure. The methamphetamine biosensor platform was produced using different concentrations of methamphetamine-AB. Complementary data to Figure 52.

Meth-AB conc.	0.25 µg/ml	1 µg/ml	2 µg/ml	10 µg/ml
$\widehat{\Delta R_{An}}$	0.3 ± 5.7%	-2.7 ± 10.3%	-27.4 ± 13.1%	-23.1 ± 16.6%
$\widehat{\Delta V_{Dirac,An}}$	4.3 ± 9.5 V	24.8 ± 3.0 V	39.8 ± 7.8 V	10.1 ± 9.4 V

Table A5. Average standardised $\widehat{\Delta R_{An}}$ values of different functionalisation combinations on FLaT graphene. Complementary data to Figure 53.

Analyte	Methamphetamine	10 µg/ml

conc. / Antibody	0.3 µg/ml	3 µg/ml	10 µg/ml	Paracetamol
Meth-AB	-26.2 ± 9.4%	-32.2 ± 15.5%	-39.9 ± 14.4%	0.6 ± 5.8%
AB2			-7.3 ± 7.4%	

Table A6. Average standardised $\widehat{\Delta V_{Dirac,An}}$ values of different functionalisation combinations on FLaT graphene. Complementary data to Figure 53.

Analyte conc. / Antibody	Methamphetamine			Paracetamol
	0.3 µg/ml	3 µg/ml	10 µg/ml	10 µg/ml
Meth-AB	16.4 ± 7.1 V	31.2 ± 7.0 V	39.2 ± 7.8 V	-2.2 ± 5.5 V
AB2			12.7 ± 3.1 V	

Table A7. $\widehat{\Delta R_{An}}$ for differently functionalised GFETs. Either unfunctionalised or PBI unfunctionalised graphene was exposed to EDC/NHS chemistry and subsequent cortisol-Fab application. Different cortisol concentrations were applied and progesterone as control was tested additionally. Complementary results to Figure 61a) and c).

Analyte conc. / Func | AB		Cortisol	Progesterone
		10 µg/ml	10 µg/ml
Unf.	Cortisol-Fab	-2.7 ± 8.6%	
PBI	Cortisol-Fab	23.6 ± 21.8%	21.8 ± 33.1%
	No AB	-23.7 ± 11.0%	

Table A8. $\widehat{\Delta V_{Dirac,An}}$ for differently functionalised GFETs. Either unfunctionalised or PBI functionalised graphene was exposed to EDC/NHS chemistry and

subsequent cortisol-Fab application. 10 µg/ml was chosen as cortisol and progesterone concentrations. Complementary results to Figure 61b) and d).

Analyte conc. / Func | AB		Cortisol	Progesterone
		10 µg/ml	10 µg/ml
Unf.	Cortisol-Fab	16.0 ± 7.1 V	
PBI	Cortisol-Fab	-23.4 ± 13.4 V	7.9 ± 6.8 V
	No AB	9.4 ± 6.0 V	

Table A9. $\widehat{\Delta R_{An}}$ of two samples (S1 and S2) after methamphetamine-AB application and of the same samples after storage in air and subsequent methamphetamine exposure. Complementary data to Figure 57a.

Methamphetamine conc.	0 µg/ml	10 µg/ml	ΔR due to methamphetamine
S1	41.9 ± 4.1	1.5 ± 4.3	40.4
S2	52.2 ± 7.6	-2.1 ± 5.8	54.3

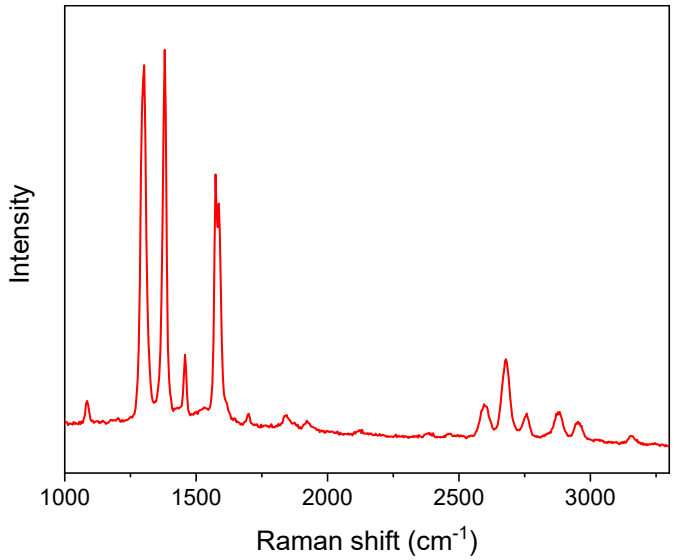

Figure A4. Raman spectrum of PBI functionalised graphene (Figure 58) showing high perylene packing density.

Table A10. $\widehat{\Delta R_{An}}$ of the same samples directly after functionalisation and after 208 days storage in N_2 for different methamphetamine concentrations. Complementary data to Figure 58a.

Methamphetamine conc.	0 µg/ml	0.3 µg/ml	3 µg/ml	10 µg/ml
Directly after functionalisation	28.6 ± 10.6	-19.1 ± 6.0	-45.7 ± 5.4	-44.5 ± 10.6
After 208 days	-22.4 ± 7.6	-43.9 ± 6.7	-56.1 ± 3.4	-67.2 ± 6.3
$\widehat{\Delta R_{An}}$ due to storage	-51.0	-24.8	-10.4	-22.7

Table A11. $\widehat{\Delta V_{Dirac,An}}$ of the same samples directly after functionalisation and after 208 days storage in N_2 for different methamphetamine concentrations. Complementary data to Figure 58b.

Methamphetamine conc.	0 µg/ml	0.3 µg/ml	3 µg/ml	10 µg/ml
Directly after functionalisation	-14.5 ± 4.0	7.8 ± 4.4	28.9 ± 3.9	16.5 ± 9.2
After 208 days	26.4 ± 5.7	35.5 ± 3.4	54.0 ± 4.6	52.3 ± 2.7
$\widehat{\Delta V_{Dirac,An}}$ due to storage	40.9	27.7	25.1	35.9

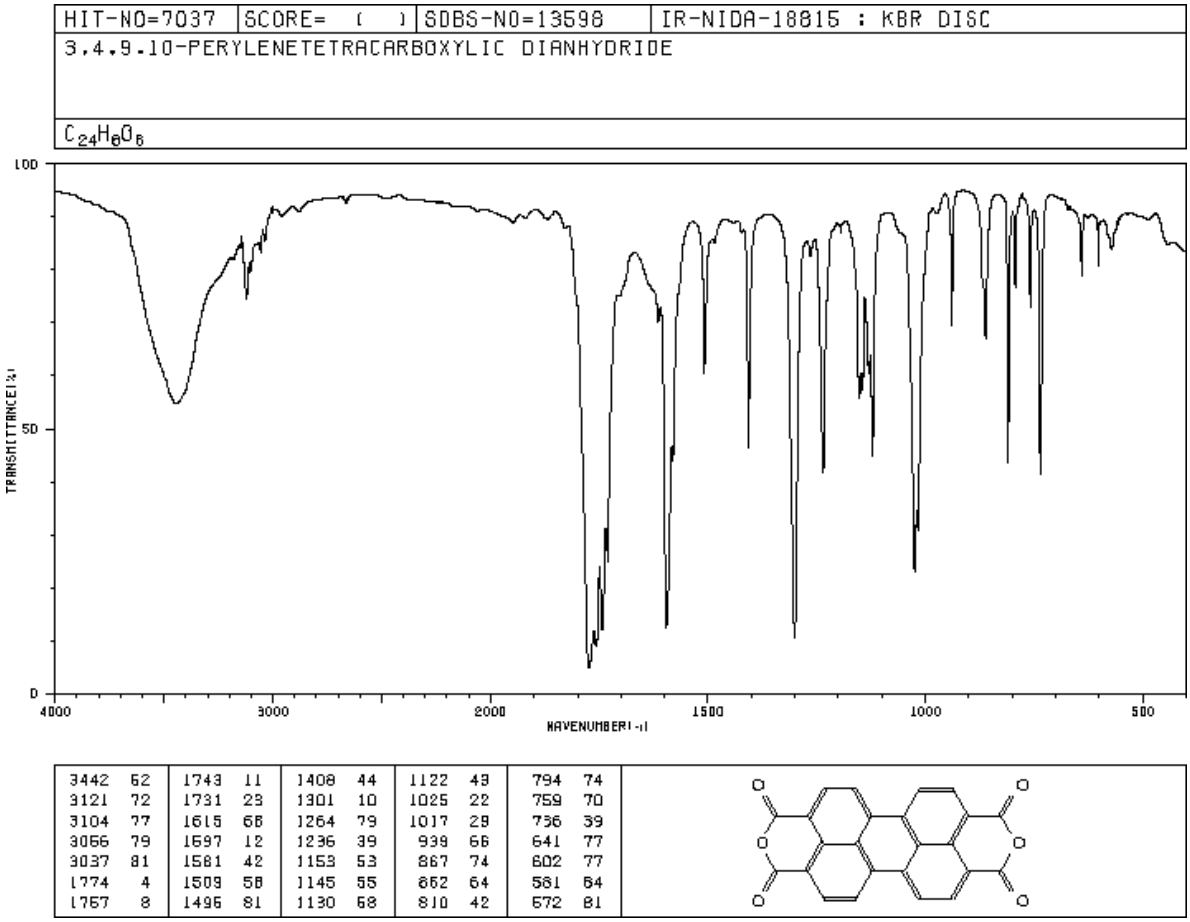

Figure A5. FTIR spectrum of PTCDA from the SDBS.[217] Extremely high agreement of peak positions with the spectrum from Figure 65a).

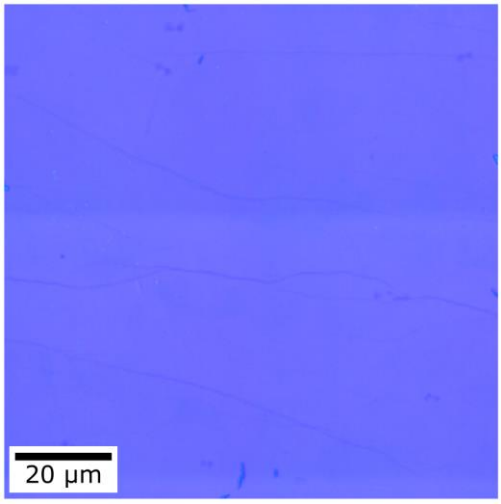

Figure A6. Optical image of the location of the Raman maps displayed in Figure 66d-g) and the PTA maps in Figure 67.

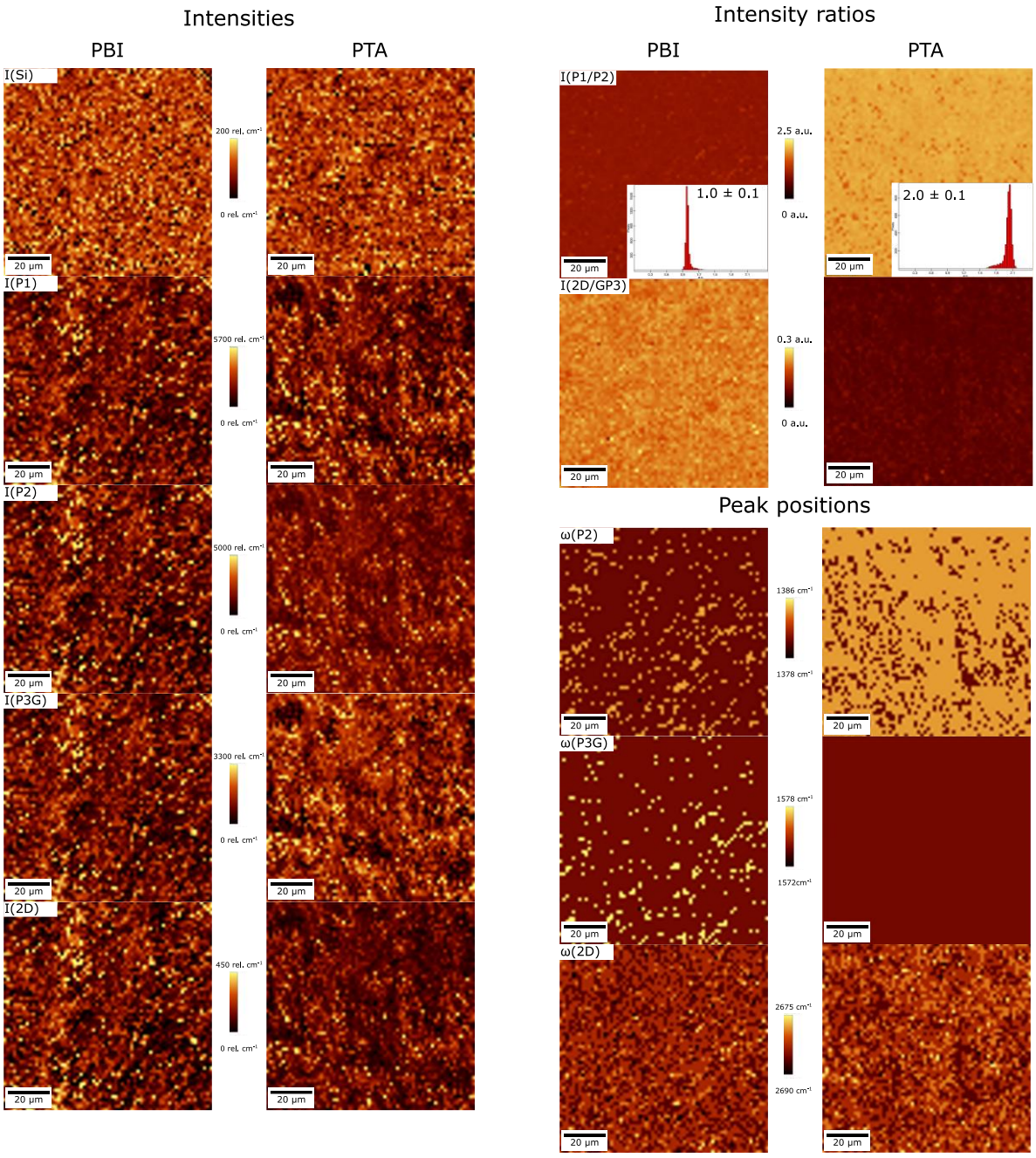

Figure A7. Complementary Raman maps of PBI and PTA FLaT graphene to Figure 67.

Table A12. AuNP /100 µm² for methamphetamine biosensor platforms generated by PBI and PTA functionalised graphene samples, after subsequent AB2-AuNP application in various concentrations. Complementary data to Figure 70a).

AB2-AuNP conc.	0.5%	20%	60%	100%

PBI	3.3	188.5 ± 35.6	450.7 ± 122.5	837.0 ± 117.2
PTA	3.6 ± 2.6	176.9 ± 18.0	520.0 ± 57.1	1142.1 ± 121.9

Table A13. AuNP cluster/100 µm² for methamphetamine biosensor platforms generated by PBI and PTA functionalised graphene samples, after subsequent AB2-AuNP application in various concentrations. Complementary data to Figure 70b).

AB2-AuNP conc.	0.5%	20%	60%	100%
PBI	0	0.7 ± 1.2	9.9 ± 3.1	15.1 ± 4.2
PTA	0	0.5 ± 0.8	9.9 ± 2.5	18.2 ± 5.5

Table A14. ΔR and ΔV_{Dirac} of methamphetamine biosensors prepared using either PBI or PTA for FLaT. Complementary data to Figure 71.

Perylene	PBI	PTA
$\widehat{\Delta R_{An}}$	-26.2 ± 9.4%	-30.1 ± 16.8%
$\widehat{\Delta V_{Dirac,An}}$	16.4 ± 7.1 V	27.5 ± 7.7

List of Publications and Presentations

Publications

- S. Akça**, L. v. Lüders**, G. S. Düsberg, W. Elsaesser, N. Nicoloso, R. Riedel, „Time resolved MIR Reflection-Absorption Spectroscopy of N_2O, CO and CH_4 Adsorption on Graphene", *The Journal of Physical Chemistry C,* **2023**, 127, 10, 4998–5003
- **L. von Lüders**, R. Tilmann, K. Lee, C. Bartlam, T. Stimpel-Lindner, T. K. Nevanen, K. Iljin, K. C. Knirsch, A. Hirsch, G. S. Duesberg, "Functionalisation of Graphene Sensor Surfaces for the Specific Detection of Biomarkers", *Angewandte Chemie International Edition*, **2023**, 202219024
- R. Tilmann, C. Weiß, C. P. Cullen, L. Peters, O. Hartwig, **L. Höltgen**, T. Stimpel-Lindner, K. C. Knirsch, N. McEvoy, A. Hirsch, G. S. Duesberg, "Highly Selective Non-Covalent On-Chip Functionalization of Layered Materials", *Advanced Electronic Materials*, **2021**, 7, 2000564

Presentations

- "Specific Detection of Methamphetamine with Non-Covalently Functionalised Graphene Field-Effect Transistors", Conference Graphene Week, Munich, Germany, **05-09 September 2022** (*oral*)
- "Specific Drug Detection with Non-Covalently Functionalized Graphene Field-Effect Transistors", Graphene2021 International Conference, Grenoble, France, **26-29 October 2021** (*oral*)
- "Functionalization of Graphene by Perylene", Conference Chem2Dmat, Dresden, Germany, **03-06 September 2019** (*poster*)
- "Functionalization of Graphene by Perylene", Graphene2019 International Conference, Rome, Italy, **25-28 June 2019** (*poster*)

List of Figures

List of Tables